UNIVERSITY OF CALIFORNIA

Los Angeles

High-dimensional Quantum Information Processing with Time-Frequency Qudits

A dissertation submitted in partial satisfaction of

the requirements for the degree

Doctor of Philosophy in Electrical and Computer Engineering

by

Kai-Chi Chang

2022

ABSTRACT OF THE DISSERTATION

High-dimensional Quantum Information Processing with Time-Frequency Qudits

by

Kai-Chi Chang
Doctor of Philosophy in Electrical and
Computer Engineering

University of California, Los Angeles, 2022
Professor Chee Wei Wong, Chair

High-dimensional entanglement in qudit states provides a route to realize large-scale, precisely controllable, practical systems for advanced quantum information processing, quantum secured communications, quantum metrology, and complex quantum computation. Many quantum platforms are currently subject to extensive research for superdense encoding, such as trapped ions, superconducting circuits, defect centers in solid-state crystals, mechanical oscillators, and photons. While all platforms provide unique advantages as well as challenges, optical quantum states are of particular interest, because they can interact with other quantum systems, and can be transmitted over long distances while preserving their quantum coherence. A large variety of quantum resources using optical quantum states has been demonstrated, however most of implementations suffer from high complexity, ultimately limiting their scalability. Mode-locked biphoton frequency combs (BFCs), which are intrinsically multimode in the temporal and frequency degrees of freedom within a single spatial mode, naturally facilitating the generation and manipulation of high-dimensional entanglement in large-scale quantum systems. Such BFCs have been demonstrated over fiber- and chip-compatible platforms. However, there is a huge gap between the maximal number of time and frequency modes and the dimensionality of the entanglement characterized experimentally, with the major challenge of certifying such high-dimensional entanglement by a number of accessible measurements. Quantifying and certifying the amount of entanglement in a high-dimensional quantum system has been a long-standing question in the quantum optics community. Therefore, there is an urgent need to generate and to certify large and

complex photon states without increasing source complexity, while still enabling coherent quantum state control and detection. In this dissertation, we focus on realization, quantification and applications of such high-dimensional optical quantum states. First, we demonstrated a high-dimensional doubly-resonant BFC by achieving record-high Hong-Ou-Mandel (HOM)-interference revivals and Franson interference recurrences. We certify a Hilbert-space high-dimensionality of at least 648 using a time-bin Schmidt number of 18 and frequency-polarization hyperentanglement in such a BFC. Second, we demonstrated first high-dimensional entanglement distribution using a singly-resonant BFC with the record-high Franson visibility 98.81% with 16 time-bins and average frequency-binned Franson visibility of 98.03% for 5 frequency-pairs at a 10-km distance. High-dimensional time-frequency entanglement is certified by frequency-bin Schmidt number of 4.17 and a measured time-bin Schmidt number of 13.13. Third, we explore the role of cavity finesse within our singly-resonant BFCs. Increasing cavity finesse can increase the probability to detect single-photons at multiple cavity round-trips and can flatten the fall-off of Franson recurrence visibilities. Fourth, we demonstrate first genuine time-reversible ultranarrow photon-pair source with over 5,000 modes using asymmetric singly-resonant BFCs operating in telecom-band. Fifth, we demonstrate essential functionalities for quantum networking, including frequency-multiplexed high-dimensional time-bin encoding with our BFC sources. We perform proof-of-principle frequency-multiplexed high-dimensional time-bin (QKD) using a singly-resonant BFC. We measured photon information efficiency (PIE) up to 15 bits per coincidence for 5 frequency pairs of a singly-resonant BFC and 5 kbits/s raw key rate towards high-dimensional quantum communication. The secure key rate (SKR) is obtained to be 1.1 kbits/s with PIE of 2.41 bits per coincidence, secured by our high-visibility frequency-binned Franson interference. Finally, we investigated the first experimental demonstration of chip-scale two-qubit SWAP gate that can be used for scalable high-dimensional quantum computing. We observe high fidelity in the SWAP gate logical basis, and phase coherent quantum fringes after SWAP operation with high visibility. We have investigated the fundamental physics of BFC on scaling its Hilbert space dimensionality for complex quantum information processing, the versability of singly-resonant BFC for real-world quantum photon efficient communications, and the silicon photonic two-qubit SWAP gate operation towards high-dimensional quantum optical computations. Our work represents an important step forward in the generation, certification and distribution of complex quantum states using telecom compatible fiber systems in a single spatial mode. Such large-scale quantum states would then be well suited for the applications, including high-dimensional entanglement teleportation,

quantum simulations, interconnecting matter qubits, on-chip quantum computing and storage, and various quantum communication protocols based on superdense time- and frequency-bin encodings.

The dissertation of Kai-Chi Chang is approved.

Jeffrey H. Shapiro

Andrei Faraon

Vwani Roychowdhury

Eric Hudson

Chee Wei Wong, Committee Chair

University of California, Los Angeles

2022

This dissertation is dedicated to my family for their unwavering support.

TABLE OF CONTENTS

LIST OF FIGURES

LIST OF TABLES

ABBREVIATIONS

BFC	Biphoton Frequency Comb
BPF	Band-pass filter
BS	Beam Splitter
CHSH	Clauser-Horne-Shimony-Holt
CNOT	Controlled-not
CW	Continuous Wave
dB	Decibel
DCM	Dispersion Compensation Module
DL	Delay line
DoF	Degree of freedoms
DWDM	Dense Wavelength Division Multiplexing
EPR	Einstein-Podolsky-Rosen
FBG	Fiber Bragg grating
FPC	Fiber polarization controller
FP	Fabry-Pérot
FSR	Free spectral range
FWHM	Full-width at half-maximum
GVD	Group velocity dispersion
HBT	Hanbury-Brown-Twiss
HOM	Hong-Ou-Mandel
ITU	International Telecommunication Union
JSA	Joint Spectral Amplitude
JSI	Joint Spectral Intensity
JTA	Joint Temporal Amplitude
JTI	Joint Temporal Intensity

LOQC Linear-optical quantum computation

LPF Long-pass filter

LPDC Low-density parity-check

MZI Mach-Zehnder interferometer

OPO Optical Parametric Oscillator

PBS Polarization Beam Splitter

PIE Photon Information Efficiency

PPKTP Periodically poled $KTiOPO_4$

QIP Quantum Information Processing

QKD Quantum Key Distribution

QPT Quantum Process Tomography

QST Quantum State Tomography

SFWM Spontaneous Four-Wave Mixing

SKR Secret-Key Rate

SMF Single Mode Fiber

SNSPD Superconducting Nanowire Single-Photon Detector

SPDC Spontaneous Parametric Down-Conversion

TE Transverse Electric

TM Transverse Magnetic

ACKNOWLEDGEMENTS

I would like to firstly thank Prof. Chee Wei Wong for being my supervisor and for supporting me both academically and financially, as well as for providing me with many great opportunities. I am thankful for his suggestions, discussions, and for the freedom and support he gave me to pursue new ideas.

I would like to thank the University of California, Los Angeles (UCLA) for their financial support in the form of a Dissertation Year Fellowship, a J. Yang Scholarship, as well as their financial support with an Electrical and Computer Engineering Department Fellowship.

I thank the Ministry of Education from Taiwan for financial support in the form of an international fellowship.

Special thanks go to all members of the Fang Lu Mesoscopic Optics and Quantum Electronics Laboratory at UCLA. In particular, I would like to thank: Dr. Xiang Cheng for his guidance, supervision, discussions and help with the experimental work included herein; Murat Can Sarihan for countless discussions and help with several experiments, including the implementation of frequency-multiplexed time-bin encoded quantum key distributions; Dr. Yoo Seung Lee for helping on multiple experimental projects; Dr. Wenting Wang for experimental guidance; Dr. Abhinav Kumar Vinod for help with theoretical work. Finally, I would like to give special thanks to Dr. James F. Mcmillan for maintaining all equipment in the laboratories, and for building countless custom mechanical and electronic components, without which the experiments would not have been possible.

I acknowledge all our group partners for their support. Special thanks to Prof. Jeffrey H. Shapiro and Dr. Franco N. C. Wong for providing rigorous theoretical and experimental supports with insightful discussions along the way. I thank Prof. Zhenda Xie for building O-band Franson interferometry, and Prof. Yan-Xiao Gong for providing theoretical modeling of BFC. I would like to express my gratitude to Dr. Vikas Anant for providing the state-of-the-art superconducting nanowire single-photon detectors (SNSPDs) and his support, without which our works would not be possibly demonstrated as successfully.

I would like to thank our external collaborators: Prof. Kocaman for designing SWAP gate chip; Prof. Mingbin Yu, Dr. Patrick Guo-Qiang Lo and Dr. Dim-Lee Kwong for fabrication of SWAP gate chip; Prof. Faraon for proving us the single-photon counters; Prof. Caram for kindly sharing their Hydraharp and Quantum Opus SNSPDs with us.

Finally, I would like to thank my wife, as well as my parents and my brother for their constant support and love. Without your encouragement, patience and sacrifice I would not be where I am now.

VITA

2010-2014	B.S. (Physics), National Central University, Taoyuan, Taiwan
2014-2016	M.S. (Electrophysics), National Chiao-Tung University, Hsinchu, Taiwan
2016-2022	Ph.D. Candidate (Electrical and Computer Engineering), University of California, Los Angeles, USA

Chapter 1

Introduction

The fundamental unit of quantum information processing (QIP) is the qubit, which is a two-state systems. High-dimensional qudit states, however, exhibits higher degree of complexity via the Hilbert space dimensionality scaling d^N (with d and N being the number of dimensions and parties, respectively), which is indispensable for the generation and the precise control of large-scale quantum systems for fundamental loophole tests of quantum nature [1-4] and real-world quantum applications. These high-dimensional systems can be used for significantly boosting the quantum information capacity, enhancing link speeds [5-10] and noise resilience in quantum communications [6, 11-15], enabling advanced quantum metrology [16, 17], and for new algorithms in quantum simulations and computations [18-21].

There are several platforms can provide the state-of-the-art encoding and decoding of large-scale quantum states. For instance, these systems span atomic [22], superconducting [23], and photonic qudits [24]. In high-dimensional photonic systems, there are two fundamentally different approaches to encode quantum information, the continuous-variable approach, and the discrete-variable approach. Whereas the high-dimensional continuous-variable methods process quantum information based on quantized electric field quadratures of the squeezed states [25, 26], the high-dimensional discrete-variable approach operates quantum information based on individual mode of single-photon Fock states [27-29].

Continuous-variable quantum information is based on the encoding in the amplitude and phase of the photons, which are continuous degrees of freedom (DoFs), and they are detectable by photon-number resolving detectors [30] or linear detectors via homodyne detections. This approach generates very large-scale photonic quantum systems for highly complex graph states and multimode entangled networks in optical parametric oscillators (OPOs), usually operating either above or below threshold [31-38]. However, the current record fidelities are below 90% [35, 39, 40], and the individual control of each frequency mode has proven difficult due to the average several hundred MHz level free-spectral range (FSR). Furthermore, their large and complex setups require sophisticated stabilized OPO systems, and so these systems are not yet fully suitable for applications outside of the lab.

Discrete-variable systems, in contrast, are based on the creation and detection of various DoFs of single-photons. This method allows the generation and precise control of individual modes in large-scale integrated quantum systems [41-44], and the state-off-the art SNSPDs can be directly used in correlation and coincidence measurements. The main advantage of discrete-variable systems is the capability of realizing unit fidelity entangled quantum states and precise control of each mode. A drawback is that current technology mostly allows for probabilistic entangled sources that scale unfavorably with an increasing N of qudits, which can be tackled by incorporating deterministic high-fidelity single-photon sources [45, 46], highly efficient SNSPDs with near-unity system detection efficiency [47-49], ultra-low dark counts [50], and sub-3 ps temporal resolution [51] for unit fidelity and deterministic QIP using single-photons.

Initial creation and control of discrete-variable photonic qudit systems have been very successful by processing quantum information on spatial, orbital angular momentum, and polarization modes [52-70]. However, polarization entanglement is intrinsically two-dimensional, and therefore limiting its scalability in generating high-dimensional states. For spatial and orbital angular momentum, despite their success, the footprint and the setups complexity of these approaches necessarily increases as the dimensionality of qudit increases, owing to the spatially distinct nature of the exploited DoFs. This ultimately poses a significant limitation to the degree of complexity that is achievable for practical systems.

In stark contrast, the discretized temporal and frequency modes, which are intrinsic characteristics in mode-locked biphoton frequency combs (BFCs) [71, 72], has been rapidly studied recently [73-92], enabling scalable generation and manipulation of high-dimensional [75-77, 80, 86, 90, 92], hyperentanglement [75, 84, 86, 92], or multipartite states [76, 78, 84, 93] in a single spatial mode. The distinct multimode temporal and frequency modes in BFC naturally allow dense quantum information encoding in their temporal and frequency correlations for practical high-dimensional quantum interconnects [94-106].

To realize the aforementioned potential and possible applications with BFCs, a major piece of functionality is still missing for linear-optical quantum computation (LOQC), as suggested by the Divincenzo's criteria [107], comprised of single-qubit rotations plus a two-qubit entangling gate, capable of synthesizing any arbitrary quantum operation. The intrinsic multiple time and frequency mode within a single spatial mode of BFC make them useful DoFs for encoding information presents a series of unique challenges for QIP, such as how to quantify and certify the genuine high-dimensional entanglement with number of accessible measurements, or how to efficiently distribute such high-

dimensional entanglement towards multi-user quantum network applications.

In this dissertation, we attempt to address these specific challenges. Through the use of the newly developed BFC [72, 75, 78, 84, 92, 108-111], a telecom device incorporating both fiber Fabry-Pérot (FP) etalons and mode-locking techniques, controlling precisely both the joint spectral intensity (JSI) and joint temporal intensity (JTI) of the spontaneous parametric down-conversion (SPDC). In the first study, we have demonstrated a high-dimensional BFC by achieving 61 Hong-Ou-Mandel (HOM) recurrences interference, a foundational two-qubit gates in the LOQC [112] and 16 Franson revivals interference, a nonlocal interferometry that is important for testing fundamental quantum nature [4], distributing time-energy entanglement and encoding large-alphabet time-bins in fiber links [5, 6, 13, 78, 113-117], both with near-unity visibility. We developed new techniques to quantify and certify such a BFC with a lower-bound of Hilbert-space dimensionality at 648 with 6.28 bits/photon classical information capacity that can potentially be encoded for classical information transmission over a quantum channel using only biphotons. This realization of a 13 photonic qudits using a doubly-resonant BFC opens new practical applications such as high-dimensional quantum secure communication, and cluster state quantum computations [92]. We have demonstrated novel high-dimensional time- and frequency-binned entanglement distribution using a singly-resonant BFC [111]. First, the spectral purity of our singly-resonant BFC is characterized by a heralded $g^{(2)}$ measurement of 0.035, verifying the pure single longitudinal resonator mode biphoton emission. After such entanglement distribution, the best time-binned and frequency-binned Franson visibility is up to 98.8% and 96.7%, respectively. The averaged decrease of Franson interference visibility after such distribution is only 2%, compared to our Franson visibilities before the distribution, showing the high-quality energy-time entanglement distribution via a singly-resonant BFC. We directly observed JTI in a mode-locked singly-resonant BFC using the second-order cross-correlation function measurements with a FSR of 5.03 GHz cavity to probe biphoton phase coherence in fiber cavity-filtered scheme for the first time. Then, we measured the time-energy entanglement of 5.03 and 15.15 GHz FSR mode-locked singly-resonant BFCs via Franson interferometry, with interference fringes observed over 6 and 2 time-bins, and with optimum central time-bin accidental-subtracted visibility of 98.97% and 97.79%, respectively. We have further investigated the role of cavity finesse F in controlling JTI of mode-locked singly-resonant BFCs on both signal-idler temporal second-order cross-correlation functions and Franson interference. Utilizing a cavity finesse F of 200, we present a theoretical ~54-fold improvement of Franson visibility compared to the Franson visibility with cavity finesse F of 11.14 at 16 cavity round-trip times, with all of the Franson interference recurrence visibilities are over than the

quantum-classical limit of 70.7%, violating Bell's inequality. We demonstrate time-reversible ultranarrow-band photon-pair generation with narrowest 42.63 MHz FSR, 4.587 MHz linewidth by asymmetric singly-resonant BFCs. We completely resolve the JTI of such source and verify the single-photon Fock state characteristics with multimode emission are preserved under time-reversal symmetry. This photon-pair source has over 5,000 modes in telecommunication-band. We implemented high-dimensional QKD with dense wavelength division multiplexing (DWDM) time-bin encoding with BFC sources [118-122]. We have encoded PIE up to 15 bits per coincidence using our frequency-multiplexed singly-resonant BFC, and the total SKR is 1.1 kbits/s with a PIE of 2.41 bits per coincidence. The security of our high-dimensional QKD scheme is based on a custom-built Franson interferometer, with highest accidental-subtracted interference visibility up to 99.66%. The performance of our high-dimensional QKD can be further increased with lower DWDM crosstalk and brighter SPDC photon source. Along with dual-basis Franson interferometry [123, 124], unconditional security of energy-time entanglement based high-dimensional QKD can be achieved with high secure-key throughput, and our scheme can be readily utilized for fully connected bipartite-entangled multi-user quantum communication network. Finally, we investigated the first experimental demonstration of chip-scale two-qubit SWAP gate, an efficient chip-scale deterministic cascaded CNOT gates that swaps the polarization DoF in single-photon with its spatial-momentum DoF [125-127]. We performed SWAP gate projection measurements, observing 97.20 ± 0.14% high fidelity in quantum gate logical basis, realizing an on-chip fidelity of up to 97.30 ± 0.30% for quantum state tomography (QST) and a net on-chip fidelity of up to 95.44 ± 0.21% for quantum process tomography (QPT). In addition, we demonstrate the polarization-to-spatial qubit transfer's phase coherence, observing an average self-interference visibility up to 98.68 ± 0.17%. Our two-qubit four-dimensional Hilbert space chip-scale SWAP gate can find future applications such as high-dimensional quantum gate operation, extending to qudits encoded in other DoFs, and for high-dimensional hyperentangled single-photon qudits [75, 84, 86, 92, 128], without requiring ancilla photons, for deterministic chip-scale QIP. To summarize, we have investigated the fundamental physics of a doubly-resonant BFC for certifying and scaling its Hilbert space dimensionality for complex QIP, the unique physics of singly-resonant BFC for real-world photon efficient entanglement distributions and QKDs, and the silicon photonic two-qubit four-dimensional SWAP gate operation for LOQC and deterministic QIP.

This dissertation is organized as follows. In Chapter 2 we describe in detail the methods and techniques used. The second chapter is structured along the development of the methodology for the results section from Chapter 3 to Chapter 5. Firstly, the methods to generate and detect photon pairs

are reviewed. Then, quantum interference and quantum state characterization are summarized in a general context, followed by a detailed introduction into high-dimensional time- and frequency-bin entanglement in mode-locked BFCs. In addition to reviewing already existing techniques, new results are also presented at the end of Chapter 2. In particular, a newly designed integrated hybrid photon pair source and engineering of JSI, novel methods to quantify Hilbert-space dimensionality of BFC, as well as a new technique to perform high-dimensional entanglement distribution using BFC are presented. We completely explore the underlying physics of singly-resonant BFCs. Chapter 3 tackles the important question of generation, certification and distribution of high-dimensional entanglement in BFCs. In Chapter 4 we highlight one of the prominent QIP task, the quantum communication testbed developed on the BFC sources. We cover our last missing piece for universal QIP, a two-qubit three-level on-chip CNOT gates in Chapter 5. We have a short summary section at the end of each chapter, stating the key areas for improvements in the future work. The Appendix section encompasses a great amount of information, including supplemental measurements, detailed theoretical results of mode-locked temporal cross-correlations, HOM, Franson and conjugate-Franson interferences, impact of cavity finesse F on JTI of BFC, Schmidt mode decompositions, entanglement of formation, design and fabrication and characterization of two-qubit SWAP gate.

Chapter 2

Methods and Techniques

2.1 Introduction

This chapter describes the methods and techniques that were used to collect and analyze the experimental results shown in Chapter 3 to 5. First, photon pair generation using nonlinear optics and the properties of optical resonators are reviewed. Second, the fundamentals of quantum interference and tomography are summarized. Then, the two types of entanglement (time-bin and frequency-bin) used in this work are introduced. Finally, a new integrated hybrid SPDC source is designed by controlling the JSI of the biphotons for generating high purity BFC, followed by the methods developed to characterize these types of high-dimensional entangled mode-locked BFC states.

2.2 Photon pair generation by means of nonlinear optical processes

One of the most common techniques to generate photonic quantum states is based on exploiting nonlinear optical interactions. While individual quantum emitters such as molecules [129-131], quantum dots [132, 133], and defect centers in crystals [134, 135] can be used to generate single photons deterministically, nonlinear optical sources are commonly used to directly generate photon pairs. These sources are therefore ideal to generate entangled quantum states, where the sources can be designed to emit photon pairs, entangled in one or more DoF [136]. The generation process is based on parametric optical interactions in nonlinear optical crystals or waveguides [137]. An important criterion for the type of nonlinear interactions possible in a given crystal or waveguide is their symmetry. Among the many different nonlinear interactions that can be achieved in second- and third-order nonlinear media, mainly two nonlinear optical interactions are used for the generation of optical quantum states: SPDC and spontaneous four wave mixing (SFWM).

SPDC entangled photon pairs are generated with a $\chi^{(2)}$ nonlinearity to convert a single higher-energy pump photon into a pair of correlated photons called signal and idler in a three-wave mixing interaction process see Fig. 2.1a. As this process conserves energy and momentum of the initial photon, the two photons are correlated, and can be entangled in many DoFs such as polarization,

orbital angular momentum, time and frequency. SFWM is a third-order nonlinear process, which is in many ways very similar to SDPC, with the difference that not only one, but two incident photons decay into a signal and idler photon, see Fig. 2.1b. Again, the energy and momentum are fully preserved in the four-wave mixing process, leading to strong correlations between the two generated photons.

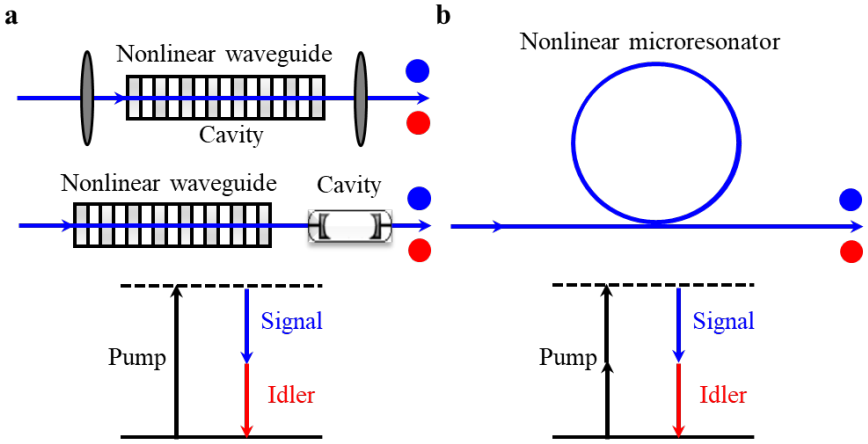

Fig. 2.1. Principles of biphoton frequency comb generation using SPDC and SFWM schemes. a) BFC generation with cavity-enhanced and post-filtered schemes. b) BFC generation with integrated on-chip microresonators. All these approaches lead to discrete energy-time correlated BFC.

The decay processes of SDPC and SFWM are essentially instantaneous (within the coherence-time of the initial photon), meaning that the signal and idler photons are generated at the same time. This strong correlation can lead to time-energy entanglement between the biphotons. Furthermore, the generation process is spatially local, meaning that the signal and idler photons are essentially created at the same position within the nonlinear crystal or waveguide. This property, together with momentum conservation can be used to generate entanglement in position and momentum. This type of entanglement is commonly exploited for ghost imaging [138], and can be used to demonstrate the famous Einstein-Podolsky-Rosen (EPR) Paradox [139]. One critical situation that has to be fulfilled in order to enable parametric frequency conversion is the phase-matching condition. Phase matching can be explained by the requirement that both energy and momentum have to be preserved in the nonlinear process [137]. In SPDC process, many different approaches have been achieved to achieve phase matching in dispersive media, such as periodic poling and birefringent phase matching. While in SFWM process, the requirement of anomalous dispersion is essential for phase matching.

2.3 Correlated photon detection measurements

Second-order correlation function $g^{(2)}(\tau)$ measurements are commonly used to identify the statistical properties of light in the temporal domain, which can be categorized into three main types: thermal, coherent, and quantum [140]. The second-order coherence can be measured using a Hanbury-Brown-Twiss (HBT) type setup [141], which consists of a beam-splitter followed by two single-photon detectors. The second-order coherence can then be extracted from coincidence measurements, as long as the temporal resolution of the single-photon detectors is higher than the first-order temporal coherence of the incident light [142]. The typical expected second-order coherence functions $g^{(2)}(\tau)$ for thermal, coherent and quantum light sources are summarized in Fig. 2.2. For a true single-photon emitter, the probability to emit two photons at the same time is zero, $g^{(2)}(0) = 0$, which is called anti-bunching. For photon-pair sources, typical photon bunching is observed, $g^{(2)}(0) = 2$. Finally, for a coherent field, the temporal photon distribution is fully random, leading to second-order coherence which is equal to 1 at all times.

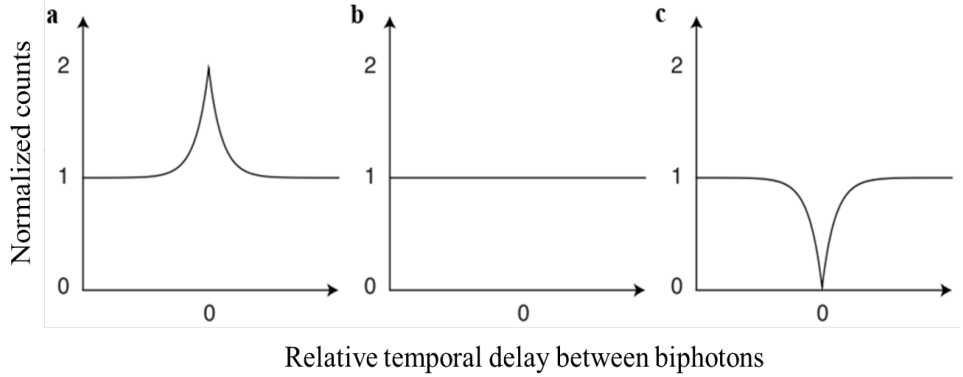

Fig. 2.2. Second-order coherence functions $g^{(2)}(\tau)$ for thermal, coherent and quantum light sources. a) Bunching statistics of thermal light. b) Coherent light statistics. c) Anti-bunching statistics of quantum light.

If the photons are generated over a spectral bandwidth which is larger than the bandwidth of the excitation field, the photons are emitted into multiple spectral modes using SPDC and SFWM sources. Indeed, it has been shown that the maximum of the second-order correlation function is directly related to the N, number of spectral modes of the photons with $g^{(2)}(0) = 1 + 1/N$ [74, 78].

For SPDC and SFWM sources, the single-photon anti-bunching behavior can also be measured on the condition of heralding, this definition has been adapted as heralded second-order correlation function $g_H^{(2)}(\tau)$. The measurement setup is done via splitting signal and idler photons first, then send one of them into a HBT type interferometer. Due to the complexity of acquiring the whole function,

usually the zero-delay value is calculated as $g_H^{(2)}(0) = \frac{C_{ABC}R_C}{C_{AC}C_{BC}}$, Where C_{ABC} denotes the triple coincidence rate of heralding and two heralded outputs, R_C stands for the heralding count rate, C_{AC} and C_{BC} are the coincidence rates between heralding and each heralded output, respectively. Detecting one photon of the photon pair result in projecting the other photon into a multimode heralded single-photon state, which exhibits non-classical antibunching behavior. Hence, $g_H^{(2)}(0) < 0.5$ means that quantum regime has been reached, and $g_H^{(2)}(0) \sim 0$ proves the high purity of the photon pair sources [111, 143]. Therefore, both the $g^{(2)}(\tau)$ and $g_H^{(2)}(0)$ measurements can therefore be used to determine the purity of the emitted photons, where pure photons are characterized by exhibiting only a single frequency mode.

2.4 Quantum interference

Quantum interference is at the basis of almost all applications harnessing optical quantum states. Quantum interference can be used to confirm the presence of entanglement [144], to transmit data in a secure way [145], to enable measurements with precision exceeding classical limits [146], and to perform quantum computation [56]. In this work, quantum interference will be used mainly as a tool to characterize the optical quantum states, generated in the SPDC and BFC sources.

In quantum mechanics, interference originates from the lack of information [147]. The interference phenomena in a Mach-Zehnder interferometer (MZI), see Fig. 2.3, can be described as single-photon interference, which arises from the absence of photon path information (or indistinguishability of photon paths). Starting with a source that emits a single photon, the photon passes through the interferometer and is then detected by a detector. After the first beam splitter (BS), the photon can take two alternative paths (1 and 2), to arrive at the detector. The probability of detecting the photon when it travels via path 1 is given by $P_1 = |a_1|^2$, with a_1 being the corresponding probability amplitude (which is in general a complex number). P_1 is directly proportional to the detection rate of the detector when path 2 is blocked. Similarly, the probability of detecting the photon when it travels via path 2 is given by $P_2 = |a_2|^2$, with the corresponding probability amplitude a_2. When both paths are open, interference occurs, and the total probability of the photon being detected is given by

$$P = |a_1 + a_2|^2 = P_1 + P_2 + 2\sqrt{P_1 P_2}\cos\varphi \tag{2.1}$$

where $\varphi = arg\{a1^* a2\}$ with 'arg' being the argument of a complex number (this corresponds to the

phase difference between the two optical paths). In quantum regime, interference occurs if and only if there is no path information anywhere in the universe. In contrast, when information is available, no interference occurs, and the probability of detecting the photon is given by

$$P = |a_1|^2 + |a_2|^2 = P_1 + P_2 \tag{2.2}$$

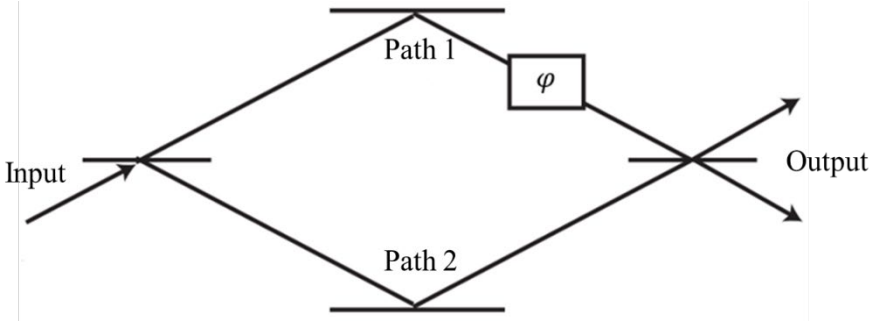

Fig. 2.3. Schematic of a standard Mach-Zehnder interferometer. An optical input is split into two paths 1 and 2 by a BS. The phase difference between these paths is described by φ. Both paths are then recombined using a second BS, and photons can be detected at one of the output ports (or both).

It is important to note that this information does not need to be extracted by a measurement; the presence of the path information alone is enough to destroy the interference [148]. Visibility V, which quantifies the quality of quantum interference can be defined as

$$V = \frac{P_{Max} - P_{Min}}{P_{Max} + P_{Min}} \tag{2.3}$$

Here P_{Max} and P_{Min} are the maximum and minimum measured values of P, respectively. It can be seen that for $P_1 = P_2$ (and complete unavailability of path information under ideal conditions) the visibility becomes unity ($V = 1$). Similarly, the complete availability of path information implies zero visibility. It is also possible to have a case where the visibility is in between 0 and 1. In such a case, if $P_1 = P_2 = P_0$, the total probability of detecting a photon is given by

$$P = 2P_0(1 + V\cos\varphi) \tag{2.4}$$

The quantum mechanical interpretation of interference thus allows us to consider the visibility as a measure of the unavailability of information.

Single photon interference discussed earlier is also often referred to as classical interference, as it can be perfectly described using classical wave optics, where a wave propagates through two paths and interferes with itself. Instead, two-photon interference, or quantum interference does not have such a classical analogy, and describes the phase dependent probability to measure biphoton coincidences. A famous example of two photon interference, which can be used to illustrate the concept, is the HOM effect, see Fig. 2.4, where two photons showing bunching behavior when they enter two different ports

of a BS [149]. If the two photons are identical (meaning they are fully indistinguishable, no information on which photon entered which port of the BS is available), the photons will always exit together at the same output port, and the probability that the two photons exit different ports becomes zero. With a detector at each output port, the probability of measuring photon coincidences goes to zero for perfectly indistinguishable photons. If a temporal delay between the photons is introduced, the photons become temporally distinguishable, can thus exit different output ports and coincidences can be detected. Furthermore, HOM interference results in a coherent superposition of either two photons exiting port 1 or port 2 of the BS. The output of two identical photons entering two different ports of a BS is therefore a path-entangled state

$$|\psi_{ent}\rangle = \frac{1}{\sqrt{2}}(|1\rangle_s|1\rangle_i + |2\rangle_s|2\rangle_i) = \frac{1}{\sqrt{2}}(|1\rangle|1\rangle + |2\rangle|2\rangle) \tag{2.5}$$

HOM interference can therefore be used to generate entanglement, and is at the basis of fundamental two-qubits gates and LOQC [112]. Reversing the HOM effect, one can immediately conclude that if a path-entangled state enters a BS, two indistinguishable photons will exit at different output ports, and the probability of detecting two photons at the same port is zero [149].

Let us consider a detail version of HOM effect for clarity. We have a BS with input ports 1 and 2 and output ports a and b. Measuring a photon at port a or b corresponds to a projection on

$$|\psi_{p,a}\rangle = \frac{1}{\sqrt{2}}(|1\rangle + i|2\rangle) \tag{2.6}$$

$$|\psi_{p,b}\rangle = \frac{1}{\sqrt{2}}(i|1\rangle + |2\rangle) \tag{2.7}$$

respectively, where the imaginary components result from a π phase shift upon reflection at the BS. For an entangled input state, the probability to measure photon coincidences at port combinations of a and b can be calculated as

$$|\psi_{ent}\rangle = \frac{1}{\sqrt{2}}(|1\rangle|1\rangle + e^{i\varphi}|2\rangle|2\rangle) \tag{2.8}$$

$$\langle\psi_{p,a},\psi_{p,b}| = \frac{1}{\sqrt{2}}(-i\langle 1,1| + \langle 1,2| + \langle 2,1| - i\langle 2,2|) \tag{2.9}$$

$$P_{a,b} = |\langle\psi_{p,a},\psi_{p,b}|\psi_{ent}\rangle|^2 = \frac{1}{4}(1+\cos\varphi) \tag{2.10}$$

$$P_{b,a} = |\langle\psi_{p,b},\psi_{p,a}|\psi_{ent}\rangle|^2 = \frac{1}{4}(1+\cos\varphi) \tag{2.11}$$

$$P_{a,a} = |\langle\psi_{p,a},\psi_{p,a}|\psi_{ent}\rangle|^2 = \frac{1}{4}(1-\cos\varphi) \tag{2.12}$$

$$P_{b,b} = |\langle\psi_{p,b},\psi_{p,b}|\psi_{ent}\rangle|^2 = \frac{1}{4}(1-\cos\varphi) \tag{2.13}$$

We can see the sum of all four possible outcomes is unity, but that for a given projection, clear interference in the photon coincidences is seen, which is the effect of two-photon interference. Similar

to the single-photon interference, it is possible to consider the visibility of HOM interference as a measure of photon distinguishability in all DoFs. Therefore, indistinguishable photons, in combination with HOM interference, generates a maximally entangled state. Vice versa, the visibility of entanglement-based two-photon interference, such as nonlocal Franson interference, can be used to confirm and quantify the presence of entanglement in the input quantum state [144].

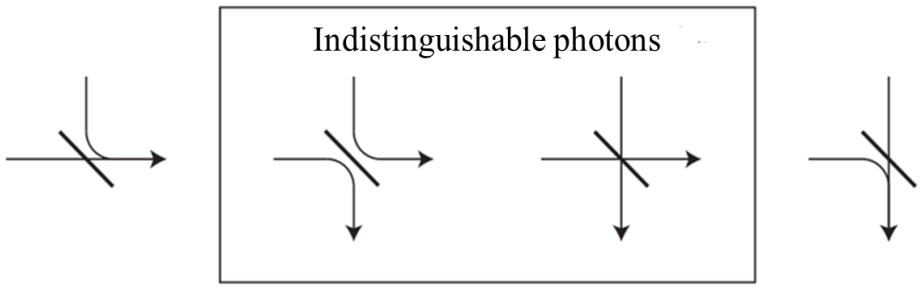

Fig. 2.4. Two-photon Hong-Ou-Mandel interference. Biphotons enter two different input ports of a BS. If the photons are perfectly identical, the two photons bunch and always exit one of the ports together, leading to a zero probability to detect coincidences between two detectors placed at the two output ports of the BS, which is called HOM dip.

Indeed, quantum entanglement, a particularly unique feature in quantum mechanics is where two or more quantum states are correlated and cannot be decided independently. A measurement of one quantum state will steer the state of the other instantaneously and nonlocally. Such entanglement is an important resource for QKD and communications protocols [5-7, 11, 13], quantum repeaters [150], quantum memories [151-154], and quantum computation [155, 156]. Photons can be entangled in different DoFs, such as spatial, orbital angular momentum, polarization [53, 56, 58, 62], time-bins [5-7, 75] and frequency-bins [75-78], which makes photons an ideal candidate for entangled sources. The most used is polarization entangled photon pairs, as polarization of photons can be conveniently manipulated and measured.

Another common and robust choice in fiber network, the time-energy entanglement, can be measured by two-photon Franson interference [144], as shown in Fig. 2.5. The nonlocal Franson interferometer is comprised of two unbalanced MZIs, each photon has 50% chance of entering the short and long paths, respectively. Therefore, there are four combinations of the paths the photons will take: $|s,s\rangle$, $|l,l\rangle$, $|s,l\rangle$ and $|l,s\rangle$, where s means the short path and l the long path. In the histogram for time intervals between the biphotons, as shown in Fig. 2.5(b), there will be three peaks, the central correlation peak comes from the superposition of indistinguishable quantum states $|s,s\rangle$ and $|l,l\rangle$, whereas the satellite peaks are from $|s,l\rangle$ and $|l,s\rangle$ states. The probabilistic amplitudes of $|s,s\rangle$ and

$|l, l\rangle$ interfere with each other on the conditions that the path difference between the arms of unbalanced MZIs is longer than the biphoton's coherence length, ruling out the possibility of the single-photon interference.

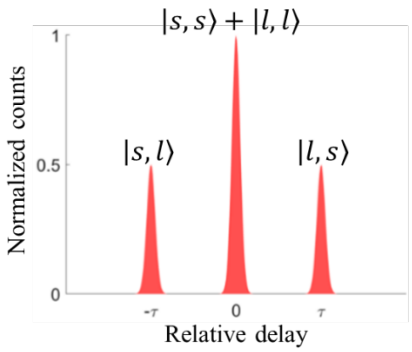

Fig. 2.5. Two-photon Franson interference. Quantum nonlocal signature of Franson interference with 3 correlation peaks separated by imbalance of a pair of MZIs. The central correlation peak comes from the superposition of indistinguishable quantum states $|s, s\rangle$ and $|l, l\rangle$, whereas the satellite peaks are from $|s, l\rangle$ and $|l, s\rangle$ states. Energy-time entanglement can be verified with Franson interference by Franson fringe visibility higher than 71%.

In real experimental schemes, the path difference should be long enough for the three temporal correlation peaks to resolve, since the timing jitter of single-photon detectors and the counting electronics bring a finite width to the coincidence peaks, and if they overlap with each other, the $|s, s\rangle$ and $|l, l\rangle$ states are no longer distinguishable with $|s, l\rangle$ and $|l, s\rangle$ states, this will result in 50% quantum interference visibility. In this work, the path difference in our Franson interferometer is designed to be ~5 ns, which satisfies the criteria for high visibility Franson interference. Post-selection is also necessary for us to achieve over 50% Franson visibility, to avoid counting all three correlation peaks, and we note that the post-selection loophole-free Franson interference has been demonstrated recently [4]. By post-selecting central peak in Franson interferometer, the number of coincidences corresponds to states $|s, s\rangle$ and $|l, l\rangle$ will be a function of the sum of phase on both unbalanced MZIs, which forms a two-photon interference fringe and hence its visibility quantifies the quality of time-energy entanglement of photons in photon pair sources. A Franson fringe visibility higher than 71% is sufficient to prove the time-energy entanglement of the quantum state [157].

Although HOM and Franson are two-photon interference effect, they are fundamentally different, the main difference is the way that interference is measured. HOM is essentially a HBT type local interferometry, whereas Franson interference occurs in nonlocal unbalanced MZIs. Therefore, HOM

interference visibility can inform us the single-photon indistinguishability in DoFs including spatial, polarization, time and frequency, and reveal the path-entanglement quality of the quantum states. On the other hand, visibility of nonlocal Franson interference can be used to confirm and quantify the presence of time-energy entanglement for the quantum state.

2.5 Quantum state and process tomography

QST is an experimental method that allows the extraction of the density matrix of a quantum state, which fully describes the quantum state [158]. Extending from HOM interference, we will illustrate an example for QST using an entangled two-photon state in two dimensions, which can be written as $|\psi_{ent}\rangle = \frac{1}{\sqrt{2}}(|1\rangle|1\rangle + |2\rangle|2\rangle)$, where 1 and 2 are two orthogonal modes. For this wave function the density matrix ρ is then given by

$$\rho = |\psi\rangle\langle\psi| = \frac{1}{2}(|1\rangle|1\rangle + |2\rangle|2\rangle)(\langle 1,1| + \langle 2,2|) \tag{2.14}$$

Using a set of orthogonal basis vectors $\{|1,1\rangle, |1,2\rangle, |2,1\rangle, |2,2\rangle\}$, this results in the ideal theoretical two-photon density matrix

$$\rho_{th} = \begin{pmatrix} 1/2 & \cdots & 1/2 \\ \vdots & \ddots & \vdots \\ 1/2 & \cdots & 1/2 \end{pmatrix} \tag{2.15}$$

where all the other elements not shown in this two-photon density matrix are 0. Since this is an entangled two-photon state in two dimensions, it is possible to measure this density matrix ρ_{th} through projection measurements (or truth table measurements) of the signal and idler qubits, resulting in a minimum of 16 required values. This approach is not limited to two-photon or two-dimensional quantum states. Indeed, it can be used for any quantum state, showing the power of this approach [159]. The photon counts collected in these projection measurements are mathematically given by:

$$n_v = C\langle\psi_v|\rho_{exp}|\psi_v\rangle \tag{2.16}$$

where C is a measurement constant dependent on the integration time. The challenge now is to reconstruct the density matrix ρ_{exp} from the measured n_v values. In particular, the measured density matrix can then be reconstructed using the following relations, where M and B have no direct physical meaning but are part of the mathematical reconstruction process

$$\rho_{exp} = \frac{1}{C}\sum_v M_v n_v \tag{2.17}$$

$$M_v = \sum_x \Gamma_x \left(\frac{1}{B}\right)_{x,v} \tag{2.18}$$

$$B_{x,y} = \langle \psi_x | \Gamma_y | \psi_x \rangle \tag{2.19}$$

$$C = \sum_k n_k \, , and \; Tr\{M_k\} = 1 \tag{2.20}$$

In addition to the measured values, a set of linearly-independent and normalized matrices Γ is required. Any set of such matrices can be used as long as they fulfill $Tr\{\Gamma_x \Gamma_y\} = \delta_{x,y}$.

A density matrix associated to a physical system has to be Hermitian and positive definite. However, the matrix extracted from measurements usually does not comply with this requirement. To retrieve a physically-meaningful density matrix, it is possible to perform a maximum-likelihood estimation, which is a method used to find the physically-realistic density matrix closest to the measured one [158]. Once the density matrix ρ_{exp} is found, we can extract the fidelity of the measured state. The state fidelity describes the overlap between the ideal theoretical and measured density matrix is given by

$$F = \left(Tr\left(\sqrt{\sqrt{\rho_{th}}\rho_{exp}\sqrt{\rho_{th}}}\right)\right)^2 \tag{2.21}$$

A fidelity of one corresponds to a perfect overlap with the ideal entangled state.

Another important quantum tomography is the QPT, it is an experimental method that allows the extraction of the process matrix of a quantum state transfer, which fully describes the quantum processes [160, 161]. After obtaining the physical process matrix, we can accurately determine the action of the gate on any arbitrary input state, including the amount of mixture added and the change in entanglement. We also evaluate useful measures of gate performance. Here, we use a fundamental two-qubit SWAP gate as an example, although the truth table measures the two-qubit SWAP operation in the logical basis, QPT is required to characterize the coherence of the SWAP operation [161].

We can estimate the SWAP operation's process matrix χ for a set of fixed operators, which are simply chosen to be the identity operator I and the Pauli operators X, Y, and Z [160]. The process matrix χ of the SWAP operation is then expressed as:

$$\chi = \Lambda \rho \Lambda \tag{2.22}$$

where the matrix ρ can be determined using QST, and the matrix Λ is defined as:

$$\Lambda = \frac{1}{2}\begin{bmatrix} I & X \\ X & -I \end{bmatrix} \tag{2.23}$$

The process fidelity is then defined as

$$\mathrm{F}_{\chi} = \frac{Tr(\chi\chi_i)}{Tr(\chi)Tr(\chi_i)} \tag{2.24}$$

where χ_i is the ideal process matrix with (I, I) component. The purity of the SWAP process matrix χ can also be defined as

$$P_{\chi} = \frac{Tr(\chi^2)}{Tr^2(\chi)} \tag{2.25}$$

which is unity for an ideal process.

With QST and QPT, maximum-likelihood reconstruction, and analysis of the resulting state and process matrix, we can fully characterize both the entangled state and the action of the gate on an arbitrary input quantum state.

2.6 Bell inequalities

In the last two decades, Bell's theorem has been a central theme of research from a variety of perspectives, mainly motivated by quantum information science, where the nonlocality of quantum theory provides many of the advantages afforded by QIP [162]. Bell nonlocality rules out the existence of local hidden variable models that describe reality [162, 163] and is the strongest type of quantum correlation [164]. EPR steering is a form of quantum correlation that lies between entanglement and Bell nonlocality [164, 165], hence, the entanglement is necessary but not sufficient for steering, while steering is necessary but not sufficient for nonlocality.

Experimentally, Bell nonlocality can be tested via the violation of a Bell inequality, meaning that a system cannot be described using local hidden variable models; similarly, steering can be tested using steering inequalities [166]. Lastly, entanglement can be verified by two-photon interference visibility higher than 71%, for example, in time-energy entanglement [157].

A Bell test measures the strength of correlations in different basis sets. As an example, let us consider a source that generates photons in an incoherent mixture of either two horizontally or vertically polarized photons, described by a density matrix

$$\rho_{mix} = \frac{1}{2}(|H\rangle|H\rangle\langle H,H| + |V\rangle|V\rangle\langle V,V|) \tag{2.26}$$

This source can provide high correlations in certain polarization settings (like H and V), however, the light is entirely uncorrelated in diagonal (i.e. $|D\rangle = (|H\rangle + |V\rangle)/\sqrt{2}$) or circular polarization (i.e. $|R\rangle = (|H\rangle + i|V\rangle)/\sqrt{2}$) basis settings. In contrary, for polarization entangled sources, where two photons are in a coherent superposition of polarization modes, described by a density matrix

$$\rho_{ent} = \frac{1}{2}((|H\rangle|H\rangle + |V\rangle|V\rangle)(\langle H,H| + \langle V,V|)) \tag{2.27}$$

where perfect correlations can be achieved in any polarization basis (horizontal, vertical, circular or a combination of them). A Bell inequality classifies the over-all correlation strength and assigns a measurable quantity, the S parameter (for two-dimensional systems), which cannot be larger than 2 in classical systems, but has a maximum of $2\sqrt{2} \approx 2.83$ for quantum systems [167, 168]. Bell inequalities are therefore often used to confirm the nonlocal quantum properties and a system.

There are different ways to measure the Bell parameter S. One way to extract the Bell parameter by means of quantum interference measurements. If the correct projections are chosen [169], it becomes possible to fit a specific function and extract the visibility of the quantum interference. For the two-photon Bell State, this projection is

$$|\psi_{proj.}\rangle = \frac{1}{2}\left(|H\rangle_s + e^{i\theta}|V\rangle_s\right)\left(|H\rangle_i + e^{i\theta}|V\rangle_i\right) \tag{2.28}$$

which results in quantum interference with twice the period compared to the quantum interference if one phase (or polarizer) is kept constant. Thus, it becomes possible to define a visibility V of the quantum interferences and fit a sinusoidal function

$$C(\theta) = 1 + V\cos(2\theta) \tag{2.29}$$

if this function can be fitted to the measured quantum interference, the visibility becomes directly proportional to the Bell parameter, $S_{fringe} = 2\sqrt{2} \times V$. Measuring a visibility higher than $V > 1/\sqrt{2} \approx 0.71$ therefore directly violates a Bell inequality [170].

The other way to measure the Bell parameter S is by extracting the correlation coefficient $E(\theta_1, \theta_2)$, for instance, in polarization entanglement of photon pairs, $E(\theta_1, \theta_2)$ of signal and idler polarization projection onto the angle set θ_1, θ_2 can be obtained from coincidences counting measurements as follows [171, 172]

$$E(\theta_1, \theta_2) = \frac{C(\theta_1,\theta_2) - C\left(\theta_1,\theta_2+\frac{\pi}{2}\right) - C\left(\theta_1+\frac{\pi}{2},\theta_2\right) + C\left(\theta_1+\frac{\pi}{2},\theta_2+\frac{\pi}{2}\right)}{C(\theta_1,\theta_2) + C\left(\theta_1,\theta_2+\frac{\pi}{2}\right) + C\left(\theta_1+\frac{\pi}{2},\theta_2\right) + C\left(\theta_1+\frac{\pi}{2},\theta_2+\frac{\pi}{2}\right)} \tag{2.30}$$

where $C(\theta_1, \theta_2)$ is the coincidences counting measurement for two different polarizers at different angle settings. According to these correlation coefficients, we can calculate the Clauser–Horne–Shimony–Holt (CHSH) S parameter from its definition [157, 167]

$$S_{CHSH} = \left|E\left(\frac{\pi}{2}, \frac{7\pi}{8}\right) + E\left(\frac{\pi}{4}, \frac{7\pi}{8}\right) + E\left(\frac{\pi}{4}, \frac{5\pi}{8}\right) - E\left(\frac{\pi}{2}, \frac{5\pi}{8}\right)\right| \tag{2.31}$$

S_{fringe} parameter obtained with quantum interference visibility sets the upper bound on the measured S_{CHSH} parameter with correlation coefficients, which can be achieved only when the polarization

analyzers are aligned with the tested quantum states and the detection efficiencies for all measurements are consistent.

The measurement of two-photon interference can therefore be used to violate a Bell inequality and confirm the presence of entanglement [168] if the correct projection vectors are chosen. The experimental challenge lies in realizing the required projection measurements for the biphotons.

2.7 Entanglement in mode-locked biphoton frequency combs

As discussed in introduction section, there is particular interest in the generation of discrete-variable entangled quantum states, as they provide easy manipulation and access to quantum modes. Therefore, this work focuses on the realization of discrete time-energy entanglement. In particular, both discrete versions of energy-time entanglement, time-bin [172] and frequency-bin [173] entanglement are ideally suited for their generation and exploitation in mode-locked BFCs, as they can be generated in a single spatial mode.

Time-bin entanglement is well-suited and commonly used for applications in quantum communications [175], but it can also be exploited for quantum computation protocols [176]. In order to perform time-bin entanglement measurements, two stable interferometers are required to implement the projection measurements, as discussed in Sec. 2.4. In particular, in this work, we used a nonlocal Franson interferometer for measuring time-energy (time-bin) entanglement. Our setup for the generation and characterization of time-bin entangled photon pairs is shown in Fig. 2.6. As both the generation and the characterization require unbalanced interferometers, the availability of very stable interferometers is paramount for experimental investigation of time-bin entanglement. We build two such stable interferometers in a multilayer thermally-insulated enclosure whose temperature is actively stabilized and monitored. The free-space optical delay line in arm2 of Franson interferometer is based on a miniaturized linear stage with closed-loop piezoelectric motor control (CONEX-AG-LS25-27P, Newport). The optical insertion loss of double-pass optical delay line is smaller than 0.4 ± 0.05 dB over the entire 360 ps delay range, providing us the capability to measure multiple time bins from discrete cavities round-trip times of our BFCs [92, 111]. For sub-femtosecond phase-sensitive quantum interference measurements, we utilize a temperature controller in arm1 of Franson interferometer to thermally adjust the relative phase difference of two unbalanced MZIs for probing time-energy entanglement in our BFCs.

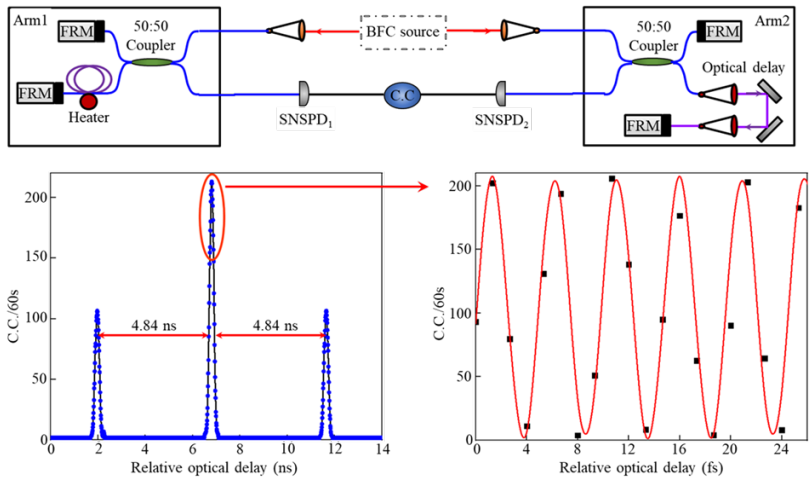

Fig. 2.6. Generation and characterization of time-bin entangled biphoton frequency comb. Schematic of typical experimental configuration. FRM, Faraday mirror; C.C., coincidence counter. The bottom plots are the measured two-photon Franson interference with 96.1% interference raw visibility that violates the Bell inequality. Fig. 2.6 published in [92].

Compared to time-bin entanglement, frequency-bin entanglement is rarely exploited until recently, this arises from two main issues related to their generation and detection: the loss during generation of frequency-bin entanglement and the mixing of discrete spectral modes for performing frequency projection measurements.

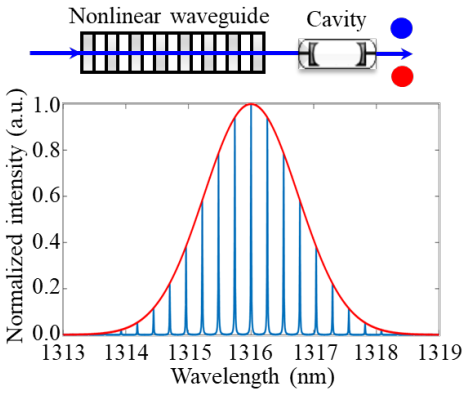

Fig. 2.7. Generation of frequency-bin entangled biphoton frequency comb. Schematic of typical experimental configuration for frequency-bin entangled BFC. The bottom plot represents the discretized BFC spectrum in telecom-band.

BFCs are ideally suited to generate frequency-bin entangled states. In particular, by using fiber cavities, photon pairs can be generated over multiple resonances symmetric to the pump, photon pairs are created into a frequency-bin entangled states, see Fig. 2.7. The advantage in the generation is three-fold: First, the FSR of the BFC can be chosen flexibly in the GHz range, making it possible to measure

mode-locked oscillations in temporal domain, and to select individual frequency modes with standard telecommunications filters [92, 111]. Second, the photons can be generated into pure states, verified by the JSI measurements and the complementary JTI measurements of BFC. And third, the BFC exhibit singly-resonant and doubly-resonant schemes, both configurations have their advantages and disadvantages, for example, singly-resonant BFC is more stable and have greater tunability, thus have more variety for non-degenerate [177] or degenerate heralding measurements [111]. In contrast, doubly-resonant BFCs are more suitable for boosting the Hilbert space dimensionality in temporal domain [92]. Both schemes can be easily switched and operated in a single experimental setup without complex free-space stabilizations, see Fig. 2.8.

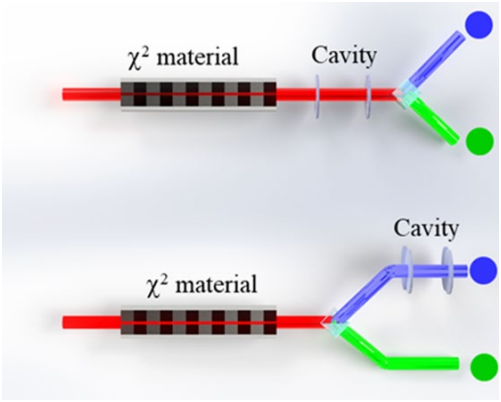

Fig. 2.8. Generation of singly- and doubly- resonant biphoton frequency comb. Schematic schemes for mode-locked doubly- and singly-resonant BFCs. The configuration is accessible for type-II SPDC sources.

2.8 Design of a high-purity integrated hybrid photon pair source

In this section, we present a newly designed high-purity integrated hybrid photon pair source and engineering of JSI in a BFC [178, 179]. High-purity photon sources are highly desired for QIP tasks because purity evaluates how pure a quantum state is [180-183]. While the density matrix of a pure quantum state can be expressed as

$$\rho_{pure} = |\psi\rangle\langle\psi| \tag{2.32}$$

a mixed state is a linear superposition of pure states

$$\rho_{mix} = \sum \rho_i(|\psi_i\rangle\langle\psi_i|) \tag{2.33}$$

the purity of the state can therefore be quantified as

$$P = Tr\{\rho^2\} \tag{2.34}$$

a pure state has a purity of 1, while that of a mixed state is less than 1, with a lower limit of $1/d$, where d is the dimension of the Hilbert space.

As discussed in Sec. 2.4, high visibility HOM interference is key to generate maximally path-entanglement, and is the basis of fundamental two-qubits gates and LOQC [112]. For implementing long-range quantum communication [184, 185], and LOQC [41, 42], consecutive photons from separate sources need to be indistinguishable. The indistinguishability between two states, whose density matrices are ρ_1 and ρ_2, can be expressed as

$$I = 1 - \frac{1}{2}\|\rho_1 - \rho_2\|^2 \tag{2.35}$$

two quantum states are fully indistinguishable when their density matrices are identical, with indistinguishability maximum of 1. For pure states

$$\rho_1 = |\psi_1\rangle\langle\psi_1| \tag{2.36}$$

$$\rho_2 = |\psi_2\rangle\langle\psi_2| \tag{2.37}$$

the indistinguishability becomes

$$I_p = \langle\psi_1|\psi_2\rangle^2 \tag{2.38}$$

now, we can connect HOM interference visibility V from two independent photon pair sources with purity P and indistinguishability I

$$V = Tr\{\rho_1\rho_2\} = \frac{Tr\{{\rho_1}^2\}+Tr\{{\rho_2}^2\}-\|\rho_1-\rho_2\|^2}{2} = P + (I-1) \tag{2.39}$$

assuming $P_1 = P_2$, therefore

$$V \leq P \tag{2.40}$$

Hence, it is important to design high purity photon pair sources for numerous quantum applications, here, we performed joint spectral analysis to estimate the frequency correlation of SPDC photons, yielding intrinsic purity with up to 95.17% [178], see Fig. 2.9.

We start from fundamental SPDC states [181]

$$|\psi\rangle = \widetilde{N} d_{eff} L \int_0^\infty \int_0^\infty \varphi(\omega_s + \omega_i)\phi(\omega_s, \omega_i) a_s^\dagger a_i^\dagger \, d\omega_s d\omega_i |0\rangle \tag{2.41}$$

where $\widetilde{N}$ is a normalization constant, d_{eff} is the effective nonlinear coefficient of the crystal, L is the length of the crystal, $a_s^\dagger$ and $a_i^\dagger$ are the creation operators of signal and idler photon, respectively. φ is the pump envelope amplitude, and ϕ represents the phase-matching envelope amplitude as

$$\phi(\omega_s + \omega_i) = e^{i\Delta kL/2} sinc(\Delta kL/2) \tag{2.42}$$

with Δk representing the phase mismatch in collinear quasi-phase-matching

$$\Delta k = 2\pi\left(\frac{n_p}{\lambda_p} - \frac{n_s}{\lambda_s} - \frac{n_i}{\lambda_i} - \frac{m}{\Lambda}\right) \tag{2.43}$$

where λ_p, λ_s, λ_i and n_p, n_s, n_i are the wavelengths and refractive indices for pump, signal and idler, respectively. And m is an odd integer referred to as quasi-phase-matching order, Λ is the poling periodicity of the nonlinear waveguide. The refractive indices are obtained according to the wavelength- and temperature- dependent Sellmeier equations at room temperature.

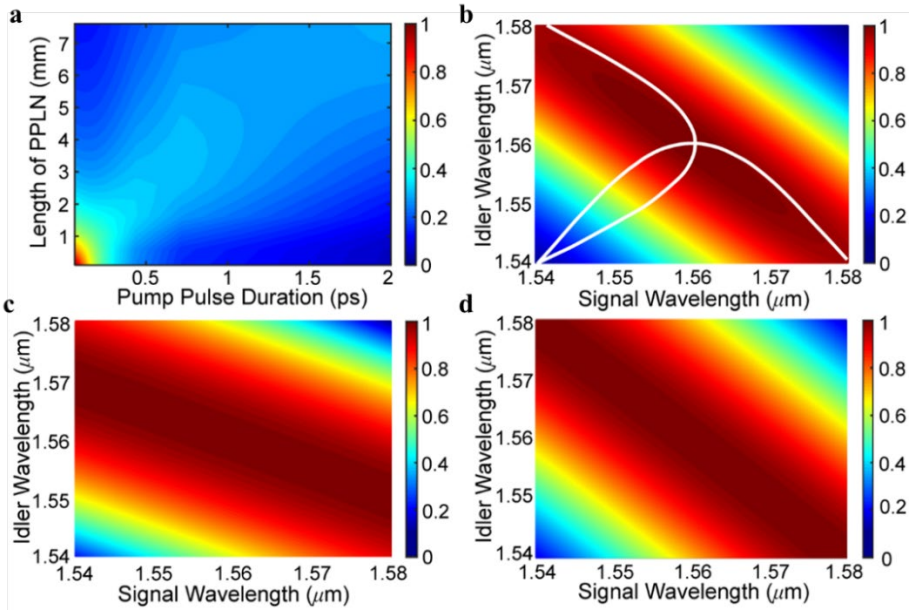

Fig. 2.9. Design maps for high-purity integrated type-II SPDC source. a) Purity of type-II SPDC photon pairs as a function of pump pulse duration and length of periodically-poled lithium niobate. b) JSI distribution of SPDC photon pairs with 100 μm length of periodically-poled lithium niobate and 0.064 ps pump pulse duration, yielding purity of 95.17% without filtering. The spectra of signal and idler are depicted by white curves. c) phase-matching envelope intensity and d) pump envelope intensity for the composed JSI. The width and thickness of Si_xN_y waveguide is fixed at 400 nm and 800 nm, respectively. Fig. 2.9 published in [178].

The JSA is defined as the product of the pump envelope amplitude φ, and the phase-matching envelope amplitude ϕ

$$f(\omega) = \varphi(\omega_s + \omega_i)\phi(\omega_s + \omega_i) \tag{2.44}$$

the JSI can then be defined as JSI $= |\text{JSA}|^2$. In order to reveal the influence of spectral correlation in the pure bipartite state $|\psi\rangle$ on the purity P, we estimate the Schmidt decomposition of the joint two-photon state. The Schmidt decomposition provides an intuitive measurement of entanglement of a pure state. This can be quantified by the Schmidt number K, which is defined as

$$K = 1/(\sum \lambda_n^2) \tag{2.45}$$

where $\sum \lambda_n^2 = 1$, with λ_n being the Schmidt mode eigenvalues. If a product state is entangled, there is

more than one Schmidt mode and $K > 1$, in contrast, a unentangled product state can be expressed with only one Schmidt mode, thus K equals unity. The purity P of the reduced photon states can then be calculated by the inverse of the Schmidt number K

$$P_s = P_i = \sum \lambda_n^2 = \frac{1}{K} \tag{2.46}$$

In order to achieve high-purity of the SPDC photons, the signal and idler photons should have near-unity Schmidt number. The pump and the phase-matching envelope amplitude should also be matched to produce a frequency-indistinguishable JSI, thus yield high purity. In Fig. 2.9a, we present the design map of purity for different periodically-poled lithium niobate length and pump pulse duration. High purity can be obtained with short periodically-poled lithium niobate length and pulse duration. But there is a trade-off between high efficiency and high purity, since shorter length of periodically-poled lithium niobate will reduce the SPDC photons generated from our hybrid waveguide device. For Si_xN_y waveguide width and thickness of 400 nm and 800 nm, we obtain the highest purity of 95.17% with 100 μm periodically-poled lithium niobate length and 64 fs pulse duration. The poling period is set to 4.3 μm to achieve phase-matching condition. Fig. 2.9b illustrates the JSI of these high-purity SPDC photons without BPF. The spectra of signal and idler photons are matched so that they are frequency-indistinguishable for high visibility HOM interference. The phase-matching envelope intensity $|\varphi|^2$ and pump envelope intensity $|\phi|^2$ for the JSI are also shown in Fig. 2.9c and 2.9d. We notice that the direction of the pump envelope intensity is tilted at $-45°$ (with positive direction of the horizontal axis), while the direction of the phase-matching envelope intensity can be at arbitrary angle θ. The $-45°$ angle of the pump envelope intensity direction comes from the energy conservation of the SPDC process, whereas the arbitrary angle θ of the phase-matching envelope intensity direction can be determined by the group velocities as [183]:

$$\tan\theta = \frac{v_p^{-1} - v_s^{-1}}{v_p^{-1} - v_i^{-1}} \tag{2.47}$$

where v_p, v_s, v_i are the group velocities of the pump, signal and idler, respectively. With the waveguide parameter combination for high purity of 95.17%, the direction of phase-matching envelope intensity is calculated to be tilted at $\theta \approx -13°$ as shown in Fig. 2.9c. This tilted angle of phase-matching envelope intensity leads to the elliptical shape of the JSI [186]. For comparison, near-circular shape of JSI is easier to achieve with PPKTP waveguide due to diagonal phase-matching envelop amplitude [181, 187]. However, the intrinsic purity of the SPDC photons from PPKTP waveguide is limited to ~83% because of the sidelobes of the sinc function in joint spectral amplitude [187], for our hybrid waveguide design, we manage to obtain high intrinsic purity despite of the

elliptical shape of JSI by optimizing the phase-matching condition.

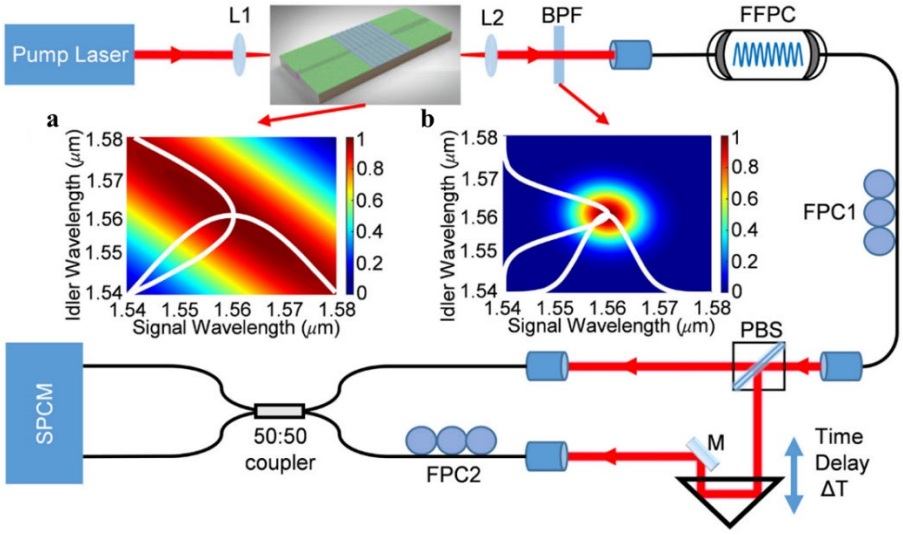

Fig. 2.10. Experimental scheme for generating high-dimensional biphoton frequency comb and observing Hong-Ou-Mandel quantum revival. L: lens; BPF: band-pass filter; FFPC: fiber FP cavity; M: reflective mirror; SPCM: single photon counting module. Inset: a) JSI distribution of the SPDC photons generated by our designed hybrid waveguide. b) JSI distribution of the filtered photons, with purity up to 99.79%. The spectra of the signal and idler photons are indicated by the white curves. Fig. 2.10 published in [178].

Based on the current waveguide configuration, we can estimate the generated SPDC signal power by [188, 189]

$$dP_S = \frac{16\pi^3 \hbar {d_{eff}}^2 L^2 c P_P}{\varepsilon_0 n_p n_s n_i {\lambda_s}^4 \lambda_i S_{eff}} sinc^2(\Delta kL/2) d\lambda_s \tag{2.48}$$

here, P_P is the pump power. We use d_{eff} = 2.8 pm/V, L = 100 μm, n_p = 2.325, $n_s = n_i$ = 2.266, $\lambda_s = \lambda_i$ = 1560 nm, P_P = 1 mW. For the designed waveguide of 800 nm thickness and 400 nm width, we have S_{eff} = 3.441 μm^2 as calculated from the mode overlap and estimate a pair generation rate of 2.87 × 10^7 pairs/s/mW of pump power within the SPDC bandwidth.

Furthermore, we also design experimental scheme and simulate the generation of high-dimensional BFC through our hybrid waveguide device. The proposed experimental scheme for generating high-dimensional BFC and observing HOM quantum revival is illustrated in Fig. 2.10. The hybrid waveguide device is pumped by a 780 nm pulse laser with 64 fs pulse duration to generate type-II SPDC photons. A BPF is then placed to block the residual pump light and further eliminate the frequency correlation between signal and idler photons. The SPDC photons can yield purity up to 99.79% with a 10 nm BPF, which lower the experimental requirement for narrow BPF. BFC is

generated by passing the SPDC photons through a FP cavity, with signal and idler photons in orthogonal polarizations. The FP cavity has a FSR of 15 GHz and bandwidth of 0.5 GHz, respectively. The corresponding repetition period T of the BFC is ~ 66.7 ps. The simulation results are obtained by scanning the optical delay ΔT from -1000 ps to 1000 ps, as shown in Fig. 2.11. The spacing between dips is estimated to be 33.3 ps, resulting from the FSR of the FP cavity [75]. The visibility of the dips decreases exponentially due to the Lorentzian lineshape spectra of the SPDC individual photons after they are passing through the FP cavity. A zoom-in of the dip around zero delay point is shown in the left inset of Fig. 2.11. The maximum HOM visibility is calculated to be 99.79%. Considering the bin spacing of 15 GHz, 83 frequency-bins can be expected within the phase-matching bandwidth in our experimental scheme. Over the optical delay range from 1000 ps to 1000 ps, 59 dips are observed in simulation, predicting HOM quantum revival at 59 time- bins. Furthermore, as shown in the right inset of Fig. 2.11, 33 time-bins with visibility beyond classical limit (50%) are obtained.

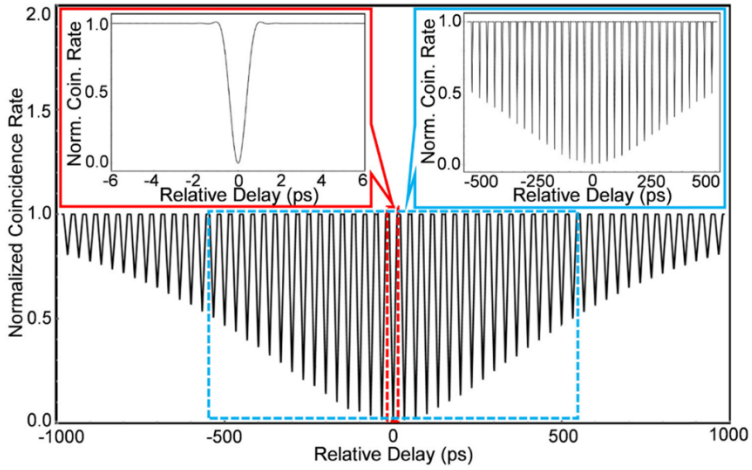

Fig. 2.11. Hong-Ou-Mandel quantum revival of the high-dimensional biphoton frequency combs. Coincidence rate is computed as a function of relative delay ΔT between the two arms of the HOM interferometer. Left inset: zoom-in coincidence around zero relative delay between two arms. The base-to-base width of the central dip is estimated to be 1.6 ps. The visibility of the central dip is calculated to be 99.79%. Right inset: zoom-in coincidence for 33 time-bins with interference visibility over 50%. Fig. 2.11 published in [178].

In summary, we designed a chip-scale hybrid Si_xN_y and thin film periodically-poled lithium niobate waveguide to generate high-purity type-II SPDC photons [178]. The hybrid waveguide device shows a peak normalized efficiency of 225% $W^{-1}cm^{-2}$ at 1560 nm for second-harmonic generation. Joint spectral analysis of the SPDC photons provides an estimation of intrinsic purity with up to 95.17% under the phase matching condition without BPF. The photon pair generation rate of our

device is estimated to be 2.87 × 10^7 pairs/s/mW within the bandwidth of SPDC. Such source can be easily combined with FP cavity to form a BFC, our calculations show 59 HOM dips with 33 of them has quantum visibility over classical limit. Our designed high-efficiency chip-scale hybrid waveguide can work as an integrated BFC source for on-chip high-dimensional QIP and practical secure QKD.

2.9 Quantification and certification of high-dimensional entanglement in mode-locked biphoton frequency combs

Quantifying and certifying the amount of entanglement in a high-dimensional quantum system has been a long-standing question in the community [121, 190]. Current challenges include the extension of well-known methods for two qubits to high-dimensional quantum systems and their application in entanglement experiments with photons. More specifically, the major challenge is the certification of high-dimensional entanglement by a number of accessible experimental measurements. An important focus of recent research is the reduction in the number of measurements required for entanglement certification to cope with increasing system dimensions [191-193].

In this work, we illustrate by using JSI and JTI measurements of BFC, Schmidt mode decomposition and entanglement of formation analysis, the high-dimensional time-energy (time-bin) and frequency-bin entanglement can be quantified and certified. First, let us start with the frequency DoF, from the JSI measurement (see Fig. 2.12a), the number of frequency-correlated pairs can be increase by decreasing the FSR of the cavity or the phase-matching bandwidth of the photon-pair sources, but the entanglement dimensionality, which relies on the phase coherence across correlated frequency-bin pairs, remains unknown. Fig. 2.12b provides an simple illustration behind this problem, with only a JSI measurement, there is not enough information to claim the presence of cross-pair coherence. There are currently two methods to encounter this problem. First, one can directly measure the JTI of correlated two-photons [143, 177], or equivalently, mode-locked oscillations in the measured coincidence counts with a period that is equal to the inverse of the cavity FSR proves the biphoton phase coherence, as in Fig. 2.13. This scheme requires the single-photon detector temporal resolution to be shorter than the time scales of the correlations, which is possible for photon sources with narrow FSR (a few GHz), or alternatively using nonlinearity-based optically gated detection [194]. The second method is by using pulse shapers and electro-optic modulators to mix the frequency bins [79, 83, 84, 86], and measure the coincidence counts with different phase settings. However, the

relatively large coupling loss of electro-optic phase modulators, pulse shapers possess practical limitation on scaling of the scheme [195].

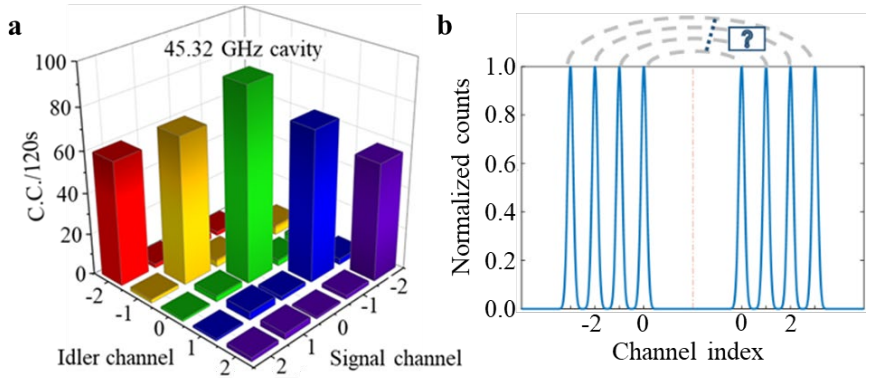

Fig. 2.12. Phase coherence in biphoton frequency combs. a) Measured JSI distribution of a doubly-resonant BFC [92]. b) Typical general form of BFC due to energy conservation [89].

It is recently claims that the two-photon HOM interference cannot speak to the presence of high-dimensional frequency-bin entanglement in BFC [88], because the HOM interferometry is insensitive to the relative phase between different comb line pairs. Our recent work shows, however, the revival of HOM time-bins, together with complementary JTI measurements such as using a conjugate-Franson interferometry [128], can certify the high-dimensional frequency-bin entanglement in BFCs [89, 92]. Beyond the local two-photon interference, our work also demonstrates the nonlocal Franson revival interferences using a BFC, although such measurements are JSI measurements, but the nonlocality nature proves the high-dimensional time-energy (time-bin) entanglement [92], with the JTI measurements, both high-dimensional frequency-bin and time-energy entanglement in BFC can be certified.

For temporal DoF, we have recently directly measured the mode-locked oscillations in our scheme. We prove the existence of biphoton phase coherence in a singly-resonant BFC, with the Franson revivals measurements for probing JSI of BFC state, we can verify both high-dimensional time-bin and frequency-bin entanglement in our BFC. Moreover, it was proposed that by using a conjugate-Franson interferometry with our BFC, due to the sensitivity of spectral phase of this interferometry, we can potentially measure the JTI of BFC state [92, 128]. The high visibility conjugate-Franson interference fringe can then be used to certify the pure mode-locked BFC state.

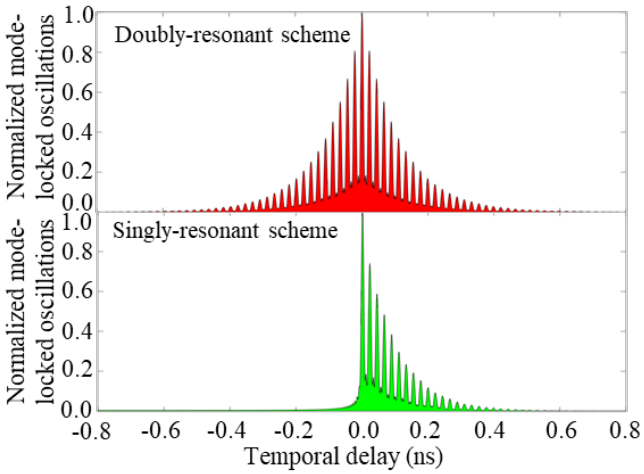

Fig. 2.13. Joint temporal intensity and Phase coherence in biphoton frequency combs. Top plot shows the JTI and biphoton phase coherence in doubly-resonant BFC, while bottom plot is the JTI and biphoton phase coherence in singly-resonant BFC. Both schemes use same FP cavity with FSR of 45.32 GHz and timing jitter of 20 ps.

With all the evidence that our high-dimensional BFC is generated with mode-locking technique, preserving biphoton phase coherence and in a non-separable state, we now discuss how to quantify and certify the high-dimensional time-energy (time-bin) and frequency-bin entanglement in our BFC state. The technique we used are mainly two ways, Schmidt mode decomposition and entanglement of formation analysis.

Schmidt mode decomposition, which is also mentioned in Sec. 2.8, can be performed for any pure state to decompose their state into bi-orthogonal product vectors and obtain Schmidt number $K = 1/(\sum \lambda_n^2)$, with $\sum \lambda_n^2 = 1$, and λ_n being the Schmidt mode eigenvalues. Schmidt number or sometimes the dimensionality of entanglement, as it represents the minimum local Hilbert space dimension required to faithfully represent the correlations of the quantum state. Schmidt mode eigenvalues can also be utilized to obtain one of prominent entanglement quantifiers: Von Neumann entropy [190]. The Von Neumann entropy is equal to the Shannon entropy of the squared Schmidt mode eigenvalues for entangled photons via

$$E(|\psi_{s,i}\rangle) \equiv S(\rho_{s,i}) = -\sum_{i=0}^{K-1} \lambda_i^2 \log(\lambda_i^2) \tag{2.49}$$

For the frequency-binned JSI measurements, the Schmidt eigenvalues are obtained from the frequency-binned JSA, given JSI = $|\text{JSA}|^2$ and the pure state of our BFC.

Turning now to the time-bin Schmidt number for JSI measurements with our BFC, to proceed in a manner analogous to what we used for the frequency-binned Schmidt mode decomposition would

require knowledge of the binned JTI. We can estimate that time-binned JTI both from our HOM and Franson recurrence visibility data, under same assumption as frequency-binned Schmidt mode decomposition, the JTA equals the square-root of the binned JTI,

$$\psi(n\Delta T) = \sqrt{|\psi(n\Delta T)|^2} \tag{2.50}$$

for the time-binned wavefunction of the BFC, where $n, \Delta T$ are the number of cavity round-trips and cavity round-trip times [92, 111].

If the frequency-bin Schmidt number extracted from experimental measurements are larger than 1, together with JTI measurements, it proves the high-dimensional frequency-bin entanglement of BFC. For time-bin Schmidt number from HOM and Franson measurements, if such number is greater than 1, they can represent high-dimensional frequency-bin and time-bin entanglement in BFCs. While time-bin Schmidt number from HOM measurements, with complementary JTI measurements, can be used to certify high-dimensional frequency-bin entanglement; time-bin Schmidt number from Franson measurements can already certify high-dimensional time-energy (time-bin) entanglement, and can be used to verify high-dimensional frequency-bin entanglement with JTI measurements. Schmidt number thus provides the lower-bound of Hilbert space dimensionality for our BFCs in both time and frequency domains.

We can also quantify the certify the high-dimensional time-energy (time-bin) entanglement of our BFCs from the lower bounds of their entanglement of formation (E_{of}). The entanglement of formation can be calculated by [192]

$$E_{of} \geq -\log_2\left(1 - \frac{B^2}{2}\right) \tag{2.51}$$

where the quantity B is defined as:

$$B = \frac{2}{\sqrt{|C|}}\left(\sum_{\substack{(j,k)\in C \\ j<k}} |\langle j,j|\rho|k,k\rangle| - \sqrt{\langle j,k|\rho|j,k\rangle\langle k,j|\rho|k,j\rangle}\right) \tag{2.52}$$

Here, $|C|$ denotes the cardinality of the set C, where C is the number of time-bin indices considered in the sum. ρ is the density matrix of the time-binned state, and $|j,k\rangle$ is the biphoton ket for the jth signal time bin and the kth idler time bin. Note that the quantity B puts a lower bound on the concurrence of ρ. For a maximally entangled state of dimension $d \times d$, we can obtain maximum concurrence of $B = \sqrt{2(d-1)/d}$, which leads to the tight bound $E_{of} = \log_2(d)$. It is obvious that E_{of} increase monotonically with concurrence B, thus concurrence can also be taken as a measure of entanglement. It is challenging to measure all the coherent terms $\langle j,j|\rho|k,k\rangle$, which requires many cascaded interferometers with controllable phases. However, we can still efficiently lower bound on the

entanglement of formation E_{of} based on the experimentally accessible data [192].

Getting entanglement of formation E_{of} surpass qubit limit ($E_{of} = 1$) for any quantum states certifies that these states possess true high-dimensional non-separability and therefore high-dimensional time-energy (time-bin) entanglement.

2.10 Summary

In this chapter, we introduce the methods and techniques that were used to collect and analyze the experimental results for this thesis. First, we review the SPDC and SFWM for numerous of quantum applications. Second, the fundamentals of quantum photon statistics, single-photon and two-photon quantum interferences (including HOM and Franson interference), quantum state and process tomography (and SWAP gate fidelity, process purity), the Bell nonlocality (and Bell inequalities), EPR steering, and entanglement are summarized. Third, the time-bin and frequency-bin entanglement in mode-locked BFC is presented. Fourth, we present a new integrated hybrid source is designed by controlling the JSI of the SPDC photons for generating high purity, indistinguishable BFC. Finally, we illustrate by utilizing JSI and JTI measurements of BFC, Schmidt mode decomposition in time and frequency domains and entanglement of formation calculation, the high-dimensional time-energy (time-bin) and frequency-bin entanglement can be quantified and certified in our BFCs

Chapter 3

Mode-locked high-dimensional biphoton frequency combs

3.1 Introduction

This chapter describes the main results with high-dimensional mode-locked quantum state generation via BFCs, making use of their multi-mode nature in time and frequency domains. The results include both the doubly- and singly-resonant BFC schemes, starting with doubly-resonant BFC characterization, quantification and boosting the high-dimensional time and frequency entanglement, then the new singly-resonant BFC with its characterization, certification, and distribution towards multi-user quantum network.

3.2 Mode-locked process and joint properties of biphoton frequency combs

Mode-locking approaches, which is an indispensable and traditional technique in classical ultrafast optics [196], and their strength lies in the phase coherence among the spectral lines, which leads to ultrahigh stability, becoming the cornerstone for applications in metrology, spectroscopy and more [197, 198]. More importantly, this mechanism plays a significant role in generating mode-locked BFCs. The first mode-locked biphotons state is observed via a cavity-enhanced SPDC source [71], and subsequently, another type of mode-locked two-photon state is proposed [199], and experimentally demonstrated using a fiber cavity to filter SPDC photons almost two decades ago [72]. More recently, the mode-locked quantum frequency combs can also be efficiently generated via SFWM in microresonators [76-78]. From Chapter 2, we know entangled photons can be generated via spontaneous parametric nonlinear processes, either directly within a resonator or in a waveguide and subsequently subjected to periodic spectral filtering, exhibit discrete spectral modes and form a BFC.

In mode-locking BFCs, the simultaneous generation of signal, idler photons within the coherence time of the biphoton results that strong temporal correlation in two-photon JTI. Moreover, the SPDC and SFWM process preserves the energy, momentum of the incident pump photon and subsequent daughter photon pairs, hence, the sum of the signal and idler frequencies is constant, yielding an anti-correlation in the JSI. Therefore, mode-locking BFCs not only have single-photon spectral phase

coherence (also occur when attenuating classical frequency comb down to single-photon level), they exhibit bi or multiphoton spectral phase coherence, which is fundamentally different from single-photon spectral phase coherence. The difference between single- and biphoton phase coherence can be understood by considering an analogy to the single- and biphoton polarization signatures. If a classical linearly polarized light field is attenuated to the single-photon level, the individual photons remain linearly polarized, but if a polarization entangled photon pair is generated, while the single-photon polarization of each individual photon is random, the biphoton polarization of the state is perfectly defined [200]. In analogy to this, it is possible to generate a time-energy entangled biphoton state where the spectral phases of the individual photons in the state are random, but the two-photon spectral phase is perfectly defined and thus is stable, which is also referred to as a mode-locked BFCs [71, 72].

As mentioned in Sec. 2.9, such biphoton phase coherence can be probed directly in JTI measurements such as second-order coherence functions $g^{(2)}(\tau)$, the mode-locked oscillations in temporal domain proves the biphoton phase coherence in BFCs based on SPDC photons [143, 177]. The theory of mode-locked temporal signal-idler cross-correlation function $g^{(2)}(\tau)$ of BFCs are provided in Appendix A.1. From the theoretical calculation [92], and experimental demonstration of conjugate-Franson interferometry [128], the biphoton phase coherence in mode-locked BFCs can also potentially be measured with conjugate-Franson revivals as a function of driving frequency shift to verify that BFC states generated with spectral filtering are indeed high-dimensional non-separable state.

3.3 Doubly-resonant mode-locked biphoton frequency combs

High-dimensional entanglement with larger Hilbert spaces enable an encoding of more bits per coincidence and thus promise increased communication capacities over quantum channels [5-7, 9] and noise resilience in quantum communications [6, 11-13]. BFCs, which are intrinsically multimode in the temporal and frequency degrees of freedom within a single spatial mode, naturally facilitating the generation and measurement of high-dimensional entanglement. In this section, we significantly increase the Hilbert space dimensionality and provide versatile tools for quantifying and certifying high-dimensional entanglement in a doubly-resonant BFC [92].

As a starting point to investigate the mode-locked BFC state generation, we focus on high-dimensional photonic state generation using SPDC photons and FP cavities and their full time and

frequency characterization. Starting from characterizing our doubly-resonant mode-locked BFC, our experimental setup is illustrated in Fig. 3.1a. The SPDC source used a type-II quasi-phase-matched, ppKTP waveguide, integrated in a fiber package for high fluence and efficiency [189]. It was pumped by a 658 nm wavelength FP laser diode, stabilized by self-injection locking. Our SPDC entangled photon source was designed to generate orthogonally-polarized, frequency-degenerate signal-idler photon pairs at 1316 nm with 245 GHz FWHM phase-matching band-width. Three high-dimensional doubly-resonant BFCs were created by sending the signal-idler photon pairs through one of three FP fiber cavities, whose FSRs are 45.32, 15.15, and 5.03 GHz, with FWHM linewidths of 1.56, 1.36, and 0.46 GHz, respectively. Each fiber cavity was mounted on a modified thermoelectric assembly with ≈ 1mK temperature-control stability. A stabilized tunable reference laser at 1316 nm was used to align each cavity's spectrum to the SPDC's degenerate frequency. The resulting BFC biphoton-as predicted by standard perturbation theory with the signal-idler differential group delay suppressed, see for example [201], can be expressed as

$$|\psi\rangle = \sum_{m=-N_0}^{N_0} \int d\Omega\, f'(\Omega) f(\Omega - m\Delta\Omega) \hat{a}_H^\dagger \left(\frac{\omega_p}{2} + \Omega\right) \hat{a}_V^\dagger \left(\frac{\omega_p}{2} - \Omega\right) |0\rangle \tag{3.1}$$

here, $\hat{a}_H^\dagger$ and $\hat{a}_V^\dagger$ are creation operators for horizontally and vertically polarized photons; $\Delta\Omega$ is the cavity FSR in rad s^{-1}; Ω is the detuning of the SPDC's biphotons from frequency degeneracy; $2N_0 + 1$ is the number of cavity lines passed by an overall bandwidth-limiting filter; $f'(\Omega) = \mathrm{sinc}(A\Omega)$ is the SPDC source's phase-matching function, where $A = 2.78/(2\pi B_{\mathrm{PM}})$ with B_{PM} being the FWHM bandwidth; and $f(\Omega - m\Delta\Omega)$ is the single frequency-bin profile defined by the cavity's Lorentzian transmission lineshape with FWHM linewidth $2\Delta\omega$

$$f(\Omega) = \frac{1}{[(\Delta\omega)^2 + \Omega^2]} \tag{3.2}$$

The signal and idler photons were cleanly separated by a PBS in our type-II SPDC configuration, so that the BFC was generated without post-selection. Using the temporal wavefunction, the BFC state can be rewritten as:

$$|\psi\rangle = \int d\tau e^{-\Delta\omega|\tau|} \sum_{m=-N_0}^{N_0} \mathrm{sinc}(Am\Delta\Omega) \cos(m\Delta\Omega\tau) \hat{a}_H^\dagger(t) \hat{a}_V^\dagger(t+\tau) |0\rangle \tag{3.3}$$

where we have used $\Delta\Omega/2\pi \ll B_{\mathrm{PM}}$. The exponential decay in equation (3.3) is slowly varying relative to the $\sum_{m=-N_0}^{N_0} \mathrm{sinc}(Am\Delta\Omega) \cos(m\Delta\Omega\tau)$ term because $\Delta\omega \ll \Delta\Omega$. Hence, the doubly-resonant BFC's temporal wavefunction has many peaks, with repetition period equal to the cavity round-trip time, $\Delta T = 2\pi/\Delta\Omega$, where $\Delta T \approx$ 22.1 ps, 66.0 ps, and 198.8 ps for the BFCs generated by the 45.32 GHz, 15.15 GHz, and 5.03 GHz cavities, respectively.

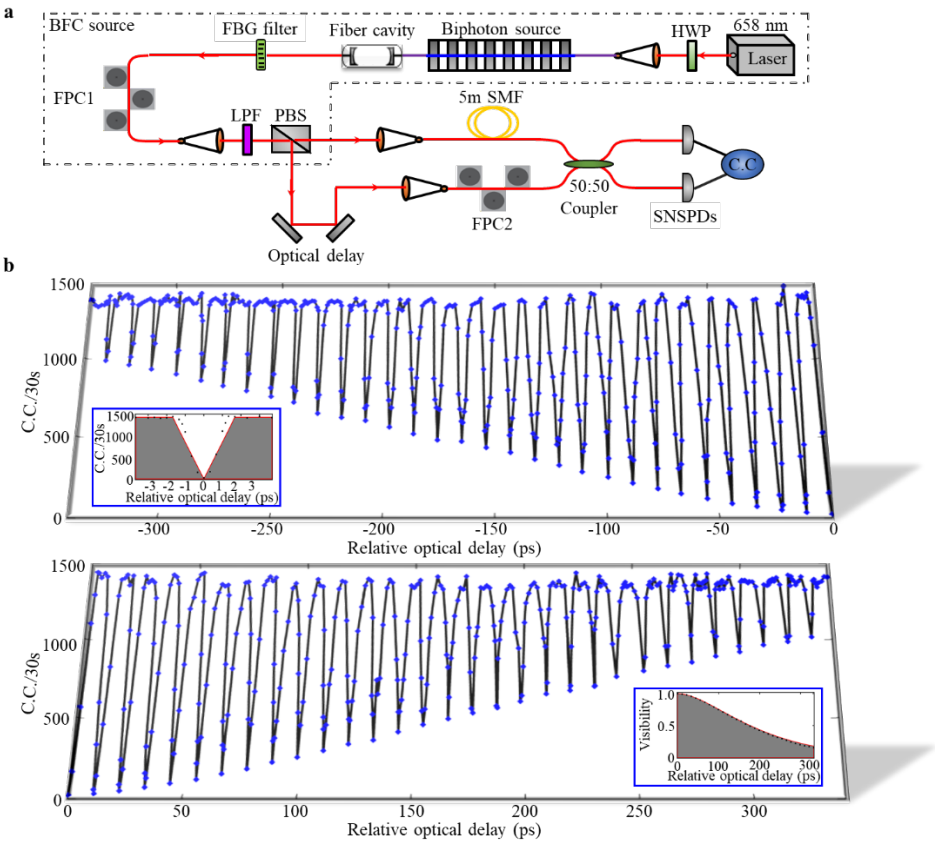

Fig. 3.1. High-dimensional BFC generation and Hong-Ou-Mandel recurrence observation. a) Illustrative experimental configuration. HWP, half-wave plate; FPC, fiber polarization controller; LPF, long-pass filter; C.C., coincidence counts. b) Coincidence counts versus relative optical delay from -340 ps to +340 ps, between the two arms of the HOM interferometer. HOM-interference recurrences are observed with up to 61 time bins. Upper left inset: zoom-in of the coincidence counts around zero relative delay between the two arms of the HOM interferometer. The dip width was fit to 3.86 ± 0.30 ps, which matches well with the reciprocal of the 245 GHz phase-matching bandwidth, as predicted by theory. The central dip visibility is 98.4% before and 99.9% after subtracting accidental coincidences. Lower right inset: measured time-bin visibilities versus the HOM optical delay compared with theory (red solid line, details in Appendix A.2). Fig. 3.1 published in [92].

A FBG of 346 GHz bandwidth and a LPF is used to spectrally select the BFC's $2N_0 + 1$ spectral modes in and to filter out remaining pump photons. The BFC wavefunction implies that HOM interference recurs at relative delays corresponding to integer multiples of the fiber cavity round-trip time [72, 75, 199], which we experimentally verified as follows. The orthogonally-polarized entangled photon pairs were divided by a PBS and directed to two arms of the HOM interferometer. A FPC in one arm of the interferometer alternates the idler photon polarization to match that of the signal photon

at the 50:50 fiber coupler. A tunable free-space optical DL with insertion loss smaller than 0.02 dB over its 220 mm travel range is used to vary the relative delay between the signal and idler photons for HOM interference. After the HOM interferometer, coincidences are recorded with two superconducting nanowire single-photon detectors (SNSPDs, ≈ 85% detection efficiency).

The HOM experimental results in Fig. 3.1b are measured with the 45.32 GHz FSR fiber cavity by scanning the relative optical delay between the biphotons from -340 ps to +340 ps with respect to the central dip. A pump power of 2 mW is chosen to avoid the multi-pair emissions that decrease two-photon interference visibility [75, 202]. The fringe visibility of the quantum interference, V_n for the nth dip is $[C_{\max} - C_{\min}(n)]/C_{\max}$, where $C_{\max}$ is the maximum coincidence count and $C_{\min}(n)$ is the nth dip's minimum coincidence count. Fig. 3.1b left inset zooms in on the central bin whose visibility is 98.4% before subtracting accidental coincidences, and 99.9% after they are subtracted. Here we note that the visibility of the central HOM dip must exceed 70.7% to be quantified as quantum biphoton interference [157] and, as the temporal delay between signal-idler increases from center dip, the HOM dips' visibilities decrease according to the fiber cavity's Lorentzian profile as described by the theory in Appendix A.2. Moreover, we note that the variation of the central HOM dip's visibility between raw and subtracted data is small (1.5%), indicating that measurement noise is quite modest at the central HOM dip (edge dips are getting close to this noise limitation). The base-to-base width of the central dip-i.e., the relative optical-delay difference between the left and right edges of the central HOM dip's triangular shape-is fitted to be 3.86 ± 0.30 ps, which agrees well with the reciprocal of our 245 GHz phase-matching bandwidth, as predicted by theory. We obtain HOM-interference recurrences for a total of 61 time bins within our setup optical-delay scanning range, which is a significant advance over our prior studies [75]. The measured repetition time of the recurrences was 11.03 ps, which corresponds to half the repetition period of the doubly-resonant BFC, and agrees well with our theoretical modeling in Appendix A.2. The visibility of the dip recurrences decreases exponentially (see Fig. 3.1b right inset) due to the Lorentzian lineshape of the BFC frequency bins. In particular, with the 45.32 GHz cavity's 11.03-ps bin spacing, our setup's ≈ 640 ps scan range allows us to observe 61 time bins given the visibility decay associated with that cavity's 1.56 GHz Lorentzian linewidth. A narrower linewidth and broader scan range would yield even more measurable time bins.

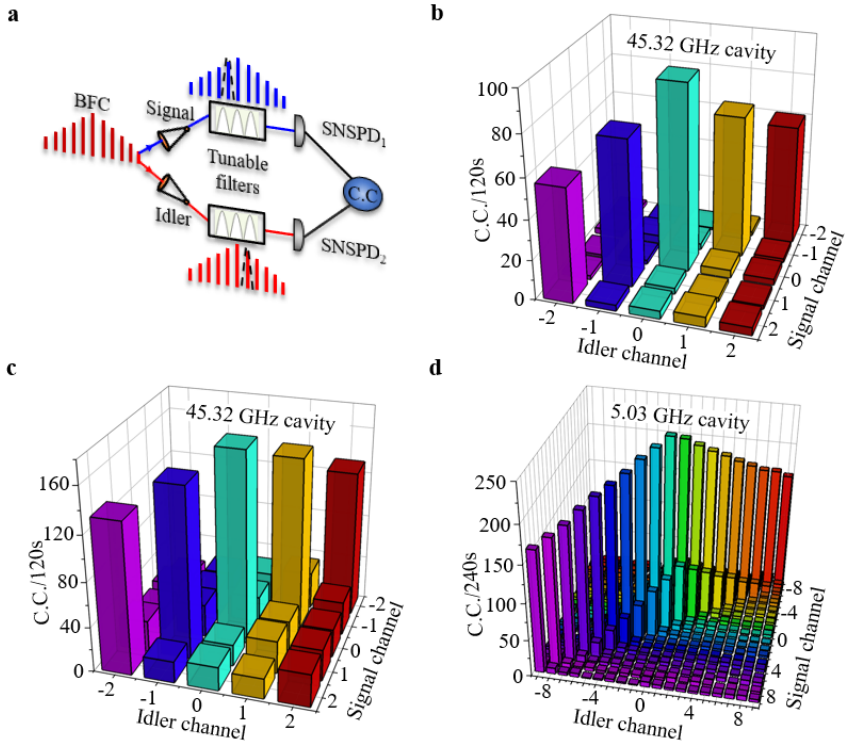

Fig. 3.2. Quantum frequency correlations of high-dimensional BFCs. a) Experimental schematic for the JSI measurements for the high-dimensional quantum state. Signal and idler photons are sent to two tunable narrowband filters for the frequency-bin correlation measurement with coincidence counting. b) Measured frequency correlations of the 45.32 GHz BFC using filters that had matched FWHM bandwidths of 300 pm and were manually tuned for scans from the −2 to +2 frequency bins from frequency degeneracy. The SPDC source was pumped at ≈ 2 mW for these measurements, which produced relatively high coincidence counts only along the diagonal elements of the correlation matrix. The cross-talk between frequency bins was less than 11.71 dB. c) Measured frequency correlations of the 45.32 GHz BFC when the SPDC crystal was pumped at ≈ 4 mW, showing increased signal-idler frequency-bin cross-talk to 6.31 dB. d) Higher-dimensional frequency-bin joint spectral intensity measurements for the 5.03 GHz BFC. The filters used here had matched FWHM bandwidths of 100 pm and were temperature tuned for scans from the −9 to +9 frequency bins from frequency degeneracy. The off-diagonal components increase compared to those in Fig. 3.2a because the effective bandwidth of the tunable narrowband filters spanned multiple FSRs in this demonstration. Fig. 3.2 published in [92].

As described earlier in Sec. 2.9, BFC's frequency-bin correlations arise from the correlation structure inherent in its JSA and hence JSI. Both the HOM and Franson recurrence interference measurements are temporal domain measurements, with repetition time of revival correspond to half of

the cavity round-trip time and cavity round-trip time, respectively. Hence, from the Fourier transform, we expect there will be time-frequency duality between HOM, Franson interference recurrences and frequency-bin correlations, the more time-bins there are the fewer frequency-bins there will be and vice versa.

To demonstrate that behavior, we measure spectral correlations between different signal-idler frequency-bin pairs. In the experiments presented in Fig. 3.2a, we use either the 45.32 GHz FSR cavity or the 5.03 GHz FSR cavity. Each frequency-bin pairs are selected by a pair of tunable narrowband filters. For the 45.32 GHz cavity measurements in Fig. 3.2b and c, the filter has a 300 pm bandwidth; for the 5.03 GHz cavity results in Fig. 3.2d, the filter has a 100 pm bandwidth. In Fig. 3.2b and c, these frequency-bins range from -2 to +2, with 0 denoting frequency degeneracy. This figure shows that the doubly-resonant BFC exhibits the energy-conservation and frequency correlation. In addition, we investigate the impact of multi-pair emissions on the signal-idler frequency-bin cross-talk, as shown in Fig. 3.2c. At ≈ 4 mW pump power, the strongest frequency-bin cross-talk increased by 5.4 dB to 6.31 dB compared to the ≈ 2 mW pump-power case shown in Fig. 3.2b.

Fig. 3.2d shows the greater number of BFC frequency-bins obtained using the 5.03 GHz FSR cavity and 100 pm bandwidth tunable filters. In this measurement, although the temperature limit of these tunable filters (≈ 100 ℃) limited the number of measurable frequency-bins, there are now many more frequency-bins compared to the case in Fig. 3.2b. We also note that higher signal-idler frequency-bin cross-talk is observed in the 5.03 GHz cavity due solely to the 100 pm bandwidth of our filter pairs, which spans several of that cavity's FSRs. We have measured and analyzed the frequency-bin (spectral-correlation) and time-bin (HOM-interference recurrence) subspaces for the BFCs we generated with the 5.03 GHz, 15.15 GHz [75] and 45.32 GHz cavities (measured HOM-interference recurrences for the 5.03 GHz cavity are shown in Appendix A.2). Theory tells us that the BFC's number of frequency-bins N_Ω equals $2\pi B_{\mathrm{PM}}/\Delta\Omega$, where $B_{\mathrm{PM}} = 245$ GHz is the FWHM phase-matching bandwidth of the SPDC source, and its number of time-bins N_T, within an inverse cavity linewidth, equals $\pi/\Delta\omega\Delta T$. Hence their product satisfies $N_T N_\Omega = \pi B_{\mathrm{PM}}/\Delta\omega$ for all three cavities. For the ideal case, in which all the frequency-bins are measurable, we find that

$$N_{T,45\ \mathrm{GHz}} N_{\Omega,45\ \mathrm{GHz}} \approx N_{T,15\ \mathrm{GHz}} N_{\Omega,15\ \mathrm{GHz}} \tag{3.4}$$

where the subscripts label the cavity FSRs, owing to the nearly identical linewidths of the two cavities. In contrast, the time-bin and frequency-bin product for the 5.03 GHz cavity should be roughly a factor of three higher, owing to its smaller cavity linewidth. We note that this time-bin and frequency-bin tradeoff for any of our three cavities supports high-dimensional encoding using time-

and frequency-bins of BFC.

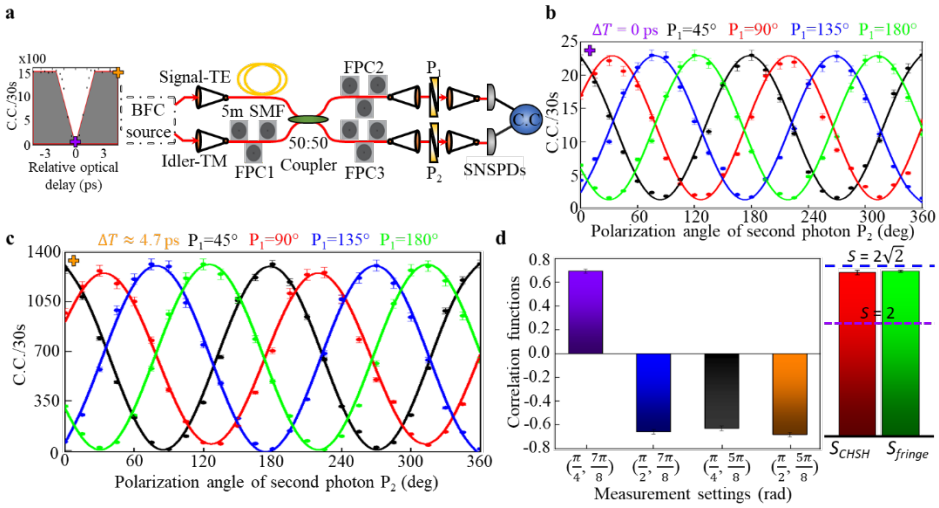

Fig. 3.3. Polarization hyperentanglement measurements of a high-dimensional 45 GHz BFC. a) Illustrative experimental scheme in which the signal and idler photons from a 45.32 GHz BFC were sent to post-selected polarization entanglement measurements. The left inset of Fig. 3.3a is also included to indicate the frequency-polarization entanglement measurements after central HOM dip. The orange and purple marks indicate the position where the measurements are performed. P: linear polarizer; b) Characterization of polarization entanglement at the central HOM dip with polarizer P_1 fixed at 45° (black curve), 90° (red curve), 135° (blue curve), and 180° (green curve). In all cases, we measured the coincidence-counting rates at the two outputs while changing polarizer P_2 from 0^{o} to 360^{o}. In all four cases the measured fringes are well fit with sinusoidal curves, having accidentals-subtracted mean visibilities of 89.98 ± 0.62%. c) By setting the relative delay to 0.7 mm (≈ 4.7 ps) away from the central HOM dip position, we measured the polarization entanglement of our BFC. d) Correlation values needed for the Clauser-Horne-Shimony-Holt (CHSH) inequality, performed for results in panel c. The abscissa label (φ_1, φ_2) denotes the measured polarization bases. The S_{CHSH} parameter was calculated to be 2.686 ± 0.037 from these correlations, which violates the CHSH inequality by 18.5 standard deviations. We obtained the maximal achievable S_{fringe} parameter to be 2.771 ± 0.016 from the mean visibility of the entanglement correlation fringes. Purple and blue dashed lines denote the classical and quantum boundaries. Error bars represent statistical errors. Fig. 3.3 published in [92].

Besides the multiple time- and frequency- bins in our doubly-resonant BFC, it also exhibits polarization entanglement due to the type-II configuration. Hence, in this work, we further enhance the

Hilbert space dimensionality of our doubly-resonant BFC via probing the polarization entanglement and frequency-polarization hyperentanglement by using the experimental setup in Fig. 3.3a. We couple the 45.32 GHz cavity BFC's outputs into low-loss fiber bench setups and performed the polarization entanglement measurement at the central HOM dip. The coupling loss for the fiber benches are ≈ 1.3 dB and ≈ 1.5 dB respectively. We measured the post-selected polarization entanglement by recording the coincidence-count rates while changing the angle of polarizer P_2 when polarizer P_1 is set at 45°, 90°, 135° and 180°. The results are shown in Fig. 3.3b, where we see that the measured fringes are well fit by sinusoidal curves, having accidentals-subtracted mean visibilities of 89.98 ± 0.62%. Here we attribute the non-optimal polarization visibility to imperfect mode matching and limited PBS extinction ratio. Subsequently, by setting the optical delay at 0.7 mm, so that the signal and idler photons have a relative delay of ≈ 4.7 ps which is outside the central HOM dip (width = 3.86 $\pm$ 0.30 ps), we measured the polarization entanglement to demonstrate our BFC's post-selected frequency-polarization hyperentanglement. As shown in Fig. 3.3c, the measured fringes have accidentals-subtracted mean visibilities of 97.96 $\pm$ 0.41%. The fitted results for Fig. 3.3c are used to obtain the correlation functions and the corresponding S parameters. The results are shown in Fig. 3.3d. We measure the coincidences at the CHSH polarizer angles for the polarization subspace, and then calculate the S_{CHSH} parameter. We choose to optimize S_{CHSH} by using $\varphi_1 = \pi/4$, $\varphi_1{}' = \pi/2$, $\varphi_2 = 5\pi/8$, $\varphi_2{}' = 7\pi/8$ [172]. We find S_{CHSH} to be 2.686 $\pm$ 0.037 from those correlation values, which violates the CHSH inequality by 18.5 standard deviations. In addition, we estimate the maximum achievable S_{fringe} parameter of 2.771 $\pm$ 0.016 from the mean visibility of the entanglement-correlation fringes. The combination of post-selected polarization entanglement and HOM interference is consistent with our BFC gives post-selected frequency-polarization hyperentanglement [203].

To further characterize and verify our doubly-resonant BFC to support its high-quality time-energy entanglement [144], we establish and stabilized a Franson interferometry which consists of two unbalanced MZIs, as shown in Fig. 3.4a. To achieve long-term stability, the MZIs are enclosed in a multilayer thermally-insulated enclosure whose temperature is actively stabilized. In Fig. 3.4a left inset the long-short path mismatch of each MZI is measured to be ΔT = 4.84 ns, which satisfies the requirement of phase-sensitive quantum fourth-order interference. We use a thermal heater in long path of arm1 to fine-tune the relative phase shift ΔT_1 between the two MZIs using our 45.32 GHz BFC. In addition, the motorized stage position ΔT_2 is fixed at the center of optimum Franson interference, with the maximum constructive interference shown in Fig. 3.4a left inset. A zoom-in shows the

Franson interference visibility of up to 96.1% (99.1% after subtracting accidental coincidences) as shown in Fig. 3.4a right inset. Fig. 3.4b shows the measured Franson interference fringes and that the recurrence period for them equals the fiber cavity round-trip time. The recurrences have a 22.09 ps period, and with fringe visibilities that decay according to the cavity Lorentzian lineshape as shown in Fig. 3.4c and in Appendix A.3. Moreover, when we move the motorized stage to a ΔT_2 in-between cavity round trips (non-integer) such as 33 ps, we indeed observe no fringes, as also shown in the inset of Fig. 3.4c. We note that we only measured for $\Delta T_2 \geq 0$, limited by the free-space optical DL in the long path of arm2, which can reach up to 360 ps in our measurements.

To give quantitative lower bounds on the time-energy entanglement of our 45.32 GHz and 15.15 GHz BFCs, we calculate the entanglement of formation by using these state's Franson interference recurrences (0^{th} to 3^{rd} order for the 45.32 GHz and 15.15 GHz BFC). In Fig. 3.4d, we compute entanglement of formation up to 1.89 ± 0.03 ebits for the 45.32 GHz BFC and that up to 1.40 ± 0.05 ebits for the 15.15 GHz BFC. The theoretical entanglement of formation for visibilities V of 0.98 and 1 are also illustrated in the dashed line plots with 2 ebits as the maximum entanglement for a 4×4 high-dimensional biphoton. The close match between our results and ideal limits bolsters a nearly non-separable high-dimensional BFC state generation in a doubly-resonant scheme. Detailed analysis numbers are also noted in Appendix B.2.

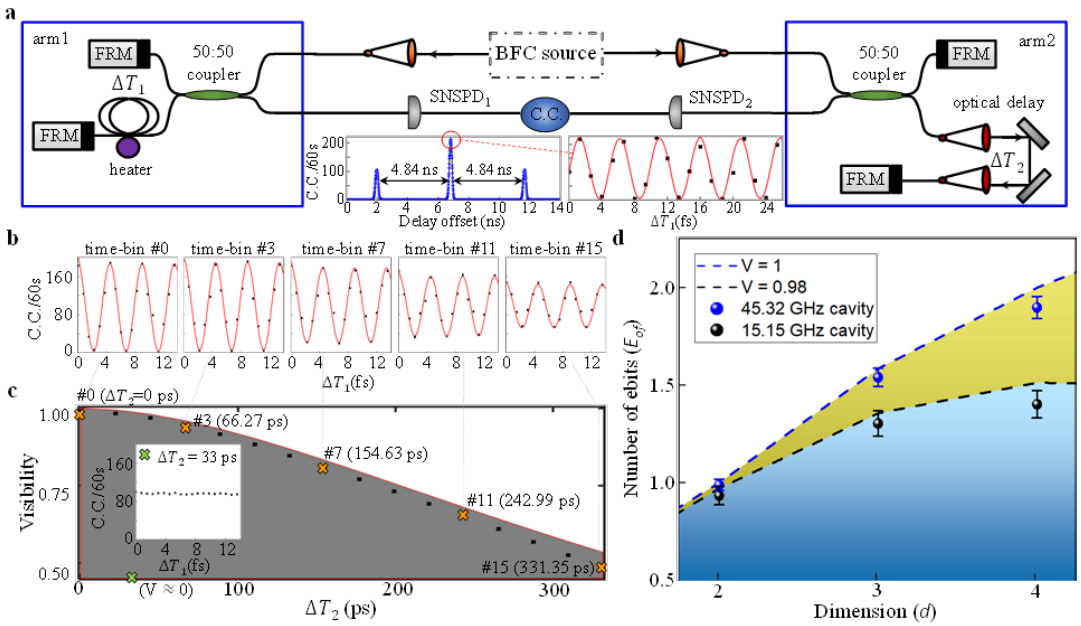

Fig. 3.4. Measured energy-time Franson revival interferometry of the high-dimensional BFC. a) Experimental Franson interference setup. Faraday mirrors (FRMs) compensates the stress-birefringence of the single-mode fiber interferometers. A compact optical delay line is used in the longer path of arm2 (ΔT_2) to provide the tunability in optical delay up to 360 ps. Left inset: temporal two-photon waveforms (in blue) of Franson interferometry for constructive interferences. Right inset: zoom-in observed phase-sensitive interference fringe (in red) versus the relative optical delay introduced by the heater in long path of arm1 (ΔT_1). The observed Franson visibility is 96.1%, or 99.07% after subtracting the accidental coincidence counts. b) and c) Witnessed visibility of the Franson revival interference fringes. The coincidence counts in Franson interference experiments are selected for 0 (time-bin 0), 3, 7, 11 and 15 (time-bin 15) round-trip times of the 45.32 GHz fiber cavity (orange crosses; each round-trip time-bin at 22.09 ps), matching well with theoretical fringe envelope (red solid line; also, further detailed in Appendix A.3). Also included with the green cross in panel c inset is the Franson interference, when measured away from the integer time-bins (such as at ΔT_2 = 33 ps), with no observable interference fringes. d) Lower bounds for the entanglement of formation (number of ebits) versus dimension d, in reconstructing the density matrix. Time-frequency entanglement containing up to 1.89 $\pm$ 0.03 ebits for the 45.32 GHz BFC out of the maximum 2 ebits when d = 4. For the 15.15 GHz BFC, the Franson interference recurrences extract 1.40 $\pm$ 0.05 ebits out of the maximum of 2 ebits (also detailed in Appendix B.2). Fig. 3.4 published in [92].

The mode-locked high-dimensional BFC affords discrete-variable (binned) entanglement in both time and frequency domains that can be quantified from our frequency-binned correlation

measurements and our HOM-interference recurrences by means of Schmidt mode decompositions [92] in the two domains. In both cases the key quantity is the Schmidt number K. For ease of Schmidt mode decomposition analysis, we assume that our BFC is close to a pure state, which is supported by our close match of maximum entanglement of formation in Fig. 3.4. Then, by extracting the Schmidt eigenvalues $\{\lambda_n\}$ from the JSI measurements in Fig. 3.2, the Schmidt number of the frequency-binned state K_Ω, can be obtained as shown in Fig. 3.5a. This parameter indicates how many frequency-binned Schmidt modes are active in the biphoton state, and therefore describes its effective dimensionality [78]. In particular, extracting the Schmidt eigenvalues $\{\lambda_n\}$ from the five resonance-pairs data of Fig. 3.2b for the 45.32 GHz FSR cavity and 2 mW pumping results in a frequency-bin Schmidt number $K_{\Omega,45\ GHz} \approx 4.31$. For the 45.32 GHz FSR cavity with 4 mW pump power, the data in Fig. 3.2c leads to $K_{\Omega,45\ GHz} \approx 3.17$, because the increased signal-idler frequency-bin cross-talk drops the purity of each diagonal frequency mode, resulting in a smaller Schmidt number. We also note that the increased multi-pair emissions responsible for this additional cross-talk makes the output of the BFC less like a biphoton. For our 15.15 GHz FSR cavity [75], we obtain a $K_{\Omega,15\ GHz} \approx 8.67$ frequency-bin Schmidt number, where the number of frequency-correlated pairs is limited only by the maximum temperature tuning of our 100 pm FBG filters. Subsequently we used the frequency-bin data from Fig. 3.2d to find the 5.03 GHz cavity's frequency-bin Schmidt number. Using the third panel in Fig. 3.5a, we obtain $K_{\Omega,5\ GHz} \approx 11.67$ for that cavity. This imperfect Schmidt number mostly due to the resolution bounds of our 100 pm bandwidth filters (the ideal Schmidt number for frequency-binned measurements is calculated in Appendix B.1.1), but it still demonstrates the scalability of our high-dimensional frequency-binned BFC. In Fig. 3.5a we compare the extracted frequency-bin Schmidt eigenvalues $\{\lambda_n\}$ for our three cavities (detailed calculations of the Schmidt eigenvalues $\{\lambda_n\}$ and the resulting Schmidt numbers are in Appendix B.1.1).

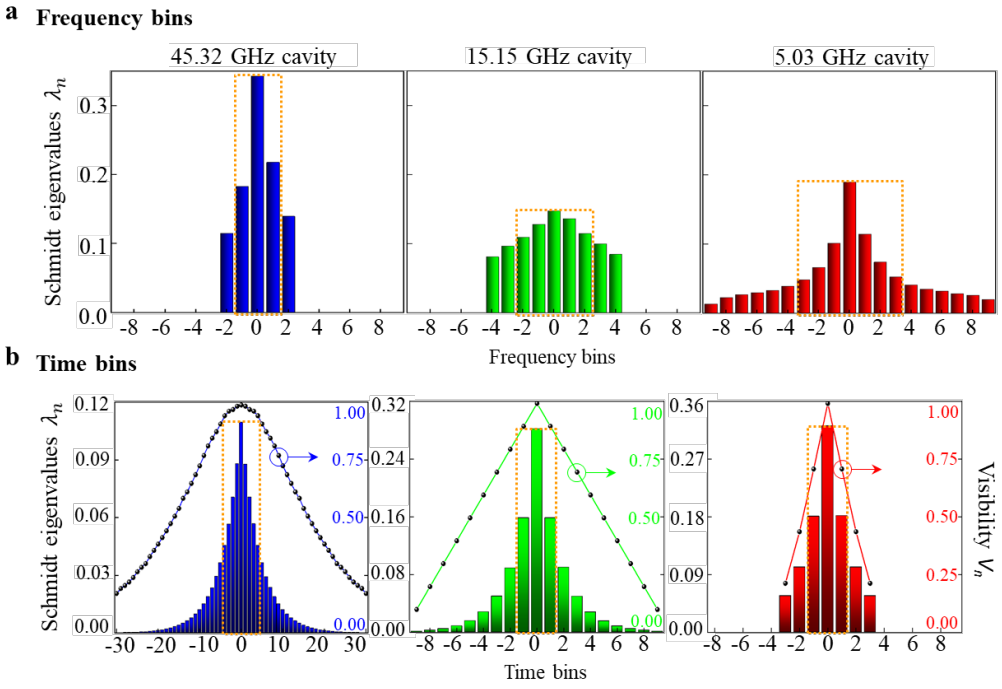

Fig. 3.5. Schmidt mode decompositions for three high-dimensional BFCs. a) The Schmidt mode eigenvalues for measured frequency-binned states obtained using our 45.32 GHz, 15.15 GHz, and 5.03 GHz FSR cavities with ≈ 2 mW pump power (calculation detailed in Appendix B.1.1). The obtained frequency-bin Schmidt numbers are $K_{\Omega,45\ \mathrm{GHz}} \approx 4.31$, $K_{\Omega,15\ \mathrm{GHz}} \approx 8.67$ and $K_{\Omega,5\ \mathrm{GHz}} \approx 11.67$ for the three cavities. b) The Schmidt mode eigenvalues versus different time bins from HOM interferometry and the corresponding visibilities of the HOM-interference recurrences. The blue, green, and red bars indicate the time-binned Schmidt eigenvalues for the 45.32 GHz, 15.15 GHz, and 5.03 GHz cavities respectively, and the black points indicate the visibilities from HOM interferometry. The central HOM dip is labeled as 0 as a reference. The dominant Schmidt mode eigenvalues for each high-dimensional BFC have been highlighted within the orange-dashed boxes and detailed in Appendix B.1.2. The obtained time-bin Schmidt numbers are $K_{T,5\ \mathrm{GHz}} \approx 5.16$, $K_{T,15\ \mathrm{GHz}} \approx 6.71$, and $K_{T,45\ \mathrm{GHz}} \approx 18.30$ for the three cavities. Fig. 3.5 published in [92].

Note that we obtain different frequency-binned BFC Schmidt numbers from the same SPDC phase-matching bandwidth by using cavities with different FSRs. From our measurements, the diagonal elements of the spectral-correlation matrix show the decreasing-envelope behavior of the BFC. Hence, with the Schmidt decomposition, we have observed BFC states with Hilbert-space dimensionalities, $K_\Omega \times K_\Omega$, having lower bounds of least 16 for the 45.32 GHz cavity, 64 for the 15.15 GHz cavity, and 121 for the 5.03 GHz cavity. Furthermore, the ideal full Hilbert-space dimensionalities are estimated to

be at least 24 (= 4.9 × 4.9) for the 45.32 GHz cavity, 400 (= 20 × 20) for the 15.15 GHz cavity, and 1156 (= 34 × 34) for the 5.03 GHz cavity, where the numbers arise from the detailed theory for the frequency-binned BFC's Schmidt number in Appendix B.1.1.

Turning now to the Schmidt number for the time-binned BFC, to proceed in a manner analogous to what we used for the frequency-binned BFC would require knowledge of the binned JTI. However, because our BFC is generated with cw pumping, this binned JTI, under the assumption of a pure-state biphoton, is a diagonal matrix with elements $|\psi(n\Delta T)|^2$, where $\psi(\tau)$ is the BFC's time-domain wavefunction from and $n\Delta T$ is the relative delay between the signal and idler photons' *n*th time bin. We can estimate that binned JTI from our HOM-interference data, as we now explain. By sampling $\psi(\tau)$ at $\tau = n\Delta T$, we get

$$|\psi(n\Delta T)|^2 = \frac{\exp\left(-2|n|\Delta\omega\Delta T\right)}{\sum_{n=-N_0}^{N_0}\exp\left(-2|n|\Delta\omega\Delta T\right)} \tag{3.5}$$

for the JTI. From Appendix A.2, we have that the visibility of the *n*th HOM dip is:

$$V_n = \exp(-|n|\Delta\omega\Delta T)\,(1 + |n|\Delta\omega\Delta T) \tag{3.6}$$

thus making it possible to find the BFC's JTI by inverting the one-to-one relation between $|n|\Delta\omega\Delta T$ and V_n. Measuring the binned JTA, whose singular-value decomposition is the Schmidt decomposition, is prohibitively difficult. Hence, we assume, that it equals the square-root of the binned JTI, and use

$$\psi(n\Delta T) = \sqrt{|\psi(n\Delta T)|^2} \tag{3.7}$$

for the time-binned wavefunction of the BFC, from which it follows that the time-bin Schmidt mode eigenvalues, $\{\lambda_n\}$, are given by:

$$\lambda_n = \frac{\mathrm{e}^{-2\pi|n|/F}}{\sum_{n=-N}^{N}\mathrm{e}^{-2\pi|n|/F}} = \frac{\sinh\left(\pi/F\right)\exp\left(-2\pi|n|/F\right)}{\cosh(\pi/F) - \exp\left(-(2N+1)\pi/F\right)}, \text{ for } 0 \le |n| \le N \tag{3.8}$$

where $F = \Delta\Omega/2\Delta\omega$ is the cavity finesse. The time-binned BFC state's Schmidt number is then found to be $K_{T,5\ GHz} \approx 5.16$, $K_{T,15\ GHz} \approx 6.71$, and $K_{T,45\ GHz} \approx 18.30$. By performing a parametric ($|n|\Delta\omega\Delta T$) fit of our experimental data to the V_n expression and then applying equation (3.6) to (3.8), we obtain the experimental values $K_{T,5\ GHz} \approx 5.11$, $K_{T,15\ GHz} \approx 6.56$, and $K_{T,45\ GHz} \approx 18.02$, which agree well with theory. All the extracted time-binned Schmidt eigenvalues are shown in Fig. 3.5b.

For the 45.32 GHz cavity's BFC, the HOM interference recurrences' lower bound on the Hilbert space dimensionality is therefore $K_{T,45\ GHz} \times K_{T,45\ GHz} = 324$. Augmenting the time-bins with the BFC's post-selected polarization entanglement doubles this dimensionality to at least 648. Furthermore, we find that the product of the time-binned and frequency-binned Schmidt numbers

(when all the frequency bins are measurable, and the measurable HOM time bins run from -340 ps to 340 ps relative delay) is similar for the 45.32 GHz and 15.15 GHz BFCs:

$$K_{T,45\ \mathrm{GHz}} K_{\Omega,45\ \mathrm{GHz}} \cong K_{T,15\ \mathrm{GHz}} K_{\Omega,15\ \mathrm{GHz}} \tag{3.9}$$

which mimics the previous BFC time-frequency product relation.

Our Schmidt mode analysis demonstrates the effective time-frequency scaling (increase/decrease in number of bins) by using our doubly-resonant BFCs. For the three fiber cavities that we measured, we have successfully scaled the time-binned Schmidt numbers from $K_{T,5\ GHz} \approx 5.11$ to $K_{T,45\ GHz} \approx 18.02$, limited by the finesses of the fiber cavities. In the frequency-binned subspace we scaled from $K_{\Omega,45\ \mathrm{GHz}} \approx 4.31$ to $K_{\Omega,5\ \mathrm{GHz}} \approx 11.67$, limited by the temperature tunability of the tunable filters. The scaling of time-frequency dimensionality is complementary, the higher the Schmidt number in time or frequency, the smaller the Schmidt number in its conjugate domain. Multiplying the highest estimated time-binned Schmidt number by its frequency-binned Schmidt number counterpart yields a total Schmidt number of 77.67, which could encode over 12 qubits ($K_T K_\Omega \times K_T K_\Omega > 2^{12}$), with potentially 6.28 bits/photon [from $\log_2(K_T K_\Omega) = 6.28$)] classical-information capacity that can be used in high-dimensional QKD with our BFCs.

To this point we have asserted that our filtering of the signal and idler outputs from a cw-pumped SPDC source generates a nearly non-separable high-dimensional BFC state. Toward that end we have reported experimental results consistent with that interpretation: HOM interference recurrences, frequency-bin correlations, Franson interference recurrences and their inferred entanglement of formation, and Schmidt mode decompositions in the time-bin and frequency-bin subspaces. Our BFC frequency-domain wavefunction's being an even function of detuning implies that its JSI determines its HOM-interference behavior [88], and in general the BFC's JSI determines its frequency-binned correlations and its Franson interference behavior (see Appendix A.2 and A.3 for details). That said, standard perturbation theory, see, e.g., [201], predicts that a cw-pumped SPDC will emit pure-state (or nearly pure-state) biphotons, and the excellent stabilization of our fiber FP cavities then implies that our filtered SPDC sources should then emit nearly non-separable BFC states. Prior experimental work supports the nearly pure-state assertion for a SPDC source's output, see [204], in which both the JSI and JTI were measured for a pulse-pumped source, and [182], in which an SPDC source was entanglement engineered to produce single spatiotemporal-mode heralded single-photon pulses. Moreover, we also note that there have been several experimental demonstrations of high dimensional frequency-bin entanglement utilizing the

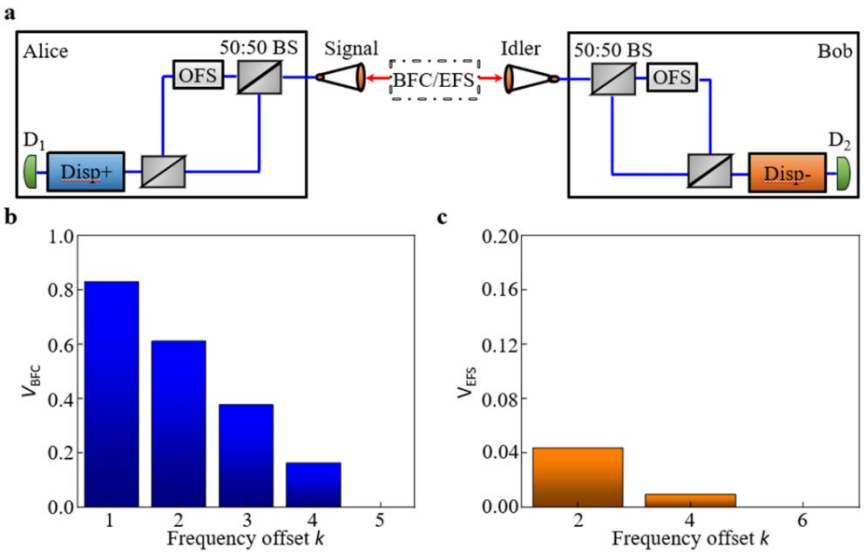

Fig. 3.6. Conjugate Franson interferometry and theoretical visibilities of conjugate Franson interference recurrences for the 45 GHz BFC and the entangled frequency-pair state. a) The proposed experimental setup for conjugate Franson interferometry. The signal and idler outputs from a filtered-SPDC source are applied to a pair of MZIs. One arm of each MZI contains an optical frequency shifter, i.e., a single-sideband modulator, that imposes frequency shifts $+\omega_m$ and $-\omega_m$ on the signal and idler, respectively. The MZI's outputs undergo positive (for the signal) and negative (for the idler) dispersions of equal magnitude that, together with the frequency shifts, ensure there is no second-order interference present in the signal-idler coincidence counts. b) BFC theoretical conjugate Franson interference has high-visibility recurrences and they occur only when the interferometer frequency offset is $k\Delta\Omega$ for integer k. c) Entangled frequency-pair state theoretical conjugate Franson interference has low-visibility recurrences and they only occur when the interferometer frequency offset is $2k\Delta\Omega$ for integer k. Appendix A.4 describes the details of conjugate Franson interferometry, comparing the BFC and entangled frequency-pair state recurrence visibilities for the 15.15 GHz and 5.03 GHz cavities. Fig. 3.6 published in [92].

sinusoidally driven phase modulator in recent years [83, 84, 86, 205]. Nevertheless, direct experimental evidence of a BFC state purity is highly desirable. One way is to perform the direct JTI measurements, we have recently observed such mode-locked oscillations in temporal domain to prove the biphoton phase coherence of our BFC, and hence verify the pure BFC state. Conjugate-Franson interferometry [127], since it is characterized by the signal-idler state's JTI, can also provide such evidence. The configuration for conjugate-Franson interferometry is shown in Fig. 3.6a. Compared to our Franson interferometry setup in Fig. 3.5a, a pair of optical frequency shifters and DCMs are

required to implement the conjugate-Franson interferometry. In particular, this configuration easily allows the desired BFC pure state to be distinguished from mixed states with the same JSI. For example, Fig. 3.6b and c compare the visibilities for conjugate-Franson interference recurrences of our 45.32 GHz BFC to those of the entangled frequency-pair state, i.e., an incoherent mixture of the pure states

$$\left|\psi_{\mathrm{EFS}}^{(\mathrm{m})}\right\rangle = \int d\Omega\, f'(\Omega)[f(\Omega + m\Delta\Omega) + f(\Omega - m\Delta\Omega)]\, \hat{a}_H^\dagger\left(\frac{\omega_p}{2} + \Omega\right)\hat{a}_V^\dagger\left(\frac{\omega_p}{2} - \Omega\right)|0\rangle \qquad (3.10)$$

for $-N_0 \leq m \leq N_0$, that has the same JSI (see Appendix A.4 for more details). By driving frequency shifters in conjugate-Franson interferometry for a BFC with matched cavity FSR, its possible to demonstrate conjugate-Franson interference recurrences that further enhance the non-separable mode-locked high-dimensional BFC state generation [128].

In this work we have demonstrated high-dimensionality time-frequency subspaces using a BFC generated by filtering the signal and idler outputs from a cw-pumped SPDC source. For a BFC generated with a 45.32 GHz FSR filter cavity we achieved 61 HOM-interference recurrences, with a maximum visibility of 98.4% (99.9%) before (after) accidental coincidences are subtracted. For a BFC generated with a 5.03 GHz FSR filter cavity, we observed high spectral correlations over 19 frequency bins. All told, for the three cavities we employed, we explored spectral and temporal correlations, and hence their Fourier-transform duality, over cavity FSRs spanning nearly an order of magnitude. We then measured up to 16 Franson interference recurrences, observing a maximum visibility of 96.0% (99.1%) before (after) accidental coincidences are subtracted. Using the 0^{th} to 3^{rd} recurrence visibilities allowed us to obtain an entanglement of formation up to 1.89 ± 0.03 ebits, where 2 is the maximum for a 4×4 dimensional biphoton as lower bound on our BFC's high-dimensional time-energy entanglement. Via Schmidt mode decompositions, we quantified the entanglement scaling of our BFCs' time-binned and frequency-binned subspaces, comparing measured values with their theoretical counterparts. For example, our 45.32 GHz cavity's post-selected frequency-polarization hyperentangled BFC achieves a time-binned Schmidt number of 18 and a Hilbert-space dimensionality of at least 648, based on the assumption of a pure state, representing an advance of almost an order of magnitude compared to our previous work. With the time-frequency duality and the frequency-polarization hyperentanglement of such a BFC, we infer a computational space of more than 12 qubits, with 6.28 bits/photon that can potentially be encoded for classical information transmission over a quantum channel using only biphotons. This high-dimensionality time-frequency state encodes multiple qubits from different DoFs onto biphoton pairs, and thus further increasing the photon

information capacity with applications in high-dimensional QIP, time-frequency cluster-state quantum computation, and high-dimensional QKD.

3.4 Singly-resonant mode-locked biphoton frequency combs

Recently demonstrated BFC can carry information in the spectro-temporal quantum modes, becomes an ideal candidate for large-scale quantum systems. Such high-dimensional BFC can be generated by SPDC with post filtering [75, 86, 92], OPO far below threshold [143, 177], or SFWM in integrated microring resonators [76, 78]. The first approach can be realized either by sending the SPDC photons through a cavity or directly carving the continuous SPDC spectra. The second approach is implemented via cavity-enhanced SPDC, where the photon pair generation is enhanced and spectrally confined by the cavity modes. The third approach utilizes third-order nonlinearity to generate photon entanglement over large frequency modes in a scalable and manufacturable platform. These BFCs are mostly doubly-resonant, namely, the signal and idler photons are simultaneously resonant to the cavity modes. On the other hand, singly-resonant BFC based on OPO has been proposed for narrow-band photon generation, where only the signal photons are resonant to the cavity mode [206]. Due to the entanglement between signal and idler photons from biphoton generation process, the idler photons still exhibit comb-like spectrum corresponding to the cavity mode structure. This singly-resonant OPO increase the brightness of the modes by a factor of the cavity finesse, while provides better stability and tunability due to the confinement to only one of the SPDC photons [207]. Recently, singly-resonant BFC has been demonstrated to generate frequency-multiplexed photon pairs over 1000 frequency modes [177], and also massive-mode polarization entangled photon pairs by means of a Sagnac interferometer [208]. Although singly-resonant BFC provides a promising QIP platform, the high-dimensional time-energy entanglement of such singly-resonant BFC has not been investigated. Moreover, the distribution of high-dimensional entanglement [78, 116, 117], which is a necessary and important precursor for practical large-scale high-dimensional quantum communication and distributed quantum networks, remains challenging. And high-dimensional time-energy entanglement distribution has yet been demonstrated on a singly-resonant BFC platform.

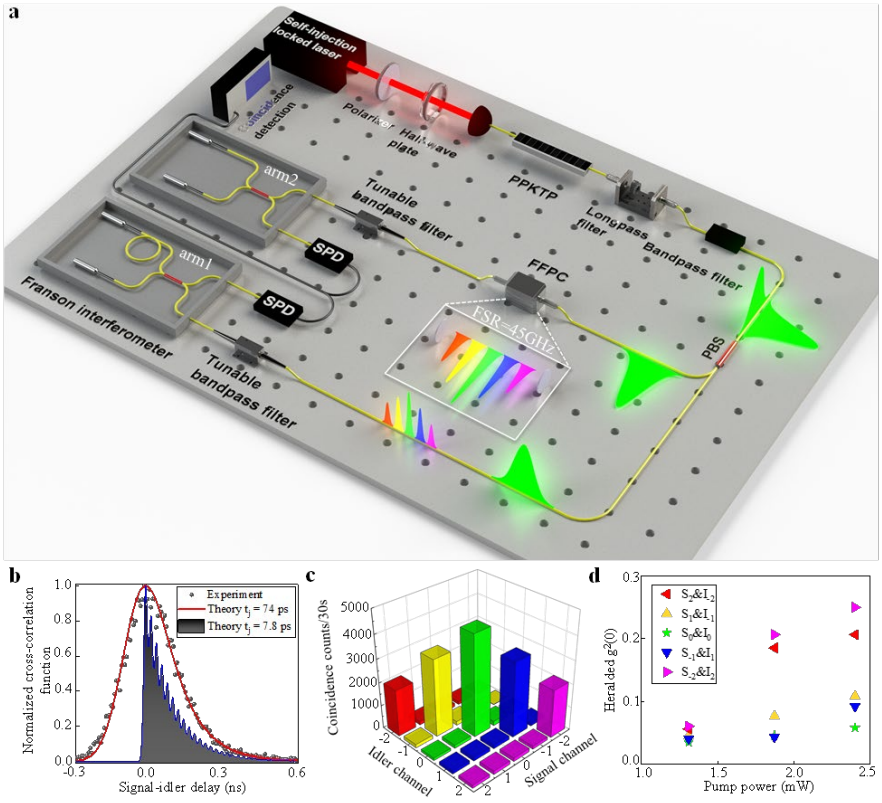

Fig. 3.7. Generation and spectro-temporal characterization of a 45 GHz singly-resonant BFC. a) Experimental schematic for generation and characterization of a singly-resonant BFC. SPD: superconducting nanowire single-photon detector. b) Experimental and theoretical temporal second-order cross-correlation function between signal and idler photons. Based on the 1.56 GHz cavity bandwidth and 45.32 GHz FSR of our fiber FP cavity, we theoretically fit our experimental results with different effective detector timing jitters. The periodic temporal oscillations of cross-correlation function for the 45.32 GHz cavity's singly-resonant BFC can be resolved when the effective timing jitter is set equal to or less than the cavity's round-trip time (detailed calculations are in Appendix A.1). c) Measured frequency-correlation matrix of our 45 GHz singly-resonant BFC within the 245 GHz SPDC bandwidth. The JSI is measured by using a pair of tunable bandpass filters with 300 pm bandwidths to select frequency bins for the signal and idler photons. Only the diagonal elements of the frequency-correlation matrix show high coincidence counts, consistent with high-dimensional frequency-bin entanglement. d) Measured heralded single-photon second-order auto-correlation function $g^{(2)}(0)$ versus the pump power for each frequency-bin pair. The minimum heralded $g^{(2)}(0) \approx 0.035$ is measured for S_0&I_0 pair at 1.3 mW pump power with a heralding rate of 16 coincidences/s. All measured heralded $g^{(2)}(0)$'s are below the classical threshold, verifying the high purity of the frequency-binned single photon states from our singly-resonant BFC.

Here, we demonstrate a full temporal and spectral characterization of singly-resonant high-dimensional BFC by only connecting the signal photons of the SPDC photon pairs to a fiber FP cavity, and distribute time-frequency-bins towards practical long-distance quantum network on a high-dimensional BFC platform [111]. Fig. 3.7a illustrates the experimental setup to generate and characterize the singly-resonant BFC. The entangled photon pairs are generated by a type-II ppKTP waveguide as Sec. 3.2. A 658 nm FP laser diode, stabilized by self-injection locking through double-pass first-order diffraction feedback using an external grating, is used to pump the ppKTP waveguide. The generated biphotons are orthogonally polarized and frequency degenerate at ≈ 1316 nm with ≈ 245 GHz bandwidth. The residual pump photons are eliminated by a LPF. A BPF with bandwidth larger than the SPDC photons is used to further clean the biphoton spectrum. Then the signal and idler photons are separated efficiently by a PBS, resulting in deterministic BFC generation. The singly-resonant BFC is generated by only passing the signal photons through a fiber FP cavity. The idler photons, although not confined in a cavity, will still exhibit comb-like spectrum in coincidence counting measurements due to intrinsic frequency correlation of SPDC photons [207]. The FP cavity has a 45.32 GHz FSR and 1.56 GHz bandwidth, stabilized with a high-performance temperature controller. In the doubly-resonant case, the polarization birefringence of the fiber etalon will result in different spectra of the signal and idler photons after they pass through the cavity. However, in the singly-resonant configuration, only the signal photons pass through the FP cavity and thus we circumvent the requirement to eliminate the polarization birefringence.

We first characterize the temporal signature of the singly-resonant BFC. Our singly-resonant configuration generates a BFC state as

$$|\psi\rangle = \sum_{m=-N}^{N} \int d\Omega\, f(\Omega - m\Delta\Omega)\mathrm{sinc}(A\Omega)\, \hat{a}_H^\dagger(\tfrac{\omega_p}{2} + \Omega)\hat{a}_V^\dagger(\tfrac{\omega_p}{2} - \Omega)|0\rangle \tag{3.11}$$

the temporal wavefunction of the singly-resonant BFC can be written as

$$|\psi\rangle = \int_0^\infty d\tau \exp(-\Delta\omega\tau) \sum_{m=-N}^{N} \mathrm{sinc}(Am\Delta\Omega)\cos(m\Delta\Omega\tau)\hat{a}_H^\dagger(t+\tau)\hat{a}_V^\dagger(t)\,|0\rangle \tag{3.12}$$

where the temporal behavior of the BFC is mainly determined by $\sin[(2N+1)\Delta\Omega\tau/2]/\sin(\Delta\Omega\tau/2)$, with a repetition time of $\Delta T = 2\pi/\Delta\Omega \approx 22.1$ ps.

Fig. 3.7b shows the normalized second-order cross-correlation function $g^{(2)}(\tau)$ between signal and idler photons, measured by SNSPDs (≈ 80% detection efficiency, PhotonSpot Inc.) with coincidence time window at 2 ns. The single-sided exponential decay of the cross-correlation function is observed, which is the temporal signature of a singly-resonant BFC [177, 206, 207]. This temporal profile of the second-order cross-correlation function $g^{(2)}(\tau)$ matches well with our theoretical

calculations with effective timing jitter of the detectors $t_j = 9.5\Delta T/\sqrt{8}$ (detailed in Appendix A.1). We note that the measured cross-correlation function cannot fully resolve the temporal oscillation signature of the 45 GHz singly-resonant BFC due to the relatively large timing jitter of our SNSPDs (~210 ps). With lower effective timing jitter of the detectors, the temporal oscillation profile can be better resolved as shown in Fig. 3.7b with $t_j = \Delta T/\sqrt{8}$. Low time-jitter SNSPDs have been recently demonstrated, which enables better temporal resolution [51]. When $t_j = 0.1\Delta T/\sqrt{8}$, the temporal signature of the 45 GHz singly-resonant BFC can be fully resolved, showing an oscillation periodicity of 22.1 ps (detailed in Appendix A.1).

Next, we characterize the frequency entanglement of our 45 GHz singly-resonant BFC through JSI measurement. We use 2 mW pump power for SPDC generation to eliminate multiphoton emission and reduce cross-talk between frequency bins. The JSI of our singly-resonant BFC is measured by a pair of tunable BPF for signal and idler photons respectively. The BPFs have a bandwidth of 300 pm, which are able to select only one-frequency bin of our singly-resonant BFC. The coincidence counts are recorded while the tunable BPFs are set at different combinations of signal-idler frequency-bin pairs. Within the 245 GHz SPDC bandwidth, 5 frequency-bins can be examined for the signal and idler of our 45 GHz singly-resonant BFC. We sweep the BPFs from -2 to +2 frequency bins, with 0^{th} frequency-bin indicating the central frequency of SPDC. We observe that high photon coincidence counts are measured only for symmetric frequency-bin pairs, shown as the diagonal elements of the frequency correlation matrix in Fig. 3.7c. This reveals the frequency correlation of the singly-resonant BFC, and is a characteristic of frequency-bin entanglement. We note that the coincidence counts fall off at frequency-bin pairs away from the central bin, which results from the Gaussian spectrum of the SPDC biphotons. For each symmetric frequency bin pair, we then measure the second-order auto-correlation $g^{(2)}(0)$ of the idler photons heralded by the signal photons. The measurement is performed using a HBT type interferometry, where the idler photons of the singly- resonant BFC are split into two paths by a 50:50 BS for auto-correlation measurement heralded by signal photons. A pair of tunable BPFs (300 pm bandwidth) are placed before the HBT interferometer to select different frequency bins. The second-order auto-correlation $g^{(2)}(0)$ is measured by recording three-fold coincidence counts between the output ports of the HBT interferometer and idler photons under the coincidence time window of 2 ns. Detecting one photon of the photon pair result in projecting the other photon into a multimode heralded single photon state, which exhibits non-classical antibunching behavior. Fig. 3.7d shows the signal-heralded $g^{(2)}(0)$ versus different pump powers for the five

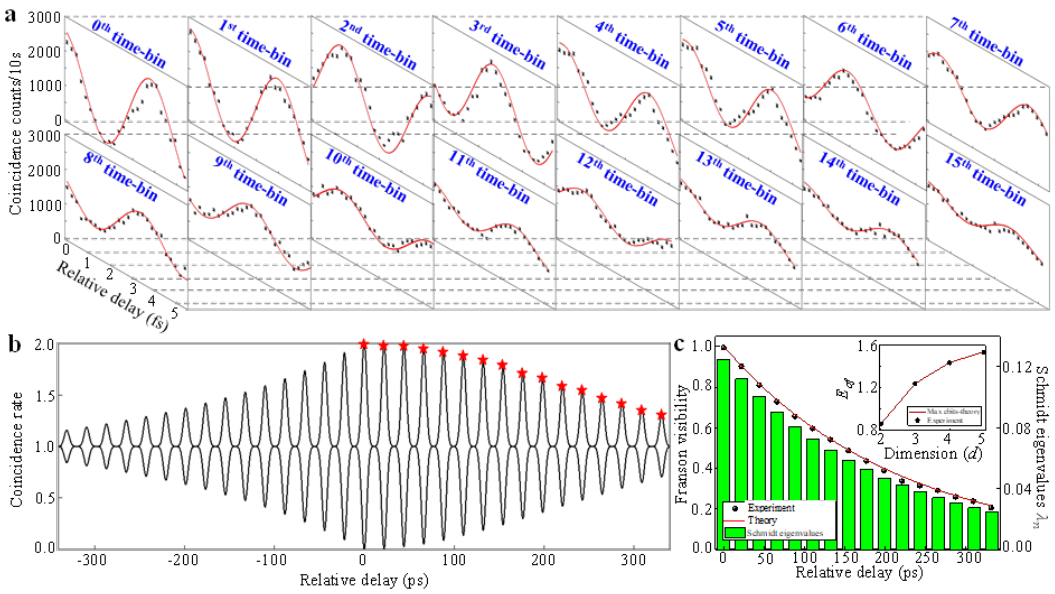

Fig. 3.8. Witness of high-dimensional energy-time entanglement via Franson-interference recurrences of the 45 GHz singly-resonant BFC. a) Measured Franson-interference recurrences within the 360 ps traveling range of arm 1's delay line. The interference fringes are obtained from 0 (0^{th} time-bin) to 15 (15^{th} time-bin) round-trip times of the 45 GHz FSR FP cavity, with the measured period of the interference recurrences found to be 22.1 ps. The maximum fringe visibility up to 99.46% is measured at 0^{th} time-bin. Franson-interference fringe visibilities were obtained with accidental coincidence counts subtracted, and the coincidence window for all the measurements is 2 ns. Error bars measured for each data point arise from Poisson statistics, experimental drift and measurement noise. b) Theoretical fringe envelope of Franson interference for the 45 GHz high-dimensional singly-resonant BFC, with superimposed experimental observations (detailed theory is presented in Appendix A.3). c) Witnessed visibility of high-dimensional Franson interference fringes and Schmidt eigenvalues as a function of relative delay between arm 1 and arm 2. The experimental (theoretical) witnessed visibilities, in percent, for the n^{th} time-bin are 99.46 (100), 90.17 (90.44), 81.03 (81.48), 72.82 (73.57), 65.6 (66.44), 59.57 (59.93), 54.03 (54.2), 48.68 (48.93), 43.54 (44.18), 38.79 (39.87), 35.72 (35.99), 31.47 (32.49), 29.12 (29.32), 25.93 (26.47), 23.79 (23.88) and 20.58 (21.57), respectively, where the exact theory from Appendix A.3 has been employed. The Franson visibility decreases due to the fiber FP cavity's finite linewidth, as captured by our theory. The Schmidt eigenvalues are extracted from Franson-interference recurrences for 16 time bins, resulting in a Schmidt number lower bound of 13.13. Inset shows the E_{of} calculated based on Franson-interference recurrences from Fig. 3.8.

symmetric frequency bin pairs. The pump power is set to be 1.3 mW, 1.8 mW and 2.4 mW respectively. At low pump power, the heralded $g^{(2)}(0)$ for all five frequency bin pairs are below 0.1, showing high purity of the frequency filtered single photon states from our singly-resonant BFC. We observe that the heralded $g^{(2)}(0)$ is proportional to the pump power, due to the Poisson statistics of the SPDC emission. With increased pump power, we note that the heralded $g^{(2)}(0)$ for each frequency bin pair diverges. At higher pump power, the heralded $g^{(2)}(0)$ for S_0 & I_0 (S_0 and I_0 denote the central frequency bin for signal and idler photons, respectively) frequency bin pair is still below 0.1. Especially, the heralded $g^{(2)}(0)$ for S_{+2} & I_{-2} and S_{-2} & I_{+2} increase faster than the case for S_{+1} & I_{-1} and S_{-1} & I_{+1} with increasing pump power. This is because the outer frequency-bin pairs have lower spectrum amplitude due to the SPDC Gaussian spectrum as shown in Fig. 3.7c. The photon states for outer frequency-bins are more sensitive to the spectral noise introduced by the increasing pump power. We also measure the heralded $g^{(2)}(0)$ for the singly resonant BFC state by only using a broadband BPF (225 GHz bandwidth) to clean up the biphoton spectrum in Appendix Fig. A16). A signal-heralded $g^{(2)}(0) \approx 0.154$ is measured for our singly-resonant BFC. We also obtain an idler-heralded $g^{(2)}(0) \approx 0.130$ by switching the role of signal and idler photons. Both heralded $g^{(2)}(0)$ are well below the classical threshold, demonstrating a high-purity heralded single photon state from our singly-resonant BFC.

Then, we characterize the high-dimensional time-energy entanglement of our singly-resonant BFC through Franson interference revivals for the first time. We first use a 1.3 nm bandwidth BPF to clean the SPDC spectrum before separating the signal and idler photons by PBS. The signal photons then pass through a 45 GHz fiber etalon to generate a singly-resonant BFC. The signal and idler photons are sent to a fiber-based Franson interferometer comprised of two unbalanced MZIs as shown in Fig. 3.7a. Each arm includes Michelson interferometers, which are temperature-controlled by Peltier modules and enclosed in a multilayered thermally-insulated housing with active temperature stabilization for long-term phase stability. In each Michelson interferometer, two output ports of the fiber 50:50 beamsplitter are spliced to two Faraday mirrors, which compensates the stress-birefringence of the single-mode fiber within the interferometer. Single photons are collected from the reflection, and the Michelson interferometers can effectively work as an MZI, with polarization instability inside the fibers accurately self-compensated. The long-short path difference of each arm shown in Fig. 3.7a is measured to be ΔT = 4.84 ns, satisfying the general requirement of phase-sensitive Franson interference [75, 92]. A tunable DL is introduced in the long path of arm1 to tune the

time difference between arm1 and arm2 up to 360 ps. This allows us to measure the Franson interference at different temporal revivals for up to 16 positive-delay time bins. A thermal heater in the long path of arm2 with ≈ 1 mK temperature control accuracy finetunes the relative phase shift between two arms of the Franson interferometer. Coincidence counts are collected between the two output ports of the Franson interferometer to obtain the interference fringe with 2 ns coincidence window, after subtracting the accidental coincidence counts.

Fig. 3.8a shows the first-time observed Franson interference revivals on a singly-resonant BFC platform. The Franson interference revivals are only observed at periodic time-bins, whereas no interference is observed between time bins. The measured period of the interference recurrences is 22.1 ps, which corresponds exactly to the round-trip time of the 45.32 GHz FP cavity ($\Delta T = 2\pi/\Delta\Omega$). Franson interferences are measured by selecting the relative delay between and arm1 and arm2 from 0 (0^{th} time-bin) to 15 (15^{th} time-bin) cavity round-trip times, limited by the 360 ps tuning range of the DL in arm1. We obtain a high Franson interference visibility of 99.46% at 0^{th} time-bin, which is well beyond the quantum threshold of $1/\sqrt{2}$ (71%) required to violate the Bell inequality. The Franson interference visibilities decrease as the relative delay increases, i.e., at higher order time-bins. This can be explained by the theoretical model detailed in Appendix A.3, which results from the phase-matching sinc function of SPDC and the Lorentzian lineshape of etalon. The measured Franson interference revivals agree well with our theoretical prediction, as shown in Fig. 3.8b. We note that, different from the symmetric Franson interference fringe envelope for the doubly-resonant BFC [75, 92], our model for the singly-resonant BFC exhibits asymmetric behavior. The Franson visibilities at positive time-bins decrease slower than those at negative time-bins, originating from the asymmetric temporal profile of the cross-correlation function. The measured Franson visibilities are in good agreement with our theoretical calculation, as shown in Fig. 3.8c. We compare the Franson visibility fitting of our singly-resonant BFC with doubly-resonant BFC in Appendix A.3, and observed faster decay for the singly-resonant case, revealing the unique asymmetric temporal profile captured by our theoretical model. Based on the measured Franson interference revivals, we quantify the time-bin entanglement of our singly-resonant BFC through Schmidt mode decomposition. We extract the Schmidt eigenvalues for each time-bin by a parametric fitting of the experimental data as shown in the inset of Fig. 3.8c. By summing up the eigenvalues from each time bin, the lower bound of the Schmidt number is obtained to be 13.13 (detailed in Appendix B.1.2). Compared with the doubly resonant case [92], the Schmidt number for time-binned singly-resonant BFC state decreases dramatically, which results from the faster visibility decay of the Franson revivals.

Another useful measure of entanglement is the entanglement of formation, which represents the minimal number of maximally entangled two-qubit states (ebits) required to produce a density matrix ρ via an arbitrary local operations and classical communication procedure [192]. It can provide a quantitative lower bound on the high-dimensional time-energy entanglement of our 45 GHz singly-resonant BFC, we extract the entanglement of formation from the Franson interference revivals of our singly-resonant BFC, as shown in the inset of Fig. 3.8b. We obtain lower bounded entanglement of formation up to 1.533 ebits when $d = 5$, with the theoretical entanglement of formation of 2.322 for a 5×5 maximally entangled pure state. Based on our theoretical model in Appendix B.2, we estimate the maximally achievable entanglement of formation according to the theoretical Franson visibilities of our 45 GHz BFC in Fig. 3.8c. The maximally achievable entanglement of formation of our singly-resonant BFC is 1.538 when $d = 5$ (detailed in Appendix B.2). Our measured entanglement of formation matches well with the maximally achievable entanglement of formation as shown in the inset of Fig. 3.8c, which supports a nearly non-separable singly-resonant BFC state generation.

Extending from the time-domain measurement of the Franson interference revivals at different time-bins, here we characterize the time-energy entanglement between different frequency-bin pairs of the singly-resonant BFC for the first time. In order to select different frequency-bins of our 45 GHz singly-resonant BFC, we use a pair of narrowband tunable BPF with 300pm bandwidth for signal and idler photons. The filtered photons are then sent to the two arms of the Franson interferometer, as shown in Fig. 3.7a. We sweep the two tunable BPFs to select frequency-bins from -2 to 2 according to the previous JSI measurement in Fig. 3.7c, and collect the Franson interference fringes by fine tuning the relative delay between two arms using the thermal heater in arm2. The tunable DL in arm1 is fixed at 0^{th} time-bin delay to obtain optimum Franson interference, with the optimized constructive and destructive Franson interferences shown in Fig. 3.9a. Fig. 3.9a shows the Franson interferences between symmetric frequency-bin pairs, which are the diagonal elements of the frequency correlation matrix shown in Fig. 3.7c. A high Franson interference visibility of 99.66% is observed for the central frequency-bin pair S_0 & I_0, this result agrees well with the high purity photon state from our singly-resonant BFC supported by the heralded $g^{(2)}(0)$ measurement in Fig. 3.7d. We also obtain high interference visibilities for other symmetric frequency-bin pairs, with an average Franson visibility of 98.03% for the 5 frequency-bin pairs. We note that the visibility of the frequency-binned Franson interference increases slightly compared to the temporal Franson interference revivals due to the narrowband filtering of the singly-resonant BFC spectrum.

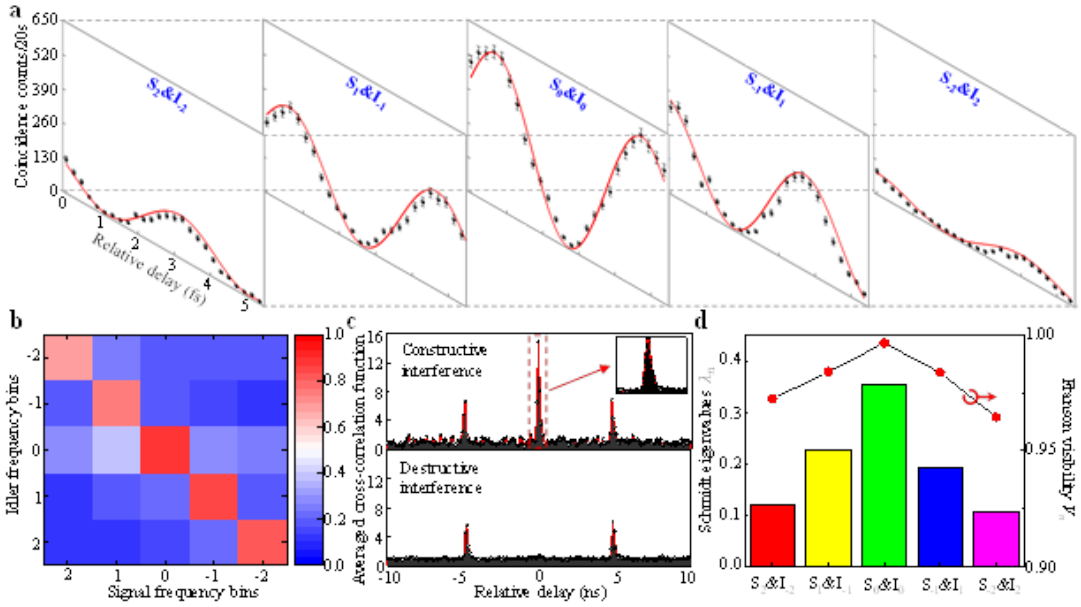

Fig. 3.9. Frequency-binned energy-time entanglement verification via Franson interference in a 45 GHz singly-resonant BFC. a) The measured Franson interference fringes, after accidentals were subtracted, for symmetric frequency-bin pairs. All the fringes were obtained at zero relative delay between arm 1 and arm 2 for optimum Franson interference. Maximum frequency-binned Franson interference is observed for $S_0\&I_0$ pair with visibility up to 99.66%. The averaged frequency-binned Franson visibility for 5 pairs is 98.03%. The coincidence window for all the measurements was 2 ns. b) The Franson interference visibility map for frequency-bin pairs within the SPDC bandwidth. Frequency bins were selected using a pair of tunable BPFs with 300 pm bandwidths, that were manually tuned to scan from the -2 to +2 frequency bins from frequency degeneracy. Only the symmetric frequency-bin pairs in anti-diagonal terms show high Franson interference visibility. c) Recorded signal-idler cross-correlation function for constructive (top) and destructive (bottom) Franson interference. The inset is the zoom-in of the central correlation peak, showing the single-sided decay temporal signature of a singly-resonant BFC. d) Extracted Schmidt eigenvalues and Franson visibilities for 5 symmetric frequency-bin pairs. Frequency-binned Franson interference visibilities are 97.24% ($S_2\&I_{-2}$), 98.42% ($S_1\&I_{-1}$), 99.66% ($S_0\&I_0$), 98.38% ($S_{-1}\&I_1$) and 96.45% ($S_{-2}\&I_2$), respectively. We extract the lower bound of the Schmidt number to be 4.17 across 5 symmetric frequency-bin pairs (detailed calculation is presented in Appendix B.1.1).

In addition to the symmetric frequency-bin pairs, we measure the Franson interference for the asymmetric frequency-bin pairs, i.e., the off-diagonal elements of the JSI matrix in Fig. 3.7c. We map the measured Franson interference visibilities for all frequency-bin pairs within the SPDC bandwidth

in Fig. 3.9b (and in Appendix Fig. A15). We observe that only antidiagonal elements in Fig. 3.9b show high visibilities, which corresponds to symmetric frequency-bin pairs, while the off-antidiagonal elements representing asymmetric frequency-bin pairs exhibit no obvious interference. This demonstrate that the time-energy entanglement will only occur between correlated spectral modes, which exhibit time-frequency correlations due to energy conservation form SPDC. Specially, when we sweep the tunable DL in arm1 of the Franson interferometer to adjust the relative delay away from the central time-bin, there is no interference recurrence in other time-bins. This is because the narrow tunable BPFs strictly limit the frequency modes to a single mode for both signal and idler photons, the beating between multiple frequency modes vanishes in time domain, which results in an exponential time decay without temporal oscillation of the signal-idler cross-correlation function [177]. The zoom-in of the central cross-correlation peak of the constructive Franson interference is shown in the inset of Fig. 3.9c. We observe a single-sided exponential time decay of the cross-correlation function showing the temporal signature of singly-resonant BFC as in Fig. 3.7b. Using detectors with better effective timing jitter, we are able to observe smoother single-sided time decay profile showing no oscillation. This single frequency mode filtering eliminates the temporal oscillation of the cross-correlation, and thus the recurrence of the Franson interferences.

We then perform the Schmidt mode decomposition based on the JSI measurements to quantify the frequency-bin entanglement of our 45 GHz singly-resonant BFC. By extracting the Schmidt eigenvalues from the measured frequency correlation matrix, we then obtain the Schmidt number for the frequency-bin entangled state of our singly-resonant BFC as shown in Fig. 3.9d. This parameter describes the lowest number of Schmidt modes in a bipartite system, and therefore gives a lower bound on its effective dimensionality. We obtain the Schmidt number by the sum of the individual Schmidt eigenvalues for each frequency-bin, which we measured to be 4.17 for the five symmetric frequency-bin pairs (detailed in Appendix B.1.1). Thus, we lower bound the Hilbert-space dimensionality of our frequency-binned singly resonant BFC state to be at least 16 (= 4.17 × 4.17). Note that the diagonal elements of the frequency correlation matrix exhibit the decreasing-envelope behavior of our singly-resonant BFC, which leads to the imperfect Schmidt number compared to the ideal case. This can be improved by utilizing a biphoton source with flat-top SPDC spectrum and a fiber etalon with flat-top transmission. In this case, the generated BFC will have equal amplitude for each frequency-bin, thus the Schmidt eigenvalues for symmetric frequency-bin pairs are consequently equal-weighted. This could lead to a maximum Schmidt number, which equals to the number of frequency modes of the frequency entangled pure state. The visibilities of the Franson interferences for

five symmetric frequency-bin pairs are also plotted together with the Schmidt eigenvalues in Fig. 3.9d. We note that the Franson interference visibilities change in accordance with the eigenvalues at each frequency-bin pair, which agrees well with the trend of heralded $g^{(2)}(0)$ for each frequency-bin pair in Fig. 3.7d.

To this point, we have fully characterized the temporal and spectral behaviors of our 45 GHz singly-resonant BFC, and verified the high-dimensional time-frequency entanglement via Franson revivals and frequency-binned interferences, as well as Schmidt mode analysis and entanglement of formation. To demonstrate that our singly-resonant BFC is suitable for long-distance quantum communications, we asymmetrically distribute the high-dimensional BFC states through a 10 km optical fiber link. The experimental scheme for high-dimensional entanglement distribution is shown in Fig. 3.12a. The singly-resonant BFC is generated by placing the FP cavity on the signal channel after the PBS. The signal photons are then sent to a local unbalanced MZI (arm1 of the Franson interferometer), while the idler photons propagate through 10 km of standard SMF and are analyzed by another unbalanced MZI (arm2 of the Franson interferometer). Thanks to the SPDC biphoton generation at $\approx$ 1316 nm, which is very close to the zero-dispersion wavelength for the standard telecommunication SMF, there is little temporal walk-off caused by the fiber dispersion. Thus, the DCM, which is normally lossy, is not necessarily required for the distribution of our high-dimensional singly-resonant BFC states. The entanglement distribution scheme is specially designed to be asymmetric according to the singly-resonant nature of the BFC. In the generation configuration of our singly-resonant BFC, only the signal photons suffer from the insertion and filtering loss of the fiber etalon. Thus, the idler photons with higher photon flux are suitable for long-distance transmission and sent through the 10 km SMF with 3.63 dB transmission loss. Note that our entanglement distribution system is built using commercially available off-the-shelf components, and can be readily implemented in many existing QKD systems.

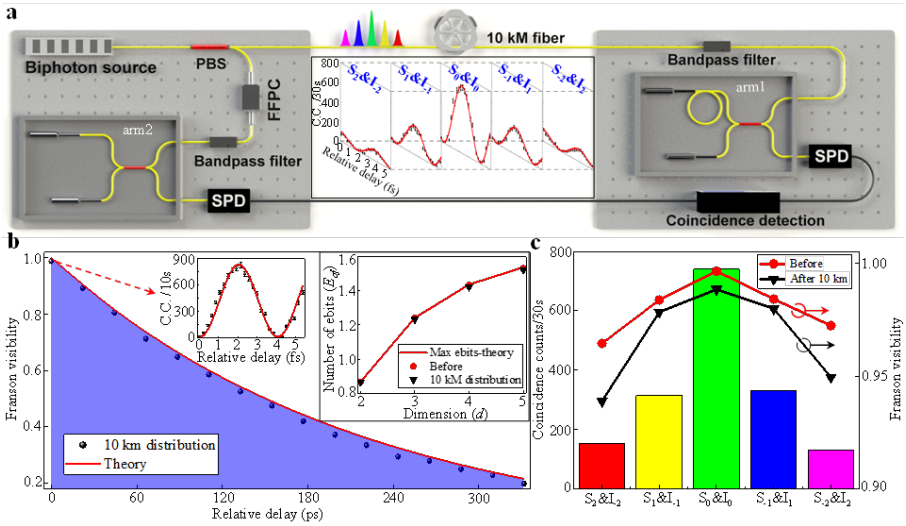

Fig. 3.10. High-dimensional time-frequency entanglement distribution of a 45 GHz singly-resonant BFC at 10 km distance. a) Illustrative experimental scheme for asymmetric entanglement distribution of high-dimensional time-frequency entanglement of a singly-resonant BFC. The singly-resonant BFC is generated by only passing the signal photons through an FFPC, while the idler photons are distributed via a 10 km fiber link. After distribution, a pair of tunable bandpass filters are used to select frequency bins for the signal and idler photons, which are then analyzed by a Franson interferometer for energy-time entanglement. The inset shows the Franson interference fringes for 5 symmetric frequency-bin pairs after 10 km distribution. b) The measured visibilities of Franson-interference recurrences after 10 km distribution. The middle inset shows the interference fringe for the central time-bin, with up to 98.81% visibility after subtracting the accidental coincidences. The Franson interference visibility decay matches well with our theoretical prediction after 10 km distribution, full data of the Franson interference fringes for 16 time bins is provided in Supplemental Information Section III. The right inset shows the E_{of} calculated based on Franson-interference recurrences before and after entanglement distribution. We lower bound E_{of} up to 1.522 ebits when d = 5 after the 10 km asymmetric distribution, which certifies a genuine three-dimensional energy-time entangled BFC state. c) The measured frequency-binned Franson-interference visibilities and the joint-spectral intensity measurements for 5 symmetric frequency-bin pairs of the singly-resonant BFC after 10 km distribution. Frequency-binned Franson interference visibilities after distribution are 94.95% (S_2&I_{-2}), 97.99% (S_1&I_{-1}), 98.85% (S_0&I_0), 97.84% (S_{-1}&I_1) and 93.89% (S_{-2}&I_2), respectively. Averaged frequency-binned Franson visibility of 96.70% is obtained, with only 1.33% degradation after distribution. These results demonstrate that the frequency-binned energy-time entanglement of our singly-resonant BFC is well preserved after 10 km distribution.

We first measure the high-dimensional time-energy entanglement of the distributed singly-resonant BFC states via nonlocal Franson interference. The Franson interference measurements at different time-bins are performed in the same fashion as introduced previously. The tunable DL in arm1 selects different time-bins, while the thermal heater in arm2 fine tunes the relative phase delay between two arms. The Franson interference fringes are obtained by recording coincidence counts in 2 ns time window with accidental coincidences subtracted. High-visibility Franson interference revivals are observed again for the singly-resonant BFC states after 10 km distribution. Fig. 3.10b shows the measured visibilities of the Franson interferences at different relative delays after 10 km distribution. The middle inset of Fig. 3.10b shows the Franson interference fringe for the central time bin, yielding a high visibility of 98.81% that strongly violates the Bell inequality (The Franson interference fringes at all 16 time-bins are detailed in Appendix Fig. A11). Specially, compared to the Franson interference revivals in Fig. 3.8a, the averaged degradation of the Franson interference visibility after 10km distribution is only 1.1%. The high visibilities of the Franson interference revivals verify the successful distribution of genuine high-dimensional time-energy entanglement of our singly-resonant BFC. The visibilities of Franson interference revivals follow the same decay trend as in Fig. 3.8c, which is captured by our theoretical model of the singly-resonant BFC. Furthermore, to quantitively lower bound the distributed high-dimensional energy-time entanglement, we calculate the entanglement of formation using the Franson interference revivals in Fig. 3.10b. In the right inset of Fig. 3.10b, we compare the number of ebits extracted from the Franson interference revivals before and after the 10 km asymmetric distribution. We obtain lower bounded entanglement of formation up to 1.522 ebits when $d = 5$ after the 10 km asymmetric distribution, which is very close to the maximally achievable entanglement of formation of 1.538 based on the theoretical model. This lower bound of entanglement of formation ≥ 1.522 certifies a genuine time-energy entangled BFC state of at least 3×3 dimensions after 10 km distribution, as maximally entangled two-qubit state only contains one ebit [192].

Next, we measure the time-energy entanglement between symmetric frequency-bin pairs of the singly-resonant BFC after 10 km asymmetric distribution. The frequency-binned time-energy entanglement is especially useful for wavelength-division multiplexing entanglement-based quantum communication network [209]. Narrowband tunable BPFs are used to select different frequency-bins for signal and idler photons, which are cascaded with the Franson interferometer for time-energy entanglement measurement as shown in Fig. 3.10a. The Franson interference fringes for five symmetric frequency-bin pairs are observed and shown in the inset of Fig. 3.10a. A high Franson interference visibility of 98.85% is obtained for the central frequency-bin pair S_0 & I_0 after 10 km

asymmetric distribution. The Franson visibilities for Frequency-bin pairs away from the central bin decrease as expected, but are still well above the quantum threshold of 71%. The frequency-binned Franson interference visibilities before and after 10 km asymmetric distribution are summarized in Fig. 3.10c. An average Franson visibility of 96.70% is obtained for all 5 frequency-bin pairs after distribution, with only 0.46% degradation compared to the case in Fig. 3.9a. These high Franson interference visibilities certify the coherent transmission of the frequency-binned time-energy entanglement of our singly-resonant BFC. Simultaneously, we record the coincidence counts of the central correlation peak for constructive interference as shown in Fig. 3.9c to extract the JSI of the singly-resonant BFC after 10km asymmetric distribution. Only the diagonal elements of the JSI have high coincidence counts as shown in Fig. 3.10c, revealing frequency-bin entanglement of the distributed BFC states.

To the best of our knowledge, this is the first demonstration of high-dimensional entanglement distribution on a singly-resonant BFC platform in both time and frequency domain. Quantum information encoded in time-bins and frequency-bins of single photons is naturally suitable for transmission over long distances using optical fiber or free-space links [121]. In particular, time-energy entanglement is ideally suited for high-dimensional QKD, with security monitored by the measurement of Franson visibility [6]. Unconditional security based on high-dimensional QKD have been proposed using Franson interferometry and conjugate-Franson interferometry [127], which has been recently demonstrated [128]. The long-distance distribution of frequency bins is demonstrated using dispersion cancellation system [78], with possible applications in wavelength-multiplexed quantum network.

In this work, we have demonstrated the high-dimensional time-frequency entanglement of a singly-resonant BFC generated by only passing the SPDC signal photons through a 45.32 GHz FP cavity. The temporal and spectral properties are characterized via JSI and JTI measurements. By exploiting the nonlocal Franson interferometry, we demonstrated high-dimensional time-energy entanglement of the singly-resonant BFC via Franson interference revivals. In addition, time-energy entanglement between symmetric frequency-bin pairs within the SPDC bandwidth is verified by frequency-binned Franson interferences. Furthermore, we take a practical step towards long-distance quantum communications, and demonstrated the first time high-dimensional time-frequency entanglement distribution of our singly-resonant BFC in an asymmetric scheme. We proved that the high-dimensional time-frequency entanglement of our singly-resonant BFC was preserved over 10 km asymmetric distribution via time-binned and frequency-binned Franson interferences. The

demonstrated singly-resonant BFC provides a versatile platform for high-dimensional QIP and secure QKD.

Remarkably, our singly-resonant BFC can be readily exploited to generate high-dimensional hyperentanglement by combining the polarization DoF. Thanks to the type-II configuration, we can generate the post-selected polarization entanglement by mixing the signal and idler photons on a 50:50 beamsplitter. Another common approach to generate polarization entanglement is using a Sagnac interferometer [208], which can also be adopted for our singly-resonant BFC. With polarization DoF, the dimensionality of our singly-resonant BFC can be doubled with an extra qubit encoded in the BFC photon pairs. The high-dimensional hyperentangled BFC states provide a useful resource for applications, such as high-capacity quantum communication [210], superdense quantum teleportation [211].

Our singly-resonant BFC platform also supports higher dimensional state generation. The dimensionality of frequency-bins is determined by the bandwidth of SPDC and the FSR of the FP cavity. For example, using a SPDC source with 2 THz bandwidth and a fiber etalon with 10 GHz will leads to a 200×200 dimensional system, which corresponds to 15 frequency-bin qubits. On the other hand, the time-bins are the Fourier transform of the frequency-bins in its conjugate time domain, thus the scaling of time-frequency dimensionality is complementary. The time-bin and frequency-bin number product satisfies $N_T N_\Omega = \pi B_{\mathrm{PM}}/\Delta\omega$ [92]. Thus, the ideal dimensionality of the time-frequency space is determined by the linewidth of the FP cavity with a given SPDC source. For example, with 2 THz SPDC bandwidth, 100 GHz cavity FSR and 1 GHz cavity linewidth, time-bin number N_T will increase to 100 with time-bin interval of 10 ps while frequency-bin number N_Ω of 20, which leads to 13 time-bin qubits. The scaling of the BFC state generation can also be realized by integrating the FP cavity with the SPDC source, which demonstrated frequency-multiplexed photon pairs covering 1400 modes with 3.5 GHz FSR of the cavity [177]; or using integrated micro-ring resonator [76, 78], where the achievable dimensionality is also bounded by the phase-matching range of the SFWM process and the FSR of the microresonator. The on-chip realization of the high-dimensional BFC will enable potential large-scale integrated QIP [212].

The singly-resonant BFC will be particularly useful and readily implemented in quantum repeater-based quantum internet [213]. Thank to our singly-resonant configuration of the BFC generation, the fiber etalon can be placed externally of the SPDC source unlike the OPO scheme. In a quantum repeater scheme with two entanglement sources [214], by inserting a FP cavity on each path of both entanglement sources to the Bell state analyzer, the photons on the other path of both sources

will be entangled in high-dimensions due to the singly-resonant configuration. This scheme enables possible high-dimensional quantum repeaters for long-distance quantum network and high-dimensional entanglement generation based on current repeater scheme. Our singly-resonant BFC provides a practical and flexible approach to increase dimensionality in time and frequency basis at a quantum node of the quantum internet.

Next, we investigate the impact of cavity finesse for our singly-resonant BFCs. In this work, we utilize mode-locked singly-resonant BFCs based on the cavity-filtered scheme with planar FP cavity that is more flexible and robust in terms of experimental implementation, compared to cavity-enhanced SPDC sources. Here, we examine the role of cavity finesse F in the mode-locked signal-idler temporal cross-correlations as well as in the time-energy entanglement via Franson interferometry with our experimental demonstrations and theoretical descriptions. First, we observed mode-locked oscillations of a singly-resonant BFC using our second-order cross-correlation function measurements with a cavity FSR of 5.03 GHz and a bandwidth of 457 MHz. Such direct JTI measurements signify the existence of phase coherence in our cavity-filtered BFC for the first time. Second, we measured the time-energy entanglement of mode-locked singly-resonant BFCs based on 15.15 and 5.03 GHz cavity via Franson interferometry, spanning up to 6 time-bins with the highest central time-bin accidental-subtracted visibility over 97% for both cavities. Such JSI measurements are consistent and complementary with our JTI measurements. Our approach does not require a stabilization system and complex cavity design as in cavity-enhanced SPDC sources. We further investigated the impact of cavity finesse F in our singly-resonant mode-locked BFCs by comparing different cavity configurations. Near-flattened Franson interference recurrences visibility can be theoretically predicted with a cavity finesse F of 200 in our scheme, violating quantum-classical threshold for a whole temporal range of 1 ns. Our results pave the way for producing high-quality mode-locked temporal correlations for time-resolved correlation-based quantum networks and can be helpful in pushing the limit of the Hilbert space dimensionality in the temporal domain [92], for high-quality long-distance high-dimensional time-energy entanglement distribution [111, 117, 215], and on-chip optical quantum information processing.

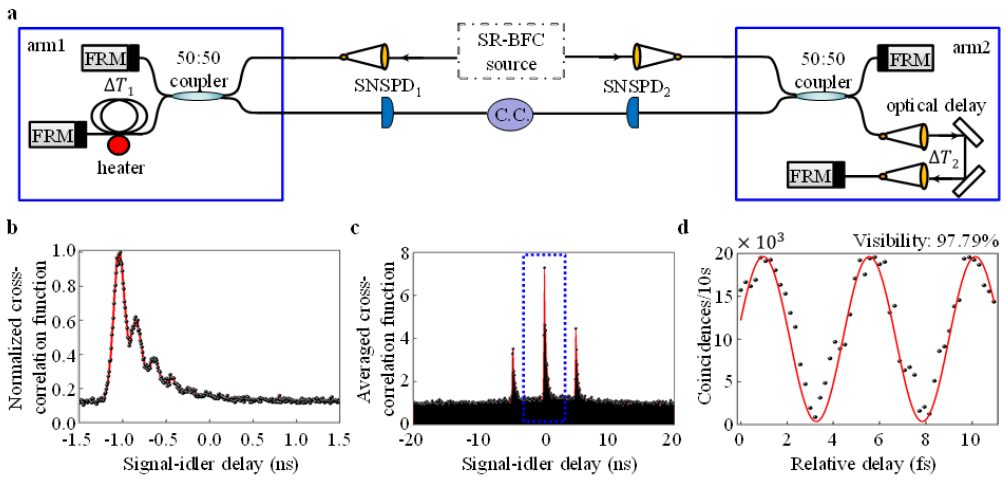

Fig. 3.11. Measured single-photon cross-correlations and time-energy entanglement using a 5 GHz singly-resonant BFC. a) Schematic of the experimental configuration. b) Measured zoom-in second-order cross-correlation function between signal and idler photons. The periodic structure traces the cavity round-trip time of 198.9 ps. A cavity bandwidth of 457 MHz can be derived by the exponential decay of the envelope. c) The signature of observed nonlocal Franson interferences was revealed with the single-sided correlation function (see highlighted region in blue dashed lines). d) The observed quantum time-energy entanglement of a 5.03 GHz FSR singly-resonant BFC source and witnessed Franson fringe with accidental-subtracted visibility of 97.79% for central time-bin.

The working principle of this experiment is illustrated in Fig. 3.11a. We used singly-resonant mode-locked BFC sources, where the SPDC source is generated by pumping a fiber-coupled type-II phase-matched ppKTP waveguide of fiber-coupling efficiency of ~50% per facet with a self-injection locked continuous-wave laser at 658 nm wavelength [189]. The singly-resonant BFCs are generated by sending the signal photons of the orthogonally-polarized, frequency-degenerate photon pairs at 1316 nm with 245 GHz FWHM phase-matching bandwidth to fiber Fabry-Perot cavity with 5.03, 15.15 GHz FSR and FWHM bandwidths of 0.46, 1.36 GHz, respectively. The generated singly-resonant mode-locked BFCs state is then directed to a stabilized Franson interferometer for nonlocal interference measurements. After the Franson interferometer, coincidences are recorded with two SNSPDs, ≈ 85% detection efficiency, root-mean-square timing jitter ~ 55 ps, PhotonSpot. Inc.. Our Franson interferometry is comprised of two unbalanced MZIs with path-length difference measured to be $\Delta T = 4.84$ ns (see Fig. 3.11c), for satisfying the requirement for probing time-energy entanglement. We used a thermal heater in the long path of arm1 to sweep and fine-tune the relative phase shift ΔT_1 between the two MZIs for probing the time-energy entanglement of our singly-resonant BFC. In

addition, the motorized stage delay in arm2 with ΔT_2 up to 360 ps was used to select different time-bins, and temperature controllers with long-term temperature stability of ≈ 1mK are implemented to stabilize our Franson interferometry.

Here, we analyze the role of cavity finesse F in the model of mode-locked singly-resonant BFC, focusing on temporal second-order cross-correlation function and Franson interference recurrences based on our experimental setup. The mode-locked signal-idler temporal second-order cross-correlation function of singly-resonant BFC can be written as [111, 177, 206]

$$K_{S'I'}^{cross}(\tau) = \int_{-\infty}^{\infty} \frac{d\omega}{2\pi} \frac{i\sqrt{N_S}\mathrm{sinc}(\omega t_{\mathrm{coh}}/2)e^{-4\omega^2 ln(2)/\Delta\omega^2} e^{i\omega(\tau - t_{\mathrm{coh}}/2)}}{1+i\frac{1}{\pi F} sin(\pi\omega/\Delta\Omega)e^{-i\pi\omega/\Delta\Omega}} \tag{3.13}$$

Here, N_S is the source brightness; $t_{\mathrm{coh}} = 3.62$ ps is the coherence time of our SPDC source; $\Delta\omega/2\pi =$ 225 GHz is the FWHM bandwidth of BPF. The key figure of merit cavity finesse F is given by

$$F = \frac{\Delta\Omega}{2\Delta\omega_c} = \frac{\pi}{\Delta\omega_c \Delta T_{cavity}} = \frac{\pi}{\sin^{-1}(\frac{1-\sqrt{1-l_{rt}}}{2\sqrt[4]{1-l_{rt}}})} = \frac{\lambda Q}{2L} \tag{3.14}$$

where $\Delta\Omega$ is the FSR of the cavity; $\Delta\omega_c$ is the cavity bandwidth, ΔT_{cavity} is cavity round-trip time, l_{rt} is the total round-trip optical losses, including scattering losses, clipping losses, absorption and transmission losses; λ is the cavity mode wavelength; Q is the cavity quality factor and L is the optical length of the cavity. For linear planar FP cavity, the cavity finesse F is proportional to cavity quality-factor Q.

By using equation (3.13) and (3.14), we can obtain the Franson interference recurrence envelopes with maximum and minimum coincidence counts as follows

$$C_{S'I'}^{max}(\tau) = \frac{\eta_{s'}\eta_{I'}}{16}\int_0^{T_g} d\tau[(\left|K_{S'I'}^{(cross)}(\tau)\right|^2) + \left|K_{S'I'}^{(cross)}(\tau - m\Delta T_{cavity})\right|^2 + 2\left|K_{S'I'}^{(cross)*}(\tau)K_{S'I'}^{(cross)}(\tau - m\Delta T_{cavity})\right|^2] \tag{3.15}$$

and

$$C_{S'I'}^{min}(\tau) = \frac{\eta_{s'}\eta_{I'}}{16}\int_0^{T_g} d\tau[(\left|K_{S'I'}^{(cross)}(\tau)\right|^2) + \left|K_{S'I'}^{(cross)}(\tau - m\Delta T_{cavity})\right|^2 - 2\left|K_{S'I'}^{(cross)*}(\tau)K_{S'I'}^{(cross)}(\tau - m\Delta T_{cavity})\right|^2] \tag{3.16}$$

where η_s', η_I' is to include all losses encountered in our measurement setup; T_g is the coincidence counting window of 2 ns. Then, we can obtain the Franson interference recurrence visibilities at n^{th} time-bin in singly-resonant biphoton frequency comb to be

$$V_n = \exp(-n\pi/F) \tag{3.17}$$

These equations allow us to evaluate the impact of cavity finesse F on signal-idler temporal second-

order cross-correlation function and visibilities for the Franson-interference recurrences numerically and compare with our experimental demonstrations in singly-resonant mode-locked BFC.

Fig. 3.11b shows the $g^{(2)}$ measurements of the signal-idler temporal second-order cross-correlation function for 5.03 GHz FSR singly-resonant BFC. Using a 5.03 GHz FSR fiber cavity, we observed a clear comblike structure of the temporal correlation, resulting from the mode-locking process of our singly-resonant BFC source. The time interval t_{rt} is measured to be ~ 200 ps, which matches well with a cavity FSR of 5.03 GHz (~ 198.8 ps). Cavity damping rate is extracted to be ~ 458.7 MHz from our measurements with the exponential decay of the mode-locked oscillations envelope, and this value closely matches the cavity bandwidth of 457 MHz. This is the first experimental measurements of signal-idler temporal second-order cross-correlation function that probe the JTI in fiber cavity-filtered mode-locked singly-resonant BFC scheme, certifying the existence of phase coherence for our multimode quantum source. Such JTI measurements, when paired with JSI measurements, can reveal genuine high-dimensional frequency-bin entanglement via providing mutual information of biphoton phase coherence [88].

We then performed Franson interference measurements for 5.03 GHz FSR singly-resonant BFC. First, we measure the quantum signature of Franson interference, the three temporally separated correlation peaks, as presented in Fig. 3.11c. We observed clear single-sided temporal second-order cross-correlation structure for all Franson correlation peaks. Fig. 3.11d shows the optimized maximum Franson interference of the central time-bin for this fiber cavity. For this measurement, we swept the thermal heater in arm1 to tune the relative phase shift ΔT_1 between the two MZIs while fixing the motorized stage position ΔT_2 at the center of the optimum Franson interference. By post-selecting coincidence events occurring within a 2 ns-wide coincidence time window while changing the phases of the interferometers (ΔT_1), we obtained maximum visibility of 97.79% for 5.03 GHz FSR singly-resonant BFC, after accidental coincidence subtraction.

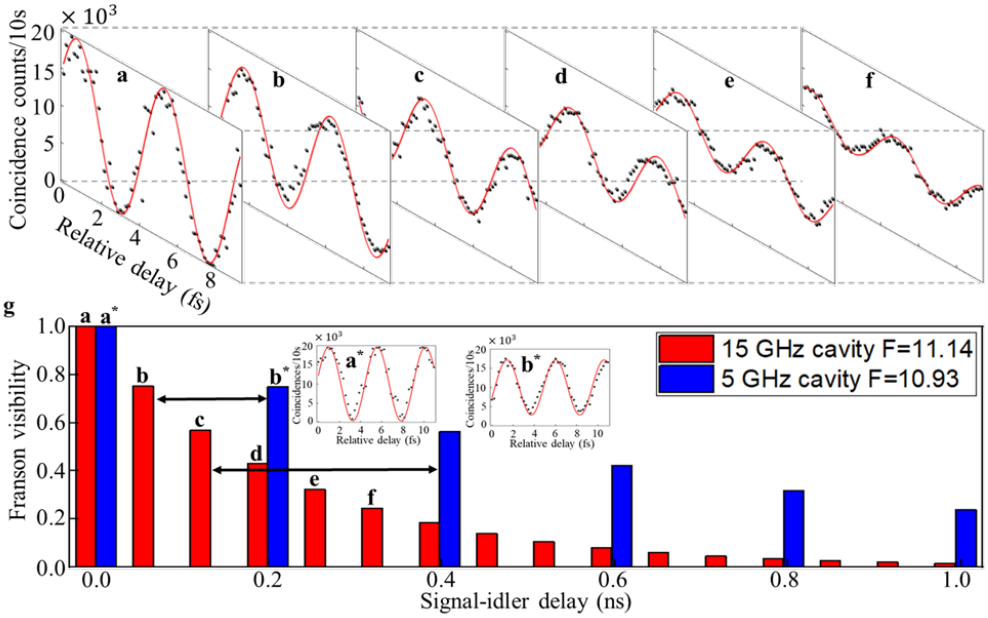

Fig. 3.12. Experimental observed discretized time-energy entanglement using 5 and 15 GHz singly-resonant BFCs. a) to f) Nonlocal Franson recurrence interference fringes, with six discrete time-bins measured in a 15.15 GHz FSR singly-resonant BFC. g) Theoretical Franson revival visibilities for 5.03 and 15.15 GHz FSR singly-resonant BFCs, with superimposed experimental observations. Also included in a* and b* are Franson recurrence time-bins in a 5.03 GHz FSR singly-resonant BFC. The experimental (theoretical) measured visibilities, in percent, for the 6 time-bins in a 15.15 GHz FSR singly-resonant BFC are 98.97 (100), 74.32 (75.43), 54.37 (56.89), 40.56 (42.91), 31.5 (32.37), 22.32 (24.41), respectively. For the two time-bins in a 5.03 GHz FSR singly-resonant BFC, the experimental (theoretical) measured visibilities in percentage are 97.79 (100), 72.23 (75.03), respectively. The two bidirectional black arrows indicate the similarity of Franson revival visibilities between 2 cavities. All measurements are performed with a coincidence window of 2 ns, and the reported visibilities are after subtracting accidental coincidences.

Due to the mode-locking process of our singly-resonant BFC, the mode-locking oscillations in the temporal domain will result in discrete time-energy entanglement. Indeed, by using both 5.03 GHz and 15.15 GHz FSR singly-resonant BFCs, we measured the Franson interference recurrences over 2 and 6 time-bins, respectively, as presented in Fig. 3.12. For a 15.15 GHz FSR singly-resonant BFC, we observed Franson interference fringes visibilities to be 98.97%, 74.32%, 54.37%, 40.56%, 31.50%, and 22.32%, after subtracting the accidental coincidence counts, as shown in Fig. 3.12a to 3.12f (see Appendix A.6 for measured quantum signature of non-integer Franson interferences for 5.03 and 15.15 GHz FSR singly-resonant BFCs). Then, we compared our experimental results with theoretical

modeling in Fig. 3.12g. In insets of Fig. 3.12g, we observed Franson interference fringes visibilities to be 97.79% and 72.32%, after accidental coincidence subtraction for a 5.03 GHz FSR singly-resonant BFC. The number of measurable time-bins is limited by the motorized stage position ΔT_2 in arm2 of our Franson interferometry. Besides, we also measure the non-integer cavity round-trip time Franson interferences for center time-bin in for both mode-locked singly-resonant BFCs, which further confirming the discretization of singly-resonant BFCs due to mode-locking process (see Appendix A.6 for measured non-integer cavity round-trip Franson interferences using both singly-resonant BFCs). The Franson interference recurrences have a 200.9 ps period for 5.03 GHz FSR fiber cavity (matching with theoretical calculations in Fig. 3.12g), this JSI measurement results are consistent with our JTI measurements in Fig. 3.11b with ~ 200 ps cavity round-trip time, confirming the mode-locked phase coherence behavior of our singly-resonant BFC. Interestingly, we find that although two fiber cavities have different FSRs and cavity bandwidths, they have similar cavity finesse F ($F_{5\text{GHz}}$=10.93 and $F_{15\text{GHz}}$=11.14), and the trend of their Franson interference recurrence visibilities match well (illustrated by bidirectional black arrows in Fig. 3.12g). This indicates that the cavity finesse F plays a key role in determining the quality of time-energy entanglement over multiple time bins. By increasing this figure of merit, the fall-off of Franson interference recurrence visibilities over multiple cavity round-trip times can be improved.

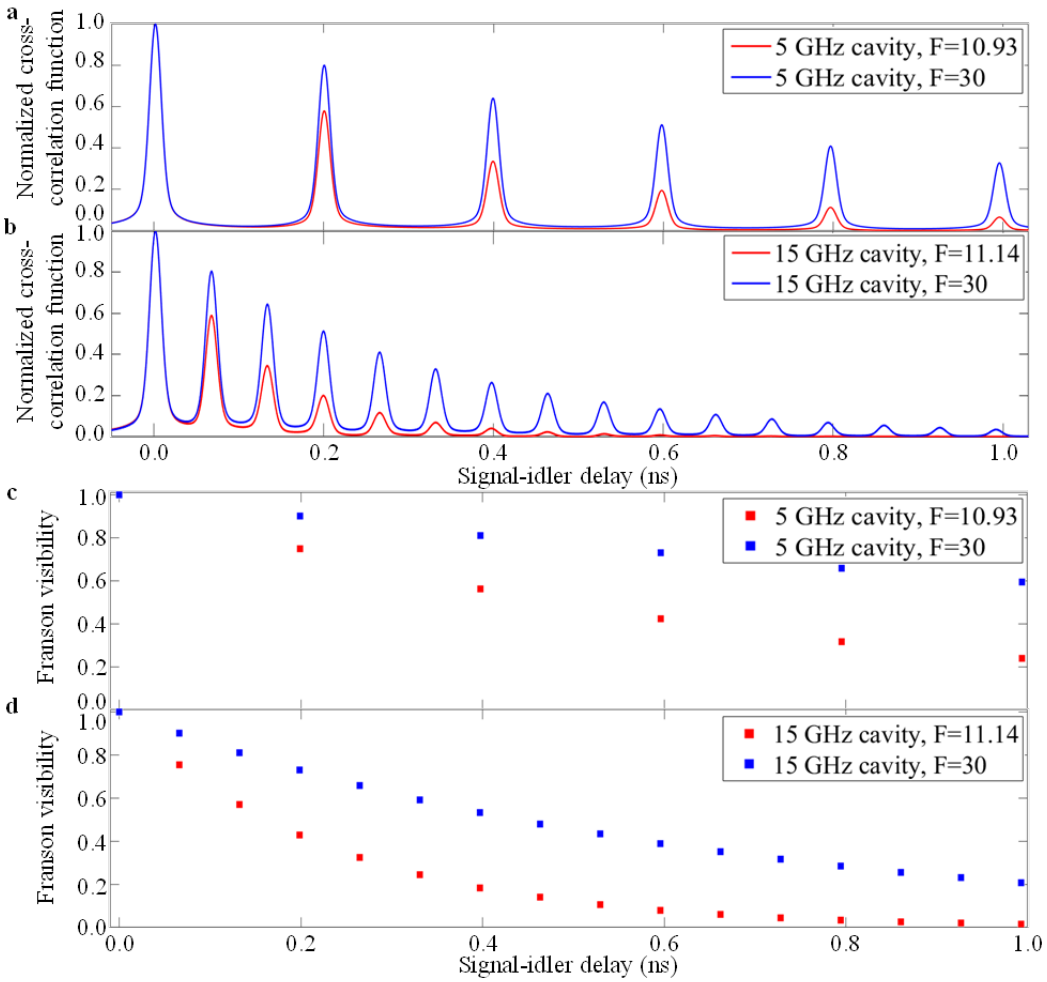

Fig. 3.13. Modeled mode-locking oscillations and nonlocal Franson revival visibilities for 5 and 15 GHz singly-resonant BFCs. a) and b) Theoretical signal-idler cross-correlation functions for 5.03, 15.15 GHz FSR singly-resonant BFC with cavity finesse *F* of 10.93, 30, 11.14, and 30, respectively. c) and d) Modeled Franson recurrence visibilities for a 5.03, 15.15 GHz FSR singly-resonant BFC with cavity finesse *F* of 10.93, 30, 11.14, and 30, respectively. For all the calculations, the FWHM timing jitter of the single-photon detector is 20 ps.

Fig. 3.13 presents the theoretical prediction of normalized signal-idler temporal second-order cross-correlation function and Franson interference recurrence visibilities for two fiber cavities. To better resolve the mode-locked oscillations, we set the FWHM timing jitter to be 20 ps, available with current single-photon detection technology [51]. In Fig. 3.13a and 3.13b, we plot the normalized signal-idler temporal second-order cross-correlation function of 5GHz and 15 GHz FSR cavities with different cavity finesse *F* for comparison. Both results show that when the cavity finesse *F* increases to 30 in cavities with the same FSR, the cavity damping rate becomes smaller, resulting in the increased

probability to detect signal photons at multiples of the cavity round-trip time t_{rt} after idler photons arrive at the single-photon detector. We observed a similar trend for Franson interference recurrence visibilities as shown in Fig. 3.13c and 3.13d. There is a clear improvement of modeled Franson visibilities when cavity finesse F is ~3 times larger than what we used in our experiments in Fig. 3.12. With a small cavity finesse F of 30, we found that all of the Franson interference recurrence visibilities can be higher than the quantum-classical limit of 70.7%, for 5.03 GHz FSR singly-resonant BFC at 1 ns temporal range. For 15.15 GHz FSR singly-resonant BFC, the Franson visibility at 16th time-bin with cavity finesse F of 30 is ~14x fold higher than that with cavity finesse F of 11.14. Due to the increasing probability of detecting mode-locked temporal oscillations at the single-photon detector with a cavity finesse of 30, the Franson interference recurrence visibilities will increase correspondingly. Our results in Fig. 3.13 show that the cavity finesse F is a key parameter for manipulating the JTI of the mode-locked biphoton states.

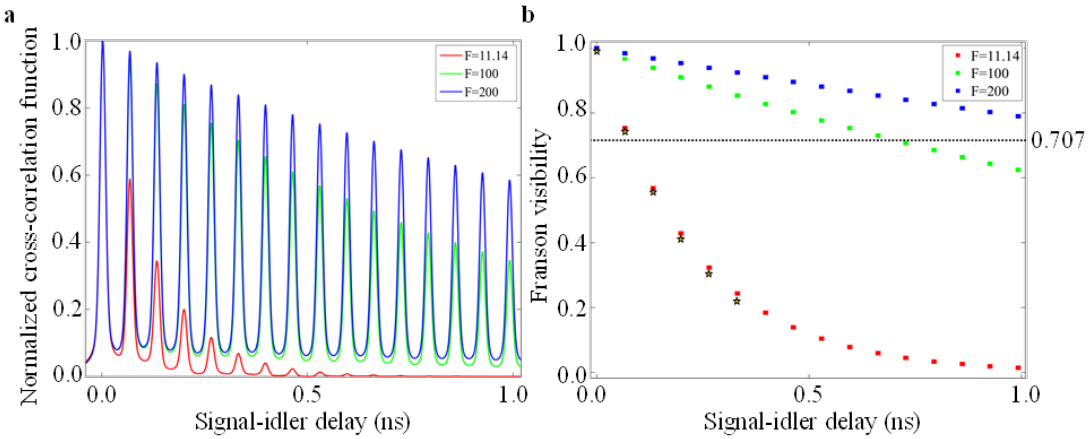

Fig. 3.14. Impact of cavity finesse on signal-idler cross-correlation functions and nonlocal Franson revival visibilities for a 15 GHz singly-resonant BFC. a) Theoretical signal-idler cross-correlation functions for a 15.15 GHz FSR singly-resonant BFC with cavity finesse F of 11.14, 100, and 200, respectively. b) Modeled Franson recurrence visibilities for a 15.15 GHz FSR singly-resonant BFC with cavity finesse F of 11.14, 100, and 200, respectively. The measured Franson recurrence visibilities are superimposed (black stars). The black dotted line is the visibility of the quantum-classical limit. For all the calculations, the FWHM timing jitter of the single-photon detector is set to be 20 ps.

We now further investigate the role of cavity finesse F in our mode-locked singly-resonant BFCs through signal-idler temporal second-order cross-correlation function and Franson recurrence interferences. Cavity finesse F tailors the intrinsic JTI of mode-locked singly-resonant BFC,

manifesting in Franson interference recurrence and signal-idler temporal second-order cross-correlation function, as can be seen in Fig. 3.12 and 3.13. For the above signal-idler temporal second-order cross-correlation functions and Franson interference recurrence, the cavity finesse *F* plays a key role because it is proportional to the number of round-trips before a single-photon leaves the cavity or is lost via dissipation. Indeed, the finesse *F* of our planar FP cavity is also related to the *Q*-factor. Therefore, increasing the cavity finesse *F* is equivalent to increasing the cavity *Q*-factor, where photons can travel more round-trips in the cavity while storing more energy before they are lost in dissipation or leave the cavity. This results in a lower cavity damping rate with the same FSR, and therefore increasing detection probability in signal-idler temporal second-order cross-correlation function after multiple cavity round-trip times t_{rt} and flattening nonlocal time-energy entangled Franson recurrence interferences in our singly-resonant mode-locked BFCs.

In Fig. 3.14, we present the signal-idler temporal second-order cross-correlation function and Franson interference recurrences in a 15.15 GHz FSR singly-resonant BFC from small to moderate cavity finesse *F*. For mode-locked oscillations in the temporal domain, we plot signal-idler temporal second-order cross-correlation function versus 3 different cavity finesse *F* of 11.14, 100, and 200 in a 15.15 GHz FSR cavity with a FWHM timing jitter of 20 ps, as shown in Fig. 3.14a. It can be seen that for a moderate cavity finesse *F* of 200, signal photons are more likely to be detected at 16 cavity round-trip times t_{rt} after idler photons are counted at the detector, resulting in higher temporal correlation peaks across a whole temporal range of 1 ns. In Fig. 3.14b, we describe the Franson interference recurrences using the same cavity finesse as Fig. 3.14a in the same temporal range of 1 ns, with our previous experimental results with cavity finesse *F* of 11.14 superimposed (black stars). It is evident that with only a cavity finesse *F* of 200, all of the Franson interference recurrence visibilities are over the quantum-classical limit of 70.7% (black dot line) and violate Bell's inequality in position and time. We further estimate the time-bin Schmidt number K_T for our results in Fig. 3.14b, and found out the time-bin Schmidt number K_T for a cavity finesse *F* of 200 is 15.92, and that for a cavity finesse *F* of 11.14 is 6.98. The effective Hilbert space dimensionality thus potentially increased from 48 to 244. In our results in Fig. 3.14, we choose to use a cavity with FSR of 15.15 GHz because this FSR is closed to maximum FSR in cavity-enhanced SPDC sources [71, 177, 207, 208, 216, 217]. Furthermore, this 15.15 GHz FSR cavity is compatible with the current FBG based telecom filter technology for performing frequency-domain projection measurements. Here, we note that our schemes are robust and flexible without a sophisticated stabilization system and avoid cavity design complexity compared with cavity-enhanced SPDC sources. First, our mode-locked BFCs are mainly

based on telecom fiber components, which do not require active stabilization systems for free-space cavity design. Second, we can easily switch from singly-resonant scheme to doubly-resonant scheme or vice versa (depending on the applications) without rebuilding the experimental setup. Third, our singly-resonant mode-locked BFCs are directly compatible with telecom spectral filtering technology such as optical tunable BPFs and DWDMs by simply using fiber cavities with larger FSRs, without relying on the cluster effect in non-degenerate doubly-resonant cavity-enhanced SPDC sources [218-221]. To further illustrate the impact of cavity finesse F on a larger FSR fiber cavity, we model the signal-idler temporal second-order cross-correlation function and Franson interference envelopes in a 50 GHz FSR singly-resonant mode-locked BFC with different cavity finesse F (see Appendix A.5). We note that although the signal-idler temporal second-order cross-correlation function measurements are limited by the detection jitter of commercial single-photon detectors for 50 GHz FSR cavity, the Franson interference measurements are experimentally accessible with current interferometric technology [192]. More importantly, Franson-type measurements are fundamental to all time-energy entanglement based quantum systems.

We have shown theoretically and experimentally that cavity finesse F acts on JTI of mode-locked singly-resonant BFCs, manifesting in signal-idler temporal second-order cross-correlation function and Franson interference recurrence. Increasing the cavity finesse F from small to moderate values leads to a lower cavity damping rate with the same FSR, increasing detection probability in signal-idler temporal second-order cross-correlation function after multiple cavity round-trip times t_{rt} and flattening the visibility decay of the Franson interference recurrence in our singly-resonant mode-locked BFCs. Our results pave the way for scaling up the Hilbert space dimensionality, ebits of entanglement of formation in temporal domain, for high-quality long-distance high-dimensional time-energy entanglement distribution, on-chip optical quantum information processing and quantum teleportation [222].

Lastly, we present the genuine time-reversible ultranarrow photon-pair source via singly-resonant BFCs for the first time. To be compatible with efficient atomic based quantum memory protocols such as electromagnetically induced transparency, controlled reversible inhomogeneous broadening or gradient echo memory, and atomic frequency comb, the single-photon sources must be at the resonance frequency of the atoms and have a narrow spectrum that matches the quantum memory bandwidth (typically between 10 and 1000 MHz for these protocols) [214]. However, the frequency bandwidth of SPDC and spontaneous four-wave mixing is on the order of 0.1 to 100 THz [214, 223, 224], which is several orders of magnitude larger than the bandwidth required for atomic quantum

memories. One way to overcome this problem is to spectrally filter the SPDC and four-wave mixing output via cavity-enhanced schemes [71, 143, 177, 207, 220], or to use post-filtered schemes [72, 75, 92]. So far, many experiments of the narrow-band photon-pair source generation have been performed by doubly-resonant [71, 217, 220], triply-resonant cavity-enhanced configurations [143, 225], and by four-wave mixing in microresonators [76, 77]. However, to the best of our knowledge, all of the previous narrow-band SPDC and four-wave mixing photon-pair sources are either not time-reversible due to the natural limitation of experimental configurations, or not compatible to 10 MHz bandwidth of highly efficient long-coherence time atomic quantum memories. While the time-reversal waveforms of singly-resonant OPO far below threshold has been demonstrated [177], the result is only for single-mode frequency filtering with a pair of bandpass filters, and the experiment is focused on frequency-multiplexed telecommunication photon-pair generation.

In this work, we demonstrate the genuine time-reversible ultranarrow telecommunication photon-pair source over 5,000 modes with asymmetric singly-resonant BFCs for the first time. In our scheme, the time-reversibility of our multimode photon-pair source is achieved via swapping a symmetric planar fiber FP cavity between signal-idler photon-pairs in the asymmetric singly-resonant BFCs. Hence, this asymmetric singly-resonant BFCs configuration preserves the intrinsic multimode structure under time-reversal symmetry without specially designed FP cavities [226, 227] and the usage of lossy narrow-band telecommunication frequency filters [177]. Indeed, here, we are able to measure temporal second-order cross-correlation revivals and heralded $g^{(2)}(0)$ for both exponential decay and time-reversed singly-resonant BFCs. We fully resolve the multimode JTI for both exponential decay and time-reversed singly-resonant BFCs, with 12 cross-correlation peaks measured at the fundamental limit of our commercial single-photon detectors for the first time. The measured cavity FSR, linewidth of exponential decay and time-reversed singly-resonant BFCs are 42.63 MHz, 4.587 MHz, and 42.64 MHz, 4.599 MHz, respectively. The reported cavity FSR is the narrowest among all the different configurations of photon-pair sources so far. We also measure and confirm single-photon Fock state for our multimode time-reversible singly-resonant BFCs. By post-selecting the measured data to 1 ns coincidence window, centering at the peak maximum for each cavity round-trips, we obtain minimum heralded $g^{(2)}(0) = 0.013 \pm 0.001$, and $g^{(2)}(0) = 0.016 \pm 0.0011$ for 0^{th} round-trip using both exponential decay and time-reversed singly-resonant BFCs. The observed minimum heralded $g^{(2)}(0)$ for 1^{st} to 4^{th} cavity round-trips are all below the anti-bunching characteristic value of 0.5. Moreover, we also measure minimum averaged heralded $g^{(2)}(0) \sim 0.2 \pm 0.002$ by using a wider

coincidence window of 30 ns for both exponential decay and time-reversed singly-resonant BFCs, which further verifies the intrinsic multimode emission and single-photon Fock state is well-preserved with time-reversal symmetry. Our photon-pair source operation can cover whole telecommunication C- and L-band, with narrowest cavity FSR of 42.64 MHz and 4.599 MHz linewidth in time-reversed scheme. Therefore, this source is directly compatible to chip-scale AFC quantum memories [153, 154] for high-dimensional multimode storage without quantum frequency conversion [228]. Our time-reversible singly-resonant BFCs are robust and versatile, and they do not need a complex stabilization system. In addition, the similar comblike spectrum for both signal and idler photons for both exponential decay and time-reversed singly-resonant BFCs can be confirmed by the time-reversal symmetric single-photon statistics measurements. By fully exploiting the time-reversible asymmetric singly-resonant BFCs in temporal domain, our sources expect to have 5864 and 5792 frequency modes, which is the highest number of photon-pairs among all the SPDC sources up to date.

The single-photons generating from our singly-resonant BFCs have a well-defined time order because the JTI of singly-resonant BFC is determined by the generation process of singly-resonant BFC. Hence, we start from the two-photon wavefunction of singly-resonant BFC in frequency-domain. The singly-resonant configuration generates the (unnormalized) BFC state whose frequency-domain wavefunction can be approximated as equation (3.11). Here: the sinc function is the SPDC's phase-matching function with $A = 1.39/\pi B_{\mathrm{PM}}$ for B_{PM} = 250 GHz being the FWHM phase-matching bandwidth; $\Delta\Omega$ is the cavity FSR in rad s^{-1}; Ω is the detuning of the SPDC biphotons from their center frequency; $2N + 1$ is the number of the cavity lines passed by the bandwidth-limiting filter; and $f(\Omega - m\Delta\Omega)$ is the spectral amplitude of the mth cavity resonance, with $f(\Omega) = 1/[\Delta\omega + i\Omega]$. The temporal wavefunction of the exponential decay singly-resonant BFC is then given by equation (3.12). The state's temporal behavior then has recurrences with cavity's round-trip time $\Delta T = 2\pi/\Delta\Omega \approx 23.46$ ns. In this configuration, only signal photon is confined by the fiber FP cavity, we will observe exponential decay waveforms with τ being the temporal delay as a consequence of the cavity round-trips.

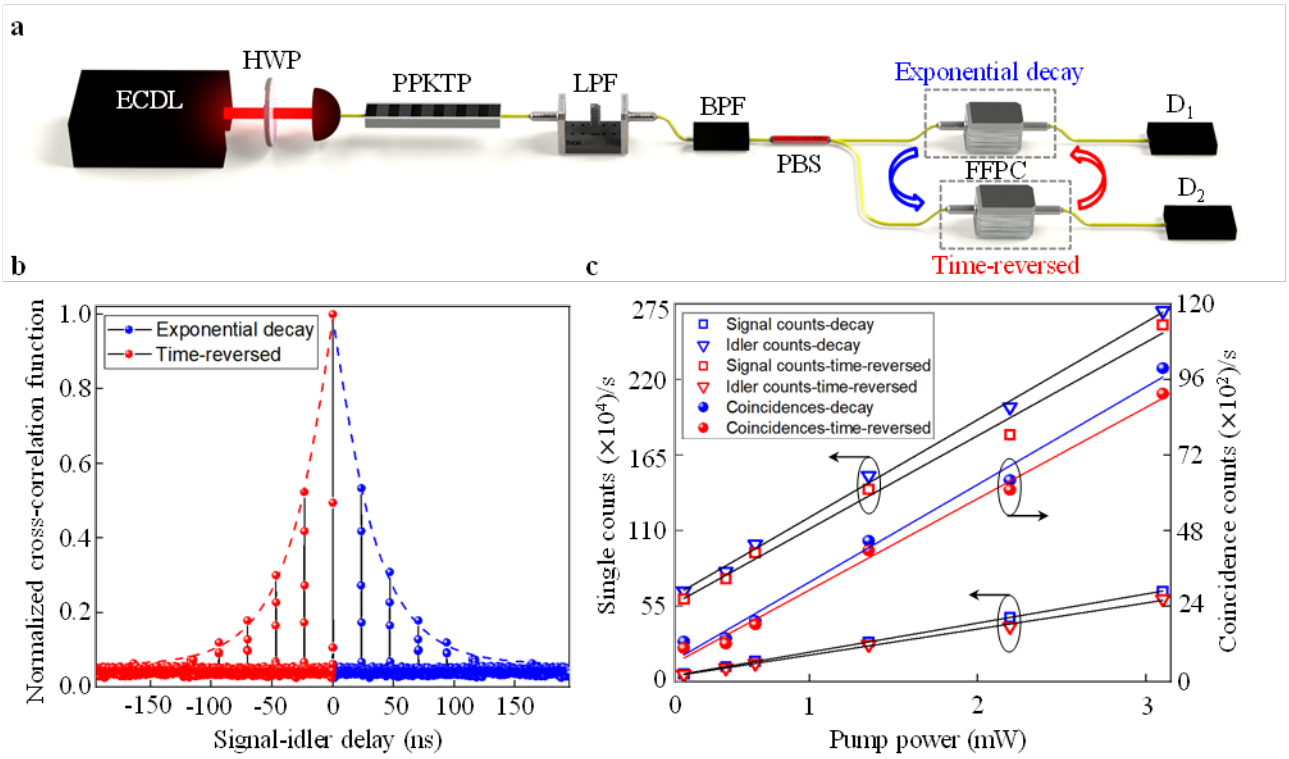

Fig. 3.15. Time-reversible ultranarrow photon-pair source via 42 MHz FSR singly-resonant BFCs. a) Schematic of experimental setup for natural exponential decayed and time-reversed SR-BFCs. ECDL: external cavity diode laser; HWP: half-wave plate; LPF: long-pass filter; BPF: bandpass filter; PBS: polarizing beam splitter; FFPC: Fiber Fabry-Perot cavity; D: detector. b) Temporal waveforms of time-reversible SR-BFCs. Both configurations can be achieved in a single experiment by switching the role of heralding single-photons. c) Observed pump dependencies of single counts of signal photons, idler photons, and coincidence counts in exponential decay and time-reversed SR-BFCs. Both the single and coincidence counts are proportional to the pump power, and the ratio of the single counts and coincidence counts are similar for time-reversible SR-BFCs. The arrows indicate the corresponding single and coincidence counts for exponential decay and time-reversed SR-BFCs.

In contrast, we can transform exponential decay to exponential growth waveforms of singly-resonant BFCs by switching the fiber FP cavity to previously heralded idler photons. The time-reversed singly-resonant BFCs temporal wavefunction can be written as:

$$|\psi_{growth}\rangle = \int_0^\infty d\tau \exp(\Delta\omega\tau) \sum_{m=-N}^{N} \mathrm{sinc}(Am\Delta\Omega)\cos(m\Delta\Omega\tau)\hat{a}_H^\dagger(t)\hat{a}_V^\dagger(t+\tau)\,|0\rangle \quad (3.18)$$

Due to time-reversal symmetry, in this configuration, only idler photon is filtered by the fiber FP cavity. We can observe exponential growth waveforms with τ being the temporal delay from the cavity round-trips. Specifically, the JTI of the exponential decay and growth singly-resonant BFCs can be

written as equation (3.13) and as follows:

$$K_{S'I'}^{cross}(-\tau) = \int_{-\infty}^{\infty} \frac{d\omega}{2\pi} \frac{i\sqrt{N_S}\mathrm{sinc}(\omega t_{\mathrm{coh}}/2)e^{-4\omega^2 ln(2)/\Delta\omega^2} e^{i\omega(-\tau - t_{\mathrm{coh}}/2)}}{1+i\frac{\Delta\Omega}{\pi\Delta\omega} sin(\pi\omega/\Delta\Omega)e^{-i\pi\omega/\Delta\Omega}} \tag{3.19}$$

respectively. Here, $t_{\mathrm{coh}} = 3.54$ ps is the coherence time of our SPDC source; $\Delta\omega/2\pi = 1097$ GHz is the FWHM bandwidth of BPF. We can understand the time-reversal symmetry of our singly-resonant BFCs is resulting from the swapping of heralding role between signal and idler photons. In this work, the time-reversal symmetry is achieved by asymmetric configurations of singly-resonant BFCs using a symmetric planar fiber FP cavity. Although the temporal wavefunction of our singly-resonant BFCs has time-reversal symmetry, both biphoton state has same frequency wavefunction.

To experimentally investigate this method, we used experimental setup shown in Fig. 3.15a. A continuous-wave external cavity diode laser at 780 nm is used for SPDC generation. The entangled photon-pairs are generated by a type-II ppKTP waveguide that was integrated in a fiber package for high photon flux and efficiency. The residual pump photons are removed by a LPF. An angle-mounted BPF with 95% passband transmission (Semrock NIR01-1570/3) is used to further clean the biphoton spectrum. Then the signal and idler photons are separated by a PBS due to the type-II phase matching. The time-reversible singly-resonant BFCs are generated by passing only the signal photons or idler photons through a fiber FP cavity. We note that if the fiber FP cavity are used in a doubly-resonant configuration-when both the signal and idler photons are filtered-the temporal wavefunction does not have time-reversal symmetry owing to the intrinsic symmetry of doubly-resonant BFC in the temporal-domain. Fig. 3.15b displays the measured temporal waveforms of time-reversible singly-resonant BFCs. We observed time-reversible multimode oscillations for both exponential decay and exponential growth singly-resonant BFCs. Both configurations can be achieved in a single experiment by switching the role of heralding single-photons for a symmetric planar fiber FP cavity. It is a double-sided transmitted symmetric planar fiber FP cavity. Due to the ultranarrow cavity FSR, we need to stabilize the temperature of this symmetric planar fiber FP cavity for single-photon statistic measurements. The temperature control of this fiber FP cavity is achieved by home-made double-temperature shielding layers with ~ 1 mK temperature control stability over 24 hours. Fig.1c is the measured pump dependencies of single counts of signal photons (blue and red squares), idler photons (blue and red triangles), and coincidence counts (blue and red circles) for central correlation peak in exponential decay and time-reversed SR-BFCs. For both SR-BFCs, the unfiltered idler (signal) photons have higher single counts than filtered signal (idler) photons due to the filtering loss of the fiber FP cavity. The single and coincidence counts are proportional to the pump power, and the ratio of

the single and coincidence counts are similar for our time-reversible SR-BFCs.

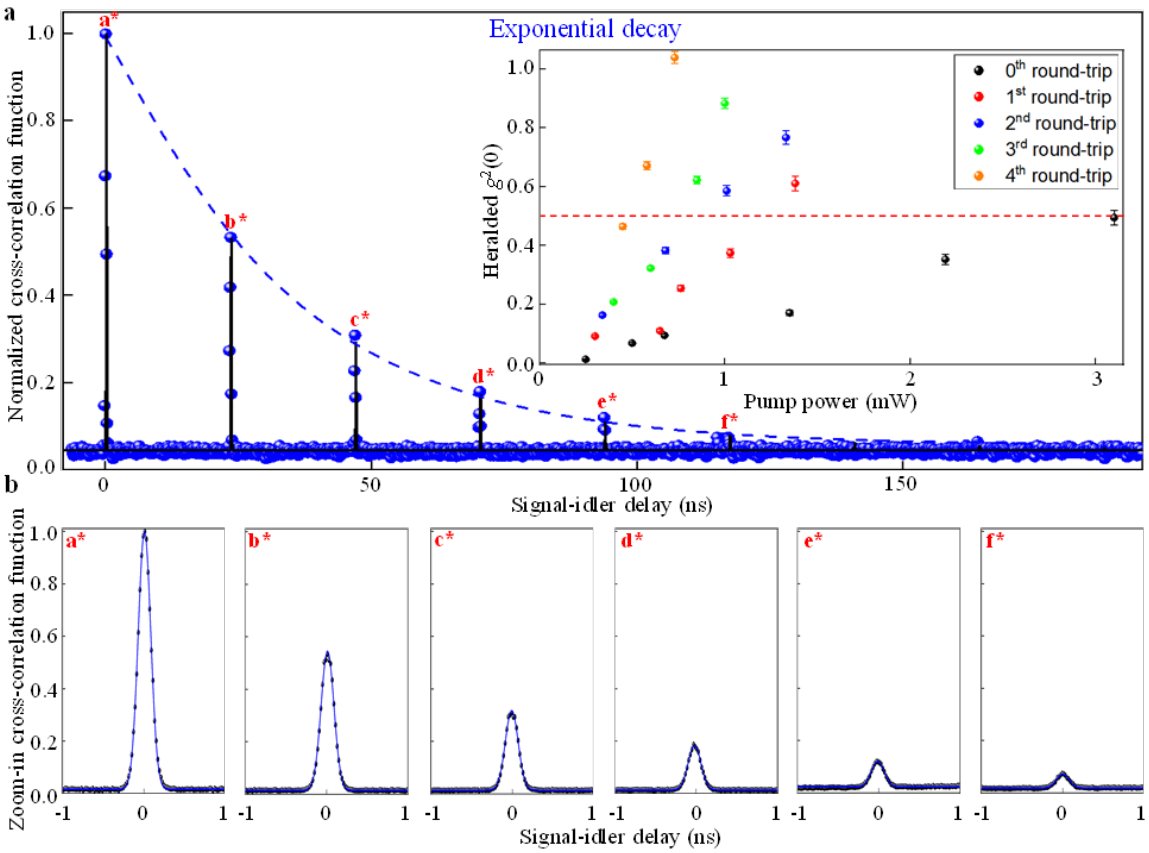

Fig. 3.16. Temporal second-order cross-correlation revivals and measured heralded $g^{(2)}(0)$ of 42 MHz exponential decayed singly-resonant BFC. a) Completely resolved second-order cross-correlation revivals in an exponential decay singly-resonant BFC. There are totally 6 measurable second-order cross-correlation revivals, from a* to f*. The left inset shows the exponential decay waveform from singly-resonant BFC, and cavity FSR is measured to be 23.46 ns, which is corresponding to 42.63 MHz. The cavity bandwidth is measured to be 4.587 MHz, deriving from the exponential decay. The cavity linewidth is measured to be 4.587 MHz, deriving from the theoretical fitting (black solid and dashed blue lines). The right inset show HBT measurements versus pump power for exponential decay singly-resonant BFC. The minimum heralded $g^{(2)}(0) = 0.013 \pm 0.002$ is measured for 0^{th} round-trip at 0.25 mW pump power with a heralding rate at 20 kHz. For 1^{st}, 2^{nd}, 3^{rd}, and 4^{th} cavity round-trips, the minimum heralded $g^{(2)}(0)$ are measured to be 0.092 ± 0.002, 0.164 ± 0.002, 0.208 ± 0.003, 0.465 ± 0.003, with 0.3, 0.34, 0.4, and 0.45 mW, respectively. Red line is the heralded $g^{(2)}(0) = 0.5$. b) Measured zoom-in temporal second-order cross-correlation revivals for all 6 peaks, from a* to f*. The peak values of each second-order cross-correlation peak are 1, 0.532, 0.308,

0.179, 0.121, 0.075, respectively. The decreasing of the peak values of second-order cross-correlation revivals can be explained by the cavity finesse of 9.29 in time-reversed SR-BFC. The temporal correlation oscillations of exponential decay SR-BFC is fully resolved due to the narrowest cavity FSR of 42.63 MHz.

Then, we measure the single-photon bunching and anti-bunching statistics of the cross-correlation function using the exponential decay singly-resonant BFC. Our results are presented in Fig. 3.16. Typically, in real JTI measurements, the sharp peaks of the cross-correlation function will be broadened due to the finite resolution time of the single-photon detectors [206]. Here, by using a ultranarrow cavity FSR of 42.63 MHz, we completely resolve the JTI of multimode singly-resonant BFC using commercial superconducting nanowire single-photon detectors for the first time (SNSPDs, ≈ 85% detection efficiency, root-mean-square timing jitter ~ 55 ps, PhotonSpot Inc.). In Fig. 3.16a, there are totally 6 measurable second-order cross-correlation revivals. The left inset shows the exponential decay waveform of multimode singly-resonant BFC, which matches with temporal wavefunction. The cavity FSR is measured to be 23.46 ns, which is corresponding to 42.63 MHz. The cavity linewidth is measured to be 4.587 MHz, deriving from the theoretical fitting (black solid and dashed blue lines). We show the measured zoom-in temporal second-order cross-correlation revivals for all 6 peaks in Fig. 3.16a. The peak values of each normalized second-order cross-correlation peak is 1, 0.532, 0.308, 0.179, 0.121, 0.075, respectively. The decreasing of the peak values of second-order cross-correlation revivals can be explained by the cavity finesse of 9.29 of exponential decay singly-resonant BFC. The FWHM of measured 6 peaks are 155.0, 154.7, 154.9, 157.3, 157.2, and 154.3 ps, respectively. The FWHM of correlation peaks is consistent with root-mean-square timing jitter of our SNSPDs (~ 55 ps), which indicate the direct measured JTI of our exponential decay singly-resonant BFCs is detected at the fundamental limit without any temporal broadening. Our results clearly show the first fully resolved JTI of exponential decay singly-resonant BFCs using commercially available single-photon detectors. We note that there are other ways to complete directly resolving JTI of multimode photon-pair sources, for instance, by using sum-frequency generation based ultrafast coincidence counting [194], or by utilizing specialized ultra-low timing jitter SNSPDs [51]. For cavity FSR compatible to telecommunication frequency-multiplexing technologies, the standard FSR is 50, 100 and 200 GHz, but such multimode emission can only be directly resolved temporally with SNSPDs with timing jitter of sub-picosecond. Then, we proceed to measure anti-bunching behavior or our exponential decay singly-resonant BFCs. In right inset of Fig. 3.16a, we show the HBT interferometer measurements versus pump power for exponential decay singly-resonant BFC. We sent

the unfiltered idler photons into HBT auto-correlation measurement heralded by filtered signal photons. The second-order auto-correlation $g^{(2)}(0)$ is measured by recording the three-fold coincidence counts between the HBT interferometer's output ports and the signal photons. Due to the narrowest cavity FSR (42.63 MHz here) and the FWHM of each cross-correlation peaks (average ~ 155.6 ps), triple coincidences signal-heralded idler auto-correlation measurement become dominated by accidentals, further increasing $g^{(2)}(0)$ due to the large coincidence time window. We choose a coincidence window of 1 ns around each individual peak maximum [225], well within the borders of the individual coincidence peak to avoid events clearly not originating from the exponential decay singly-resonant BFC. This allows us to accumulate sufficient coincidence counts for

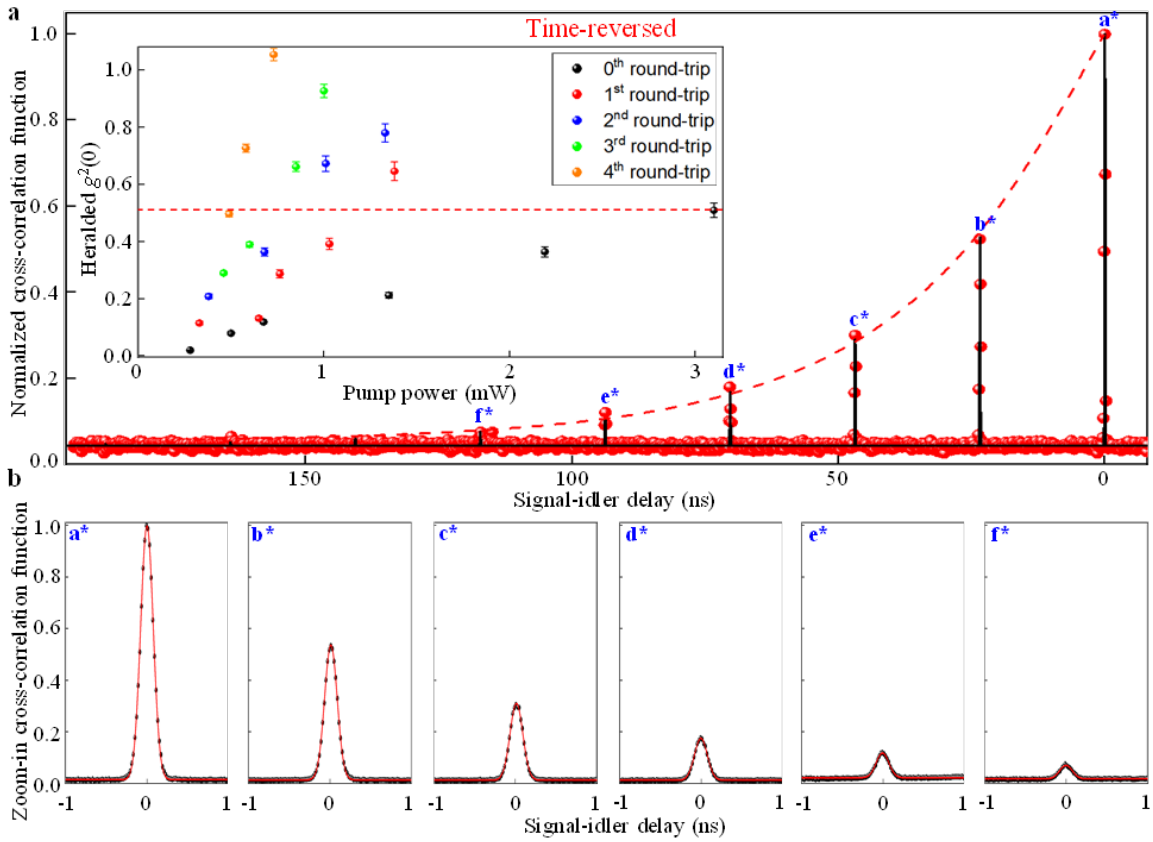

Fig. 3.17. Temporal second-order cross-correlation revivals and measured heralded $g^{(2)}(0)$ of 42 MHz time-reversed singly-resonant BFC. a) Completely resolved second-order cross-correlation revivals in a time-reversed configuration. There are totally 6 measurable second-order cross-correlation revivals, from a* to f*. The left inset shows the exponential growth waveform from the time-reversed singly-resonant BFC. Cavity FSR is measured to be 23.45 ns, which is corresponding to 42.64 MHz. The cavity linewidth is measured to be 4.599 MHz, deriving from the theoretical fitting (black solid and red dashed lines). The right inset is HBT measurements versus pump power for time-

reversed singly-resonant BFC. The minimum heralded $g^{(2)}(0) = 0.016 \pm 0.002$ is measured for 0^{th} round-trip at 0.28 mW pump power with a heralding rate at 24 kHz. For 1^{st}, 2^{nd}, 3^{rd}, and 4^{th} cavity round-trips, the minimum heralded $g^{(2)}(0)$ are measured to be 0.115 ± 0.002, 0.207 ± 0.002, 0.247 ± 0.003, 0.496 ± 0.003, with 0.33, 0.38, 0.46, and 0.49 mW, respectively. Red line is the heralded $g^{(2)}(0) = 0.5$. b) Measured zoom-in temporal second-order cross-correlation revivals for all 6 peaks, from a* to f*. The peak values of each second-order cross-correlation peak are 1, 0.530, 0.303, 0.180, 0.120, 0.076, respectively. The decreasing of the peak values of second-order cross-correlation revivals can be explained by the cavity finesse of 9.27 in time-reversed singly-resonant BFC.

meaningful single-photon statistics in a reasonable time frame, without being dominated by background noise. The minimum heralded $g^{(2)}(0) = 0.013 \pm 0.001$ is measured for 0th round-trip at 0.25 mW pump power with a heralding rate at 20 kHz. For 1^{st}, 2^{nd}, 3^{rd}, and 4^{th} cavity round-trips, the minimum heralded $g^{(2)}(0)$ is measured to be 0.092 ± 0.0011, 0.164 ± 0.0013, 0.208 ± 0.0016, 0.465 ± 0.0018, with 0.3, 0.34, 0.4, and 0.45 mW, respectively. At low pump power, the heralded $g^{(2)}(0)$ values for all five cavity round-trip are below 0.5, showing single-photon Fock state generation from our exponential decay singly-resonant BFC. The increasing of minimum heralded $g^{(2)}(0)$ for multiple cavity round-trips versus the 0^{th} cavity round-trip is due to the decreasing signal-to-noise ratio for those cross-correlation peaks, and the cavity finesse of our singly-resonant BFC. We observe that the heralded $g^{(2)}(0)$ is proportional to the pump power, due to the Poisson statistics of the SPDC emission.

In Fig. 3.17, we directly generate time-reversed singly-resonant BFC by swapping the symmetric planar fiber FP cavity from signal to idler photons. Indeed, as predicted by Eq. (3), we clearly observe exponential growth multimode singly-resonant BFC, with 6 measurable second-order cross-correlation revivals in Fig. 3.17a. The cavity FSR in this time-reversed configuration is measured to be 23.45 ns, which is corresponding to 42.64 MHz. The cavity linewidth is measured to be 4.599 MHz, deriving from the exponential growth waveform. Fig. 3.17b shows the measured zoom-in temporal second-order cross-correlation revivals for all 6 peaks, and the FWHM of each peak is 154.4, 155.2, 154.1, 157.3, 155.1, and 154.4 ps, respectively. The FWHM of correlation peaks is consistent with root-mean-square timing jitter of our SNSPDs (~ 55 ps), indicating the completely resolved JTI without any temporal broadening in our time-reversed singly-resonant BFC. The peak values of each second-order cross-correlation peak is 1, 0.530, 0.303, 0.180, 0.120, 0.076, respectively. The decreasing of the peak values of second-order cross-correlation revivals is due to the cavity finesse of 9.27 in time-reversed SR-BFC. Thanks to the similarity between signal and idler frequency spectrums and the near-

degenerate configuration, our time-reversed singly-resonant BFC also behaves as single-photon Fock state with multimode emission. Fig. 3.17a right inset summaries the HBT measurement results using time-reversed SR-BFC. In this configuration, we sent the unfiltered signal photons into HBT auto-correlation measurement heralded by filtered idler photons. To avoid increasing accidental coincidence counts for heralded $g^{(2)}(0)$ measurements, we use coincidence window of 1 ns around each individual peak maximum to capture the true coincidence counts produced by our time-reversed singly-resonant BFC source. The minimum heralded $g^{(2)}(0) = 0.016 \pm 0.002$ is measured for 0^{th} round-trip at 0.28 mW pump power with a heralding rate at 24 kHz. For 1^{st}, 2^{nd}, 3^{rd}, and 4^{th} cavity round-trips, the minimum heralded $g^{(2)}(0)$ is measured to be 0.115 ± 0.002, 0.207 ± 0.002, 0.247 ± 0.003, 0.496 ± 0.003, with 0.33, 0.38, 0.46, and 0.49 mW, respectively. Our results are consistent with single-photon statistics, and the results for exponential decay SR-BFC in Fig. 3.16. For low pump powers, the heralded $g^{(2)}(0)$ values for all five cavity round-trip are below 0.5, and heralded $g^{(2)}(0)$ is proportional to pump power. The increasing of minimum heralded $g^{(2)}(0)$ for multiple cavity round-trips versus the 0^{th} cavity round-trip can be explained from the decreasing signal-to-noise ratio for those cross-correlation peaks, and

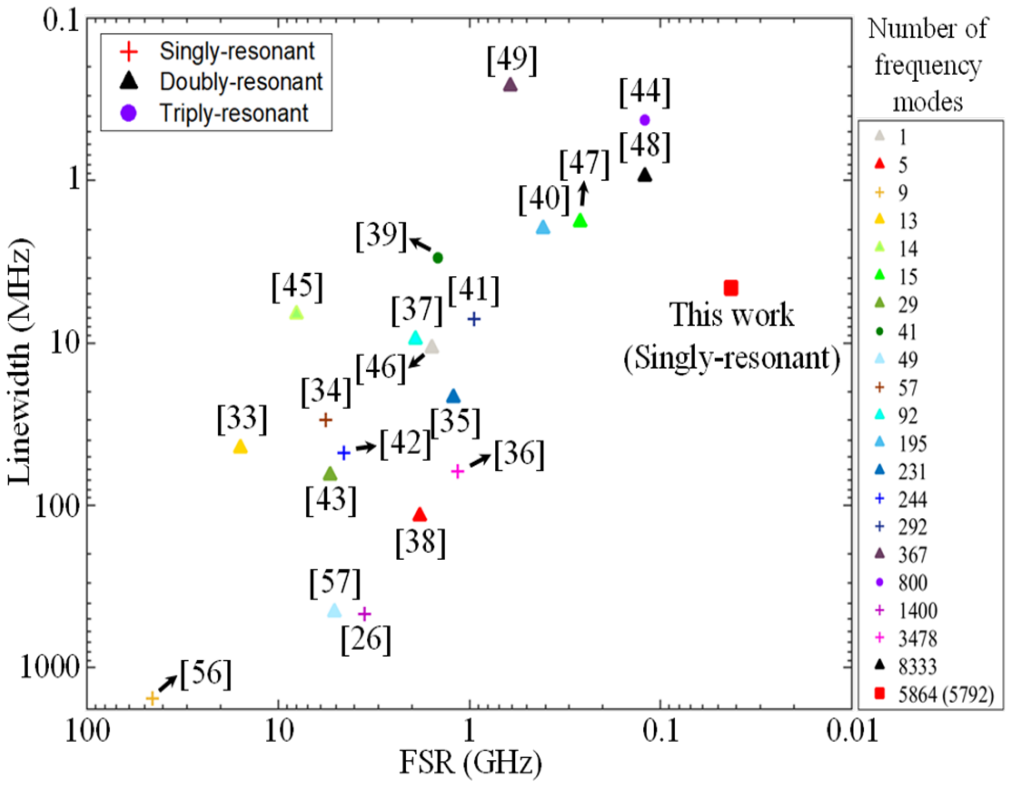

Fig. 3.18. Comparison of FSR and linewidth of post-filtered BFC and cavity-enhanced SPDC photon-pair sources. The multimode quantum sources are characterized by FSR (GHz) and linewidth (MHz). The selected cavity-enhanced SPDCs and post-filtered BFCs include singly-resonant [111,

177, 207, 216, 217, 229], doubly-resonant [71, 109, 218, 220, 230-237], and triply-resonant [143, 225] configurations. To the best of our knowledge, this work represents the narrowest FSR photon-pair source with highest reported number of frequency modes 5864 and the longest temporal coherence time of 218 ns among all the reported SR photon-pair sources up to date.

the cavity finesse of our time-reversed singly-resonant BFC. To further confirms the intrinsic multimode emission with single-photon anti-bunching characteristics of our time-reversed singly-resonant BFC, we measure averaged heralded $g^{(2)}(0) = 0.208 \pm 0.002$ by using a larger coincidence window of 30 ns (see Appendix A.7 for details). Our results show that the single-photon quantum nature is well-preserved during the time-reversal process for our ultranarrow-band singly-resonant BFCs. Moreover, all the measurement data for exponential decay and exponential growth singly-resonant BFCs can be collected in a single experiment without redesign and rebuild and restabilizing experimental setup as in cavity-enhanced SPDC sources.

In Fig. 3.18, we compare the cavity FSR and bandwidth of some of the state-of-the art cavity-enhanced SPDC and post-filtered BFC sources to our time-reversible ultranarrow-band photon-pair source. Most of these sources are doubly-resonant OPO or triply-resonant OPO operating far below threshold since there has not been much work done on singly configuration based multimode sources. The multimode quantum sources are characterized by FSR (GHz) and bandwidth (MHz). TThe selected cavity-enhanced SPDCs and post-filtered BFCs include singly-resonant [111, 177, 207, 216, 217], doubly-resonant [71, 75, 92, 229-237, 92], and triply-resonant [143, 225] configurations. The blue area indicates the typical bandwidth of electromagnetically induced transparency based quantum memory, and the green area is the operating bandwidth of controlled reversible inhomogeneous broadening/gradient echo memory and atomic frequency comb based quantum memories. This work represents the narrowest FSR photon-pair source with highest reported number of frequency modes of 11655 (via time-reversibility of our asymmetric singly-resonant BFCs) and megahertz-level bandwidth among all the reported cavity-enhanced SPDC and post-filtered BFC sources up to date.

3.5 Summary

In this chapter, we introduce main results with high-dimensional mode-locked quantum state generation via doubly-resonant and singly-resonant BFCs, making use of their multi-mode nature in time and frequency domains. We first introduce the mode-locked mechanism and the joint properties of BFCs, and how to certify its high-dimensional pure state generation with JSI measurements

(frequency correlation, HOM and Franson recurrence measurements), JTI measurements (second-order coherence functions $g^{(2)}(\tau)$ and conjugate-Franson revival measurements), Schmidt mode decomposition and entanglement of formation.

For the first work, we focus on the time-frequency entanglement in a doubly-resonant BFC, generating by filtering the signal and idler outputs with a fiber FP cavity with 45.32 GHz FSR and 1.56 GHz FWHM from a cw-pumped type-II SPDC. We generate a BFC whose time-binned/frequency-binned Hilbert space dimensionality is at least 324. Such BFC's dimensionality doubles up to 648, after combining with its post-selected polarization entanglement, indicating a potential 6.28 bits/photon classical-information capacity. The doubly-resonant BFC exhibits recurring HOM dips over 61 time-bins with a maximum visibility of 98.4% without correction for accidental coincidences. In a post-selected measurement, it violates the CHSH inequality for polarization entanglement by up to 18.5 standard deviations with an S_{CHSH} of up to 2.771. It has Franson interference recurrences in 16 time-bins with a maximum visibility of 96.1% without correction for accidental coincidences. From the zeroth- to the third-order Franson interference, we infer an entanglement of formation up to 1.89 ± 0.03 ebits, where 2 ebits is the maximal entanglement for a 4×4 dimensional biphoton, as a lower bound on the 61 time-bin BFC's high-dimensional entanglement. To further characterize time-binned/frequency-binned BFCs we obtain Schmidt mode decompositions of BFCs generated using cavities with 45.32, 15.15, and 5.03 GHz FSRs. These decompositions confirm the time-frequency scaling from Fourier-transform duality. Moreover, we present the theory of conjugate-Franson interferometry because it is characterized by the state's JTI, which can further help to distinguish between pure-state BFC and mixed state entangled frequency pairs. In summary, our BFC serves as a platform for high-dimensional QIP and high-dimensional QKD.

For the second work, we generate the high-dimensional BFC via SPDC in a singly-resonant configuration by connecting only the signal photons to a FP cavity, consequently the idler photons have the same comb signature due to conservation of energy in the biphoton generation process. The high-dimensional time-energy entanglement of the singly-resonant BFC is witnessed through Franson interference revivals for the first time, with 99.46% visibility over integer time-bins. Time-energy entanglement between different frequency-bin pairs of the singly-resonant BFC is also verified by Franson interference for the first time, with an average visibility up to 98.03% for the symmetric frequency-bin pairs. Frequency entanglement of the singly-resonant BFC is also characterized by Schmidt mode decomposition of the JSI, with measured Schmidt number of 4.16 across 5 frequency-bins. Furthermore, this high-dimensional time-frequency entangled singly-resonant BFC state is

asymmetrically distributed over a 10 km optical fiber. After distribution, high-dimensional time-frequency entanglement is examined by Franson interference, with up to 98.81% visibility achieved over time-bins and averaged 96.70% visibility across symmetric frequency-bins. Additionally, we estimate the entanglement of formation up to 1.523 ebits from Franson interference revivals after distribution as a lower bound on the high-dimensional time-energy entanglement of our singly-resonant BFC, which certifies a genuine three-dimensional time-energy entangled BFC state and matches well with the 1.538 ebits theoretical bound. Our high-dimensional entanglement demonstration of the present singly-resonant BFC provides a versatile platform for high-efficient QIP and high channel capacity quantum network communications, and also exploring fundamental research towards violation of locality and reality in high-dimensional system.

In the third work, we examine this limitation by examining the Franson interferences of mode-locked singly-resonant BFCs with different cavity parameters and provide a feasible method to overcome it. First, we observe mode-locked temporal oscillations in a 5.03 GHz FSR singly-resonant BFC using second-order cross-correlation function measurements by probing biphoton phase coherence in fiber etalon based BFC for the first time. Second, we measured the time-energy entanglement of 15.15 and 5.03 GHz FSR singly-resonant BFC via Franson interferometry. Franson interference recurrences are observed in 6 and 2 time-bins, with optimum central time-bin accidental-subtracted visibility over 97% for both cavities. Third, by theoretically examining the impact of cavity finesse F on both temporal second-order cross-correlation functions and Franson interference recurrences, we find that increasing cavity finesse F can significantly improve the cavity damping rate. This improvement then leading to the increasing detection probability in signal-idler temporal second-order cross-correlation function after multiple cavity round-trip times and the flattening Franson recurrence interferences in our mode-locked singly-resonant BFCs. For a 15.15 GHz FSR singly-resonant BFC with a cavity finesse F of 200, we present a theoretical ~54x fold improvement of Franson visibility compared to the Franson visibility with cavity finesse F of 11.14 at 16 cavity round-trip times. Our configuration is versatile and robust against changes in cavity parameters that can be designed for various quantum applications such as high-dimensional time-energy entanglement distribution, high-dimensional entanglement-based quantum key distribution, and wavelength-multiplexed quantum network.

For the fourth work, we demonstrate the genuine time-reversible ultranarrow-band telecommunication photon-pair source over 5,000 modes with asymmetric singly-resonant BFCs for the first time. In our scheme, the time-reversibility of our multimode photon-pair source is achieved

via swapping a symmetric planar fiber FP cavity between signal-idler photon-pairs in the asymmetric singly-resonant BFCs. Hence, this asymmetric singly-resonant BFCs configuration preserves the intrinsic multimode structure under time-reversal symmetry without specially designed FP cavities [226, 227] and the usage of lossy narrow-band telecommunication frequency filters [177]. Indeed, here, we are able to measure temporal second-order cross-correlation revivals and heralded $g^{(2)}(0)$ for both exponential decay and time-reversed singly-resonant BFCs. We fully resolve the multimode JTI for both exponential decay and time-reversed singly-resonant BFCs, with 12 cross-correlation peaks measured at the fundamental limit of our commercial single-photon detectors for the first time. The measured cavity FSR, linewidth of exponential decay and time-reversed singly-resonant BFCs are 42.63 MHz, 4.587 MHz, and 42.64 MHz, 4.599 MHz, respectively. The reported cavity FSR is the narrowest among all the different configurations of photon-pair sources so far. We also measure and confirm single-photon Fock state for our multimode time-reversible singly-resonant BFCs. By post-selecting the measured data to 1 ns coincidence window, centering at the peak maximum for each cavity round-trips, we obtain minimum heralded $g^{(2)}(0) = 0.013 \pm 0.002$, and $g^{(2)}(0) = 0.016 \pm 0.002$ for 0^{th} round-trip using both exponential decay and time-reversed SR-BFCs. The observed minimum heralded $g^{(2)}(0)$ for 1^{st} to 4^{th} cavity round-trips are all below the anti-bunching characteristic value of 0.5. Moreover, we also measure minimum averaged heralded $g^{(2)}(0) \sim 0.208 \pm 0.002$ by using a wider coincidence window of 30 ns for both exponential decay and time-reversed singly-resonant BFCs, which further verifies the intrinsic multimode emission and single-photon Fock state is well-preserved with time-reversal symmetry. Moreover, our photon-pair source operation within telecommunication-band, with narrowest cavity FSR of 42.64 MHz and 4.599 MHz linewidth in time-reversed fashion. Therefore, this source is directly compatible to chip-scale AFC quantum memories for high-dimensional multimode storage without quantum frequency conversion. Our time-reversible singly-resonant BFCs are robust and versatile, and they do not need a complex stabilization system By fully exploiting the time-reversible asymmetric singly-resonant BFCs in temporal domain, our sources expect to have 5864 and 5792 frequency modes, which is the highest number of photon-pairs among all the BFC sources up to date.

Chapter 4

Frequency-multiplexed high-dimensional quantum key distribution using biphoton frequency combs

4.1 Introduction

This chapter describes frequency-multiplexed high-dimensional QKD using both singly-resonant and doubly-resonant BFCs. Conventional QKD protocols often encode information using binary format. For example, BB84 uses horizontal (or left-handed circular) polarization to represent bit 0 and vertical (or right-handed circular) polarization to represent bit 1. In this encoding scheme, the key capacity, which is also referred to as the PIE, is limited to 1 bit per photon. Moreover, QKD systems typically operate in photon-starved conditions, and therefore the maximum key rate is limited by the PIE and the photon flux. One solution to increase the PIE is to encode information in a high-dimensional Hilbert space. Besides, high-dimensional encoding has been proved to be more resilient to noise [6, 9, 13, 15].

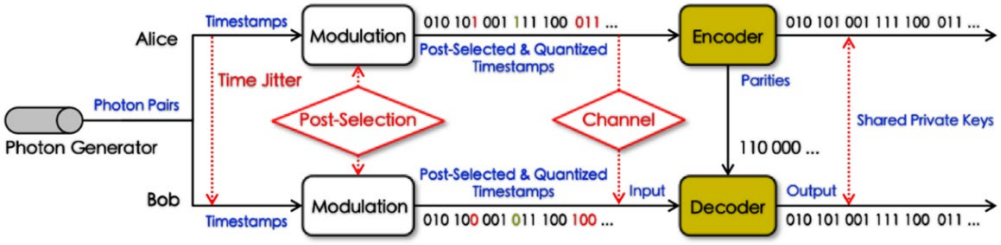

Fig. 4.1. Block diagram of high-dimensional time-bin QKD protocol. There are 3 steps for this protocol: 1) Entangled photon pairs are generated and sent to Alice and Bob; 2) Timestamps of the sequences are quantized and post-selected into multi-bit data streams; 3) Error correction codes are adopted to extract a common sequence from the post-selected data streams; this sequence is used as the private key for the secure quantum communication.

A few different DoFs have been studied for improving PIE, including time [238], orbital angular momentum [13, 15], position momentum [239], and time-energy [6, 9]. In this chapter, we focus the discussion on a scheme employing high-dimensional arrival-time encoding. We report an experimental demonstration of high-dimensional QKD with time-bin encoding using energy-time entangled BFC sources. Its security against a collective Gaussian attack is quantified through Franson interferometry. The Franson measurements in chapter 3 bounds the temporal correlation of the entangled photon pairs, which quantifies Eve's Holevo information. Finally, we report that we have obtained a maximum SKR

of 1.1 kbit/s with a PIE of 2.41 bits per coincidence using a 45.32 GHz FSR singly-resonant BFC.

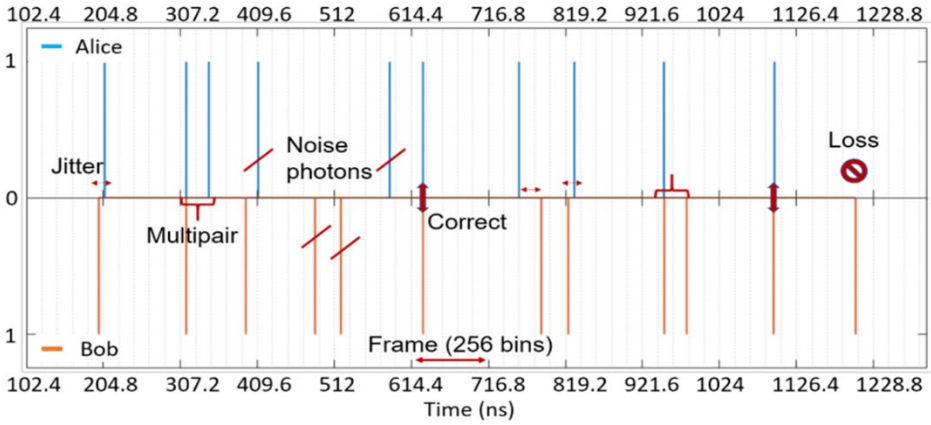

Fig. 4.2. Photon arrival time at Alice and Bob. Arrival timestamps of photons are quantized into bins with a bin width 400ps and consecutive 256 (can be any other powers of 2) bins are grouped into frames. Frames containing multi-pairs and losses are discarded such that each selected frame has exactly one photon from Alice and from Bob.

4.2 Frequency-multiplexed high-dimensional time-bin encoding with biphoton frequency combs

Wavelength-division multiplexing technology multiplexes a number of optical signals with different wavelengths into a single optical fiber and increases the classical communication channel capacity. Here, we report the high-dimensional QKD demonstration using time-bin encoding of energy-time entangled photon pairs from 45.32 FSR GHz singly- and doubly-resonant BFCs. Taking advantage of the multimode nature of the BFC in frequency domain, discretized frequency bins of the BFC are naturally suitable for wavelength multiplexing. Combined with time-bin encoding, this can further increase PIE and SKR at the cost of post-filtering and DWDMs. For the experimental results present in this chapter, we use the experimental setup in Fig. 3.2a for doubly-resonant BFC, and that in Fig. 3.7a for singly-resonant BFC.

After frequency-multiplexing singly- and doubly-resonant BFCs, we measured the raw photon timestamps multiple times for both Alice and Bob and processed the data for error-correction. Our time-bin encoding protocol is presented in Fig. 4.1. The entangled photon streams received by Alice and Bob are inevitably nonidentical due to a variety of practical issues, including timing jitters, photon losses, and dark counts, all of which reduce the secure key rate communicated over entangled photon

pairs. We post-filtered the single counts by dividing the duration into frames that were then discretized into time bins. For each frame we compared Alice and Bob's raw timestamps and discarded frames in which Alice and Bob did not each record a single count. This procedure results in a raw keystream comprised of Alice and Bob's assigning binary numbers to their time-binned count in each frame. Hence, we use symbol error rate, which is derived from correct symbol rate (number of corrected frames/number of total frames) to characterize the quality of our quantum channels [6]. The example raw data stream in given in Fig. 4.2. The raw keystream has two types of errors, viz., global errors, which are due to a combination of photon losses and dark counts, and local errors, which are due to the detectors' timing jitter. Global errors result in large discrepancies between Alice and Bob's raw-keystream bin numbers, whereas local errors result small bin-number errors.

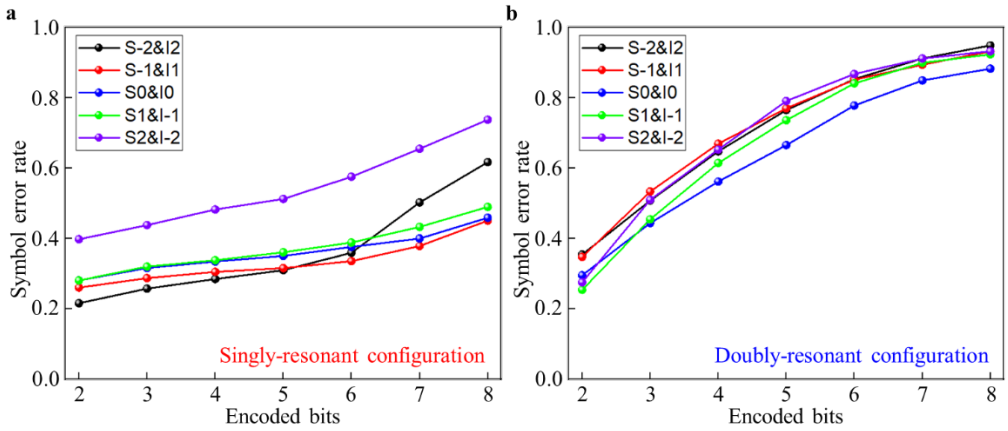

Fig. 4.3. Symbol error rate for 45 GHz singly- and doubly-resonant BFCs. a) The measured symbol error rate for a 45 GHz singly-resonant biphoton frequency comb. b) The measured symbol error rate for a 45 GHz doubly-resonant biphoton frequency comb. The measured symbol error rate is lower for a singly-resonant biphoton frequency comb, due to the high signal-to-noise ratio. In both cases, the symbol error rate increases as number of encoded bits increases.

Fig. 4.3 is the extracted symbol error rate using 1000 ps bin width for 45 GHz singly- and doubly-resonant BFCs. We can clearly see the symbol error rate for singly-resonant BFC is better than that of doubly-resonant BFC for high-dimensional encoding (over 2 encoded bits). There are 4 frequency-bin pairs have symbol error rate less than 50% for 8 encoded bits in singly-resonant BFC, while doubly-resonant BFC has symbol error rate ~50% at 3 bits encoding for 5 frequency-bin pairs. The main difference of symbol error rates for both BFCs is due to the nature of experimental configurations. The singly-resonant BFC has higher signal-to-noise ratio than doubly-resonant BFC (assuming all other factors are fixed) since only signal or idler photons are filtered by fiber FP cavity, whereas both signal

and idler suffer filtering loss in doubly-resonant BFC.

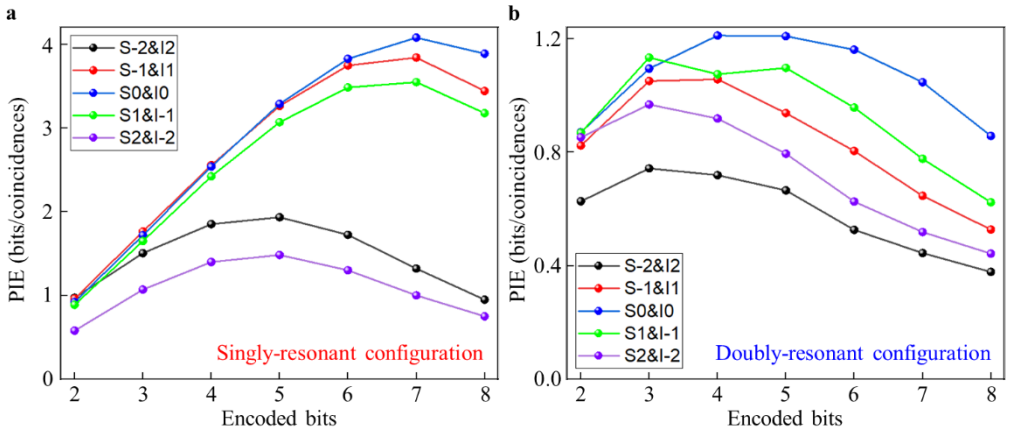

Fig. 4.4. Extracted photon information efficiency for 45 GHz singly- and doubly-resonant BFCs. a) Measured PIE in number of effective transmitted bits per coincidence for each entangled conjugate frequency-bin pair using a 45 GHz singly-resonant biphoton frequency comb. b) PIE for a 45 GHz doubly-resonant biphoton frequency comb. The measured PIE is higher for a singly-resonant biphoton frequency comb, due to the high signal-to-noise ratio. In both cases, there is optimum encoding bits for best PIE.

4.3 Benchmark on photon information efficiency and secret-key rate performances of singly- and doubly-resonant biphoton frequency combs

To achieve efficient information reconciliation in the presence of these error types we use the layered LPDC code from previous literatures [240, 241]. Using this code, we have calculated the Shannon information upper bound on the PIE, the key bits we can send per coincidence under highly-erroneous channel conditions. We have collected keystreams and encoded them using different discretization bin widths and encoded number of bits. Fig. 4.4 shows the extracted PIE for 45.32 GHz FSR singly- and doubly-resonant BFCs using frequency-multiplexing high-dimensional time-bin encoding. In Fig. 4.4a, the highest measured PIE for a singly-resonant BFC is ~4.1 bits per coincidence, while a doubly-resonant BFC has maximum PIE of only ~1.2 bits per coincidence, which is due to the higher signal-to-noise ratio of singly-resonant configuration. We note that the frequency-bin pairs which is closer to the central wavelength of SPDC photons contribute more on PIE versus frequency-bin pairs that is farer from the central wavelength of SPDC photons. This can be understood from the spectrum lineshape of SPDC photons (245 GHz bandwidth) as well as the FSR of the fiber cavity. In both

configurations, there is optimum encoding bits for best PIE.

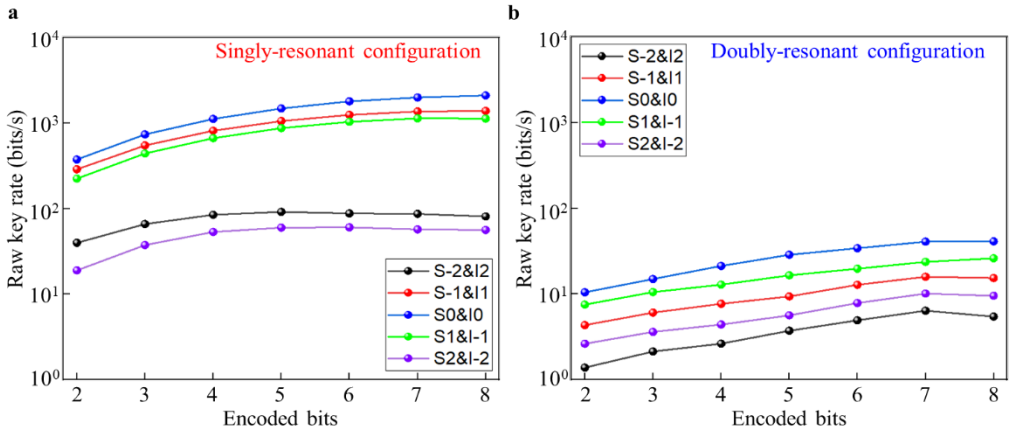

Fig. 4.5. Raw key rate for 45 GHz singly- and doubly-resonant BFCs. a) Measured raw key rate in number of effective transmitted bits per coincidence for each entangled conjugate frequency-bin pair using a 45 GHz singly-resonant biphoton frequency comb. b) Raw key rate for a 45 GHz doubly-resonant biphoton frequency comb. The measured raw key rate is higher for a singly-resonant biphoton frequency comb, due to the high signal-to-noise ratio.

Then, we multiplied PIE with number of coincidences per second of each frequency-bin pairs to obtain the raw key rate using both BFCs. Our results are summarized in Fig. 4.5. The measured raw key rate is higher for a singly-resonant BFC compared to a doubly-resonant BFC across all 5 frequency-bin pairs. Fig. 4.5 follows similar trend as Fig. 4.4, the photon flux for central and +1, -1 frequency-bin pairs contribute to the most of PIE and hence the majority of raw key rate. We observed that the highest raw key rate channels do not necessarily have the highest PIE. This is because the increasing throughput causes an increase in error rates due to a higher chance of accidental coincidences in a same frame.

The security of our frequency-multiplexed high-dimensional time-bin QKD is based on optimality of Eve's Gaussian collective attack for Alice and Bob's time-frequency covariance matrix [6, 9, 127]. The secure PIE is given by $\Delta I_{AB} = \beta I_{AB} - \chi^E$, in bits per coincidence, where β is the reconciliation efficiency, I_{AB} is Alice and Bob's Shannon information, χ^E is Eve's Holevo information for collective Gaussian attacks. From the measured frequency-binned Franson visibility, we calculate Eve's Holevo information. Our results are given by Fig. 4.6, it shows the Eve Holevo information bound for 5 frequency-bin pairs in a 45.32 GHz FSR singly-resonant BFC using accidental-subtracted Franson visibility in Fig. 3.9. The relatively large Eve information leak is due to the non-ideal accidental-subtracted Franson visibilities. Note that we do not perform security analysis for doubly-

resonant BFC, owing to their larger filtering loss and small photon flux. Then, we can finally obtain the SKR of our 45.32 GHz FSR singly-resonant BFC using frequency-multiplexed high-dimensional time-bin QKD.

Frequency-bin pairs	Accidental-subtracted Franson visibility	Holevo upper bound (bits/coincidences)
S2&I-2	0.9724	3.811
S1&I-1	0.9842	3.402
S0&I0	0.9966	2.233
S-1&I1	0.9838	3.421
S-2&I2	0.9645	3.995

Fig. 4.6. Eve Holevo information bound for 5 frequency-bin pairs in a 45 GHz singly-resonant BFC. Computed upper-bound Eve's Holevo information using high-visibility frequency-binned Franson interference across 5 pairs in a singly-resonant biphoton frequency comb [127]. The Franson visibility used here is after accidental-subtraction.

Our results are summarized in Fig. 4.7. First, we show the total PIE and raw key rate for all 5 frequency-bin pairs using both BFCs. The total PIE and overall raw key rate of singly-resonant BFC is ~3.5x, and ~50x higher than those of doubly-resonant BFC under similar experimental condition. The highlighted black circle is the maximized SKR of a 45.32 GHz FSR singly-resonant BFC, which is found to be 1.1 kbits/s with a 2.41 bits per coincidence. For secure PIE and SKR, only the S_0&I_0, S_{-1}&I_1), and S_1&I_{-1}frequency-bin pairs of singly-resonant BFC are used in order to obtain positive secure PIE and SKR. The encoded bits were chosen to be 7 for optimizing both the secure PIE and SKR. We expect the SKR can be further improved either by using a higher brightness entangled photon source, or by utilizing a cavity-enhanced SPDC configuration [177].

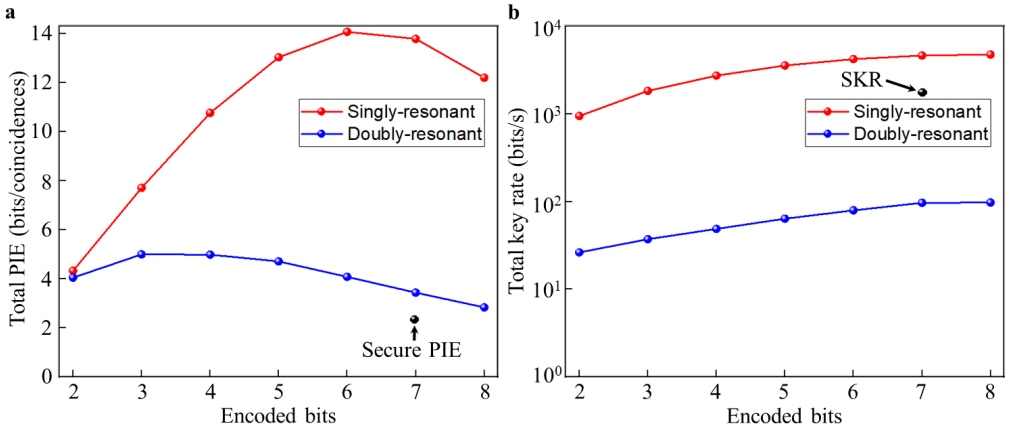

Fig. 4.7. Total photon information efficiency and key rate for 45 GHz singly- and doubly-resonant BFCs. a) Measured total PIE in number of effective transmitted bits per coincidence using all channels of 45 GHz singly- and doubly-resonant biphoton frequency combs. b) Summed raw key rate across 5 frequency-bin pairs for 45 GHz singly- and doubly-resonant biphoton frequency combs. The total PIE and overall raw key rate of singly-resonant biphoton frequency comb is ~3.5x, and ~50x higher than those of doubly-resonant biphoton frequency comb. The highlighted black circle is the maximized SKR of 45 GHz singly-resonant biphoton frequency comb, which is found to be 1.1 kbits/s with a 2.41 bits per coincidence.

4.4 Summary

In this chapter, we presented a proof-of-principle experimental demonstration of the frequency-multiplexed high-dimensional time-bin QKD protocol using BFCs. The security of this protocol was guaranteed by the frequency-binned Franson interference visibilities. For a 45.32 GHz FSR singly-resonant BFC, we measured a secure PIE of 2.14 bits per coincidence, corresponding to an SKR of 1100 bits/s. The performance of this system is limited by the source brightness and the difficulty to tightly bound Eve's Holevo information. With photon sources that have ∼1 GHz photon pair rate, and the near unity raw Franson visibility [242], we expect the frequency-multiplexed high-dimensional time-bin QKD can reach Gigabits/s SKR with PIE over 10 bits per coincidence, providing sufficient bandwidth for quantum secure communication and multi-user quantum networks.

Chapter 5

A two-qubit four-dimensional SWAP gate for efficient quantum interface

5.1 Introduction

Two-qubit entangling gate, which operates on one qubit conditioned on the state of the other, is a necessary component for constructing any arbitrary quantum operation to fulfill universal QIP [107]. While photonics excels for single-qubit gates, the inherent difficulty in realizing photon-photon interactions has made the two-qubit gate a persistent obstacle in photonic QIP. While two-qubit gates succeed only probabilistically in this paradigm, LOQC [112] is in principle scalable with polynomial auxiliary resource requirements and has laid the foundation for many subsequent advances in photonic QIP. Hybrid quantum sub-systems exploiting diverse qubit modalities or material transitions for applications in quantum sensing and quantum computing have also made remarkable advances [243, 244]. Consequently, efficient quantum interfaces have been proposed [245, 246] to interconnect disparate subsystems [103, 247] or convert between different DoFs [248-250] for coherent qubit transfer.

In this work, we demonstrate a chip-scale two-qubit gate, an efficient quantum interface that deterministically, and with high fidelity, swaps a photon's polarization qubit with its spatial-momentum qubit.

5.2 A chip-scale polarization-spatial two-qubit SWAP interface

The biphoton's state lies in a four-dimensional Hilbert space spanned by two orthogonal polarizations and two orthogonal spatial modes. The on-chip SWAP operation is accomplished with a three-gate cascade comprised of a polarization-controlled NOT (PC-NOT) gate, a momentum-controlled NOT (MC-NOT) gate, and another PC-NOT gate. The MC-NOT gate is designed for and nanofabricated on a two-level-aligned silicon photonics platform, consisting of an integrated polarization rotator and a polarization-mode converter. Fig. 5.1a left panel shows SWAP gate operation that swaps arbitrary values of qubits A and B without measuring or perturbing them. When qubits A and B are encoded,

respectively, in the polarization and spatial-momentum mode of a single photon, SWAP gate operation can be realized with the three-gate cascade shown in Fig. 5.1a right panel [248, 251]. In probabilistic linear optical quantum processing, most of the quantum logic operations are performed on two qubits, usually qubits of the same modality from two different photons. Here, a SWAP gate can coherently exchange states non-deterministically between qubits residing on different photons. In our single-photon two-qubit SWAP gate, qubit states are exchanged deterministically between the polarization and momentum DoF of the *same* photon, which suggests that robust on-chip multi-qubit single-photon logic of higher order should be sought [251-254]. The polarization qubit (P) is based on the two polarization eigenstates $|H\rangle$ and $|V\rangle$, which correspond to the transverse electric (TE) and transverse magnetic (TM) polarizations of our quantum photonic chip. Our experiments use a type-II phase matched SPDC waveguide source that produces $|V_S H_I\rangle$ biphotons in a single spatial mode, where the subscripts S and I denote the signal and idler qubits. The momentum qubit (M) is based on two spatial-momentum eigenstates $|T\rangle$ and $|B\rangle$, which correspond to the top and bottom channels of the quantum chip. Our experiments illuminate either the SWAP chip's top or bottom channels with polarization-rotated signal photons from the SPDC source, resulting in input state $|\Psi_T\rangle_{IN} = \big(|T_S H_S\rangle + e^{i\varphi}|T_S V_S\rangle\big)\otimes|H_I\rangle/\sqrt{2}$ for top-channel illumination and $|\Psi_B\rangle_{IN} = \big(|B_S H_S\rangle + e^{i\varphi}|B_S V_S\rangle\big)\otimes|H_I\rangle/\sqrt{2}$ for bottom-channel illumination, where $|H_I\rangle$ acts as a herald for the two qubits contained in its signal-photon companion. Defining $|0_{PS}\rangle = |H_S\rangle$, $|1_{PS}\rangle = |V_S\rangle$, $|0_{MS}\rangle = |T_S\rangle$, and $|1_{MS}\rangle = |B_S\rangle$ to be the logical-basis states, the input states become $|\Psi_T\rangle_{IN} = \big(|0_{MS}0_{PS}\rangle + e^{i\varphi}|0_{MS}1_{PS}\rangle\big)\otimes|H_I\rangle/\sqrt{2}$ and $|\Psi_B\rangle_{IN} = \big(|1_{MS}0_{PS}\rangle + e^{i\varphi}|1_{MS}1_{PS}\rangle\big)\otimes|H_I\rangle/\sqrt{2}$, which result in output states $|\Psi_T\rangle_{OUT} = \big(|1_{MS}1_{PS}\rangle + e^{i\varphi}|0_{MS}1_{PS}\rangle\big)\otimes|H_I\rangle/\sqrt{2}$ and $|\Psi_B\rangle_{OUT} = \big(|1_{MS}0_{PS}\rangle + e^{i\varphi}|0_{MS}0_{PS}\rangle\big)\otimes|H_I\rangle/\sqrt{2}$, respectively, in which the signal photon's polarization and spatial-momentum qubits have been swapped.

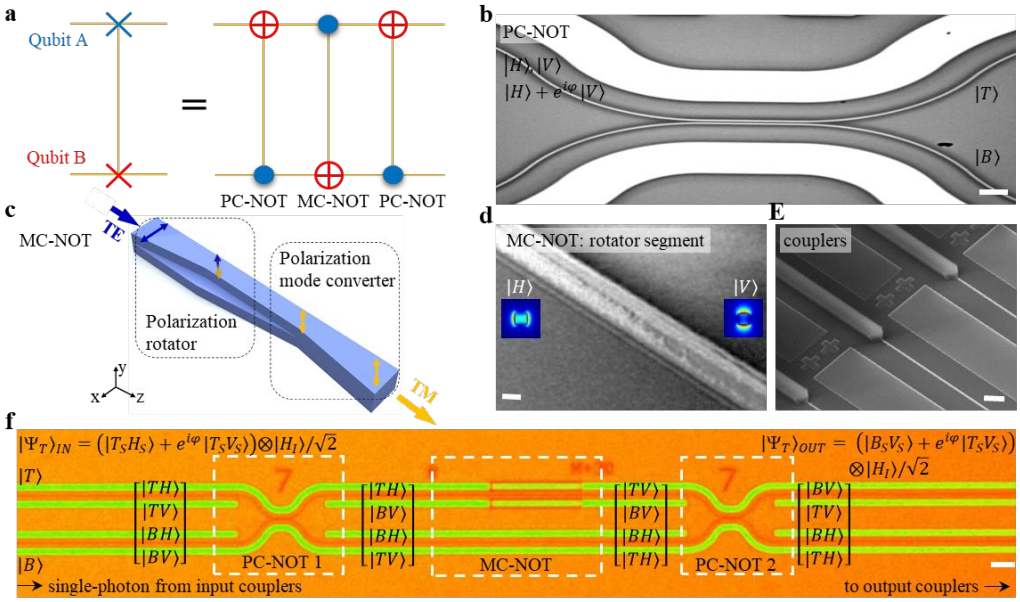

Fig. 5.1. A chip-scale polarization-spatial two-qubit SWAP interface. a) Illustrative two-qubit SWAP gate interface scheme. This can be realized, for single photon carrying qubit A in its polarization and qubit B in its spatial-momentum modes, by applying sequentially a PC-NOT gate, an MC-NOT gate and another PC-NOT gate, which are controlled by qubits A, B and A, respectively. b) Scanning electron micrograph of the chip-scale SWAP gate's first-stage PC-NOT gate realized by an optimized integrated-photonics polarized coupler. Scale bar: 2 μm. c) Schematic of an integrated two-level polarization rotator and polarization mode converter, enabling the second-stage MC-NOT gate for the SWAP operation. d) Scanning electron micrograph of the MC-NOT gate's nanofabricated rotator segment. Scale bar: 500 nm. e) Scanning electron micrograph of the inverse taper couplers for improved free-space qubit-to-chip coupling. Scale bar: 20 μm. f) Optical micrograph of the complete SWAP gate operation using the cascaded PC-NOT / MC-NOT / PC-NOT architecture. Scale bar: 10 μm. An example of input state ($|\Psi_T\rangle_{IN}$) for top channel of the SWAP gate is denoted, leading to the output state $|\Psi_T\rangle_{OUT}$, where signal photon's polarization qubit is swapped to spatial-momentum qubit. State vectors at each NOT gate segment represent the resulting states of each gate operation on four possible input states $[|TH\rangle, |TV\rangle, |BH\rangle, |BV\rangle]$.

The preceding SWAP operation is accomplished in our silicon photonics platform with three cascaded C-NOT gates designed so that the control and target qubits exchange roles in the middle C-NOT gate [255], as depicted in Fig. 5.1a right panel. In our architecture, the PC-NOT gate is realized by a silicon-photonics polarized directional coupler as shown in Fig. 5.1b. The silicon MC-NOT gate is realized by a specially designed two-layer polarization structure that, as shown in Fig. 5.1c, consists

of two stages: (1) a polarization rotation stage, which tapers and rotates the qubit polarization by 90° and (2) a polarization-maintaining mode conversion stage, which converts the qubit mode profile to match the output waveguide. The polarization rotation stage is shown in Fig. 5.1d. Because the polarization rotation and mode conversion are only implemented for the top channel, as shown in Fig. 5.1f, the two-layer polarization structure thus performs the MC-NOT operation. Detailed design-space maps and optimization of the MC-NOT and PC-NOT gates are described in Appendix C.1. Each of the PC-NOT and MC-NOT gates has a silicon dioxide top cladding, with a rectangular silicon waveguide of 460 nm × 220 nm width-height cross-section, and with relatively small birefringence between the TE and TM modes for the polarization operations and diversity [256, 257]. The optimized PC-NOT gate has a waveguide-to-waveguide gap of 400 nm with a designed 11.5 μm coupling length, ensuring that the TE mode remains in its original waveguide while the TM mode crosses over to the other waveguide, with achieved average extinction ratio of ≈ 18 dB for different input-output ports and polarization combinations (detailed in Appendix C.2). The optimized MC-NOT gate has two 110 nm step-height layers, in a self-aligned nanofabrication approach across the wafer to ensure high TM-to-TE polarization extinction ratio, and with tapered widths down to 150 nm and uniform 30 nm lateral offsets (detailed in Appendix C.2). Our designed MC-NOT gate achieved a high extinction ratio of ≈ 20 dB for both TE and TM modes. The sidewall roughness is minimized for low waveguide loss, to ensure good SWAP gate performance. In addition, to ensure good coupling efficiency, adiabatic inverse tapers are designed for mode-index transformation at the input-output facets as shown in Fig. 5.1e, with less than 3 dB loss for each facet.

5.3 Experimental characterization of the two-qubit SWAP gate

Our two-qubit SWAP gate measurement setup is shown schematically in Fig. 5.2a. CW-pumped SPDC in a 1.5 cm ppKTP waveguide designed for type-II phase matching at ≈1556 nm produces orthogonally-polarized signal-idler biphotons [75, 92]. The pump is a FP laser diode stabilized with self-injection locking, through a double-pass first-order diffraction feedback with an external grating. Tunable single-longitudinal mode lasing is achieved between 775.0 nm and 793.0 nm, enabling tunable SPDC with signal wavelengths from 1552.5 to 1559.6 nm, as shown in Fig. 5.2a inset. A LPF blocks the residual pump photons after the SPDC, and an angle-mounted BPF with 5 to 6 optical depth and a 95% passband transmission further suppresses pump photons. Here, the

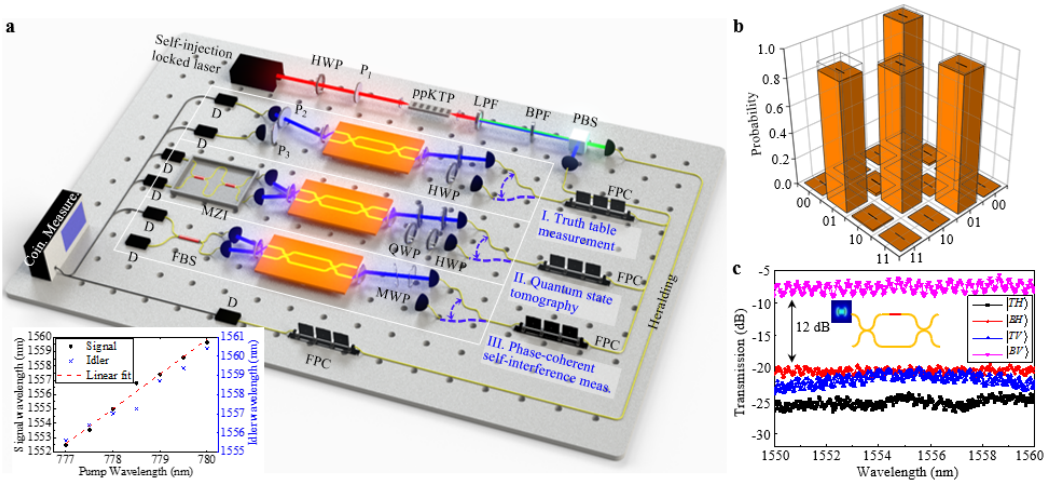

Fig. 5.2. Experimental configuration for characterization of the single-photon two-qubit SWAP gate. a) Schematic of the heralded single-photon measurements generated via SPDC, with the three modular experiments: (I) truth table characterization, (II) quantum state tomography, and (III) phase-coherence self-interference measurements. Input polarization qubits are controlled by a half-wave plate and then fed to the gate through free-space coupling. Output spatial-momentum qubits are examined by a polarization analyzer for truth table measurement, by Bloch state measurements for the quantum state tomography, and interfered in 50:50 BS for phase preservation checks on the SWAP operation. Successful SWAP operation is heralded by coincidence counting between signal and heralding channel. P_i: linear polarizer. MWP: multi-order waveplate. QWP: quarter-wave plate. FBS: 50:50 fiber BS. D: superconducting nanowire single-photon detector. Bottom left inset: signal and idler photon wavelengths as a function of the pump wavelength. The red dashed line is a linear fit on the signal photon wavelength. b) Measured (solid bars) and ideal (transparent bars) truth table for the PC-NOT gate in the computational basis. A total of around 90,000 coincidence counts is recorded in 160 seconds, yielding an average fidelity of 96.80 $\pm$ 0.10 %. c) Classical input-output cross-talk characterization for the SWAP gate. Of the 16 input-output state combinations, those for the 4 outputs from the $|TH\rangle$ input is shown here (the other 12 are in Appendix C.3), where an extinction ratio of at least 12-dB is observed across all output states, and from 1550 nm to 1560 nm.

biphoton state $|V_S H_I\rangle$ is generated by SPDC. The signal and idler photons are then separated by the PBS. The signal photons are fed to the SWAP gate while the idler photons are directed to the detector for heralding. A two-in two-out free-space coupling system accesses the top and bottom channels of the SWAP chip at both its input and output facets. For each input channel, half-wave, quarter-wave and/or multi-order waveplates control the input polarization state for each measurement setup shown

in Fig. 5.2a. The polarization state of the signal photon becomes $|H\rangle$ or $|V\rangle$ or the superposition state given earlier according to the waveplate combination. The input spatial-momentum state is controlled by switching the input fiber (blue dashed line) to top or bottom channel of the SWAP gate, resulting in $|T\rangle$ or $|B\rangle$. Thus, the input states to our SWAP gate are in the four-dimensional Hilbert space spanned by $|TH\rangle$, $|TV\rangle$, $|BH\rangle$ and $|BV\rangle$, corresponding to $|00\rangle$, $|01\rangle$, $|10\rangle$ and $|11\rangle$ in the logical basis.

To characterize our PC-NOT gate, we measure an individual PC-NOT gate located on the same chip with our SWAP gate, with the same parameters as the SWAP gate's PC-NOTs. The characterization is performed using the measurement scheme shown in Fig. 5.2a (I). Fig. 5.2b shows the resulting measured truth table obtained for the four input states: $|00\rangle$, $|01\rangle$, $|10\rangle$ and $|11\rangle$ in the computational basis. The solid bars depict the experimentally measured truth table M_{exp} while the transparent bars illustrate the ideal truth table M_{ideal}. The fidelity of the measured PC-NOT truth table with respect to the ideal one is calculated by $F = (1/4)Tr\left(\frac{M_{exp}{M_{ideal}}^T}{M_{ideal}{M_{ideal}}^T}\right)$. In our PC-NOT gate, we achieved an average fidelity of 97.76 ± 0.19%, across the four basis states. We note that the residual deviation from unit fidelity is bounded by the PC-NOT's finite polarization-extinction ratio (detailed in Appendix C.1 and 2), and the ≈ 0.9 dB coupling difference between the $|H\rangle$ and $|V\rangle$ states. Similarly, to characterize our MC-NOT gate, we measure an individual MC-NOT gate located on the same chip with our SWAP gate, with the same parameters as the SWAP gate's MC-NOT. The MC-NOT gate is examined by coupling a linearly-polarized swept C-band tunable laser, with the gate output through a polarizer. The classical transmission measurement shows an extinction ratio of more than 20 dB over the C-Band wavelengths (detailed in Appendix C.2).

In order to characterize the two-qubit SWAP operation, we first measured our PC-NOT | MC-NOT | PC-NOT circuit architecture with a swept 1556 nm tunable laser. Of the 16 polarization spatial-momentum input-output combinations, the classical transmissions – across a 10 nm spectrum – from the $|TH\rangle$ basis state at the SWAP gate's input to the 4 basis states at that gate's output are shown in Fig. 5.2c. The results for the other 12 input-output combinations are presented in Appendix C.3. Over ≈ 12 dB cross-talk suppression is consistently achieved, befitting the desired ≈1556 nm qubit working wavelength. Residual spectral fluctuations in the SWAP gate arise from FP reflections at the input and output facets and also coupling variations across the 10 nm spectrum. Current limits on the ≈ 12 dB cross-talk suppression in the four basis states arises mainly from the finite polarization extinction ratio of the PC-NOT and MC-NOT gates, as detailed in Appendix C.1 and 2 (broader 100 nm band characterization of the SWAP gate is also detailed in Appendix C.3).

5.4 Truth table measurement and quantum state tomography of the two-qubit SWAP gate

Having demonstrated sufficiently low cross-talk between the basis states, we next performed the heralded two-qubit SWAP operation in the computational basis, with the truth table measurement setup illustrated in Fig. 5.2a (I). The idler photon is detected by a superconducting nanowire single-photon detector (SNSPD; with ≈ 85% detection efficiency) to herald the presence of a signal photon. The signal photon is sent to the $|B\rangle$ or $|T\rangle$ channels with $|H\rangle$ or $|V\rangle$ polarization by tuning the half-wave plate. Polarizers P_2 and P_3 are rotated for polarization selection at the output ports. Coincidence counting is then performed using SNSPD's at the P_2 and P_3 outputs with internal timing delays to match that of the heralding detection. By recording the coincidence rates versus the polarization angle, we obtained the SWAP gate's projection probabilities shown in Fig. 5.3a, i.e., the SWAP gate's truth table. Measurements were made at 1556 nm, 1557 nm, and 1558 nm wavelengths. The measured truth tables yield a wavelength-averaged fidelity $\bar{F}_{gate,truth}$ of 97.21 $\pm$ 0.14% (98.53% after background subtraction), in support of the excellent performance in the logical basis. We note that the deviations from unity in the two-qubit truth-table's fidelity mainly arise from the imperfect extinction ratio of the PC-NOT and MC-NOT gates and the MC-NOT gate's unbalanced photon loss. These non-idealities are examined in detail in Appendix C.4, and can be mitigated by more adiabatic polarization-mode conversion and tighter suppression of the cross-polarization. In addition, we note that the waveguide loss and unbalanced coupling efficiency between the $|H\rangle$ and $|V\rangle$ states contribute to the truth-table fidelity reduction by ≈ 0.55% (see Appendix C.4 for details). On-chip silicon polarization couplers with improved extinction ratio and insertion loss have been demonstrated [257], which can bring our chip's truth-table fidelity up to near unity. Although the truth table measures the two-qubit SWAP operation in the logical basis, QPT is required to characterize the coherence of the SWAP operation [161, 258].

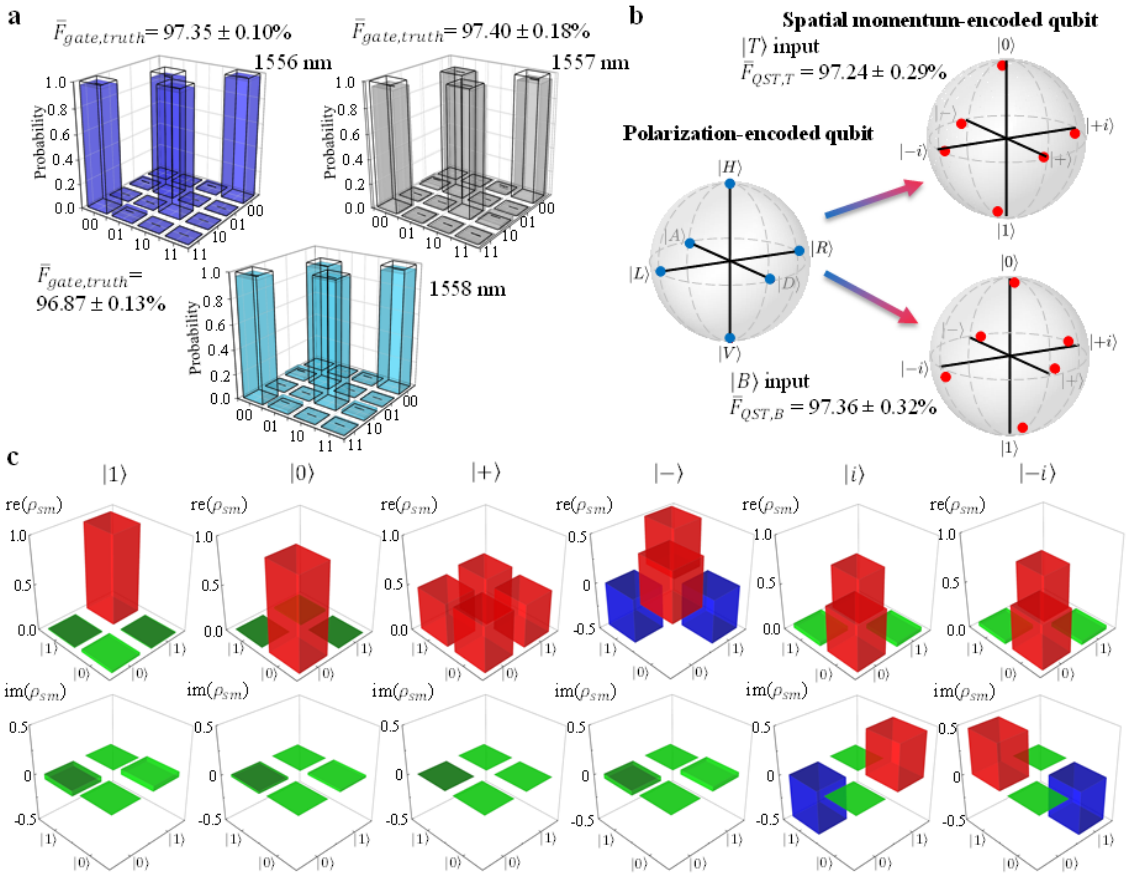

Fig. 5.3. Single-photon truth table measurement and quantum state tomography of the SWAP gate. a) Normalized coincidence counting rates of the projected output state for a given input state. The solid bars (transparent bars) represent the measured (ideal) truth table in the computational basis. A total of around 100,000 coincidence counts is recorded in 160 secs for each truth table measurement, yielding truth table fidelities of 97.35 (97.65) ± 0.10 % at 1556 nm, 97.40 (97.57) ± 0.18% at 1557 nm, and 96.87 (97.00) ± 0.13% at 1558 nm before (after) background subtraction. b) Left: Bloch-sphere representation of six polarization-encoded input states $|H\rangle$, $|V\rangle$, $|D\rangle$, $|A\rangle$, $|R\rangle$ and $|L\rangle$ prepared by bulk optics (blue dots). Right: Measured output spatial-momentum encoded states $|0\rangle$, $|1\rangle$, $|+\rangle$, $|-\rangle$, $|i\rangle$ and $|-i\rangle$ by Mach-Zehnder interferometer represented by red dots on the Bloch sphere for $|T\rangle$ (top right) and $|B\rangle$ (bottom right) spatial-momentum encoded input states. Indicated fidelity represents the average over the six measured states. c) Real (top) and imaginary (bottom) part of the reconstructed density matrix of measured spatial momentum-encoded states $|0\rangle$, $|1\rangle$, $|+\rangle$, $|-\rangle$, $|+i\rangle$ and $|-i\rangle$ for top channel input. The state fidelity between ideal ρ_{pol} and measured ρ_{sm} are calculated to be 97.21%, 97.56%, 96.72%, 97.30%, 97.46% and 97.21%, respectively.

First, we use free-space half-wave and quarter-wave plates to prepare the signal photon in an input set of six polarization states ρ_{pol} $(|H\rangle, |V\rangle, |D\rangle = (|H\rangle + |V\rangle)/\sqrt{2}, |A\rangle = (|H\rangle - |V\rangle)/\sqrt{2}, |R\rangle =$

$(|H\rangle + i|V\rangle)/\sqrt{2}, |L\rangle = (|H\rangle - i|V\rangle)/\sqrt{2})$, that are applied individually to the $|T\rangle$ or $|B\rangle$ inputs to the SWAP gate for QST. Measuring the corresponding output spatial-momentum states ρ_{sm} provides the QST for these polarization inputs. The six input polarizations are shown in Fig. 5.3b as Bloch vectors, and the reconstructed density matrices for each polarization and spatial-momentum state are provided in Appendix C. The output qubit after the SWAP operation is projected on a customized MZI with over 20 dB extinction ratio and two tunable DLs, with the measurement setup shown in Fig. 5.2a (II). The first tunable DL is placed before the MZI to tune the phase between output photons from the $|T\rangle$ and $|B\rangle$ spatial modes before they encounter each other in the MZI. The second tunable DL, which is in the MZI's upper arm, tunes the phase between the two arms. The six spatial-momentum states are then analyzed by the MZI to perform the QST, with coincidence counts collected from the two output ports of MZI. An example full density matrix results of the QST for the $|T\rangle$ spatial mode input is shown in Fig. 5.3c, which directly corresponds to the Bloch vectors in Fig. 5.3b. The state fidelity is defined as: $F = (Tr(\sqrt{\sqrt{\rho_{pol}}\rho_{sm}\sqrt{\rho_{pol}}}))^2$, which describes the overlap between the input polarization states and the measured output spatial-momentum states. From tomography with the top channel input, we achieved an averaged fidelity $\bar{F}_{QST,T}$ of 97.24 ± 0.29% for the overlap between the six polarization-encoded states and the output spatial-momentum states. QST results for the bottom channel input are given in Fig. 5.4; for its six polarization-encoded states, we obtained an average state fidelity $\bar{F}_{QST,B}$ of 97.36 ± 0.32%. These high fidelity spatial-momentum states, with an average fidelity of 97.30 ± 0.30%, confirm the successful SWAP operation from polarization qubits to spatial-momentum qubits.

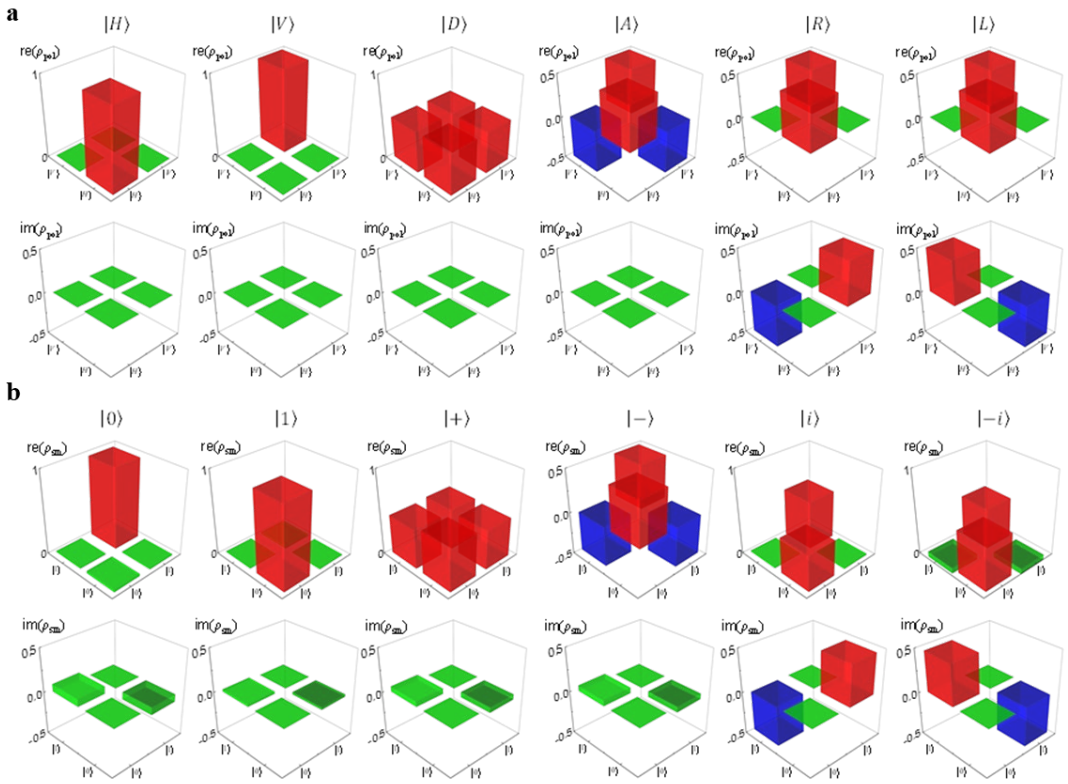

Fig. 5.4. Density matrix of ρ_{pol} ideal polarization-encoded states $|H\rangle, |V\rangle, |D\rangle, |A\rangle, |R\rangle, |L\rangle$, and density matrix ρ_{sm} of measured spatial-momentum encoded states $|0\rangle, |1\rangle, |+\rangle, |-\rangle, |+i\rangle, |-i\rangle$ for $|B\rangle$ input states. The state fidelities between ideal ρ_{pol} and measured ρ_{sm} are calculated to be 97.88%, 97.28%, 96.96%, 97.34%, 97.55% and 97.18% respectively.

5.5 Quantum process fidelity, phase coherence, and Bell violation of the two-qubit SWAP gate

Fig. 5.5 a and b show our QPT of our SWAP gate. This single-photon two-qubit SWAP gate operation process can be represented by a reconstructed process matrix χ, defined as $\rho_{sm} = \sum_{mn} \chi E_m \rho_{pol} E_n^{\dagger}$, where $E_{m(n)}$ are the identity I and Pauli matrices X, Y and Z respectively. The SWAP gate's process matrix can be obtained by inputting the polarization states to the SWAP gate via top and bottom input channels, and measuring the spatial-momentum encoded states from the outputs, as demonstrated in Fig. 5.5 a and b. The process fidelity is defined as $F_{\chi} = \frac{Tr(\chi\chi_i)}{Tr(\chi)Tr(\chi_i)}$, where χ_i is the ideal process matrix with unit (I, I) component. The X, Y and Z component of the matrix χ represent the probability of a

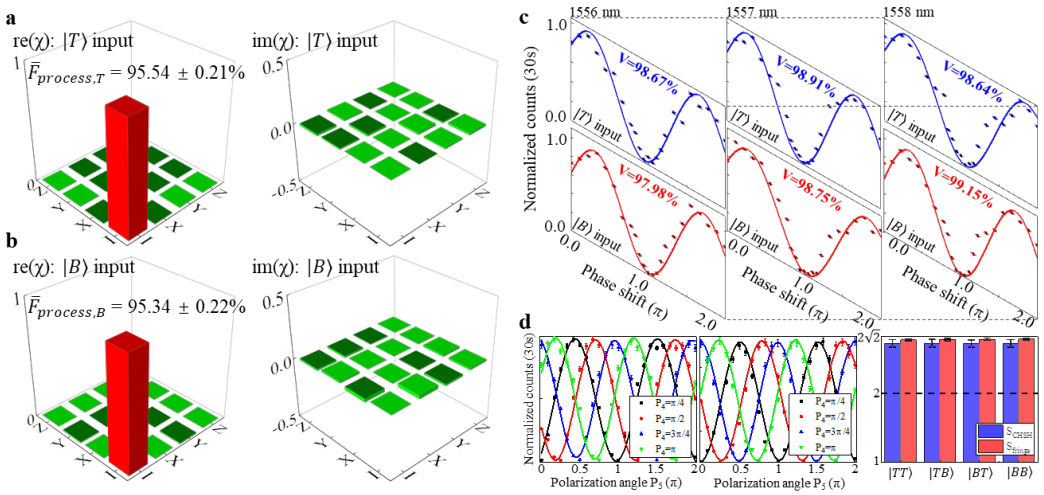

Fig. 5.5. Quantum process fidelity, phase coherence, and Bell violation of the single-photon two-qubit SWAP operation. a) Reconstructed process matrix χ of the SWAP gate for $|T\rangle$ spatial-momentum encoded input states with 95.54 ± 0.21% process fidelity, and b) for $|B\rangle$ spatial-momentum encoded input states with 95.34 ± 0.22 % process fidelity. c) Measured at 1556 nm, 1557 nm, and 1558 nm, the phase interference has fringe visibilities of 98.67 ± 0.17 % (99.40%), 98.91 ± 0.16 % (99.28%), and 98.64 ± 0.18 % (98.91%) respectively for $|T\rangle$ input state before (after) background subtraction. For the $|B\rangle$ input state, the fringe visibilities are 97.98 ± 0.21% (98.50%), 98.75 ± 0.17 % (99.03%), and 99.15 ± 0.14 % (99.42%), respectively, before (after) background subtraction. d) Verification of temporal-mode matching after the SWAP operation via polarization Bell's-inequality violation. The input polarization state is selected to maximize the post-SWAP signal photons at the detected channels. The temporal overlap of the post-SWAP signal photons with the idler-photon companions are optimized before their being combined on a 50:50 fiber BS. Polarizers P_4 and P_5 are placed after the fiber beam splitter for polarization projection measurement. Coincidence counts are collected by rotating P_5 for projection measurement of the top or bottom channel output photons, while P_4 was fixed at different analysis angles. Left panel: polarization interference for $|T\rangle$ input and $|T\rangle$ output, with averaged 97.86 ± 0.52% visibility after the SWAP operation. Middle panel: polarization interference for $|T\rangle$ input and $|B\rangle$ output, with averaged 98.12 ± 0.59% visibility. Right panel: Measured S_{CHSH} and S_{fringe} for four different input-output combinations. For $|T\rangle$ channel input, mean S_{CHSH} is calculated to be 2.720 ± 0.055. For $|B\rangle$ channel input, mean S_{CHSH} is calculated to be 2.718 ± 0.054. The averaged S_{CHSH} for the four input-output combinations is 2.719 ± 0.055, violating the CHSH inequality by 13.19 standard deviations. Error bars are given based on Poissonian statistics.

bit-flip or phase flip errors in the SWAP operation. We also evaluate the purity of the SWAP process matrix χ, defined as $P_\chi = \frac{Tr(\chi^2)}{Tr^2(\chi)}$, which is unity for an ideal process. Our two-qubit SWAP gate is found to achieve a quantum process fidelity $\bar{F}_{process,T}$ of 95.54 ± 0.21% with process purity of 91.59 ± 0.19% for $|T\rangle$ spatial-momentum input qubit. For the $|B\rangle$ spatial-momentum input qubit, we obtained $\bar{F}_{process,B}$ of 95.34 ± 0.22% with process purity of 91.60 ± 0.62%. The average process fidelity for $|T\rangle$ and $|B\rangle$ input states is 95.44 ± 0.21%. In addition, we note the sources of process fidelity non-ideality come from the bulk-optics imperfections in generating the input polarizations, the differential propagation loss and coupling efficiency mismatch between $|H\rangle$ and $|V\rangle$ states, and the residual misalignment of the spatial mode projection in the MZI.

Going beyond SWAP operation with $|H\rangle$ and $|V\rangle$ input states, we characterized its performance with input polarizations of the form $|H\rangle + e^{i\varphi}|V\rangle$. An ideal SWAP operation is a coherent phase-preserving process, and the output state of the signal photon can be written as $|T\rangle + e^{i(\varphi+\delta)}|B\rangle$, where the phase difference φ between the orthogonal polarizations is transferred to the spatial modes and a constant phase δ accounts for the path length difference between the $|T\rangle$ and $|B\rangle$ spatial-momentum modes at the output. The $|T\rangle$ and $|B\rangle$ SWAP outputs of the signal photon are combined with a 50:50 fiber BS, as shown in Fig. 5.2a (III), whose outputs are detected in coincidence with the heralding idler photon to yield a self-interference measurement of the signal photon as a function of φ. An adjustable path delay ΔT (not illustrated in the schematic) is included in the bottom channel of the SWAP output for balancing the lengths of the two interferometer arms.

In our measurements we start with a 45° linearly polarized qubit $|H\rangle + |V\rangle$, and the phase shift φ is introduced via a tuned pair of multi-order waveplates (illustrated in Fig. 5.2a (III)) with their optic axes aligned to the $|V\rangle$ polarization. They are mounted on two motorized rotation stages for simultaneous counter-rotation along their optic axes. A tunable phase delay φ is imposed between $|H\rangle$ and $|V\rangle$ at the input by applying a rotation θ to one waveplate, while the transverse displacement of the beam is canceled with the counter rotation with the same angle magnitude for the other waveplate. The SWAP gate chip and the interference paths are carefully isolated from environmental noise for the phase-sensitive measurements. By sweeping the relative phase φ between the $|H\rangle$ and $|V\rangle$ polarizations of the input state of the signal photon, we probe the phase coherence of our SWAP gate operation by self-interference between the SWAP output's $|T\rangle$ and $|B\rangle$ spatial-momentum states.

Fig. 5.5c shows the self-interference fringes of the two spatial-momentum modes of the signal photon after the SWAP operation, at 1556 nm, as measured in coincidence with the heralding idler photon.

For the $|T\rangle$ spatial-momentum input state, a raw fringe visibility of 98.67 ± 0.17% is obtained (99.40% after background subtraction). This interference can also be observed when the polarization qubit is input through the bottom channel, with a raw visibility of 97.98 ± 0.21% (98.50% after background subtraction). The phase coherent polarization-spatial-momentum two-qubit SWAP operation is also verified at the wavelength of 1557 nm and 1558 nm with high visibility fringes as shown in Fig. 5.5c, obtaining a wavelength-averaged 98.68% ± 0.17% interference visibility between the $|T\rangle$ and $|B\rangle$ spatial-momentum SWAP output states. These observed high visibility fringes demonstrate successful coherence transfer from the input's polarization qubit to the output's spatial-momentum qubit. As noted earlier, the residual sources of decoherence include the MC-NOT's imperfect qubit rotation, its spatial-mode contamination, and its unbalanced photon losses as detailed in Appendix C.4. Moreover, we note that the phase interference is long-term robust and can maintain high visibility up to 96.56% over 24 hours in free-running operation without feedback stabilization (see Fig. 5.6), enabling the practical implementation of the phase-preserving single-photon two-qubit SWAP gate.

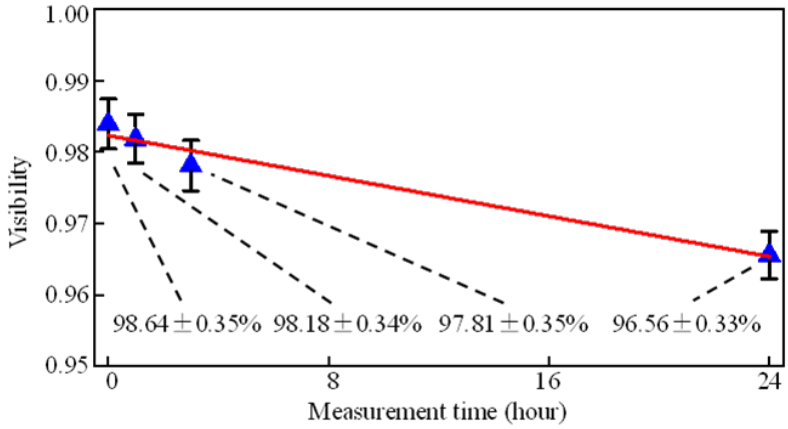

Fig. 5.6. Long-term stability of phase coherence measurement with arbitrary input-polarization qubit at 1558 nm. The data points are fringe visibilities without background subtraction. The red solid line is the numerical fit. Error bars are given by one standard deviation assuming Poissonian statistics.

In order to examine the temporal-mode matching between the idler (heralding) and post-SWAP signal photons, we performed polarization-interference measurements (experimental setup detailed in Fig. 5.7a) between them. The input polarization state of the signal photon is selected to maximize the SWAP gate's output flux; for example, for the $|T_{in}\rangle|B_{out}\rangle$ input-output combination, we choose horizontal polarization for the top channel input ($|TH\rangle$) so that the output swapped state is $|BV\rangle$. The idler photon and the post-SWAP signal photon are combined using a 50:50 fiber BS after the idler photon's polarization has been adjusted by a fiber polarization controller so that it is orthogonal to the

signal photon's polarization at the fiber beam-splitter's input. This polarization orthogonality ensures that the BS's post-selected output is polarization entangled and the quality of that entanglement can be quantified by quantum interference measurements. The path difference between the signal and idler photons is compensated by a fiber tunable DL to optimize their quantum interference fringes. Two polarizers P_4 and P_5 are placed after the fiber BS for free-space polarization projection measurement. Coincidence counts are collected by rotating P_5 for projection measurement of the top or bottom channel output photons, while the polarization angle of P_4 was fixed at 45°, 90°, 135° and 180° respectively. Fig. 5.5d shows the interference fringes for two of the four different input-output combinations ($|T_{in}\rangle|T_{out}\rangle$, $|T_{in}\rangle|B_{out}\rangle$, $|B_{in}\rangle|T_{out}\rangle$ and $|B_{in}\rangle|T_{out}\rangle$). For the $|T\rangle$ spatial-momentum input state, the left panel of Fig. 5.5d shows the measured fringe visibility of 97.86 ± 0.52% for the top channel output, and the middle panel shows the measured fringe visibility of 98.12 ± 0.59% for the bottom channel output (details of the $|B\rangle$ spatial-momentum input states are in Fig. 5.7b). Both measured visibilities are well above the quantum threshold $1/\sqrt{2}$ required to violate the Bell's inequality.

In each case, we calculate the S_{CHSH} parameter from the measured correlation coefficients (see Appendix C.5) and estimate the maximal achievable S_{fringe} parameter by mean fringe visibilities. The right panel of Fig. 5.5d shows the obtained S_{CHSH} and S_{fringe} values for the four different input-output combinations. For the $|T\rangle$ and $|B\rangle$ spatial-momentum input states respectively, we observed an average S_{CHSH} at 2.720 ± 0.055 and 2.718 ± 0.054, which violate the CHSH inequality by 13.09 and 13.30 standard deviations. This CHSH inequality violation supports the temporal mode preservation after the SWAP chip operation. Overall, we obtain a mean S_{CHSH} for $|T\rangle$ and $|B\rangle$ spatial-momentum input states of 2.719 ± 0.055, violating the CHSH inequality by 13.19 standard deviations. In our SWAP gate, the mean $S_{fringe} = 2\sqrt{2} \times V$, the upper bound of S_{CHSH} and achieved only when the polarization analyzers are aligned with the tested quantum states along with consistent detection efficiencies, is found to be 2.772 ± 0.016 for the $|T\rangle$ channel and 2.780 ± 0.015 for the $|B\rangle$ channel. The misalignment of the polarization analyzers and fluctuation of the fiber-to-chip coupling leads to a small deviation between the measured S_{CHSH} and S_{fringe}. The spatial-mode overlap between the post-SWAP signal photons and the heralding idler photons are ensured by the taper coupler on the silicon chip and collecting to a single mode fiber, while the temporal-mode overlap is matched at the 50:50 fiber BS by tuning a fiber tunable DL. These high-visibility polarization-interference fringes demonstrate that the photons can be coherently preserved and efficiently overlapped with their counterparts after the SWAP operation.

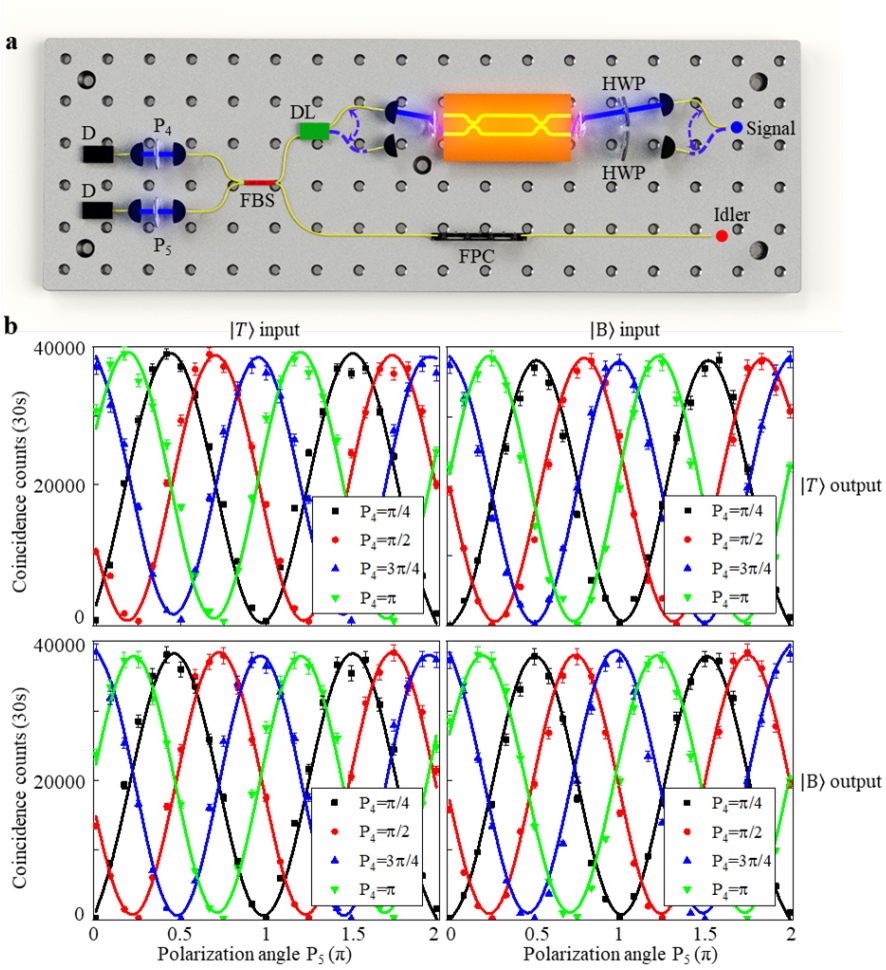

Fig. 5.7. Polarization interference measurement after two-qubit SWAP operation for different input channels. a) Experimental schematic of polarization interference measurement after SWAP gate operation between signal and idler photons. HWP: half-wave plate. b) Polarization interference measurements from the top-channel input showing an average visibility of 97.99% ± 0.55% after the SWAP operation. Polarization interference measurements from the bottom-channel input showing an average visibility of 98.28% ± 0.52% after the SWAP operation.

5.6 Summary

In this work, we have demonstrated the two-qubit four-dimensional Hilbert space of two spatial modes and two polarization modes, we have shown an averaged truth table fidelity of 97.21 ± 0.14% (98.53% after background subtraction) from an on-chip SWAP gate. QST of the single-photon swapped spatial-momentum qubit is also verified, with an average 97.30 ± 0.30% fidelity. The quantum process of the

SWAP operation is further quantified by QPT, with 95.44 ± 0.21% fidelity. Furthermore, the relative phase between the orthogonal polarizations from the input qubit can be coherently transferred to the spatial-momentum qubit after the SWAP operation. This phase coherent process is examined by heralded single-photon self-interference between the $|T\rangle$ and $|B\rangle$ spatial-momentum output states, with mean visibility up to 98.68 ± 0.17%. After the SWAP operation, the converted qubits can be efficiently overlapped with the correlated idler photons after the SWAP operation, resulting in an average CHSH *S*-parameter up to 2.719 ± 0.055 and a Bell's inequality violation up to 13.19 standard deviations via polarization interference measurement. We present a successful demonstration on a two-level triple-stage quantum photonic circuit integration in the linear silicon photonic chip. With the silicon chip-scale platform, high-density photonic integration involving different DoFs might be possible for future applications, extending to high-dimensional quantum gate operation [259], with intrinsic good phase stability and compactness. By optimizing the fabrication parameters and chip coupling, near-unity fidelity of the polarization operation can be examined. Furthermore, the single-photon two-qubit SWAP operation might be extended to qubits encoded in other DoFs, such as orbital angular momentum or time-bins, and perhaps even developed for high-dimensional hyperentangled single-photon qudits [121, 260], without requiring ancilla photons, for deterministic chip-scale QIP and LOQC.

Appendix A

Modeling and measurements of signal-idler cross-correlation, Hong-Ou-Mandel, Franson and conjugate-Franson interferometry for singly- and doubly-resonant biphoton frequency combs

A.1 Theory of mode-locked temporal signal-idler cross-correlation function

In this section we derive and evaluate the signal-idler cross-correlation function for the singly-resonant biphoton frequency comb (BFC). Before doing so, however, we will replace the approximate result for that BFC's frequency-domain (unnormalized) biphoton wave function,

$$\psi(\Omega) = \sum_{m=-N}^{N} \frac{\mathrm{sinc}(A\Omega)}{\Delta\omega + i(\Omega - m\Delta\Omega)} \tag{A.1}$$

and the exact result is,

$$\psi(\Omega) = \frac{\mathrm{sinc}(\Omega t_{\mathrm{coh}}/2) e^{-4\Omega^2 \ln(2)/\Delta\omega_c^2} e^{-i\Omega t_{\mathrm{coh}}/2}}{1 + i\frac{\Delta\Omega}{\pi\Delta\omega} \sin(\pi\Omega/\Delta\Omega) e^{-i\pi\Omega/\Delta\Omega}} \tag{A.2}$$

where $t_{\mathrm{coh}} = 2A = 2.78/\pi B_{\mathrm{PM}} = 3.61$ ps is the coherence time associated with the $B_{\mathrm{PM}} = 245$ GHz full-width half-maximum (FWHM) phase-matching bandwidth, $\Delta\Omega = 45.32$ GHz is the fiber Fabry-Pérot cavity's (FFPC's) free spectral range (FSR), $\Delta\omega/\pi = 1.56$ GHz is the fiber FP cavity's FWHM linewidth, and $\Delta\omega_c/\pi = 225$ GHz is the FWHM bandwidth of the 1.3 nm bandpass filter (BPF) used to clean the signal and idler spectra produced by spontaneous parametric down-conversion (SPDC) in our periodically-poled $KTiOPO_4$ (ppKTP) waveguide.

Armed with the singly-resonant BFC's biphoton exact wave function from equation (A.2), we are now ready to evaluate its coincidence-counting (second-order) signal-idler cross-correlation function. The frequency-domain biphoton wave function produced by continuous-wave (cw) SPDC, after filtering by the BPF and fiber FP cavity, is proportional to the phase-sensitive cross-spectrum of the post-filtering signal and idler's photon-units baseband field operators in the exact, Gaussian-state theory of cw SPDC,

$$\psi(\Omega) \propto S_{SI}^{(p)}(\Omega) \equiv \int d\tau \left\langle \hat{E}_S(t+\tau)\, \hat{E}_I(t) \right\rangle e^{-i\Omega\tau} \tag{A.3}$$

where angle brackets denote quantum average. In the absence of detector timing jitter, it then follows that the cross-correlation function we are seeking satisfies

$$R_{SI}(\tau) \propto \int_0^{T_g} dt\, |\Psi(t+\tau)|^2 \tag{A.4}$$

where $\Psi(t)$ is the singly-resonant BFC's (unnormalized) time-domain biphoton wave function, i.e., the inverse Fourier transform of $\psi(\Omega)$, and T_g is the duration of the coincidence gate. Because our detectors do have timing jitter, the observed cross correlation becomes

$$R_{SI}^{\text{obs}}(\tau) = \int d\mu \, R_{SI}(\mu) \frac{\exp[-(\tau-\mu)^2/2t_j^2]}{\sqrt{2\pi t_j^2}} \tag{A.5}$$

where we have assumed a zero-mean, variance t_j^2, Gaussian-distributed combined timing jitter from the two detectors.

From equation (A.2) and (A.4) it can be shown that $R_{SI}(\tau)$ has recurring peaks at $\tau = t_{\text{coh}}/2 + n\Delta T$ for n = 0, 1, 2, …, where $\Delta T = 2\pi/\Delta\Omega = 22.1$ ps is the cavity round-trip time, but going forward we will suppress their $t_{\text{coh}}/2$ offset from $n\Delta T$. These peaks are increasingly blurred by detector timing jitter as t_j increases, and can easily be washed out. To quantify this behavior, we used the results presented above to numerically evaluate

$$\tilde{R}_{SI}(\tau) \equiv \frac{R_{SI}^{obs}(\tau-\tau_{\text{max}})}{R_{SI}^{obs}(\tau_{\text{max}})} \tag{A.6}$$

where τ_{max} is the time at which $R_{SI}^{obs}(\tau)$ takes on its maximum value. This form of the correlation function achieves its peak value, $\max_\tau \tilde{R}_{SI}(\tau) = 1$, at $\tau = 0$, regardless of root-mean-square timing jitter t_j, thus making it well suited to displaying the impact of timing jitter on the observed signal and idler's coincidence-counting cross correlation, as seen in the main text's Fig. 3.7b.

In Appendix Fig. A1, we have plotted three examples of $\tilde{R}_{SI}(\tau)$ versus τ in ns for the source parameters of our 45.32 GHz singly-resonant BFC: $t_j = 0.78$ ps (blue curve), $t_j = 7.8$ ps (red curve), and $t_j = 74$ ps (black curve). In the main text's Fig. 3.7a, we have shown good agreement between our experiment and the theoretical result when $t_j = 74$ ps. Although the temporal oscillation signature of the singly-resonant BFC is completely blurred out by the timing jitter in our measurements, our modeling clearly shows that as $t_j/\Delta T$ decreases the comb structure can be resolved. For example, when $t_j = 7.8$ ps, the singly-resonant BFC's structure produced by our 45.32 GHz FSR, 1.56 GHz FWHM bandwidth FFPC can be seen in $\tilde{R}_{SI}(\tau)$. Moreover, with $t_j = 0.78$ ps, near-perfect cavity resonances appear in $\tilde{R}_{SI}(\tau)$, and we note that such low-jitter SNSPDs have been demonstrated recently [51]. In Appendix Fig. A2, we plot the three cases for doubly-resonant BFC with 45.32 GHz FSR. Different from singly-resonant BFC, doubly-resonant BFC have symmetric temporal waveforms. Similar, because of the broadening from the finite temporal resolution of SNSPDs, the low-jitter

SNSPDs are necessary for resolving the temporal oscillations completely.

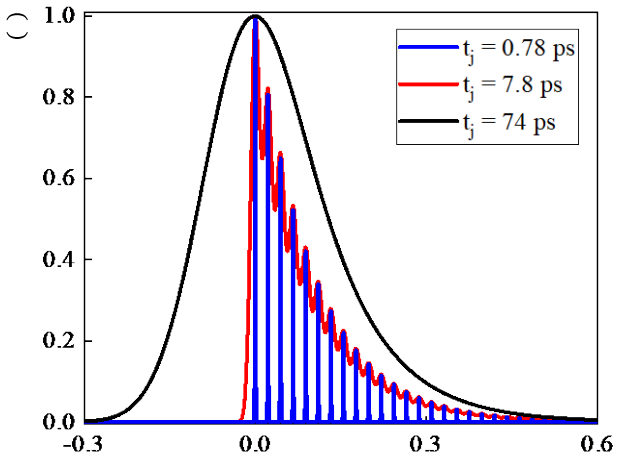

Appendix Fig. A1. Effect of timing jitter on the normalized coincidence-counting (second-order) signal-idler cross-correlation function $\widetilde{R}_{SI}(\tau)$ of singly-resonant BFC. For the source parameters of our 45.32 GHz singly-resonant BFC. The three cases shown are: $t_j = 0.78$ ps (blue curve), $t_j = 7.8$ ps (red curve), and $t_j = 74$ ps (black curve).

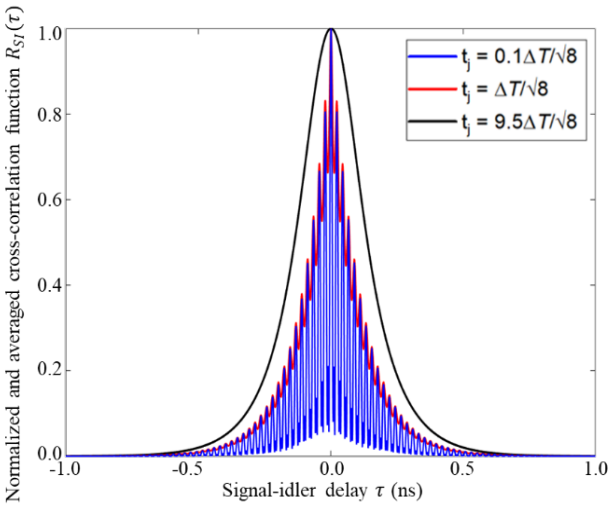

Appendix Fig. A2. Effect of timing jitter on the normalized coincidence-counting (second-order) signal-idler cross-correlation function $\widetilde{R}_{SI}(\tau)$ of doubly-resonant BFC. For the source parameters of our 45.32 GHz doubly-resonant BFC. The three cases shown are: $t_j = 0.78$ ps (blue curve), $t_j = 7.8$ ps (red curve), and $t_j = 74$ ps (black curve).

A.2 Theory and measurements of Hong-Ou-Mandel revival interferences

Here, we discuss the theory of Hong-Ou-Mandel (HOM) revival interferences produced by doubly-resonant BFCs. Quantum interference occurs in our HOM interferometer's 50:50 fiber coupler. For an ideal 50:50 fiber coupler, the field operators at detectors D_1 and D_2 are

$$\hat{E}_1(t) = \frac{1}{\sqrt{2}}\left[\hat{E}_S(t) + \hat{E}_I(t+\delta T)\right],\ \hat{E}_2(t) = \frac{1}{\sqrt{2}}\left[\hat{E}_S(t) - \hat{E}_I(t+\delta T)\right] \tag{A.7}$$

where the signal (S) and idler (I) field operators entering the coupler are given by

$$\hat{E}_K(t) = \frac{1}{\sqrt{2\pi}}\int d\omega\, \hat{a}_K(\omega)e^{-i\omega t} \tag{A.8}$$

and δT is the HOM interferometer's relative arrival-time delay. We can write the biphoton coincidence rate as

$$R_{12} \propto \int d\tau G_{12}^{(2)}(t, t+\tau) \tag{A.9}$$

where the second-order correlation function is given by

$$G_{12}^{(2)}(t, t+\tau) = \left|\langle 0|\hat{E}_1(t)\hat{E}_2(t+\tau)|\psi\rangle\right|^2 \tag{A.10}$$

with $|\psi\rangle$ being the BFC state. For the following calculations, we assume ideal cw pumping. Then, substituting equation (A.7) and (A.8) into equation (A.10), we obtain

$$G_{12}^{(2)}(t, t+\tau) \propto |\psi(\tau+\delta T) - \psi(-\tau+\delta T)|^2 \tag{A.11}$$

where $\psi(t) \equiv \int \Phi(\Omega)\ e^{i\Omega t}d\Omega$ is the BFC state's (unnormalized) joint temporal amplitude (JTA), and $\Phi(\Omega)$ is its (unnormalized) joint spectral amplitude (JSA). By evaluating equation (A.9), we obtain the coincidence rate

$$R_{12} \propto 1 - \frac{\mathrm{Re}\left[\int \Phi^*(-\Omega)\Phi(\Omega)e^{2i\Omega\delta T}d\Omega\right]}{\int|\Phi(\Omega)|^2 d\Omega} \tag{A.12}$$

For our BFC source, $\Phi(\Omega)$ has the following form

$$\Phi(\Omega) = \textstyle\sum_m f'(\Omega)h(\Omega)f(\Omega - m\Delta\Omega) \tag{A.13}$$

where $f'(\Omega) = \mathrm{sinc}(A\Omega)$ is the phase-matching function, with FWHM bandwidth $B_{PM} = 2.78/2\pi A$. FBG's rectangular filter function is $h(\Omega) = \mathrm{rect}(\Omega/B)$, with B being its bandwidth. To compare theory with the measured 45.32 GHz FSR cavity HOM interference recurrences, we use the following parameter values: $A = 181$ ps, $B/2\pi = 346$ GHz, $\Delta\Omega/2\pi = 45.32$ GHz, and $\Delta\omega/\pi = 1.563$ GHz. In what follows, we will neglect the frequency-bin overlaps in $\Phi(\Omega)$, because $\Delta\Omega \gg \Delta\omega$, and so we obtain the following result for the BFC's (unnormalized) joint spectral intensity (JSI),

$$|\Phi(\Omega)|^2 = \textstyle\sum_{m=-N_0}^{N_0} \frac{\mathrm{sinc}^2(A\Omega)}{[(\Delta\omega)^2 + (\Omega - m\Delta\Omega)^2]^2} \tag{A.14}$$

where $N_0 = [B/2\Delta\Omega]$ is the integer part of $B/2\Delta\Omega$. Furthermore, because $B > B_{PM} \gg \Delta\omega$, we can reduce equation (A.14) to

$$|\Phi(\Omega)|^2 \cong \sum_{m=-N_0}^{N_0} \frac{\mathrm{sinc}^2(Am\Delta\Omega)}{[(\Delta\omega)^2+(\Omega-m\Delta\Omega)^2]^2} \tag{A.15}$$

From this result we then find that

$$\int |\Phi(\Omega)|^2 d\Omega = \frac{\pi}{2(\Delta\omega)^3} \sum_{m=-N_0}^{N_0} \mathrm{sinc}^2(Am\Delta\Omega) \tag{A.16}$$

and

$$\int \Phi^*(-\Omega)\Phi(\Omega) e^{2i\Omega\delta T} d\Omega =$$

$$\frac{\pi e^{-2\Delta\omega|\delta T|}(1+2\Delta\omega|\delta T|)}{2(\Delta\omega)^3} \left[\sum_{m=-N_0}^{N_0} \mathrm{sinc}^2(Am\Delta\Omega)\cos(2m\Delta\Omega\delta T)\right] \tag{A.17}$$

Combining equation (A.12) and (A.17), we get our final theoretical result for the BFC HOM interference recurrences,

$$R_{12} \propto 1 - \frac{e^{-2\Delta\omega|\delta T|}(1+2\Delta\omega|\delta T|)}{\sum_{m=-N_0}^{N_0} \mathrm{sinc}^2(Am\Delta\Omega)} \left[\sum_{m=-N_0}^{N_0} \mathrm{sinc}^2(Am\Delta\Omega)\cos(2m\Delta\Omega\delta T)\right] \tag{A.18}$$

The normalized theoretical coincidence rate for the doubly-resonant BFC generated using our 45.32 GHz cavity is plotted for -340 ps $\leq \delta T \leq$ 340 ps in Appendix Fig. A3. Here we see interference recurrences with an $\approx$ 11.02 ps period, which matches well with the 11.03 ps period found in our measurements. The linewidth of each HOM-interference recurrence and its visibility fall-off for time bins farther away from zero relative delay also match with our measurements.

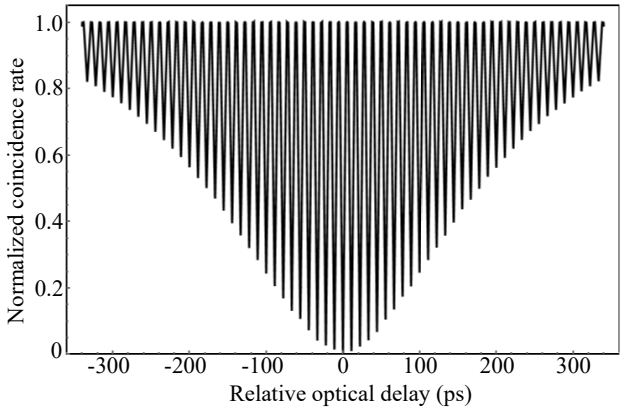

Appendix Fig. A3. Modeling of the Hong-Ou-Mandel interference recurrences for the 45 GHz doubly-resonant BFC. The normalized theoretical coincidence rate as a function of relative optical delay between the signal and idler photons. There are 61 interference recurrences for the whole optical-delay scanning range. The visibility decay away from zero relative delay arises from the Lorentzian lineshape of cw-pumped SPDC photons filtered by a fiber FP cavity. Appendix Fig. A3 published in [92].

We also calculated the HOM-interference recurrences for the 5.03 GHz FSR doubly-resonant

BFC using the following parameter values: $A = 1.81$ ps, $B/2\pi = 346$ GHz, $\Delta\Omega/2\pi = 5.03$ GHz, and $\Delta\omega/\pi = 0.457$ GHz. The result, plotted in Appendix Fig. A4, is consistent with the experimental data shown in Appendix Fig. A5. We see that there are fewer interference fringes compared to those in Appendix Fig. A3, which is a consequence of the 5.03 GHz cavity's smaller FSR, and the ≈ 99.6 ps recurrence period matches well with the 99.4 ps period seen in our measurements.

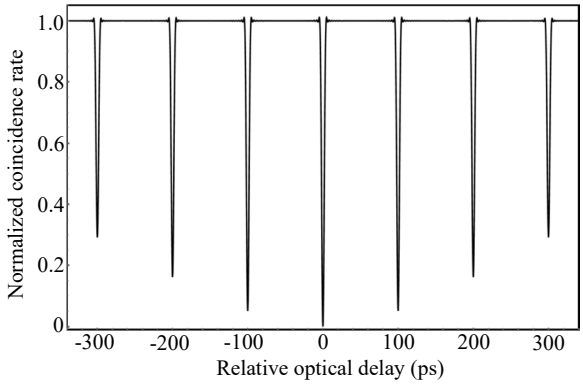

Appendix Fig. A4. Modeling of the Hong-Ou-Mandel interference recurrences for the 5 GHz doubly-resonant BFC. The normalized theoretical coincidence rate as a function of relative optical delay. There are 7 interference recurrences for the whole optical-delay scanning range, which agrees well with the experimental results shown in Appendix Fig. A5. Appendix Fig. A5 published in [92].

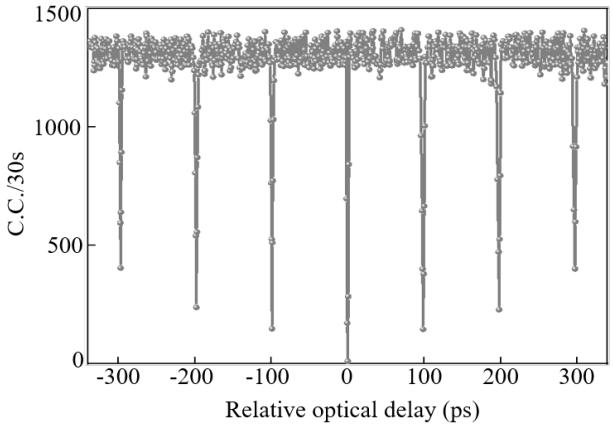

Appendix Fig. A5. Experimental Hong-Ou-Mandel interference recurrences for the 5 GHz doubly-resonant BFC. Coincidence counts versus relative optical delay between the two arms of the HOM interferometer. A total of 7 HOM-interference recurrences are observed. Appendix Fig. A5 published in [92].

The visibilities of the HOM-interference recurrences drop less rapidly in Appendix Fig. A4 compared to what is seen in Appendix Fig. A3 – despite 5.03 GHz cavity's lower finesse of ≈ 10 – because of the limited scan range of the relative optical delay for observing the recurrence visibilities'

fall-off.

A.3 Theory and measurements of Franson revival interferences

Following the discussion of HOM interference of doubly-resonant BFCs, here, we present the theory of Franson interference of such high-dimensional source. In Franson interferometry's two unbalanced MZIs, the field operators at their respective detectors, D_1 and D_2, are

$$\hat{E}_1(t) = \frac{1}{\sqrt{2}}\left[\hat{E}_S(t) + \hat{E}_S(t - \Delta T_1)\right],\ \widehat{E}_2(t) = \frac{1}{\sqrt{2}}\left[\hat{E}_I(t) - \hat{E}_I(t - \Delta T_2)\right] \tag{A.19}$$

where the signal (S) and idler (I) field operators entering the Franson interferometer, $\hat{E}_K(t)$ for $K = S, I$, are given by

$$\hat{E}_K(t) = \frac{1}{\sqrt{2\pi}}\int d\omega\ \hat{a}_K(\omega)e^{-i\omega t} \tag{A.20}$$

Here, ΔT_1 and ΔT_2 – the delay differences between each MZI's long and short paths – are sufficient to ensure that there is no long-short second-order interference. We can write the biphoton coincidence rate as

$$R_{12} \propto \int d\tau G_{12}^{(2)}(t, t + \tau) \tag{A.21}$$

where

$$G_{12}^{(2)}(t, t + \tau) = \left|\langle 0|\hat{E}_1(t)\hat{E}_2(t + \tau)|\psi\rangle\right|^2 \tag{A.22}$$

with $|\psi\rangle$ being the BFC state. For the following calculations, we assume ideal cw pumping. Then, we get

$$G_{12}^{(2)}(t, t + \tau) = \left|\psi(\tau) + \psi(\tau - \delta T)e^{\frac{-i\omega_p(\Delta T_1 + \Delta T_2)}{2}}\right|^2 \tag{A.23}$$

where, as before, $\psi(t) = \int \Phi(\Omega)\ e^{i\Omega t}d\Omega$ is the BFC's JTA, $\Phi(\Omega)$ is its JSA, and

$$\delta T = \Delta T_1 - \Delta T_2 \tag{A.24}$$

By evaluating equation (A.23), we obtain the coincidence rate

$$R_{12} \propto 1 + |\Gamma(\delta T)|\cos(\frac{\omega_p \delta T}{2} + \omega_p \Delta T_2 + \varphi) \tag{A.25}$$

where $\Gamma(\delta T) = \int|\Phi(\Omega)|^2 e^{i\Omega\delta T} / \int|\Phi(\Omega)|^2 d\Omega$, and

$$\Gamma(\delta T) = |\Gamma(\delta T)|e^{i\varphi} \tag{A.26}$$

For our BFC source, $\Phi(\Omega)$ is given by equation (A.16), thus we obtain

$$\int|\Phi(\Omega)|^2 e^{i\Omega\delta T}d\Omega =$$

$$\frac{\pi e^{-\Delta\omega|\delta T|}(1+\Delta\omega|\delta T|)}{2(\Delta\omega)^3}\left[2\sum_{m=1}^{N_0}\mathrm{sinc}^2(Am\Delta\Omega)\cos(m\Delta\Omega\delta T)+1\right] \quad \text{(A.27)}$$

Combining equation (A.25) and (A.27), we get our final theoretical result for the doubly-resonant BFC's Franson interference recurrences as

$$R_{12} \propto 1+\frac{e^{-\Delta\omega|\Delta T|}(1+2\Delta\omega|\delta T|)}{\sum_{m=-N_0}^{N_0}\mathrm{sinc}^2(Am\Delta\Omega)}\left[2\sum_{m=1}^{N_0}\mathrm{sinc}^2(Am\Delta\Omega)\cos(m\Delta\Omega\delta T)+1\right] \times\cos\left[\omega_p\left(\frac{\delta T}{2}+\Delta T_2\right)\right] \quad \text{(A.28)}$$

We can model our experimental results with the theoretical parameters above and the experiment's ΔT_2 = 4.84 ns. The Franson interference visibility for the doubly-resonant BFC generated using our 45.32 GHz FSR cavity is plotted for -340 ps ≤ $\delta T \leq$ 340 ps in Appendix Fig. A6. Here we see an interference-recurrence pattern with an ≈ 22.1 ps period, which matches well with the 22.09 ps period found in our measurements. The width of each Franson recurrence and the fall-off in visibility for time bins increasingly far from zero delay also match with the experimental observations.

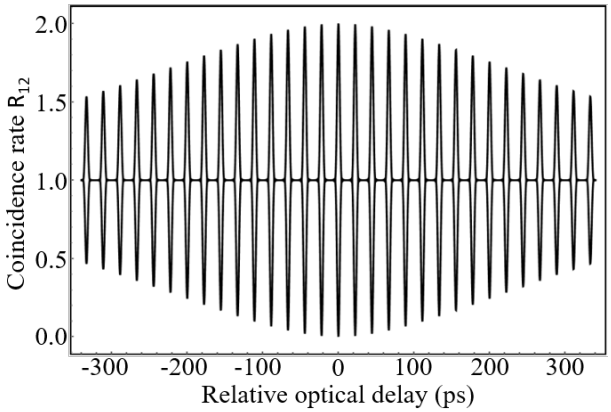

Appendix Fig. A6. Modeling of the Franson interference recurrences for the 45 GHz FSR doubly-resonant BFC. Theoretical fringe envelope of Franson interference for the BFC generated using the 45.32 GHz FSR fiber cavity. There are 31 recurrences for the whole optical-delay scanning range in which we have measured 16 time-bins, limited by our optical delay tuning range. The fall-off in the coincidence rate away from zero delay arises from the Lorentzian lineshape of the SPDC-generated photons after they have passed through the fiber cavity. Appendix Fig. A6 published in [92].

In Appendix Fig. A7 we present Franson interference fringes at relative delays ΔT_2 equal to 0, 3, 5, 7, 9, 11, 13, and 15 cavity round-trip times for the 45.32 GHz FSR doubly-resonant BFC.

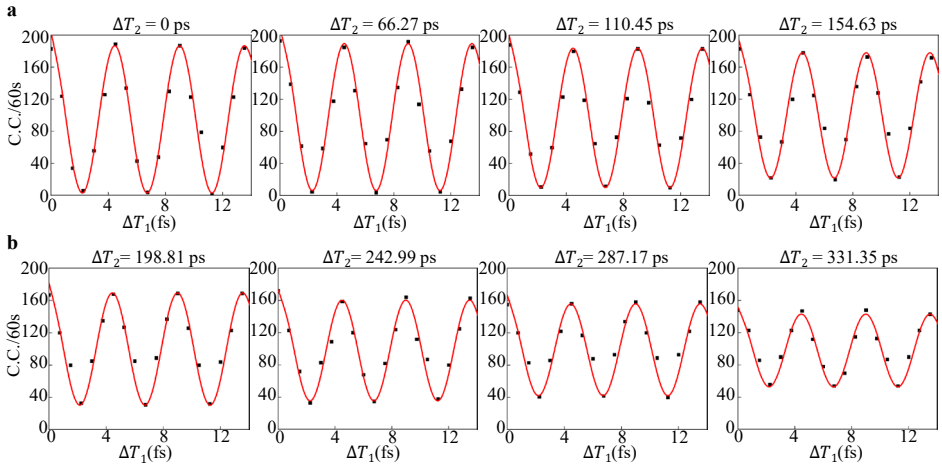

Appendix Fig. A7. Franson interference fringes for the 45 GHz FSR doubly-resonant BFC. a) and b) Measured Franson interference fringes as a function of ΔT_1, when ΔT_2 is set to 0, 3, 5, 7, 9, 11, 13, and 15 cavity round-trip times. The fringe visibilities obtained from these data are compared to theory in Appendix Table A1 and shown in the Sec. 3.3. Appendix Fig. A7 published in [92].

Appendix Table A1. Franson visibilities of the 45 GHz FSR doubly-resonant BFC for different optical delays. Appendix Table A1 published in [92].

Cavity round-trip time	Visibility V_{th} (theoretical)	Visibility V_{exp} (experimental)
0	100.0%	99.1%
3	95.9%	94.4%
5	90.2%	88.3%
7	83.2%	80.1%
9	75.6%	73.1%
11	68.0%	65.0%
13	60.5%	56.7%
15	53.4%	48.7%

Then, we present the theory for the singly-resonant BFC's Franson-interference recurrences. With accidentals subtracted – with its dispersive terms suppressed – lead to the following expression for the normalized (time-average value = 1) envelope of the (accidentals subtracted) Franson-interference recurrences as a function of the idler-signal (arm 1 – arm 2 in the main text Fig. 3.8) relative delay, $\delta\tau$:

$$C_{\pm}(\delta\tau) = 1 \pm \frac{2\int_0^{Tg} d\tau\, \mathrm{Re}[K_{SI}^{(p)}(\tau)K_{SI}^{(p)*}(\tau+\delta\tau)]}{\int_0^{Tg} d\tau\left[\left|K_{SI}^{(p)}(\tau)\right|^2+\left|K_{SI}^{(p)}(\tau+\delta\tau)\right|^2\right]} \quad \text{(A.29)}$$

Here, T_g is the duration of the coincidence gate, and $K_{SI}^{(p)}(\tau)$ is the phase-sensitive cross correlation of the singly-resonant BFC's photon-units, baseband field operators,

$$K_{SI}^{(p)}(\tau) \equiv \left\langle \hat{E}_S(t+\tau)\hat{E}_I(t) \right\rangle = \int \frac{d\Omega}{2\pi} S_{SI}^{(p)}(\Omega) e^{i\Omega\tau} \tag{A.30}$$

Using that result in numerically evaluating equation (A.29) then yields the desired envelope function for the (accidentals subtracted) Franson-interference recurrences. Using the source parameters for our 45.32 GHz singly-resonant BFC and $T_g = 2$ ns, we obtained the results shown in main text Fig. 3.9b for -340 ps $\leq \delta\tau \leq$ 340 ps. As shown in main text Fig. 3.9, our measured (accidentals subtracted) visibility peaks for $0 \leq \delta\tau \leq$ 340 ps are in excellent agreement with our theoretical predictions; with our equipment setup we could not access negative $\delta\tau$ values.

A.4 Theory of conjugate-Franson revival interferences

This section will introduce an entangled mixed state whose HOM-interference recurrences, frequency-bin correlations, and Franson interference recurrences are identical to those of the pure-state doubly-resonant BFC. This mixed state, however, can be distinguished from the pure-state BFC via conjugate-Franson interferometry. First, we discuss the pure-state versus mixed-state in filtered-SPDC measurements. Our pure-state BFC, in normalized form, is

$$|\psi_{\mathrm{BFC}}\rangle \;=\; \int \Phi_{\mathrm{BFC}}(\Omega)\hat{a}_H^\dagger\left(\frac{\omega_p}{2}+\Omega\right)\hat{a}_V^\dagger\left(\frac{\omega_p}{2}-\Omega\right)|0\rangle\, d\Omega \tag{A.31}$$

where

$$\Phi_{\mathrm{BFC}}(\Omega) \;\propto\; \sum_{m=-N_0}^{N_0} \frac{\mathrm{sinc}(Am\Delta\Omega)}{(\Delta\omega)^2+(\Omega-m\Delta\Omega)^2} \tag{A.32}$$

with $\int |\Phi_{\mathrm{BFC}}(\Omega)|^2\, d\Omega = 1$. This state's JSI is therefore

$$\mathrm{JSI}_{\mathrm{BFC}}(\Omega) = |\Phi_{\mathrm{BFC}}(\Omega)|^2 \;= \sqrt{\frac{2\Delta\omega^3}{\pi}} \frac{\sum_{m=-N_0}^{N_0} \frac{\mathrm{sinc}^2(Am\Delta\Omega)}{\left[(\Delta\omega)^2+(\Omega-m\Delta\Omega)^2\right]^2}}{\sqrt{\sum_{n=-N_0}^{N_0} \mathrm{sinc}^2(An\Delta\Omega)}} \tag{A.33}$$

It is obvious that the BFC's frequency-bin correlations are immediate consequences of its JSI. Hence, we see that the BFC's Franson interference recurrences are determined by that state's JSI. Finally, because $\Phi_{\mathrm{BFC}}(-\Omega) = \Phi_{\mathrm{BFC}}(\Omega)$, we can show that the doubly-resonant BFC's HOM-interference recurrences are also determined by that state's JSI. Hence, entangled mixed states that possess this same JSI and a symmetric JSA cannot be distinguished from the doubly-resonant BFC by means of frequency correlation, HOM and Franson revival measurements. To illustrate that possibility, we now introduce the entangled frequency-pair state (EFS).

The EFS is an entangled mixed state whose density operator is

$$\hat{\rho}_{\mathrm{EFS}} = \sum_{m=0}^{N_0} \rho_{\mathrm{EFS}}(m) \left|\psi_{\mathrm{EFS}}^{(\mathrm{m})}\right\rangle \left\langle\psi_{\mathrm{EFS}}^{(\mathrm{m})}\right| \tag{A.34}$$

where

$$|\psi_{\mathrm{EFS}}^{(\mathrm{m})}\rangle \;=\; \int \Phi_{\mathrm{EFS}}^{(m)}(\Omega)\hat{a}_H^{\dagger}\left(\frac{\omega_p}{2}+\Omega\right)\hat{a}_V^{\dagger}\left(\frac{\omega_p}{2}-\Omega\right)|0\rangle\, d\Omega \tag{A.35}$$

with

$$\Phi_{\mathrm{EFS}}^{(0)}(\Omega) \propto \frac{1}{(\Delta\omega)^2+\Omega^2}$$

$$\Phi_{\mathrm{EFS}}^{(m)}(\Omega) \propto \frac{1}{\sqrt{2}}\left(\frac{\mathrm{sinc}(Am\Delta\Omega)}{(\Delta\omega)^2+(\Omega+m\Delta\Omega)^2} + \frac{\mathrm{sinc}(Am\Delta\Omega)}{(\Delta\omega)^2+(\Omega-m\Delta\Omega)^2}\right),\ \text{for } m = 1, 2, \ldots, N_0 \tag{A.36}$$

$\int |\Phi_{\mathrm{EFS}}^{(m)}(\Omega)|^2 d\Omega = 1$, for all m, and the $\{\rho_{\mathrm{EFS}}(m)\}$ being a probability mass function that makes the EFS's JSI match that of the BFC state, i.e.,

$$\mathrm{JSI}_{\mathrm{EFS}}(\Omega) = \sum_{m=0}^{N_0} \rho_{\mathrm{EFS}}(m)\left|\Phi_{\mathrm{EFS}}^{(m)}(\Omega)\right|^2 \;=\; |\Phi_{\mathrm{BFC}}(\Omega)|^2 \;=\; \mathrm{JSI}_{\mathrm{BFC}}(\Omega) \tag{A.37}$$

Because the EFS and BFC have identical JSIs, their frequency-bin correlations, Franson interference recurrences will be indistinguishable. In addition, because $\Phi_{\mathrm{BFC}}(-\Omega) = \Phi_{\mathrm{BFC}}(\Omega)$ and $\Phi_{\mathrm{EFS}}^{(m)}(-\Omega) = \Phi_{\mathrm{EFS}}^{(m)}(\Omega)$, these two states will also have the same HOM-interference recurrences.

Next, we move on to the discussion of Conjugate-Franson interferometry, which was proposed in [127] for security checking in time-frequency-entangled, high-dimensional QKD. The basic configuration for conjugate-Franson interferometry is shown in Sec. 3.3. Conjugate-Franson interferometry of the doubly-resonant BFC and the EFS turn out to have the following coincidence rates,

$$R_{12}^{\mathrm{BFC}}(\phi_S, \phi_I) \propto 1 + \int d\Omega\, \mathrm{Re}\left[\Phi_{\mathrm{BFC}}^{*}(\Omega)\Phi_{\mathrm{BFC}}(\Omega - 2\omega_m)e^{i(\phi_S+\phi_I)}\right] \tag{A.38}$$

and

$$R_{12}^{\mathrm{EFS}}(\phi_S, \phi_I) \propto 1 + \sum_{m=0}^{N_0} \rho_{\mathrm{EFS}}(m) \int d\Omega\, \mathrm{Re}\left[\Phi_{\mathrm{EFS}}^{(m)*}(\Omega)\Phi_{\mathrm{EFS}}^{(m)}(\Omega - 2\omega_m)e^{i(\phi_S+\phi_I)}\right] \tag{A.39}$$

where ϕ_S and ϕ_I are phase shifts incurred by wavelength-scale length differences between the two arms of each MZI. It is clear from equation (A.38) and (A.39) that the conjugate-Franson interferometer's single-sideband modulation in one arm of each of its MZIs prevents their coincidence rates from being determined by their input states JSIs. Indeed, it is easily shown, that these conjugate-Franson coincidence rates can be rewritten as

$$R_{12}^{\mathrm{BFC}}(\phi_S, \phi_I) \propto 1 + \int d\tau\, \mathrm{JTI}_{\mathrm{BFC}}(\tau)\cos(\omega_m\tau + \phi_S + \phi_I) \tag{A.40}$$

and

$$R_{12}^{\mathrm{EFS}}(\phi_S, \phi_I) \propto 1 + \int d\tau\, \mathrm{JTI}_{\mathrm{EFS}}(\tau)\cos(\omega_m\tau + \phi_S + \phi_I) \tag{A.41}$$

where the (normalized) JTIs are given by $\mathrm{JTI}_{\mathrm{BFC}}(\tau) = |\Psi_{\mathrm{BFC}}(\tau)|^2$ and $\mathrm{JTI}_{\mathrm{EFS}}(\tau) = \sum_{m=0}^{N_0} \rho_{\mathrm{EFS}}(m)\left|\Psi_{\mathrm{EFS}}^{(m)}(\tau)\right|^2$. Thus it is not surprising that conjugate-Franson interferometry should be able to discriminate between the BFC and the EFS even when they have identical JSIs.

The doubly-resonant BFC only has appreciable conjugate-Franson interference at $\omega_m = |k|\Delta\Omega$ for $|k| = 1, 2, \ldots, 2N_{0,}$ where its visibilities satisfy

$$V_{\mathrm{BFC}}(k\Delta\Omega) = \frac{\sum_{m=-N_0}^{N_0-|k|} \mathrm{sinc}(Am\Delta\Omega)\mathrm{sinc}[A(m+|k|)\Delta\Omega}{\sum_{n=-N_0}^{N_0} \mathrm{sinc}^2(An\Delta\Omega)} \tag{A.42}$$

In contrast, the EFS has only appreciable conjugate-Franson interference at $|k| = 1, 2, \ldots, 2N_{0,}$ where its visibilities obey

$$V_{BFC}(k\Delta\Omega)(k\Delta\Omega) = \frac{\mathrm{sinc}^2(2Ak\Delta\Omega)}{\sum_{n=-N_0}^{N_0} \mathrm{sinc}^2(An\Delta\Omega)} \tag{A.43}$$

These results provide a clear and measurable signature for the doubly-resonant BFC, as shown in the Appendix Fig. A8 and A9, for the 15.15 GHz cavity and 5.03 cavity cases respectively.

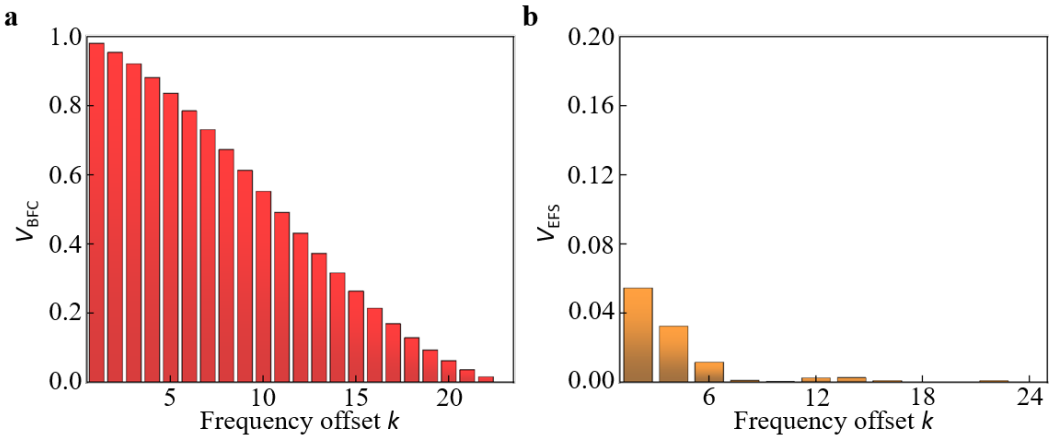

Appendix Fig. A8. Visibilities of conjugate-Franson interference recurrences for the 15 GHz FSR doubly-resonant BFC and the entangled frequency-pair state with the same JSI. a) BFC conjugate-Franson interference has high-visibility recurrences, and they occur only when the interferometer frequency offset is $k\Delta\Omega$ for integer k. b) EFS conjugate-Franson interference has low-visibility recurrences, and they only occur when the interferometer frequency offset is $2k\Delta\Omega$ for integer k. Appendix Fig. A8 published in [92].

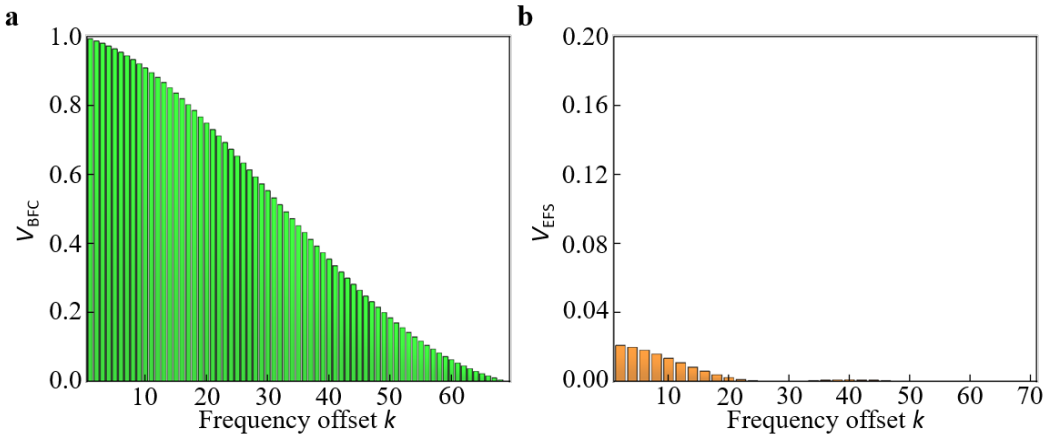

Appendix Fig. A9. Visibilities of conjugate-Franson interference recurrences for the 5 GHz FSR doubly-resonant BFC and the entangled frequency-pair state with the same JSI. a) BFC conjugate-Franson interference has high-visibility recurrences, and they occur only when the interferometer frequency offset is $k\Delta\Omega$ for integer k. b) EFS conjugate-Franson interference has low-visibility recurrences, and they only occur when the interferometer frequency offset is $2k\Delta\Omega$ for integer k. Appendix Fig. A9 published in [92].

A.5 Impact of cavity finesse on 50 GHz FSR mode-locked singly-resonant biphoton frequency comb

To further illustrate the impact of cavity finesse F on a larger FSR fiber cavity, we model the signal-idler temporal second-order cross-correlation function and Franson interference envelopes in a 50 GHz FSR singly-resonant mode-locked BFC with different cavity finesse F.

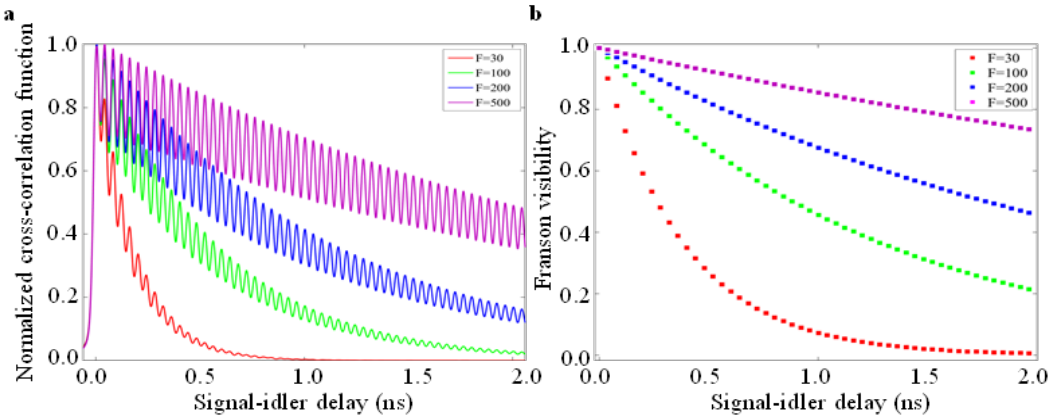

Appendix Fig. A10. Theoretical modeling of signal-idler temporal second-order cross-correlation function and Franson revivals visibility for a 50 GHz FSR cavity singly-resonant mode-locked BFC with different finesse *F*. a) Here, we model the signal-idler temporal second-order cross-correlation function versus 4 different cavity finesse F in a 50 GHz FSR cavity with FWHM timing jitter of 20 ps. Due to the denser temporal spacing of mode-locked oscillations from a larger cavity FSR (compared to 15.15 GHz FSR in Fig. 3.14), for a cavity finesse F of 500, there is a probability of over 50% to detect signal photons at 49 cavity round-trip times t_{rt} after idler photons are counted at detector across the whole temporal range of 1 ns. b) We plot the Franson interference recurrences for 4 different cavity finesse F of 30, 100, 200, and 500 in the same temporal range of 1 ns. We note that with only a moderate cavity finesse F of 500, all of the Franson interference recurrence visibilities surpass the quantum-classical threshold of 70.7%, confirming the time-energy entanglement over a temporal range of 1 ns.

A.6 Additional Franson interference measurements for singly-resonant biphoton frequency combs

In this section, we first show all high-dimensional Franson recurrence interferences for 45.32 GHz FSR singly resonant BFC after a asymmetric entanglement distribution with a 10 km fiber spool. We also compared the experimental time-bin visibilities for the post-distribution Franson interference recurrences with Appendix A.3's theory, which presumes perfect entanglement distribution. Our results are shown both in the main text's Fig. 3.10 and in Appendix Fig. A11, A12. The average deviation of experiment from theory is ≈ 4.25%, indicating efficient distribution of our singly-resonant BFC's time-binned energy-time entanglement.

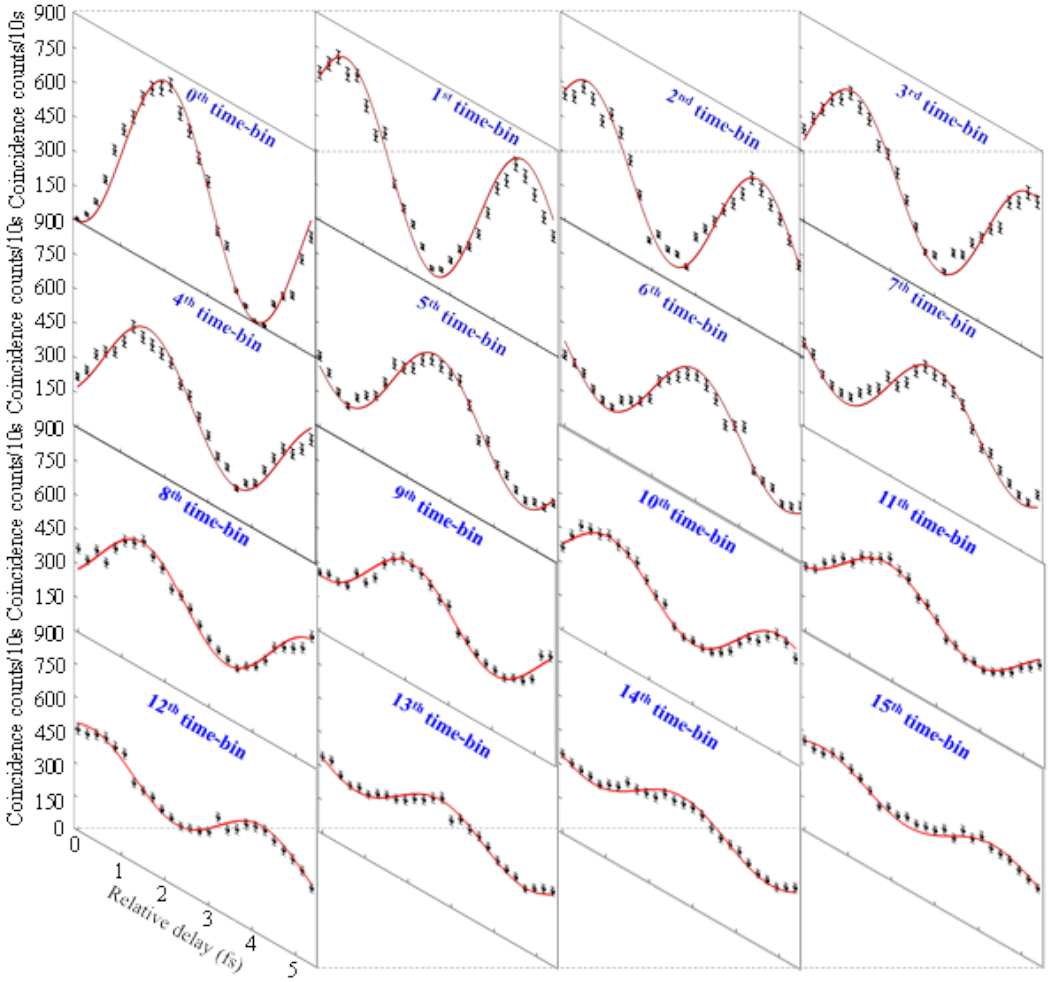

Appendix Fig. A11. Franson interference fringes – obtained with a 2 ns duration coincidence gate and accidentals subtracted – for 16 time bins of a 45 GHz singly-resonant BFC after a 10 km asymmetric entanglement distribution. The highest visibility, 98.81%, is observed for the central (0^{th}) time bin; bins 0 through 3 have visibilities exceeding the 70.7% value needed to violate Bell's inequality; and bins 0 through 6 have visibilities exceeding the 50% value that is the classical limit. These results clearly demonstrate high-quality 10 km asymmetric distribution of the singly-resonant BFC's time-binned energy-time entanglement.

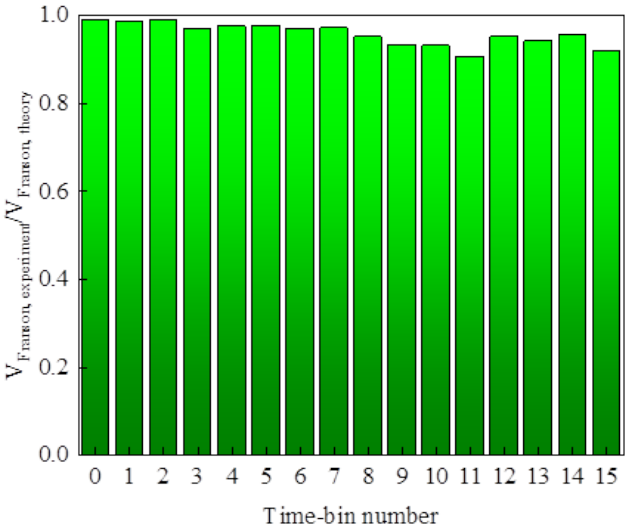

Appendix Fig. A12. Comparison between experimental visibilities of Franson-interference recurrences for time bins 0 through 15 after 10 km asymmetric distribution. We use our 45.32 GHz singly-resonant BFC with theory that assumes perfect distribution.

Then, we continue to examine frequency-binned Franson interference using a pair of tunable BPFs. we present the measured Franson-interference patterns for all 25 frequency-bin pairs within our source's bandwidth. The visibilities extracted from these interference patterns were shown as the visibility map in main text's Fig. 3.9b. Due to SPDC's energy conservation, only frequency-correlated photon pairs show energy-time entanglement in our singly-resonant BFC. Therefore, only the symmetric frequency-bin pairs exhibit high Franson interference visibilities in Appendix Fig. A13, with average raw visibility of 87.25%. As the frequency-bin pairs move away from frequency degeneracy, both their singles and coincidence rates decrease because of the SPDC phase-matching function. The reduced number of coincidences ultimately become comparable to the accidentals. Indeed, measurements on uncorrelated frequency-bin pairs, show no obvious fringes and their coincidence counts are almost at the noise floor. Thus, in Appendix Fig. A13 we did not subtract accidental coincidences, but we did do that subtraction in the main text's Fig. 3.9a because there we only showed the 5 symmetric frequency-bin pairs. Also, after 10 km asymmetric entanglement distribution, we chose to make Franson interference measurements only for the symmetric frequency-bin pairs, see the interference fringes shown in the main text's Fig. 3.10a inset.

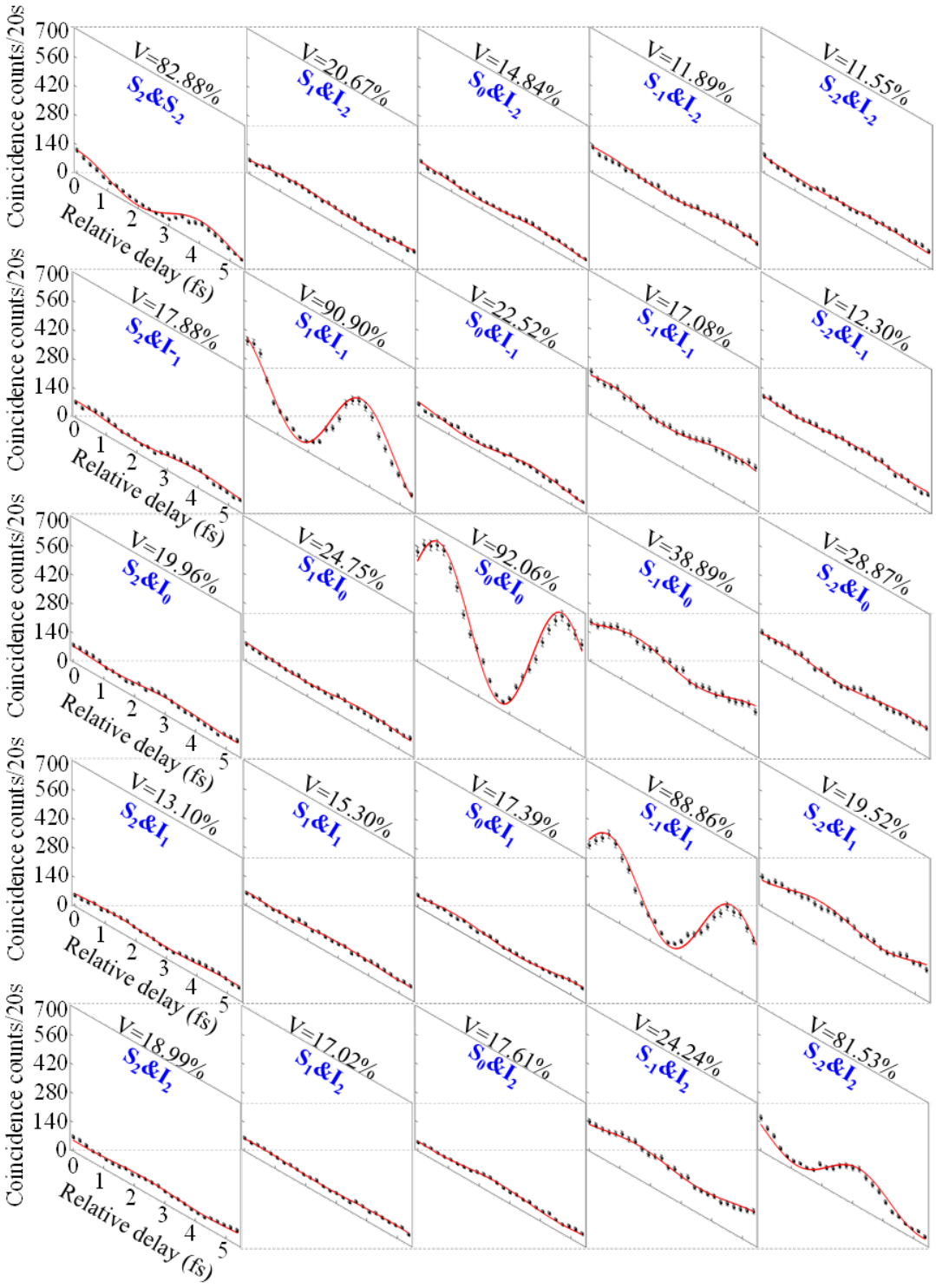

Appendix Fig. A13. Franson interference fringes for 25 frequency-bin pairs of the 45 GHz singly-resonant BFC. Frequency-bin pairs and corresponding visibilities are denoted for each interference pattern, with high interference visibilities only occurring for symmetric frequency-bin pairs.

Here, we present the extra Franson interference measurements for 5 and 15 GHz FSR singly-resonant BFCs, and our results are summarized in Appendix Fig. A14 and A15.

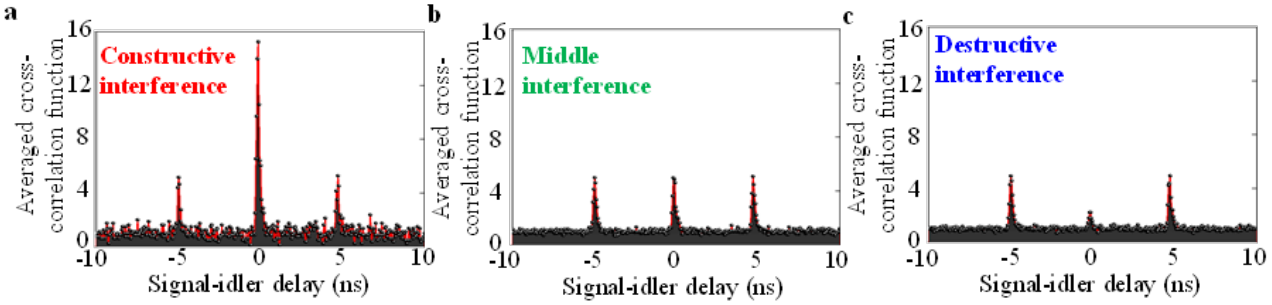

Appendix Fig. A14. The signature of Franson interference for 15 GHz singly-resonant BFC. a) to c) We measured three correlation peaks for different phase shifts induced by varying the thermal heater in the long path of arm1, where it is clear that only the central peak intensity changes, while the lateral peaks are unaffected. The phases for the measurements reported in Fig. A14a and A14c were such that the middle peak was maximized and minimized, respectively. By post-selecting the central correlation peak and changing the phases of the interferometers (ΔT_1), we have obtained maximum Franson visibilities for 0^{th} time-bin over 98.99% in 15.15 GHz FSR singly-resonant BFC after subtracting accidental coincidences.

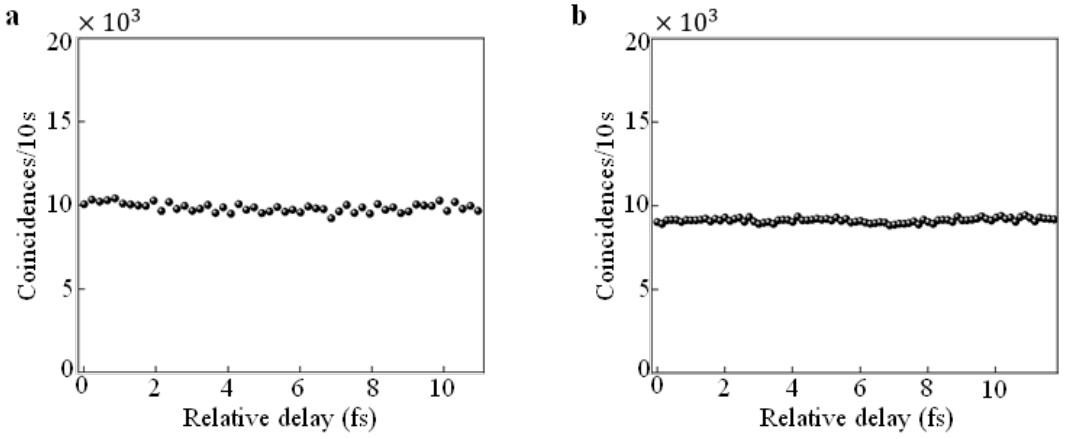

Appendix Fig. A15. The measured Franson interferences at non-integer cavity round-trip time in 5, 15 GHz FSR mode-locked singly-resonant BFCs. When we move the motorized stage to a ΔT_2 in-between cavity round trip (non-integer) such as 360 ps, we observe no Franson interference fringes. The measured average coincidence counts are consistent with our results in Fig. 3.12.

A.7 Supplemental heralded auto-correlation measurements for singly-resonant biphoton frequency combs

In this section we present additional information about the heralded $g^{(2)}(0)$ auto-correlation measurements of the singly-resonant BFC. At 0.2 mW pump power we measured $g^{(2)}(0) \approx 0.154$. Exchanging the roles of signal and idler, so that the idler illuminated the heralding detector while the signal beam illuminated the 50:50 BS, we obtained $g^{(2)}(0) \approx 0.130$ at 0.6 mW pump power. Both results are well below the classical threshold. Moreover, because the signal beam's singles rate is considerably lower than the idler's, reliable idler-heralded $g^{(2)}(0)$ measurements could not be obtained at as low a pump power as signal-heralded measurements could. Appendix Fig. A16 shows the expected effect on $g^{(2)}(0)$ of increased pump power, viz., $g^{(2)}(0)$ increases because of increased presence of multi-pair emissions from the SPDC source. We note that the non-zero values of heralded $g^{(2)}(0)$ are primarily due to multi-pair SPDC emissions. Also, the idler-heralded $g^{(2)}(0)$ is lower than the signal-heralded $g^{(2)}(0)$ because it is less likely that two signal photons could survive the higher losses in the signal channel to produce a coincidence.

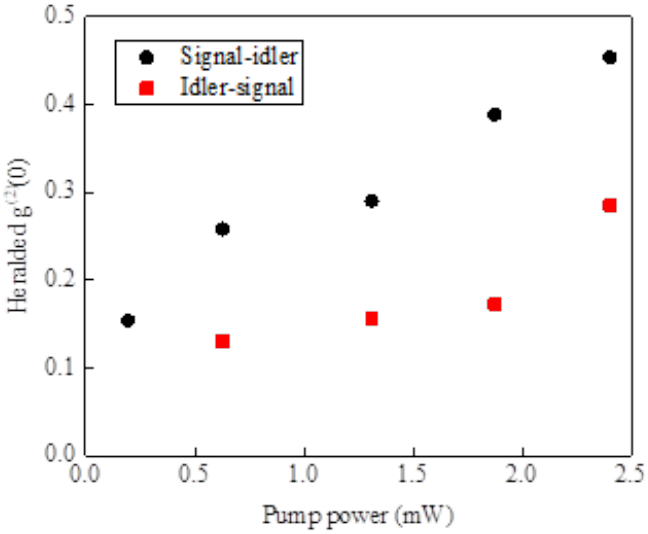

Appendix Fig. A16. Measured heralded $g^{(2)}(0)$ values versus the pump power for the 45 GHz singly-resonant BFC. Signal-heralded measurements (black points), idler-heralded measurements (red points).

Here, we further verify the multimode emission single-photon Fock state is generated within our time-reversible singly-resonant BFCs. In Appendix Fig. A17, a coincidence window of 30 ns is used for including multimode emission of our time-reversible singly-resonant BFCs. The minimum measured heralded $g^{(2)}(0) = 0.204 \pm 0.002$ and $g^{(2)}(0) = 0.212 \pm 0.002$ reveals the multimode emission with

single-photon Fock state with our photon-pair source. The non-ideal heralded $g^{(2)}(0)$ value can be explained by the decreasing signal-to-noise ratio, due to a wider coincidence window and the ultranarrow FSR of the cavity, and by relatively small cavity finesse.

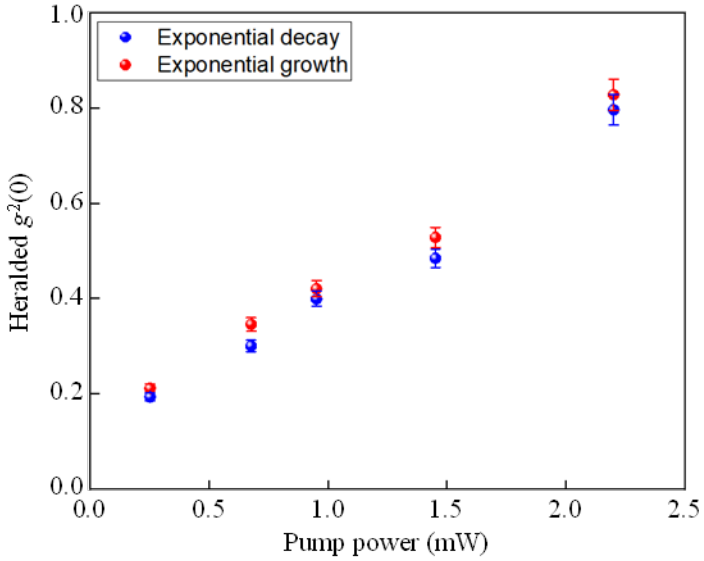

Appendix Fig. A17. Measured heralded $g^{(2)}(0)$ versus the pump power for exponential decay and growth 42 MHz singly-resonant BFCs using a 30 ns coincidence window. HBT measurements for time-reversible SR-BFCs. The minimum heralded $g^{(2)}(0) = 0.204 \pm 0.002$ and $g^{(2)}(0) = 0.212 \pm 0.002$ is measured using a wider coincidence window of 30 ns, which includes 0^{th} and 1^{st} cavity round-trip correlation peaks from both exponential decay and exponential growth SR-BFCs.

Appendix B

Schmidt mode decompositions and entanglement of formation

B.1 Schmidt eigenvalues and Schmidt numbers

B.1.1 Frequency-binned Schmidt eigenvalues and Schmidt numbers

In this section, we discuss the Schmidt eigenvalues and Schmidt numbers for frequency-binned doubly-resonant BFC states: experimental results versus theory. Appendix Table B1 presents the Schmidt eigenvalues inferred from the frequency-bin correlation measurements shown in Sec. 3.2. They were obtained from performing a Schmidt decomposition on the frequency-correlation matrix [261-263]. The Schmidt eigenvalues of the frequency-binned BFC state are the eigenvalues found from that diagonalization, and the Schmidt number they imply from Sec. 3.2. For the following Appendix Tables, we use boldface to highlight and consider the dominant Schmidt modes that comprise over 60% of the total Schmidt eigenvalues for each measurement we have performed using frequency-bin correlation measurements and HOM recurrence measurements.

Appendix Table B1. Measured frequency-bin Schmidt eigenvalues and Schmidt numbers for the 45 GHz doubly-resonant BFCs with pump powers ≈ 2 mW (left) and ≈ 4 mW (right). The dominant Schmidt eigenvalues are shown in boldface. Appendix Table B1 published in [92].

Number of frequency bins	Schmidt eigenvalues	Schmidt number	Number of frequency bins	Schmidt eigenvalues	Schmidt number
2	0.140	4.310	2	0.112	3.17
1	**0.218**		1	0.165	
0	**0.343**		0	0.499	
-1	**0.183**		-1	0.130	
-2	0.115		-2	0.091	

The results of performing the same frequency-bin Schmidt decomposition on the data we obtained for ≈ 2 mW pumping of the 15.15 GHz cavity setup is given in Appendix Table B2. Here the 8.671 inferred Schmidt number is limited by the tunability of our 100 pm filters.

Appendix Table B2. Measured frequency-bin Schmidt eigenvalues and Schmidt number for the 15 GHz doubly-resonant BFC and ≈ 2 mW pump power. The dominant Schmidt eigenvalues are shown in boldface. Appendix Table B2 published in [92].

Number of frequency bins	Schmidt eigenvalues	Schmidt number
4	0.084	8.67
3	0.100	
2	**0.114**	
1	**0.136**	
0	**0.147**	
-1	**0.128**	
-2	**0.109**	
-3	0.096	
-4	0.081	

The frequency-bin Schmidt decomposition for our 5.03 GHz BFC yielded the Schmidt eigenvalues and Schmidt number shown in Appendix Table B3. The maximum possible Schmidt number for this measurement is 19, and our 11.67 result is mainly limited by the bandwidth and tunability of our 100 pm filters.

Appendix Table B3. Measured frequency-bin Schmidt eigenvalues and Schmidt number for the 5 GHz doubly-resonant BFC and ≈ 2 mW pump power. The dominant Schmidt eigenvalues are shown in boldface. Appendix Table B3 published in [92].

Number of frequency bins	Schmidt eigenvalues	Number of frequency bins	Schmidt eigenvalues	Schmidt number
9	0.020	**-1**	**0.101**	11.67
8	0.026	**-2**	**0.066**	
7	0.028	**-3**	**0.048**	
6	0.032	-4	0.039	
5	0.035	-5	0.033	
4	0.041	-6	0.030	
3	**0.052**	-7	0.027	
2	**0.074**	-8	0.023	
1	**0.114**	-9	0.013	
0	**0.190**			

For comparison purposes, and to derive our frequency-binned BFC's Hilbert-space dimensionality under ideal conditions, we conclude this section by presenting theoretical results for their Schmidt eigenvalues and their Schmidt numbers. We can write the BFC's frequency-binned JSI as

$$|\psi(n_s\Delta\Omega, n_I\Delta\Omega)|^2 = \frac{\mathrm{sinc}^2(2.78 n_s\Delta\Omega/2\pi B_{PM})}{\sum_{n_s=-N_0}^{N_0}\mathrm{sinc}^2(2.78 n_s\Delta\Omega/2\pi B_{PM})}\delta_{n_s n_I}, \text{ for } -N_0 \le n_s, n_I \le N_0 \qquad \text{(B.1)}$$

where $n_s\Delta\Omega$ is the positive detuning of the signal photon's radian frequency from degeneracy and $n_I\Delta\Omega$ is the negative detuning of the idler photon's radian frequency from degeneracy, and $\delta_{n_s n_I}$ is the

Kronecker delta function. The J_Ω matrix, whose diagonalization provides the Schmidt eigenvalues, is then obtained, because it is diagonal, and its diagonal elements

$$\lambda_n = \frac{sinc^2(2.78n_s\Delta\Omega/2\pi B_{PM})}{\sum_{n_s=-N_0}^{N_0} sinc^2(2.78n_s\Delta\Omega/2\pi B_{PM})}, \text{ for } -N_0 \leq n \leq N_0 \tag{B.2}$$

are the Schmidt eigenvalues we are seeking. From these eigenvalues the theoretical Schmidt number for the frequency-binned BFC is therefore

$$K_\Omega = (\sum_{n=-N_0}^{N_0} \lambda_n^2)^{-1} = \frac{[\sum_{n_s=-N_0}^{N_0} \mathrm{sinc}^2(2.78n_s\Delta\Omega/2\pi B_{PM})]^2}{\sum_{n_s=-N_0}^{N_0} \mathrm{sinc}^4(2.78n_s\Delta\Omega/2\pi B_{PM})} \tag{B.3}$$

The theoretical Schmidt numbers for the frequency-binned doubly-resonant BFC states are found to be 4.89, 20.21, and 34.39 for 45.32 GHz, 15.15 GHz, and 5.03 GHz FSR cavities, respectively. Hence the ideal Hilbert-space dimensionalities for frequency-binned BFCs scales with the FSR of the cavity and the phase-matching bandwidth of SPDC sources used to generate that BFC state.

Then, we use the same method to extract Schmidt eigenvalues and corresponding Schmidt number for singly-resonant BFC, as shown in Appendix Table B4.

Appendix Table B4. Measured frequency-bin Schmidt eigenvalues and Schmidt numbers for the 45 GHz singly-resonant BFC. Appendix Table B4 published in [92].

Number of frequency bins	Schmidt eigenvalues	Schmidt number
2	0.119	4.17
1	0.228	
0	0.355	
-1	0.191	
-2	0.106	

B.1.2 Time-binned Schmidt eigenvalues and Schmidt numbers

We now obtained our doubly-resonant BFCs time-binned Schmidt eigenvalues from the visibilities of their measured HOM-interference recurrences via the procedure described in the Sec. 3.2. Appendix Tables B5 show the dominant Schmidt eigenvalues we found for the 45.32 GHz, 15.15 GHz, and 5.03 GHz BFCs, note that the time-bin Schmidt number are given in Sec. 3.2.

Appendix Table B5. Measured dominant time-bin Schmidt eigenvalues for the doubly-resonant BFC generated using a) the 45 GHz cavity, b) the 15 GHz cavity, and c) the 5 GHz cavity. Appendix Table B5 published in [92].

a

Number of time bins	Schmidt eigenvalues
4	0.045
3	0.056
2	0.070
1	0.087
0	0.109
-1	0.087
-2	0.070
-3	0.056
-4	0.045

b

Number of time bins	Schmidt eigenvalues
1	0.158
0	0.281
-1	0.158

c

Number of time bins	Schmidt eigenvalues
1	0.181
0	0.321
-1	0.180

Then, we perform Schmidt mode decomposition for the Franson revival interferences in time domain using our singly-resonant BFC, as described in Sec. 3.3. Here, we summarize our time-bin Schmidt mode decomposition results in Appendix Table B6.

Appendix Table B6. Measured time-bin Schmidt eigenvalues and Schmidt numbers for the 45 GHz singly-resonant BFC.

Time-bin number	Schmidt eigenvalues	Schmidt number
0	0.121	13.13
1	0.110	
2	0.099	
3	0.089	
4	0.080	
5	0.073	
6	0.066	
7	0.059	
8	0.053	
9	0.047	
10	0.044	
11	0.038	
12	0.035	
13	0.032	
14	0.029	
15	0.025	

As explained previously, the Schmidt mode decomposition for the time-binned 45.32 GHz singly-resonant BFC is derived from the visibilities of the Franson-interference recurrences. Evaluating the

approximate (unnormalized) time-domain biphoton wave function at the Franson-interference recurrence times we get,

$$\Psi(n\Delta T) = \exp(-n\Delta\omega\Delta T)\sum_{m=-N}^{n}\mathrm{sinc}(Am\Delta\Omega) \tag{B.4}$$

from which it readily follows that the nth bin's visibility is $V_n = \exp(-n\Delta\omega\Delta T)$, as stated in the main text. Equation (B.4) then leads to the main text's theoretical expressions for the time-binned Schmidt eigenvalues $\{\lambda_n\}$, and its Schmidt number K_T:

$$\lambda_n = \frac{\mathrm{e}^{-\pi n/F}}{\sum_{m=0}^{M}\mathrm{e}^{-\pi m/F}}, \text{ for } 0 \le n \le M \tag{B.5}$$

and

$$K_T = \frac{\sinh^2[\pi(M+1)/2F]\sinh(\pi/F)}{\sinh^2(\pi/2F)\sinh[\pi(M+1)/F]} \tag{B.6}$$

where M+1 is the number of time bins and F is the fiber FP cavity's finesse. Assuming, that the time-binned singly-resonant BFC's JTA equals the square root of its JTI, the experimental time-binned Schmidt eigenvalues and Schmidt number are

$$\lambda_n = \frac{V_n}{\sum_{m=0}^{M}V_n}, \text{ for } 0 \le n \le M \tag{B.7}$$

and

$$K_T = \frac{(\sum_{n=0}^{M}V_n)^2}{\sum_{n=0}^{M}V_n^2} \tag{B.8}$$

We do not, however, expect the approximate time-binned biphoton wave function to be as accurate for the singly-resonant BFC as it is for the doubly-resonant BFC, because the slower frequency-domain fall off with only the signal being fiber FP cavity filtered leads to greater overlap between the contributions from adjacent and near-adjacent cavity resonances. Appendix Table B6 shows the measured time-bin Schmidt eigenvalues and Schmidt number for the 45.32 GHz singly-resonant BFC. Its 13.13 Schmidt number is in excellent agreement with the 13.19 theoretical value obtained using the exact theory based on equation (B.8).

B.2 Entanglement of formation and ebits

In this section, we quantify the high-dimensional time-energy entanglement of our doubly- and singly-resonant BFC from lower bounds of their entanglements of formation for results presented in Sec. 3.2 and 3.3. This quantity is useful when we do not have access to all the elements of the density matrix. In our experimental setup, there are technical limitations that prevented our measuring all the elements of the doubly- and singly-resonant BFC's full density matrix. These limitations were due to: (1) our

Franson interferometry only having a free-space motorized optical-delay line in its arm2; and (2) that stage's 360 ps travel range being aligned with the 0^{th} time-bin close to the stage's starting position. Thus, we measured only one side of the time-energy Franson interference revival time-bins.

Appendix Table B7 shows the resulting 3×3 submatrix elements for 45.32 GHz cavity's Franson interference. Here, the blue entries are measurements, the green entries follow from presuming our BFC has time-bin symmetry – as seen, e.g., in that doubly-resonant BFC's HOM-interference recurrences – and the black entries are obtained by extrapolating the visibilities using the cavity's Lorentzian lineshape.

Appendix Table B7. Franson interference 3×3 submatrix elements for obtaining a lower bound on the entanglement of formation for the 45 GHz doubly-resonant BFC. Appendix Table B7 published in [92].

Visibility	0^{th} time-bin	1^{st} time-bin	2^{nd} time-bin
0^{th} time-bin	**99.1%**	**98.3%**	**96.9%**
1^{st} time-bin	**98.3%**	**99.1%**	**95.1%**
2^{nd} time-bin	**96.9%**	**95.1%**	**99.1%**

Appendix Table B8 shows the 45.32 GHz and 15.15 GHz cavities' entanglement of formation lower bounds for $d = 2$ to 4. They were obtained, using the measured Franson interference visibilities in the Sec. 3.2. Note that we chose not to go to higher d values here because increasing d makes the bounds increasingly dependent on submatrix elements derived from extrapolation rather than from direct measurements. Within that limited d range, our highest entanglements-of-formation lower bounds are 1.89 ± 0.03 ebits for the 45.32 GHz cavity's doubly-resonant BFC and 1.40 ± 0.05 ebits for the 15.15 GHz cavity's doubly-resonant BFC. Both were attained at $d = 4$, where 2 ebits corresponds to a maximally-entangled pure state of that dimensionality.

Appendix Table B8. Entanglements of formation lower bounds for the 45 GHz and the 15 GHz doubly-resonant BFCs. Appendix Table B8 published in [92].

Dimension *d*	**Maximum entangled ebits**	**ebits for 45.32 GHz BFC**	**ebits for 15.15 GHz BFC**
2	1	0.98	0.93
3	1.58	1.54	1.30
4	2	1.89	1.40

Next, to calculate the lower-bound on high-dimensional time-energy entanglement for our singly-resonant BFC, we used our asymmetry Franson interference recurrence visibilities shown in Sec. 3.3.

Appendix Table B9 shows the resulting 5×5 submatrix elements for 45.32 GHz cavity's Franson interferences before an entanglement distribution. Here, the blue entries are measurements, the green entries follow from presuming our singly-resonant BFC has time-bin symmetry, and the black entries are obtained by extrapolating the visibilities using the cavity's Lorentzian lineshape from our theory presented in Appendix A.3. Similarly, we also perform entanglement of formation calculation for singly-resonant BFC's Franson interference recurrence visibilities after a 10-km asymmetric entanglement distribution. Appendix Table B10 list all the resulting 5×5 submatrix elements. Using the 0^{th} to 4^{th} order Franson recurrence visibilities allowed us to obtain lower bound of entanglement of formation 1.533, and 1.522 ebits before and after the asymmetric entanglement distribution of 10 km distance with our 45.32 GHz singly-resonant BFC. Appendix Table B11 summarized the number of ebits before and after such entanglement distribution.

Appendix Table B9. Franson interference 5×5 submatrix visibilities for retrieving a lower bound on the entanglement of formation for a 45 GHz singly-resonant BFC before entanglement distribution.

Visibility	0^{th} time-bin	1^{st} time-bin	2^{nd} time-bin	3^{rd} time-bin	4^{th} time-bin
0^{th} time-bin	**99.46%**	**90.17%**	**81.03%**	**72.82%**	**65.60%**
1^{st} time-bin	**90.17%**	**99.46%**	**72.82%**	**65.60%**	**59.57%**
2^{nd} time-bin	**81.03%**	**72.82%**	**99.46%**	**59.57%**	**54.03%**
3^{rd} time-bin	**72.82%**	**65.60%**	**59.57%**	**99.46%**	**48.68%**
4^{th} time-bin	**65.60%**	**59.57%**	**54.03%**	**48.68%**	**99.46%**

Appendix Table B10. Franson interference 5×5 submatrix visibilities for retrieving a lower bound on the entanglement of formation for a 45 GHz singly-resonant BFC after an asymmetric entanglement distribution.

Visibility	0^{th} time-bin	1^{st} time-bin	2^{nd} time-bin	3^{rd} time-bin	4^{th} time-bin
0^{th} time-bin	**98.81%**	**89.28%**	**80.54%**	**71.28%**	**64.81%**
1^{st} time-bin	**89.28%**	**98.81%**	**71.28%**	**64.81%**	**58.54%**
2^{nd} time-bin	**80.54%**	**71.28%**	**98.81%**	**58.54%**	**52.57%**
3^{rd} time-bin	**71.28%**	**64.81%**	**58.54%**	**98.81%**	**47.52%**
4^{th} time-bin	**64.81%**	**58.54%**	**52.57%**	**47.52%**	**98.81%**

Appendix Table B11. Entanglements of formation lower bounds for the 45 GHz singly-resonant BFC.

Dimension *d*	Maximum entangled ebits-Theory	Ebits for 45.32 GHz BFC at 0-km	Ebits for 45.32 GHz BFC at 10-km
2	0.8653	0.8646	0.8641
3	1.2416	1.2405	1.2321
4	1.4374	1.4351	1.4227
5	1.5387	1.5329	1.5228

Appendix C

Design, fabrication and characterization of two-qubit SWAP gate

C.1 Design and operation maps of the two-qubit SWAP gate components: PC-NOT and MC-NOT gates

The design map for the PC-NOT gate was prepared with an eigenmode solver through super-mode analysis of the silicon polarized directional-coupler photonics structure as functions of waveguide and gap widths. The eigenmode results were verified through a detailed propagator analysis using the finite-difference time-domain (FDTD) method and a proper parameter set was selected for our PC-NOT implementation. Here, polarization splitting is satisfied by carefully selecting the coupler length to equal to the transverse magnetic (TM) coupling length, which is about ten times smaller than that for the transverse electric (TE) case. Varying gap widths, crossover coupling lengths and waveguide widths are illustrated for the optimal coupling length and cross-channel energy fraction in Appendix Fig. C1. The silicon waveguides were designed with 220 nm thickness for operation in the C-band. Appendix Fig. C1a and C1b show the coupling length for the given configurations. By fixing the waveguide width to 460 nm, the energy fractions coupled to the cross-channel were monitored for varying coupler lengths and gap widths, as shown in Appendix Fig. C1c and C1d. The optimized design for the PC-NOT gate has a waveguide-to-waveguide gap width of 400 nm and a coupling length of 11.5 μm. With this parameter combination, the TE mode remains in its channel while the TM mode crosses over to the other channel with maximized efficiency, thus ensuring optimal PC-NOT gate operation.

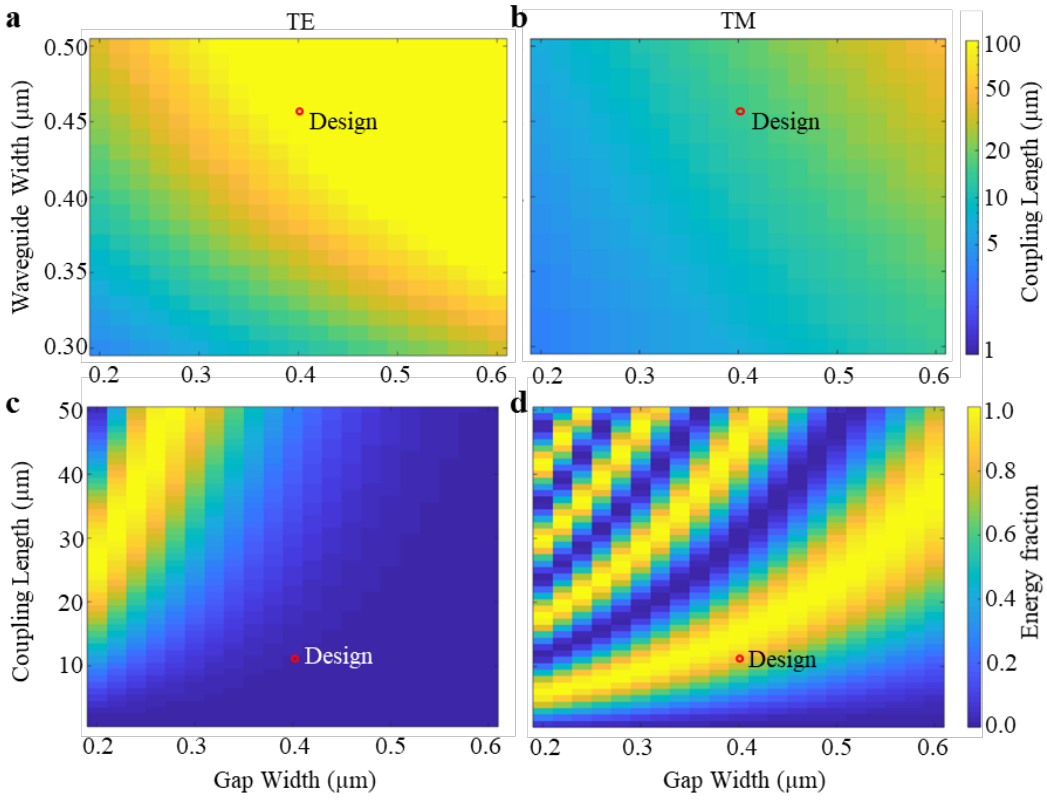

Appendix Fig. C1. Design map for the silicon integrated photonics PC-NOT gate. Cross-over coupling length versus waveguide and gap widths of the TE a) and TM b) modes. Fraction of the energy coupled to the cross-channel versus coupler length and gap width for TE c) and TM d) modes with a waveguide width of 460 nm. The thickness of the device is fixed at 220 nm. The red circle denotes the designed and fabricated device choice.

The design for the MC-NOT gate is based on a silicon integrated photonics two-level polarization rotator [264]. The polarization rotator was designed with a silicon thickness of 220 nm and analyzed through eigenmode expansion simulations. As shown in Appendix Fig. C2b, the designed polarization rotator consists of a polarization rotation section (A and B) and a mode conversion section (C). Sections A and B are asymmetric rib waveguides that rotate the polarization angle of the waveguide mode, and Section C is a nano-tapered waveguide in which the polarization of the local mode is maintained. The length of each section is varied independently to obtain the best conversion efficiency. This continuous waveguide structure prevents extra loss induced by the mode mismatch, which is crucial to implementing a low-loss polarization rotator. The conversion efficiency of each section is evaluated by a detailed propagation analysis using the FDTD method, with the results versus length shown in Appendix Fig. C2c. Optimal conversion efficiency of each section is obtained with the

lengths set to 80 μm, 200 μm and 80 μm for sections A, B and C, respectively. With the optimized waveguide structure, the extinction ratio for the polarization rotation operation was examined across different wavelengths to determine the optimal operating wavelength for the SWAP gates, as shown in Appendix Fig. C2a.

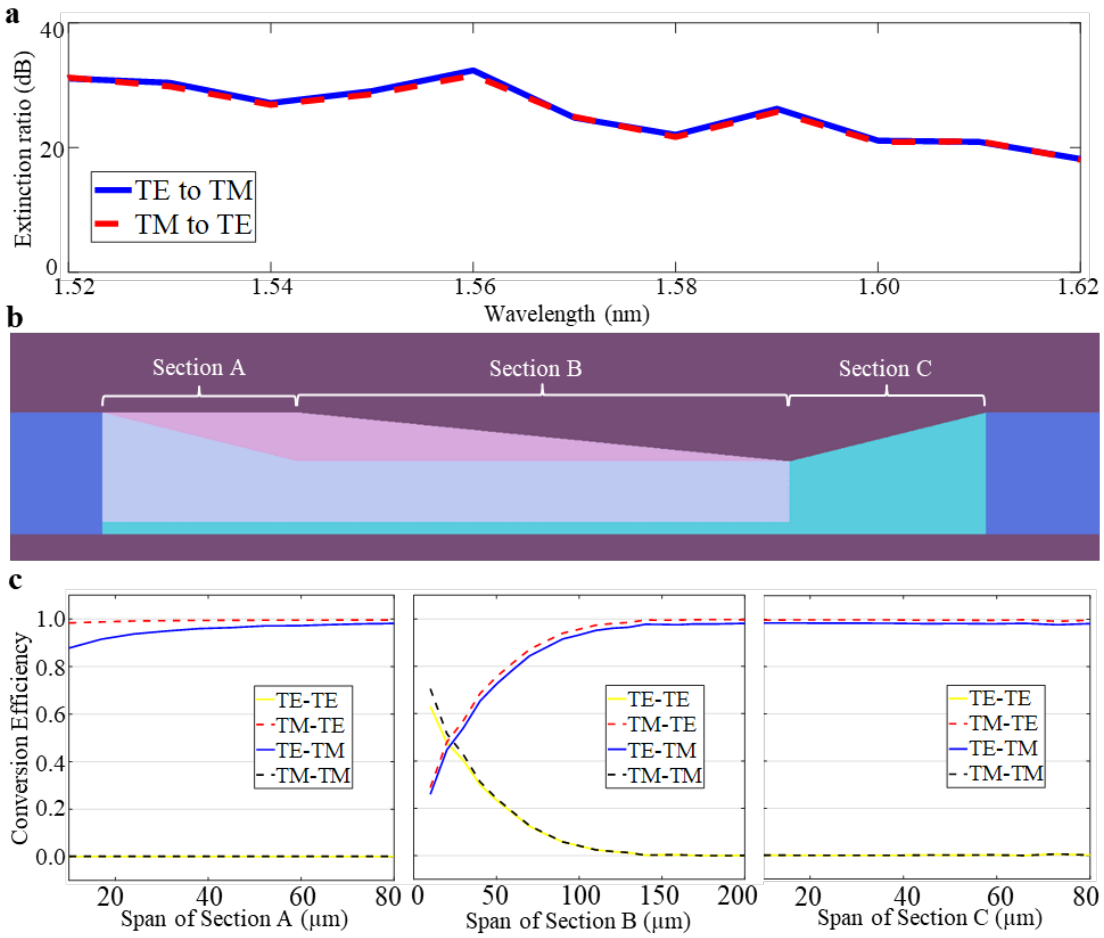

Appendix Fig. C2. Design map for the silicon integrated photonics MC-NOT gate. a) Extinction ratio of the MC-NOT gate versus operation wavelength for both TE-to-TM and TM-to-TE mode conversions. b) Top view of the MC-NOT gate's design model. c) Conversion efficiency changes along the length for each individual section of the MC-NOT gate.

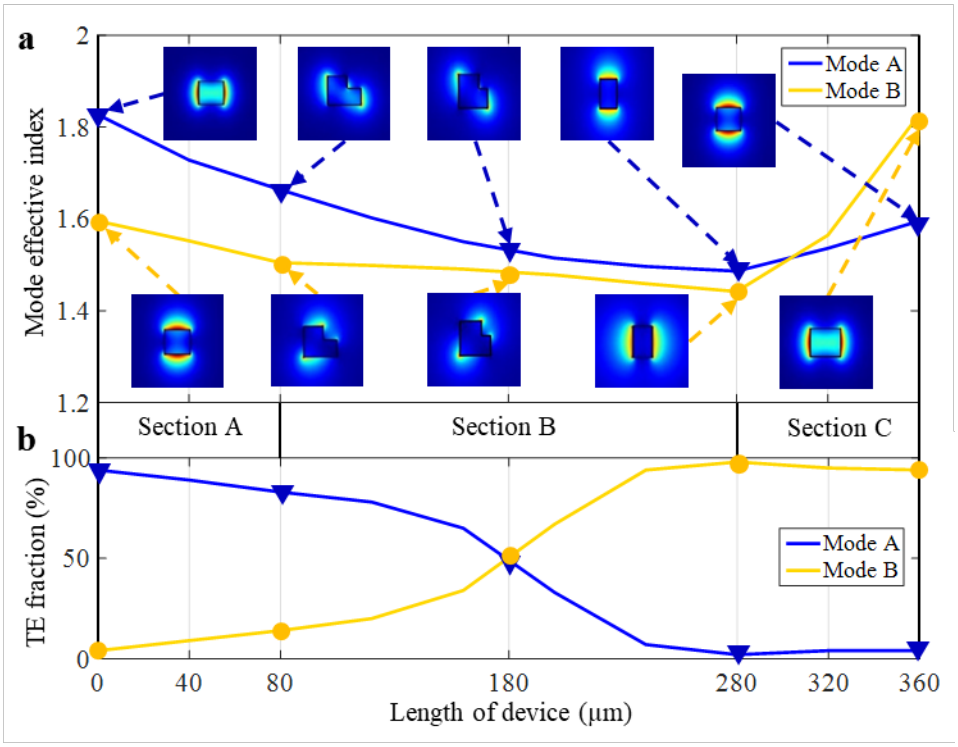

Appendix Fig. C3. Local mode analysis of the silicon integrated photonics MC-NOT gate. a) Effective refractive indices of the two local modes along the device. Inset: *E*-field profiles of two modes at different positions in each section. b) TE polarization fraction for the two local modes along the MC-NOT gate.

The final design was examined by monitoring the fundamental TE and TM modes throughout the device using eigensolver analysis. The evolution of the effective refractive indices and polarization states (TE fraction) of the two local modes are illustrated in Appendix Fig. C3. The inset of Appendix Fig. C3 depicts the *E*-field intensity for each mode. At the input to section A, there are two local modes A and B with TE-like and TM-like polarizations, respectively. The input TE-like mode couples to mode A and the TM-like mode couples to mode B. The polarization direction is gradually rotated along the waveguide from section A to B due to the asymmetry in both horizontal and vertical directions of the waveguide. The continuous change of the TE fraction also specifies the polarization rotation. The polarization directions of the local modes are continuously rotating and achieve 90° rotation at the output of section B. Despite that, the TE fractions for modes A and B are the same at the midpoint of section B, with the polarization directions of modes A and B being perpendicular at this point, as depicted in the insets of Appendix Fig. C3a. Under adiabatic conditions, only one of modes A or B is excited, preventing their mixing and thus ensuring high conversion efficiency. Two local modes continue to propagate through section C without polarization rotation, and they are converted to

the input mode set because the waveguide cross section of section C is the same as section A's. At this point, polarization rotation is complete. We also note that the sidewall roughness in near the neck region of section B or at the beginning of section C will result in the TE and TM modes suffering different losses, because the TE-like mode is more spread out than the TM-like mode in the neck region and also more sensitive to sidewall. The loss induced by the sidewall roughness can be reduced by improving the fabrication process [265]. The designed low-loss small-footprint polarization rotator was used for the top channel of our SWAP-gate implementation, as shown in Sec. 4.1, and thus works effectively as an MC-NOT gate.

C.2 Nanofabrication and characterization of the PC-NOT and MC-NOT gates

The Prior efforts to fabricate an integrated polarization rotator are described in [266-273]. The rotator requires two-level fabrication with two-mask alignment. Misalignment of the two masks (or levels) creates scattering losses and reduces the TM-to-TE extinction ratio, limiting the performance of the resulting MC-NOT gate and ultimately the SWAP gate. To mitigate misalignment, M. Yu and D.-L. Kwong developed a mask design that minimizes the ill effects of misalignment in the two-level polarization rotator [274]. Even with this improved mask design, a ± 60 nm misalignment will decrease the extinction ratio and rotation efficiency.

To overcome misalignment, we have developed a self-aligned two-level nanofabrication approach in order to achieve the TM-to-TE extinction ratio required for the polarization rotator, MC-NOT gate, and SWAP gate. Appendix Fig. C4a illustrates the two mask layers implemented in our tapeout. Both are dark-field masks with Layer 1 patterned in a hard mask (aluminum) and Layer 7 patterned in a photoresist. The respective dimensions of sections A, B and C are illustrated for both Layer 1 and Layer 7. Appendix Fig. C4b illustrates the combination of both mask layers which then serves as the single mask for the first 220 nm Si reactive ion etch for sections A, B and C. After this etch, the Layer 7 resist is stripped via a resist developer, leaving the already-patterned hard mask. This hard mask — already self-aligned to the first etch — serves as the mask to define the 110 nm etch for sections A and B.

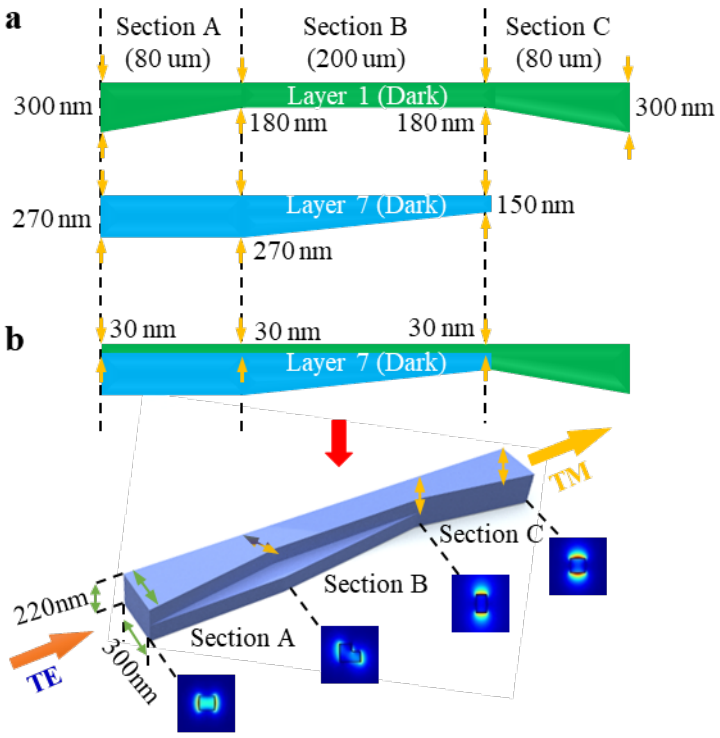

Appendix Fig. C4. Self-aligned two-level nanofabrication approach. a) Two mask layers implemented in the nanofabrication of our silicon chip's design tapeout. Both are dark-field masks with Layer 1 patterned in a hard mask and Layer 7 patterned in a photoresist. b) The combination of both mask layers serves as the single mask for the first 220 nm Si reactive ion etch for sections A, B and C. This self-aligned two-level fabrication approach guarantees 30 nm layer-to-layer offset without alignment error.

Our self-alignment procedure eliminates the need for alignment between the two Si etch steps, where alignment might be difficult to achieve in the second lithography owing to the step-height relief of the Si waveguides. The only two-level alignment (Layer 7 to Layer 1) is before the first etch, with a relatively flat surface for lithography patterning. It is also easier to inspect and verify the 30 nm lateral offset via metrology, before the etch, of this relatively flat surface. To guarantee the 30 nm lateral offset between Layer 1 and Layer 7 (as shown in Appendix Fig. C4a), the second lithography resist pattern is inspected after lithography and patterning across the whole wafer. If any 30 nm offset across the whole 8-inch wafer span deviates by more than ± 60 nm, the resist is stripped, and the second lithography step is repeated until a more uniform 30 nm lateral offset is obtained. In this foundry cleanroom, our two-level alignment's accuracy is guaranteed within ± 60 nm bounds across the entire wafer.

To test the performance of each logical operation within our SWAP gate, we performed classical transmission measurements on the individual PC-NOT and MC-NOT gates separately. The PC-NOT gate's transmission spectrum was measured with a swept C-band tunable laser via a 2×2 input-output free-space coupling system that selects the PC-NOT gate's top and bottom channels for its input and output. The input light's polarization is set by a polarizer and a half-wave plate, and the output light is measured using a polarizer. The transmission for different input/output polarization and channel combinations at different wavelengths is shown in Appendix Fig. C5. We obtained an average extinction ratio (for the desired output of the corresponding input) of more than 18 dB between 1520 nm to 1620 nm, which confirms the good overall performance of the PC-NOT gate.

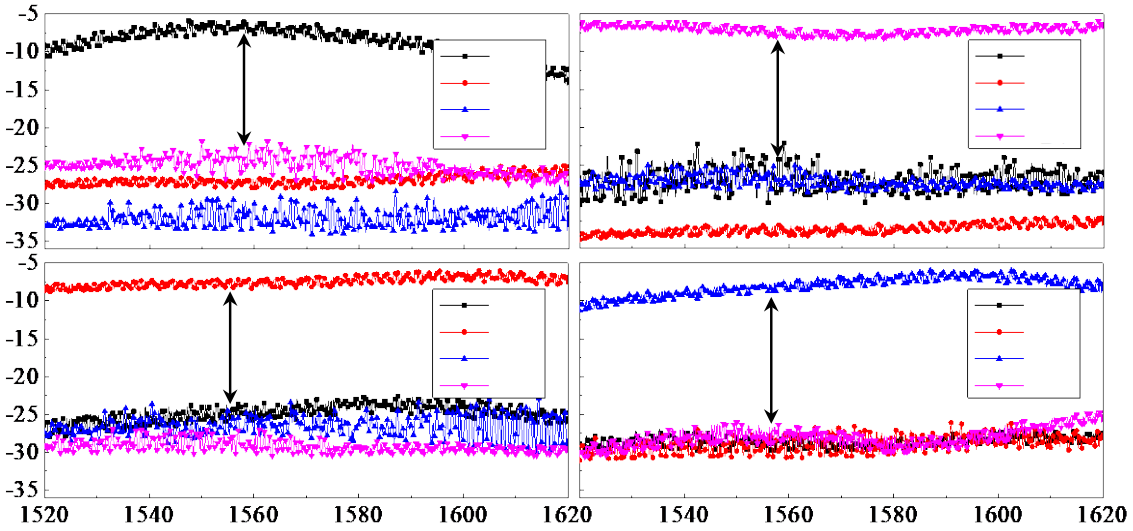

Appendix Fig. C5. Characterization of the silicon integrated photonics PC-NOT gate. Classical transmission measurements between different input-output ports and polarization combinations, along with wavelength characterization over 100 nm. Good overall performance of more than 18-dB extinction ratio is achieved in the C-band.

The MC-NOT gate's performance was characterized by classical transmission measurements for different input polarizations. The swept C-band tunable laser was linearly polarized by an input polarizer to excite TE-like and TM-like modes at the input of the silicon waveguide. For both polarization characterization measurements, polarized light is input from the same side of the waveguide and the output light is measured by adjusting the polarization axis of the output polarizer. Appendix Fig. C6 shows the measured extinction ratio of the MC-NOT gate. We obtain an extinction ratio of more than 20 dB in the C-band, agreeing well with our numerical simulations for the polarization-conversion extinction ratios (shown in Appendix Fig. C6 inset). This extinction value is

mainly limited by the alignments of rotation angles between the collimating fibers and the waveguide. These good performance characteristics of the individual PC-NOT and MC-NOT gates bode well for the overall SWAP operation that is realized with the PC-NOT, MC-NOT, PC-NOT cascade.

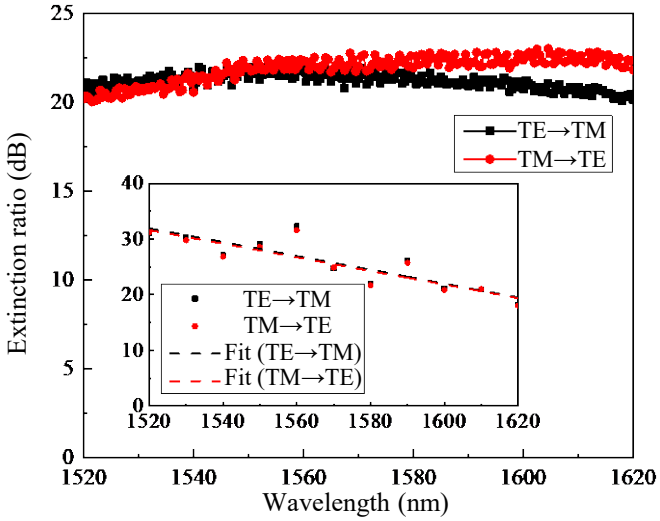

Appendix Fig. C6. Characterization of the silicon integrated photonics MC-NOT gate. Measured extinction ratios of the MC-NOT gate obtained by wavelength scanning across a 100-nm spectrum. Inset: extinction-ratio modeling the MC-NOT gate across a 100-nm spectrum.

C.3 Spectral and broadband characterization of the two-qubit SWAP gate

Appendix Fig. C7 summarizes the cross-talk characterization of the SWAP gate, with 16 input-output states and for wavelengths from 1550 nm to 1560 nm. We characterized the SWAP gate architecture with a swept C-band tunable laser. Input polarization states were prepared with bulk optics and fed to the SWAP gate chip through a 2-in 2-out free-space fiber coupling system to access the top and bottom channels. Thus, the cross-talk of the SWAP gate was characterized for the four-basis states: $|TH\rangle$, $|TV\rangle$, $|BH\rangle$ and $|BV\rangle$. Consistent performance was achieved from 1550 nm to 1560 nm with extinction ratios of more than 12 dB obtained for all four inputs. Spectral variations were observed due to laser instability and uneven waveguide coupling misalignment at different wavelengths. The extinction ratio of the SWAP gate is mainly bounded by the finite extinction ratios of the PC-NOT and MC-NOT gates, and also by the polarization misalignment between the output waveguide mode and the projection polarizers. These limits are due to imperfect fabrication and waveguide surface and sidewall roughness, resulting in propagation loss and impure optical modes. Higher extinction ratios can be realized by using a better fabrication process [265, 275, 276].

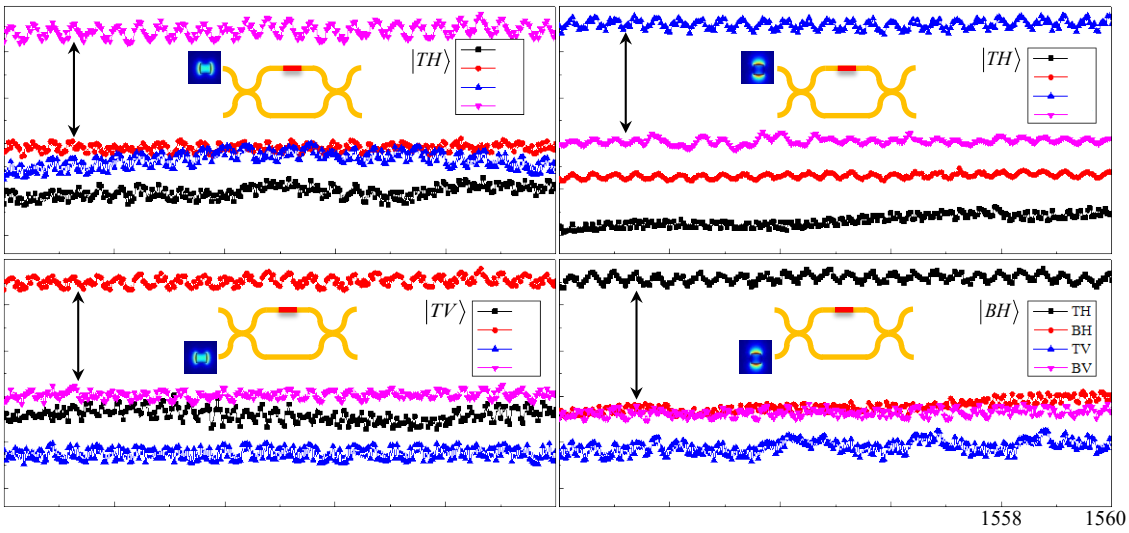

Appendix Fig. C7. Characterization of cross-talk suppression in the SWAP gate, for 16 input-output state combinations. Measurements were taken from 1550 nm to 1560 nm, covering the $|T\rangle, |B\rangle, |H\rangle, |V\rangle$ combinations. At least 12 dB cross-talk suppression was observed across all states, and was bounded primarily by the finite polarization extinction ratio in the PC-NOT and MC-NOT gates.

In Appendix Fig. C8 we illustrate the broader-band 100-nm transmission spectrum of the SWAP gate (using another device on the same chip), from 1520 nm to 1620 nm. Good performance can still be achieved in the optical telecommunications C-band with more than 12 dB cross-talk suppression. The four-basis state cross-talk arises mainly from the finite polarization extinction ratio of the PC-NOT and MC-NOT gates. The decreased cross-talk suppression at longer wavelengths is attributed to the free-space to chip coupling falloff at those wavelengths. The chip's insertion loss is related to fabrication defects and waveguide surface roughness, which affect the coupling and transmission losses. The total (input-chip-output) insertion loss can be further reduced to below 6 dB by better engineering of the coupler structure.

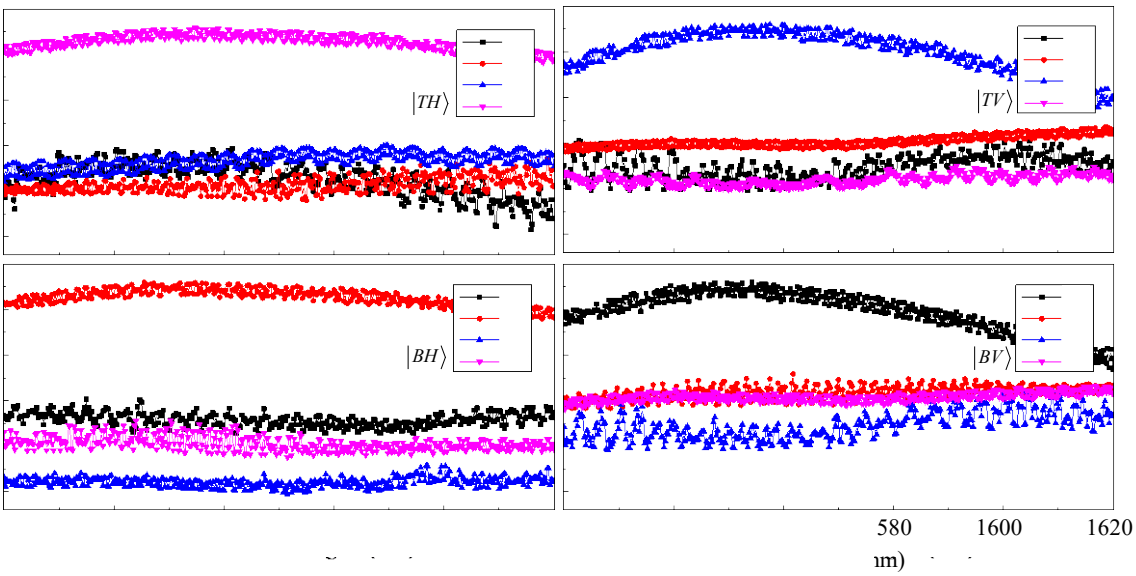

Appendix Fig. C8. Cross-talk characterization between different input-output ports and polarization combinations scanning across 100 nm spectrum. Within the optical communications C-band (1530 nm to 1565 nm), a cross-talk suppression of more than 12 dB is obtained across the four bases in our silicon SWAP gate.

C.4 Impact of imbalanced photon loss and cross-polarization suppression on the SWAP gate fidelity

In order to improve our SWAP gate's performance in pursuit of near-unity gate fidelity, we analyzed the impact on fidelity of imperfect qubit rotation, spatial-mode contamination from cross-polarization suppression, and unbalanced photon loss. First, we used the simulation results from Appendix. C.1 to model the truth tables of our PC-NOT, MC-NOT and SWAP gates. These are shown in Appendix Fig. C9a to C9c, respectively. According to our SWAP gate design parameters, we predict average gate fidelities of 98.64% for our PC-NOT gate, 99.27% for our MC-NOT gate and 98.23% for our SWAP gate. We also plot the gate fidelities as a function of the extinction ratios of the PC-NOT and MC-NOT gates in Appendix Fig. C9d and C9e, based on the transformation matrix model. We define output states as Output = $M_{PC} \times M_{MC} \times M_{PC} \times$Input, where M_{PC} and M_{MC} are the transformation matrices of the PC-NOT and MC-NOT gates, respectively. The modelled fidelities are calculated for various extinction ratios of the PC-NOT and MC-NOT gates. According to the characterization of individual PC-NOT and MC-NOT gates in Appendix. C.1 and C.2, we can

calculate the modelled fidelities with the measured extinction ratio of each gate. With the measured extinction ratio of 19.1 dB for the PC-NOT gate, we obtained a modelled fidelity of 98.79% for the SWAP gate operation; with the measured extinction ratio of 22.0 dB for the MC-NOT gate, we estimated a SWAP gate fidelity of 99.69%. Both fidelities are calculated while assuming other components are perfect at between 1556 nm and 1558 nm. Here, we also plot the fidelities as a function of the photon loss of the MC-NOT gate in Appendix Fig. C9f. Taking account of the imperfect extinction ratios of each individual C-NOT gate and the unbalanced loss, we estimated a gate fidelity of 97.70% assuming 0.2 dB photon loss of the MC-NOT gate, agreeing well with the experimental results shown in Sec. 4.3 (97.21 ± 0.14%). We attribute the ~ 0.55% fidelity imperfection to the photon loss of the silicon waveguide and the coupling efficiency difference between different input and output states.

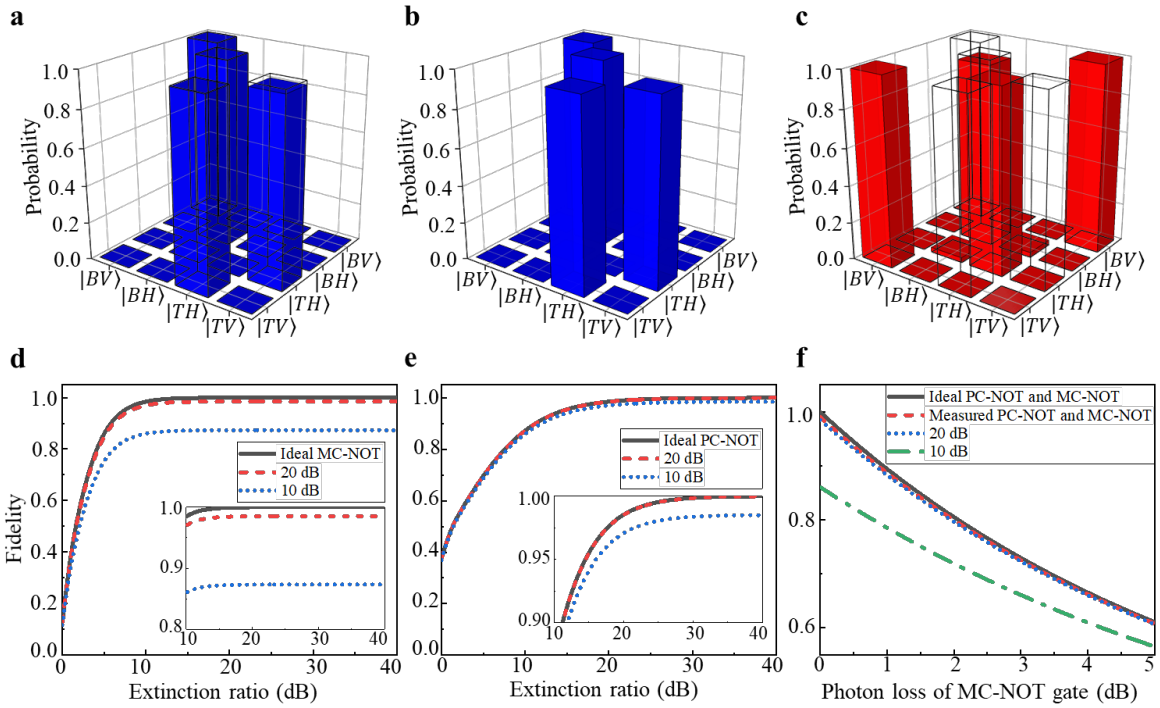

Appendix Fig. C9. Fidelity modelling for SWAP input-output gate fidelity vs. TE-TM extinction ratios of the PC-NOT and MC-NOT gates, and loss of the MC-NOT gate. a) to c) Truth tables calculated for the PC-NOT, MC-NOT and SWAP gates, based on the simulation results in Supplementary Section II, yields average gate fidelities of 98.64%, 99.27% and 98.23%, respectively. d) and e) The modelled fidelities versus the PC-NOT gates' extinction ratio for various MC-NOT gate extinction ratios, and the MC-NOT gate's extinction ratio for various PC-NOT gate extinction ratios. Inset is the zoom-in view near the high-fidelity region. f) Modelled fidelities as functions of photon

loss of MC-NOT gate for different extinction ratios of the PC-NOT and MC-NOT gates. Based on our device characterization results in Section. II, we calculated average gate fidelity of 97.70% for four-basis input states, assuming 0.2 dB photon loss from the MC-NOT gate.

C.5 Bell-CHSH correlation coefficients from polarization interference measurement after the SWAP operation

In this section, we present the measured Bell-CHSH correlation coefficients for four different input-output combinations, for the results shown in Sec. 4.5.

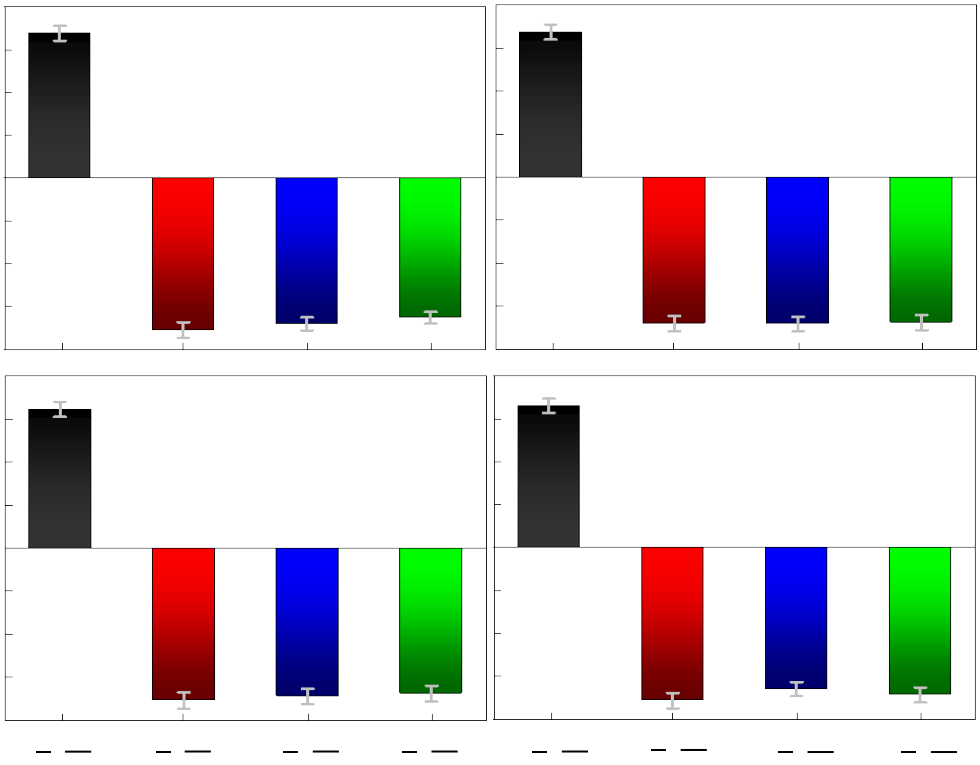

Appendix Fig. C10. Measured Bell-CHSH correlation coefficients for four different input-output combinations. For $|T_{in}\rangle|T_{out}\rangle$, we measured S_{CHSH} is 2.720 ± 0.054; for $|T_{in}\rangle|B_{out}\rangle$, S_{CHSH} is measured to be 2.721 ± 0.056; for $|B_{in}\rangle|T_{out}\rangle$, the measured S_{CHSH} is 2.716 ± 0.055; for $|B_{in}\rangle|B_{out}\rangle$, S_{CHSH} is measured to be 2.720 ± 0.053.

According to the measured polarization interference fringes in Sec. 4.5, we calculated both the parameters S_{CHSH} and S_{fringe}. The correlation coefficient, $E(\theta_1, \theta_2)$, for signal and idler polarization

projection onto the angle set (θ_1, θ_2) is obtained from coincidence-count measurements. Appendix Fig. C10 shows the measured Bell-CHSH correlation coefficients for four different input-output combinations.

According to these correlation coefficients, we calculate the CHSH *S*-parameter, for the top-channel input, the mean measured S_{CHSH} is 2.720 ± 0.055, which violates the CHSH inequality by 13.09 standard deviations; For the bottom-channel input, the mean measured S_{CHSH} is calculated to be 2.718 ± 0.054, which violates the CHSH inequality by 13.30 standard deviations. The measured S_{CHSH} and S_{fringe} values are in good agreement, which confirms the high level of mode overlap after the SWAP operation of our gate. We also note the small discrepancy between the measured S_{CHSH} and the Tsirelson's bound of $2\sqrt{2}$ [277], which results from misalignment of the measurement projectors, flux fluctuations of the two-photon source, and chip coupling.

References

[1] T. Vértesi, S. Pironio, and N. Brunner, Closing the detection loophole in Bell experiments using qudits, Phys. Rev. Lett. **104**, 060401 (2010).

[2] L. K. Shalm, E. Meyer-Scott, B. G. Christensen, P. Bierhorst, M. A. Wayne, M. J. Stevens, T. Gerrits, S. Glancy, D. R. Hamel, M. S. Allman, and K. J. Coakley, Strong loophole-free test of local realism, Phys. Rev. Lett. **115**, 250402 (2015).

[3] M. Giustina, M. A. Versteegh, S. Wengerowsky, J. Handsteiner, A. Hochrainer, K. Phelan, F. Steinlechner, J. Kofler, J. Å. Larsson, C. Abellán, and W. Amaya, Significant-loophole-free test of Bell's theorem with entangled photons, Phys. Rev. Lett. **115**, 250401 (2015).

[4] F. Vedovato, C. Agnesi, M. Tomasin, M. Avesani, J. Å. Larsson, G. Vallone, and P. Villoresi, Postselection-loophole-free Bell violation with genuine time-bin entanglement, Phys. Rev. Lett. **121**, 190401 (2018).

[5] I. Ali-Khan, C. J. Broadbent, and J. C. Howell, Large-alphabet quantum key distribution using energy-time entangled bipartite states, Phys. Rev. Lett. **98**, 060503 (2007).

[6] T. Zhong, H. Zhou, R. D. Horansky, C. Lee, V. B. Verma, A. E. Lita, A. Restelli, J. C. Bienfang, R. P. Mirin, T. Gerrits, S. W. Nam, F. Marsili, M. D. Shaw, Z. Zhang, L. Wang, D. Englund, G. W. Wornell, J. H. Shapiro, and F. N. C. Wong, Photon-efficient quantum key distribution using time-energy entanglement with high-dimensional encoding, New J. Phys. **17**, 022002 (2015).

[7] N. T. Islam, C. C. W. Lim, C. Cahall, J. Kim, and D. J. Gauthier, Provably secure and high-rate quantum key distribution with time-bin qudits, Sci. Adv. **3**, e1701491 (2017).

[8] M. Epping, H. Kampermann, and D. Bruß, Multi-partite entanglement can speed up quantum key distribution in networks, New J. Phys. **19**, 093012 (2017).

[9] C. Lee, D. Bunandar, Z. Zhang, G. R. Steinbrecher, P. B. Dixon, F. N. C. Wong, J. H. Shapiro, S. A. Hamilton, and D. Englund, Large-alphabet encoding for higher-rate quantum key distribution, Opt. Express **27**, 17539-17549 (2019).

[10] I. Vagniluca, B. Da Lio, D. Rusca, D. Cozzolino, Y. Ding, H. Zbinden, A. Zavatta, L. K. Oxenløwe, and D. Bacco, Efficient time-bin encoding for practical high-dimensional quantum key distribution, Phys. Rev. Appl. **14**, 014051 (2020).

[11] H. Bechmann-Pasquinucci, and A. Peres, Quantum cryptography with 3-state systems, Phys. Rev. Lett. **85**, 3313 (2000).

[12] N. J. Cerf, M. Bourennane, A. Karlsson, and N. Gisin, Security of quantum key distribution using d-level systems, Phys. Rev. Lett. **88**, 127902 (2002).

[13] S. Ecker, F. Bouchard, L. Bulla, F. Brandt, O. Kohout, F. Steinlechner, R. Fickler, M. Malik, Y. Guryanova, R. Ursin, and M. Huber, Overcoming noise in entanglement distribution, Phys. Rev. X **9**, 041042 (2019).

[14] F. Zhu, M. Tyler, N. H. Valencia, M. Malik, and J. Leach, Is high-dimensional photonic entanglement robust to noise? AVS Quan. Sci. **3**, 011401 (2021).

[15] M. Doda, M. Huber, G. Murta, M. Pivoluska, M. Plesch, and C. Vlachou, Quantum key distribution overcoming extreme noise: simultaneous subspace coding using high-dimensional entanglement, Phys. Rev. Appl. **15**, 034003 (2021).

[16] B. Koczor, S. Endo, T. Jones, Y. Matsuzaki, and S. C. Benjamin, Variational-state quantum metrology, New J. Phys. **22**, 083038 (2020).

[17] M. Tsang, F. Albarelli, and A. Datta, Quantum semiparametric estimation, Phys. Rev. X **10**, 031023 (2020).

[18] B. P. Lanyon, M. Barbieri, M. P. Almeida, T. Jennewein, T. C. Ralph, K. J. Resch, G. J. Pryde, J.

L. O'brien, A. Gilchrist, and A. G. White, Simplifying quantum logic using higher-dimensional Hilbert spaces, Nat. Phys. **5**, 134-140 (2009).

[19] I. M. Georgescu, S. Ashhab, and F. Nori, Quantum simulation, Rev. Mod. Phys. **86**, 153 (2014).

[20] D.-S. Wang, D. T. Stephen, and R. Raussendorf, Qudit quantum computation on matrix product states with global symmetry, Phys. Rev. A **95**, 032312 (2017).

[21] S. McArdle, S. Endo, A. Aspuru-Guzik, S. C. Benjamin, and X. Yuan, Quantum computational chemistry, Rev. Mod. Phys. **92**, 015003 (2020).

[22] J. Zhang, G. Pagano, P. W. Hess, A. Kyprianidis, P. Becker, H. Kaplan, A. V. Gorshkov, Z.-X. Gong and C. Monroe, Observation of a many-body dynamical phase transition with a 53-qubit quantum simulator, Nature **551**, 601-604 (2017).

[23] F. Arute, K. Arya, R. Babbush, D. Bacon, J. C. Bardin, R. Barends, R. Biswas, S. Boixo, F. G. S. L. Brandao, D. A. Buell, B. Burkett, Y. Chen, Z. Chen, B. Chiaro, R. Collins, W. Courtney, A. Dunsworth, E. Farhi, B. Foxen, A. Fowler, C. Gidney, M. Giustina, R. Graff, K. Guerin, S. Habegger, M. P. Harrigan, M. J. Hartmann, A. Ho, M. Hoffmann, T. Huang, T. S. Humble, S. V. Isakov, E. Jeffrey, Z. Jiang, D. Kafri, K. Kechedzhi, J. Kelly, P. V. Klimov, S. Knysh, A. Korotkov, F. Kostritsa, D. Landhuis, M. Lindmark, E. Lucero, D. Lyakh, S. Mandrà, J. R. McClean, M. McEwen, A. Megrant, X. Mi, K. Michielsen, M. Mohseni, J. Mutus, O. Naaman, M. Neeley, C. Neill, M. Y. Niu, E. Ostby, A. Petukhov, J. C. Platt, C. Quintana, E. G. Rieffel, P. Roushan, N. C. Rubin, D. Sank, K. J. Satzinger, V. Smelyanskiy, K. J. Sung, M. D. Trevithick, A. Vainsencher, B. Villalonga, T. White, Z. J. Yao, P. Yeh, A. Zalcman, H. Neven and J. M. Martinis, Quantum supremacy using a programmable superconducting processor, Nature **574**, 505-510 (2019).

[24] J. M. Arrazola, V. Bergholm, K. Brádler, T. R. Bromley, M. J. Collins, I. Dhand, A. Fumagalli, T. Gerrits, A. Goussev, L. G. Helt, J. Hundal, T. Isacsson, R. B. Israel, J. Izaac, S. Jahangiri, R. Janik, N. Killoran, S. P. Kumar, J. Lavoie, A. E. Lita, D. H. Mahler, M. Menotti, B. Morrison, S. W. Nam, L. Neuhaus, H. Y. Qi, N. Quesada, A. Repingon, K. K. Sabapathy, M. Schuld, D. Su, J. Swinarton, A. Száva, K. Tan, P. Tan, V. D. Vaidya, Z. Vernon, Z. Zabaneh and Y. Zhang, Quantum circuits with

many photons on a programmable nanophotonic chip, Nature **591**, 54-60 (2021).

[25] S. L. Braunstein, and P. Van Loock, Quantum information with continuous variables, Rev. Mod. Phys. **77**, 513 (2005).

[26] C. Weedbrook, S. Pirandola, R. García-Patrón, N. J. Cerf, T. C. Ralph, J. H. Shapiro, and S. Lloyd, Gaussian quantum information, Rev. Mod. Phys. **84**, 621 (2012).

[27] P. Kok, W. J. Munro, K. Nemoto, T. C. Ralph, J. P. Dowling, and G. J. Milburn, Linear optical quantum computing with photonic qubits, Rev. Mod. Phys. **79**, 135 (2007).

[28] R. Horodecki, P. Horodecki, M. Horodecki, and K. Horodecki, Quantum entanglement, Rev. Mod. Phys. **81**, 865 (2009).

[29] J. W. Pan, Z. B. Chen, C. Y. Lu, H. Weinfurter, A. Zeilinger, and M. Żukowski, Multiphoton entanglement and interferometry, Rev. Mod. Phys. **84**, 777 (2012).

[30] B. E. Kardynał, Z. L. Yuan, and A. J. Shields, An avalanche-photodiode-based photon-number-resolving detector, Nat. Photon. **2**, 425-428 (2008).

[31] N. C. Menicucci, S. T. Flammia, and O. Pfister, One-way quantum computing in the optical frequency comb, Phys. Rev. Lett. **101**, 130501 (2008).

[32] O. Pinel, P. Jian, R. M. De Araujo, J. Feng, B. Chalopin, C. Fabre, and N. Treps, Generation and characterization of multimode quantum frequency combs, Phys. Rev. Lett. **108**, 083601 (2012).

[33] S. Yokoyama, R. Ukai, S. C. Armstrong, C. Sornphiphatphong, T. Kaji, S. Suzuki, J.-I Yoshikawa, H. Yonezawa, N. C. Menicucci and A. Furusawa, Ultra-large-scale continuous-variable cluster states multiplexed in the time domain, Nat. Photon. **7**, 982-986 (2013).

[34] M. Chen, N. C. Menicucci, and O. Pfister, Experimental realization of multipartite entanglement of 60 modes of a quantum optical frequency comb, Phys. Rev. Lett. **112**, 120505 (2014).

[35] J. Roslund, R. M. de Araújo, S. Jiang, C. Fabre, and N. Treps, Wavelength- multiplexed quantum networks with ultrafast frequency combs, Nat. Photon. **8**, 109-112 (2014).

[36] S. Gerke, J. Sperling, W. Vogel, Y. Cai, J. Roslund, N. Treps, and C. Fabre, Full multipartite entanglement of frequency-comb Gaussian states, Phys. Rev. Lett. **114**, 050501 (2015).

[37] Y. Cai, J. Roslund, G. Ferrini, F. Arzani, X. Xu, C. Fabre and N. Treps, Multimode entanglement in reconfigurable graph states using optical frequency combs, Nat. Commun. **8**, 1-9 (2017).

[38] X. Zhu, C.-H. Chang, C. González-Arciniegas, A. Pe'er, J. Higgins, and O. Pfister, Hypercubic cluster states in the phase-modulated quantum optical frequency comb, Optica **8**, 281-290 (2021).

[39] S. Armstrong, J. F. Morizur, J. Janousek, B. Hage, N. Treps, P. K. Lam, and H. A. Bachor, Programmable multimode quantum networks, Nat. Commun. **3**, 1-8 (2012).

[40] M. V. Larsen, X. Guo, C. R. Breum, J. S. Neergaard-Nielsen, and U. L. Andersen, Deterministic generation of a two-dimensional cluster state, Science **366**, 369-372 (2019).

[41] J. Wang, S. Paesani, Y. Ding, R. Santagati, P. Skrzypczyk, A. Salavrakos, J. Tura, R. Augusiak, L. Mancinska, D. Bacco, D. Bonneau, J. W. Silverstone, Q. Gong, A. Acin, K. Rottwitt, L. K. Oxenlowe, J. L. O'Brien, A. Laing, and M. G. Thompson, Multidimensional quantum entanglement with large-scale integrated optics, Science **360**, 285-291 (2018).

[42] X. Qiang, X. Zhou, J. Wang, C. M. Wilkes, T. Loke, S. O'Gara, L. Kling, G. D. Marshall, R. Santagati, T. C. Ralph, J. B. Wang, J. L. O'Brien, M. G. Thompson, and J. C. F. Matthews, Large-scale silicon quantum photonics implementing arbitrary two-qubit processing, Nat. Photon. **12**, 534-539 (2018).

[43] J. C. Adcock, C. Vigliar, R. Santagati, J. W. Silverstone, and M. G. Thompson, Programmable four-photon graph states on a silicon chip, Nat. Commun. **10**, 1-6 (2019).

[44] D. Llewellyn, Y. Ding, I. I. Faruque, S. Paesani, D. Bacco, R. Santagati, Y.-J. Qian, Y. Li, Y.-F. Xiao, and M. Huber, Chip-to-chip quantum teleportation and multi-photon entanglement in silicon, Nat. Phys. **16**, 148-153 (2019).

[45] H. Wang, Y.-M. He, T.-H. Chung, H. Hu, Y. Yu, S. Chen, X. Ding, M.-C. Chen, J. Qin, X. Yang, R.-Z. Liu, Z.-C. Duan, J.-P. Li, S. Gerhardt, K. Winkler, J. Jurkat, L.-J. Wang, N. Gregersen, Y.-H. Huo, Q. Dai, S. Yu, S. Höfling, C.-Y. Lu and J.-W. Pan, Towards optimal single-photon sources from polarized microcavities, Nat. Photon. **13**, 770-775 (2019).

[46] R. Uppu, H. T. Eriksen, H. Thyrrestrup, A. D. Uğurlu, Y. Wang, S. Scholz, A. D. Wieck, A. Ludwig, M. C. Löbl, R. J. Warburton, P. Lodahl and L. Midolo, On-chip deterministic operation of quantum dots in dual-mode waveguides for a plug-and-play single-photon source. Nat. Commun. **11**, 1-6 (2020).

[47] F. Marsili, V. B. Verma, J. A. Stern, S. Harrington, A. E. Lita, T. Gerrits, I. Vayshenker, B. Baek, M. D. Shaw, R. P. Mirin and S. W. Nam, Detecting single infrared photons with 93% system efficiency, Nat. Photon. **7**, 210-214 (2013).

[48] D. V. Reddy, R. R. Nerem, S. W. Nam, R. P. Mirin, and V. B. Verma, Superconducting nanowire single-photon detectors with 98% system detection efficiency at 1550 nm, Optica **7**, 1649-1653 (2020).

[49] J. Chang, J. W. N. Los, J. O. Tenorio-Pearl, N. Noordzij, R. Gourgues, A. Guardiani, J. R. Zichi, S. F. Pereira, H. P. Urbach, V. Zwiller, S. N. Dorenbos, and I. Esmaeil Zadeh, Detecting telecom single photons with 99.5-2.07+0.5% system detection efficiency and high time resolution, APL Photon. **6**, 036114 (2021).

[50] Y. Hochberg, I. Charaev, S. W. Nam, V. Verma, M. Colangelo, and K. K., Berggren, Detecting sub-GeV dark matter with superconducting nanowires, Phys. Rev. Lett. **123**, 151802 (2019).

[51] B. Korzh, Q.-Y. Zhao, J. P. Allmaras, S. Frasca, T. M. Autry, E. A. Bersin, A. D. Beyer, R. M. Briggs, B. Bumble, M. Colangelo, G. M. Crouch, A. E. Dane, T. Gerrits, A. E. Lita, F. Marsili, G. Moody, C. Peña, E. Ramirez, J. D. Rezac, N. Sinclair, M. J. Stevens, A. E. Velasco, V. B. Verma, E.

E. Wollman, S. Xie, D. Zhu, P. D. Hale, M. Spiropulu, K. L. Silverman, R. P. Mirin, S. W. Nam, A. G. Kozorezov, M. D. Shaw, and K. K. Berggren, Demonstration of sub-3 ps temporal resolution with a superconducting nanowire single-photon detector, Nat. Photon. **14**, 250 (2020).

[52] D. Bouwmeester, J. W. Pan, M. Daniell, H. Weinfurter, and A. Zeilinger, Observation of three-photon Greenberger-Horne-Zeilinger entanglement, Phys. Rev. Lett. **82**, 1345 (1999).

[53] A. Mair, A. Vaziri, G. Weihs, and A. Zeilinger, Entanglement of the orbital angular momentum states of photons, Nature **412**, 313-316 (2001).

[54] A. Vaziri, G. Weihs, and A. Zeilinger, Experimental two-photon, three-dimensional entanglement for quantum communication, Phys. Rev. Lett. **89**, 240401 (2002).

[55] A. Vaziri, J. W. Pan, T. Jennewein, G. Weihs, and A. Zeilinger, Concentration of higher dimensional entanglement: qutrits of photon orbital angular momentum, Phys. Rev. Lett. **91**, 227902 (2003).

[56] P. Walther, K. J. Resch, T. Rudolph, E. Schenck, H. Weinfurter, V. Vedral, M. Aspelmeyer, and A. Zeilinger, Experimental one-way quantum computing, Nature **434**, 169-176 (2005).

[57] G. Vallone, G. Donati, R. Ceccarelli, and P. Mataloni, Six-qubit two-photon hyperentangled cluster states: Characterization and application to quantum computation, Phys. Rev. A **81**, 052301 (2010).

[58] A. C. Dada J. Leach, G. S. Buller, M. J. Padgett, E. Andersson, Experimental high-dimensional two-photon entanglement and violations of generalized Bell inequalities, Nat. Phys. **7**, 677-680 (2011).

[59] J. Romero, D. Giovannini, S. Franke-Arnold, S. M. Barnett, and M. J. Padgett, Increasing the dimension in high-dimensional two-photon orbital angular momentum entanglement, Phys. Rev. A **86**, 012334 (2012).

[60] M. Krenn, M. Huber, R. Fickler, R. Lapkiewicz, S. Ramelow, and A. Zeilinger, Generation and

confirmation of a (100×100)-dimensional entangled quantum system, Proc. Natl Acad. Sci. **111**, 6243-6247 (2014).

[61] A. E. Willner, H. Huang, Y. Yan, Y. Ren, N. Ahmed, G. Xie, C. Bao, L. Li, Y. Cao, Z. Zhao, J. Wang, M. P. J. Lavery, M. Tur, S. Ramachandran, A. F. Molisch, N. Ashrafi, and S. Ashrafi, Optical communications using orbital angular momentum beams, Adv. Opt. Photon. **7**, 66-106 (2015).

[62] M. Malik, M. Erhard, M. Huber, M. Krenn, R. Fickler, and A. Zeilinger, Multi-photon entanglement in high dimensions, Nat. Photon. **10**, 248-252 (2016).

[63] M. Krenn, J. Handsteiner, M. Fink, R. Fickler, R. Ursin, M. Malik, and A. Zeilinger, Twisted light transmission over 143 km, Proc. Natl. Acad. Sci. **113**, 13648-13653 (2016).

[64] A. Babazadeh, M Erhard, F. Wang, M. Malik, R. Nouroozi, M. Krenn, and A. Zeilinger, High-dimensional single-photon quantum gates: concepts and experiments, Phys. Rev. Lett. **119**, 180510 (2017).

[65] F. Wang, M. Erhard, A. Babazadeh, M. Malik, M. Krenn, and A. Zeilinger, Generation of the complete four-dimensional Bell basis, Optica **4**, 1462-1467 (2017).

[66] M. Krenn, A. Hochrainer, M. Lahiri, and A. Zeilinger, Entanglement by path identity, Phys. Rev. Lett. **118**, 080401 (2017).

[67] M. Erhard, R. Fickler, M. Krenn, and A. Zeilinger, Twisted photons: new quantum perspectives in high dimensions, Light: Sci. Appl. **7**, 17146 (2018).

[68] D. Cozzolino, D. Bacco, B. Da Lio, K. Ingerslev, Y. Ding, K. Dalgaard, P. Kristensen, M. Galili, K. Rottwitt, S. Ramachandran, and L. K. Oxenløwe, Orbital angular momentum states enabling fiber-based high-dimensional quantum communication, Phys. Rev. Appl. **11**, 064058 (2019).

[69] F. Brandt, M. Hiekkamäki, F. Bouchard, M. Huber, and R. Fickler, High-dimensional quantum gates using full-field spatial modes of photons, Optica **7**, 98-107 (2020).

[70] J. Kysela, M. Erhard, A. Hochrainer, M. Krenn, and A. Zeilinger, Path identity as a source of high-dimensional entanglement, Proc. Natl. Acad. Sci. **117**, 26118-26122 (2020).

[71] Z. Y. Ou, and Y. J. Lu, Cavity enhanced spontaneous parametric down-conversion for the prolongation of correlation time between conjugate photons, Phys. Rev. Lett. **83**, 2556 (1999).

[72] Y. J. Lu, R. L. Campbell, and Z. Y. Ou, Mode-locked two-photon states, Phys. Rev. Lett. **91**, 163602 (2003).

[73] C. Reimer, L. Caspani, M. Clerici, M. Ferrera, M. Kues, M. Peccianti, A. Pasquazi, L. Razzari, B. E. Little, S. T. Chu, D. J. Moss, and R. Morandotti, Integrated frequency comb source of heralded single photons, Opt. Express **22**, 6535-6546 (2014).

[74] C. Reimer, M. Kues, L. Caspani, B. Wetzel, P. Roztocki, M. Clerici, Y. Jestin, M. Ferrera, M. Peccianti, A. Pasquazi, B. E. Little, S. T. Chu, D. J. Moss and R. Morandotti, Cross-polarized photon-pair generation and bi-chromatically pumped optical parametric oscillation on a chip, Nat. Commun. **6**, 1-7 (2015).

[75] Z. Xie, T. Zhong, S. Shrestha, X. Xu, J. Liang, Y. X. Gong, J.C. Bienfang, A. Restelli, J. H. Shapiro, F. N. C. Wong, and C. W. Wong, Harnessing high-dimensional hyperentanglement through a biphoton frequency comb, Nat. Photon. **9**, 536-542 (2015).

[76] C. Reimer, M. Kues, P. Roztocki, B. Wetzel, F. Grazioso, B. E. Little, S. T. Chu, T. Johnston, Y. Bromberg, L. Caspani, D. J. Moss, and R. Morandotti, Generation of multiphoton entangled quantum states by means of integrated frequency combs, Science **351**, 1176-1180 (2016).

[77] J. A. Jaramillo-Villegas, P. Imany, O. D. Odele, D. E. Leaird, Z.-Y. Ou, M. Qi, and A. M. Weiner, Persistent energy-time entanglement covering multiple resonances of an on-chip biphoton frequency comb, Optica **4**, 655-658 (2017).

[78] M. Kues, C. Reimer, P. Roztocki, L. R. Cortés, S. Sciara, B. Wetzel, Y. Zhang, A. Cino, S. T.

Chu, B. E. Little, D. J. Moss, L. Caspani, J. Azaña, and R. Morandotti, On-chip generation of high-dimensional entangled quantum states and their coherent control, Nature **546**, 622-626 (2017).

[79] H.-H. Lu, J. M. Lukens, N. A. Peters, O. D. Odele, D. E. Leaird, A. M. Weiner, and P. Lougovski, Electro-optic frequency beam splitters and tritters for high-fidelity photonic quantum information processing, Phys. Rev. Lett. **120**, 030502 (2018).

[80] P. Imany, J. A. Jaramillo-Villegas, O. D. Odele, K. Han, D. E. Leaird, J. M. Lukens, P. Lougovski, M. Qi, and A. M. Weiner, 50-GHz-spaced comb of high-dimensional frequency-bin entangled photons from an on-chip silicon nitride microresonator, Opt. Express **26**, 1825-1840 (2018).

[81] H.-H. Lu, O. D. Odele, D. E. Leaird, and A. M. Weiner, Arbitrary shaping of biphoton correlations using near-field frequency-to-time mapping, Opt. Lett. **43**, 743-746 (2018).

[82] P. Imany, O. D. Odele, M. S. Alshaykh, H.-H. Lu, D. E. Leaird, and A. M. Weiner, Frequency-domain Hong-Ou-Mandel interference with linear optics, Opt. Lett. **43**, 2760-2763 (2018).

[83] H.-H. Lu, J. M. Lukens, N. A. Peters, B. P. Williams, A. M. Weiner, and P. Lougovski, Quantum interference and correlation control of frequency-bin qubits, Optica **5**, 1455-1460 (2018).

[84] C. Reimer, S. Sciara, P. Roztocki, M. Islam, L. R. Cortés, Y. Zhang, B. Fisher, S. Loranger, R. Kashyap, A. Cino, S. T. Chu, B. E. Little, D. J. Moss, L. Caspani, W. J. Munro, J. Azaña, M. Kues, and R. Morandotti, High-dimensional one-way quantum processing implemented on d-level cluster states, Nat. Phys. **15**, 148-153 (2019).

[85] H.-H. Lu, J. M. Lukens, B. P. Williams, P. Imany, N. A. Peters, A. M. Weiner, and P. Lougovski, A controlled-NOT gate for frequency-bin qubits, npj. Quan. Inf. **5**, 1-8 (2019).

[86] P. Imany, J. A. Jaramillo-Villegas, M. S. Alshaykh, J. M. Lukens, O. D. Odele, A. J. Moore, D. E. Leaird, M. Qi and A. M. Weiner, High-dimensional optical quantum logic in large operational spaces. npj. Quan. Inf. **5**, 1-10 (2019).

[87] H.-H. Lu, N. Klco, J. M. Lukens, T. D. Morris, A. Bansal, A. Ekström, G. Hagen, T. Papenbrock, A. M. Weiner, M. J. Savage, and P. Lougovski, Simulations of subatomic many-body physics on a quantum frequency processor, Phys. Rev. A **100**, 012320 (2019).

[88] N. B. Lingaraju, H.-H. Lu, S. Seshadri, P. Imany, D. E. Leaird, J. M. Lukens, and A. M. Weiner, Quantum frequency combs and Hong-Ou-Mandel interferometry: the role of spectral phase coherence, Opt. Express **27**, 38683-38697 (2019).

[89] H.-H. Lu, Quantum Information Processing With Frequency-Bin Qudits, Doctoral dissertation, Purdue University Graduate School (2020).

[90] P. Imany, N. B. Lingaraju, M. S. Alshaykh, D. E. Leaird, and A. M. Weiner, Probing quantum walks through coherent control of high-dimensionally entangled photons, Sci. Adv. **6**, eaba8066 (2020).

[91] H.-H. Lu, E. M. Simmerman, P. Lougovski, A. M. Weiner, and J. M. Lukens, Fully arbitrary control of frequency-bin qubits, Phys. Rev. Lett. **125**, 120503 (2020).

[92] K.-C. Chang, X. Cheng, M. C. Sarihan, A. V. Kumar, Y. S. Lee, T. Zhong, Y.-X. Gong, Z. Xie, J. H. Shapiro, F. N. C. Wong, and C. W. Wong, 648 Hilbert Space Dimensionality in a Biphoton Frequency Comb: entanglement of formation and Schmidt mode decomposition, npj Quan. Inf. **7**, 48 (2021).

[93] L. Lu, L. Xia, Z. Chen, L. Chen, T. Yu, T. Tao, W. Ma, Y. Pan, X. Cai, Y. Lu, and S. Zhu, Three-dimensional entanglement on a silicon chip, npj Quan. Inf. **6**, 1-9 (2020).

[94] P. Kumar, Quantum frequency conversion, Opt. Lett. **15**, 1476-1478 (1990).

[95] J. M. Donohue, M. Agnew, J. Lavoie, and K. J. Resch, Coherent ultrafast measurement of time-bin encoded photons, Phys. Rev. Lett. **111**, 153602 (2013).

[96] R. Fickler, R. Lapkiewicz, M. Huber, M. P. J. Lavery, M. J. Padgett, and A. Zeilinger, Interface

between path and orbital angular momentum entanglement for high-dimensional photonic quantum information, Nat. Commun. **5**, 1-6 (2014).

[97] M. Bock, P. Eich, S. Kucera, M. Kreis, A. Lenhard, C. Becher and J. Eschner, High-fidelity entanglement between a trapped ion and a telecom photon via quantum frequency conversion, Nat. Commun. **9**, 1-7 (2018).

[98] A. P. Higginbotham, P. S. Burns, M. D. Urmey, R. W. Peterson, N. S. Kampel, B. M. Brubaker, G. Smith, K. W. Lehnert and C. A. Regal, Harnessing electro-optic correlations in an efficient mechanical converter, Nat. Phys. **14**, 1038-1042 (2018).

[99] X. Lu, Q. Li, D. A. Westly, G. Moille, A. Singh, V. Anant, and K. Srinivasan, Chip-integrated visible-telecom entangled photon pair source for quantum communication, Nat. Phys. **15**, 373-381 (2019).

[100] Z. Xie, K.-H. Luo, K.-C. Chang, N. C. Panoiu, H. Herrmann, C. Silberhorn, and C. W. Wong, Efficient C-band single-photon upconversion with chip-scale Ti-indiffused pp-$LiNbO_3$ waveguides, Appl. Opt. **58**, 5910-5915 (2019).

[101] N. Lauk, N. Sinclair, S. Barzanjeh, J. P. Covey, M. Saffman, M. Spiropulu, and C. Simon, Perspectives on quantum transduction, Quan. Sci. Technol. **5**, 020501 (2020).

[102] J. G. Bartholomew, J. Rochman, T. Xie, J. M. Kindem, A. Ruskuc, I. Craiciu, M. Lei, and A. Faraon, On-chip coherent microwave-to-optical transduction mediated by ytterbium in YVO 4, Nat. Commun. **11**, 1-6 (2020).

[103] M. Mirhosseini, A. Sipahigil, M. Kalaee, and O. Painter, Superconducting qubit to optical photon transduction, Nature **588**, 599-603 (2020).

[104] E. Altman, K. R. Brown, G. Carleo, L. D. Carr , E. Demler, C. Chin, B. DeMarco, S. E. Economou, M. A. Eriksson, K.-M. C. Fu, M. Greiner, K. R.A. Hazzard, R. G. Hulet, A. J. Kollár, B. L. Lev, M. D. Lukin, R. Ma, X. Mi, S. Misra, C. Monroe, K. Murch, Z. Nazario, K.-K. Ni, A. C. Potter,

Pe. Roushan, M. Saffman, M. Schleier-Smith, I. Siddiqi, R. Simmonds, M. Singh, I. B. Spielman, K. Temme, D. S. Weiss, J. Vučković, V. Vuletic, J. Ye, and M. Zwierlein, Quantum simulators: Architectures and opportunities, PRX Quan. **2**, 017003 (2021).

[105] Y. Alexeev, D. Bacon, K. R. Brown, R. Calderbank, L. D. Carr, F. T. Chong, B. DeMarco, D. Englund, E. Farhi, B. Fefferman, A. V. Gorshkov, A. Houck, J. Kim, S. Kimmel, M. Lange, S. Lloyd, M. D. Lukin, D. Maslov, P. Maunz, C. Monroe, J. Preskill, M. Roetteler, M. J. Savage, and J. Thompson, Quantum computer systems for scientific discovery, PRX Quan. **2**, 017001 (2021).

[106] D. Awschalom, K. K. Berggren, H. Bernien, S. Bhave, L. D. Carr, P. Davids, S. E. Economou, D. Englund, A. Faraon, M. Fejer, S. Guha, M. V. Gustafsson, E. Hu, L. Jiang, J. Kim, B. Korzh, P. Kumar, P. G. Kwiat, M. Loncar, M. D. Lukin, D. A. B. Miller, C. Monroe, S. W. Nam, P. Narang, J. S. Orcutt, M. G. Raymer, A. H. Safavi-Naeini, M. Spiropulu, K. Srinivasan, S. Sun, J. Vučković, E. Waks, R. Walsworth, A. M. Weiner, and Z. Zhang, Development of quantum interconnects (quics) for next-generation information technologies, PRX Quan. **2**, 017002 (2021).

[107] D. P. DiVincenzo, The physical implementation of quantum computation, Fortschritte der Physik: Prog. Phys. **48**, 771-783 (2000).

[108] K.-C. Chang, X. Cheng, M. C. Sarihan, D. Mendinueto, Y. S. Lee, T. Zhong, Y. Gong, Z. Xie, J. H. Shapiro, F. N. C. Wong, and C. W. Wong, High-dimensional energy-time entanglement up to 6 qubits per photon through biphoton frequency comb, in Conference on Lasers and Electro-Optics, OSA Technical Digest (Optical Society of America, 2019), paper JTu3A.6.

[109] K.-C. Chang, X. Cheng, M. C. Sarihan, A. V. Kumar, Y. S. Lee, T. Zhong, Y. Gong, Z. Xie, J. H. Shapiro, F. N. C. Wong, and C. W. Wong, High-dimensional time-frequency entanglement and Schmidt number witnesses using a biphoton frequency comb, in Conference on Lasers and Electro-Optics, OSA Technical Digest (Optical Society of America, 2020), paper JTh2A.23.

[110] K.-C. Chang, X. Cheng, M. C. Sarihan, A. V. Kumar, Y. S. Lee, T. Zhong, Y.-X. Gong, Z. Xie, J. H. Shapiro, F. N. C. Wong, and C. W. Wong, Quantification of High-dimensional Energy-time Entanglement in a Biphoton Frequency Comb, in Conference on Lasers and Electro-Optics, OSA

Technical Digest (Optical Society of America, 2021), paper FM3M.6

[111] K.-C. Chang, X. Cheng, M. C. Sarihan, F. N. C. Wong, J. H. Shapiro, and C. W. Wong, High-dimensional Energy-time Entanglement Distribution via a Biphoton Frequency Comb, in Conference on Lasers and Electro-Optics, OSA Technical Digest (Optical Society of America, 2021), paper FF1A.7

[112] E. Knill, R. Laflamme, and G. J. Milburn, A scheme for efficient quantum computation with linear optics, Nature **409**, 46-52 (2001).

[113] I. Marcikic, H. De Riedmatten, W. Tittel, H. Zbinden, M. Legré, and N. Gisin, Distribution of time-bin entangled qubits over 50 km of optical fiber, Phys. Rev. Lett. **93**, 180502 (2004).

[114] T. Honjo, H. Takesue, H., Kamada, Y. Nishida, O. Tadanaga, M. Asobe, and K. Inoue, Long-distance distribution of time-bin entangled photon pairs over 100 km using frequency up-conversion detectors, Opt. Express **15**, 13957-13964 (2007).

[115] T. Inagaki, N. Matsuda, O. Tadanaga, M. Asobe, and H. Takesue, Entanglement distribution over 300 km of fiber, Opt. Express **21**, 23241-23249 (2013).

[116] D. Aktas, B. Fedrici, F. Kaiser, T. Lunghi, L. Labonté, and S. Tanzilli, Entanglement distribution over 150 km in wavelength division multiplexed channels for quantum cryptography, Laser Photon. Rev. **10**, 451-457 (2016).

[117] F. Steinlechner, S. Ecker, M. Fink, B. Liu, J. Bavaresco, M. Huber, T. Scheidl, and R. Ursin, Distribution of high-dimensional entanglement via an intra-city free-space link, Nat. Commun. **8**, 1-7 (2017).

[118] M. C. Sarihan, K.-C. Chang, X. Cheng, Y. S. Lee, T. Zhong, H. Zhou, Z. Zhang, F. N. C. Wong, J. H. Shapiro, and C. W. Wong, High-dimensional quantum key distribution with biphoton frequency combs through energy-time entanglement, in Conference on Lasers and Electro-Optics, OSA Technical Digest (Optical Society of America, 2019), paper FTh1A.3.

[119] S. Yang, M. C. Sarihan, K.-C. Chang, C. W. Wong, and L. Dolecek, Efficient information reconciliation for energy-time entanglement quantum key distribution, In 2019 53rd Asilomar Conference on Signals, Systems, and Computers (1364-1368). IEEE.

[120] M. C. Sarihan, K.-C. Chang, X. Cheng, Y. S. Lee, C. Chen,T. Zhong, H. Zhou, Z. Zhang, F. N. C. Wong, J. H. Shapiro, and C. W. Wong, Frequency-multiplexed rate-adaptive quantum key distribution with high-dimensional encoding, in Conference on Lasers and Electro-Optics, OSA Technical Digest (Optical Society of America, 2020), paper FF3C.3.

[121] M. C. Sarihan, K.-C. Chang, X. Cheng, Y. S. Lee, C. Chen, T. Zhong, H. Zhou, Z. Zhang, F. N. C. Wong, J. H. Shapiro, and C. W. Wong, Proof-of-Principle Frequency-Bin Quantum Key Distribution with Biphoton Frequency Combs, in Conference on Lasers and Electro-Optics, OSA Technical Digest (Optical Society of America, 2021), paper ATu1S.6.

[122] X. Cheng, M. C. Sarihan, K.-C. Chang, C. Chen, F. N. C. Wong, and C. W. Wong, Secure High Dimensional Quantum Key Distribution Based on Wavelength-Multiplexed Time-Bin Encoding, in Conference on Lasers and Electro-Optics, OSA Technical Digest (Optical Society of America, 2021), paper STh1D.3.

[123] Z. Zhang, J. Mower, D. Englund, F. N. C. Wong, and J. H. Shapiro, Unconditional security of time-energy entanglement quantum key distribution using dual-basis interferometry, Phys. Rev. Lett. **112**, 120506 (2014).

[124] C. Chen, J. H. Shapiro, F. N. C. Wong, Experimental demonstration of conjugate-Franson interferometry, Phys. Rev. Lett. **127**, 093603 (2021).

[125] H. Boo, Y. S. Lee, H. Yang, K.-C. Chang, and C. W. Wong, Polarization-diverse metasurfaces for high-dimensional spatial-mode entanglement generation, in Conference on Lasers and Electro-Optics, OSA Technical Digest (Optical Society of America, 2020), paper FFTB.1.

[126] X. Cheng, K.-C. Chang, Z. Xie, Y. S. Lee, M. C. Sarihan, A. K. Vinod, Y. Li, S. Kocaman, T.

Zhong, M. Yu, D.-L. Kwong, J. H. Shapiro, F. N. C. Wong, and C. W. Wong, An efficient on-chip single-photon SWAP gate for entanglement manipulation, in Conference on Lasers and Electro-Optics, OSA Technical Digest (Optical Society of America, 2020), paper FM2R.5

[127] X. Cheng, Z. Xie, K.-C. Chang, M. C. Sarihan, Y. S. Lee, A. K. Vinod, Y. Li, X. Xu, S. Kocaman, M. Yu, D.-L. Kwong, J. H. Shapiro, F. N. C. Wong, and C. W. Wong, Quantum State Tomography of an On-chip Polarization-Spatial Qubit SWAP Gate, in Conference on Lasers and Electro-Optics, OSA Technical Digest (Optical Society of America, 2021), paper FF2I.2.

[128] M. Erhard, M. Krenn, and A. Zeilinger, Advances in high-dimensional quantum entanglement, Nat. Rev. Phys. **2**, 365-381 (2020).

[129] P. Siyushev, G. Stein, J. Wrachtrup, I. Gerhardt, Molecular photons interfaced with alkali atoms, Nature **509**, 66-70 (2014).

[130] M. Rezai, J. Wrachtrup, and I. Gerhardt, Coherence properties of molecular single photons for quantum networks, Phys. Rev. X, **8**, 031026 (2018).

[131] C. Toninelli, I. Gerhardt, A. S. Clark, A. Reserbat-Plantey, S. Götzinger, Z. Ristanović, M. Colautti, P. Lombardi, K. D. Major, I. Deperasińska, W. H. Pernice, F. H. L. Koppens, B. Kozankiewicz, A. Gourdon, V. Sandoghdar and M. Orrit, Single organic molecules for photonic quantum technologies, Nat. Mater. **20**, 1-14 (2021).

[132] S. Buckley, K. Rivoire, and J. Vučković, Engineered quantum dot single-photon sources. Rep. Prog. Phys. **75**, 126503 (2012).

[133] N. Somaschi, V. Giesz, L. De Santis, J. C. Loredo, M. P. Almeida, G. Hornecker, S. L. Portalupi, T. Grange, C. Antón, J. Demory, C. Gómez, I. Sagnes, N. D. Lanzillotti-Kimura, A. Lemaítre, A. Auffeves, A. G. White, L. Lanco and P. Senellart, Near-optimal single-photon sources in the solid state, Nat. Photon. **10**, 340-345 (2016).

[134] E. Togan, Y. Chu, A. S. Trifonov, L. Jiang, J. Maze, L. Childress, M. G. Dutt, A. S. Sørensen, P.

R. Hemmer, A. S. Zibrov, and M. D. Lukin, Quantum entanglement between an optical photon and a solid-state spin qubit, Nature **466**, 730-734 (2010).

[135] N. H. Wan, T.-J. Lu, K. C. Chen, M. P. Walsh, M. E. Trusheim, L. De Santis, E. A. Bersin, I. B. Harris, S. L. Mouradian, I. R. Christen, E. S. Bielejec and D. Englund, Large-scale integration of artificial atoms in hybrid photonic circuits, Nature **583**, 226-231 (2020).

[136] J. Barreiro, N. Langford, N. Peters, and P. Kwiat, Generation of Hyperentangled Photon Pairs, Phys. Rev. Lett. **95**, 260501 (2005).

[137] R. W. Boyd, *Nonlinear optics*, (Academic Press 1992).

[138] J. H. Shapiro, Computational ghost imaging, Phys. Rev. A **78**, 061802 (2008).

[139] J. C. Howell, R. S. Bennink, S. J. Bentley, and R. W. Boyd, Realization of the einstein-podolsky-rosen paradox using momentumand position-entangled photons from spontaneous parametric down conversion, Phys. Rev. Lett. **92**, 210403 (2004).

[140] L. Mandel, and E. Wolf, Coherence properties of optical fields, Rev. Mod. Phys. **37**, 231 (1965).

[141] R. H. Brown, and R. Q. Twiss, Correlation between photons in two coherent beams of light, Nature **177**, 27-29 (1956).

[142] M. Kolobov, The spatial behavior of nonclassical light, Rev. Mod. Phys. **71**, 1539 (1999).

[143] M. Scholz, L. Koch, and O. Benson, Statistics of narrow-band single photons for quantum memories generated by ultrabright cavity-enhanced parametric down-conversion, Phys. Rev. Lett. **102**, 063603 (2009).

[144] J. D. Franson, Bell inequality for position and time, Phys. Rev. Lett. **62**, 2205 (1989).

[145] A. K. Ekert, Quantum cryptography based on Bell's theorem, Phys. Rev. Lett. **67**, 661 (1991).

[146] S. Pirandola, B. R. Bardhan, T. Gehring, C. Weedbrook, and S. Lloyd, Advances in photonic quantum sensing, Nat. Photon. **12**, 724-733 (2018).

[147] B.-G. Englert, Fringe visibility and which-way information: an inequality, Phys. Rev. Lett. **77**, 2154 (1996).

[148] X. Y. Zou, L. J. Wang, L. Mandel, Induced coherence and indistinguishability in optical interference, Phys. Rev. Lett. **67**, 318 (1991).

[149] C. K. Hong, Z. Y. Ou, L. Mandel, Measurement of subpicosecond time intervals between two photons by interference, Phys. Rev. Lett. **59**, 2044 (1987).

[150] L.-K. Chen, H.-L. Yong, P. Xu, X.-C. Yao, T. Xiang, Z.-D. Li, C. Liu, H. Lu, N.-L. Liu, L. Li, T. Yang, C.-Z. Peng, B. Zhao, Y.-A. Chen, and J.-W. Pan, Experimental nested purification for a linear optical quantum repeater, Nat. Photon. **11**, 695-699 (2017).

[151] A. I. Lvovsky, B. C. Sanders, and W. Tittel, Optical quantum memory, Nat. Photon. **3**, 706-714 (2009).

[152] E. Saglamyurek, N. Sinclair, J. Jin, J. A. Slater, D. Oblak, F. Bussières, M. George, R. Ricken, W. Sohler, and W. Tittel, Broadband waveguide quantum memory for entangled photons, Nature **469**, 512-515 (2011).

[153] I. Craiciu, M. Lei, J. Rochman, J. M. Kindem, J. G. Bartholomew, E. Miyazono, T. Zhong, N. Sinclair, and A. Faraon, Nanophotonic quantum storage at telecommunication wavelength, Phys. Rev. Appl. **12**, 024062 (2019).

[154] I. Craiciu, M. Lei, J. Rochman, J. G. Bartholomew, and A. Faraon, Multifunctional on-chip storage at telecommunication wavelength for quantum networks, Optica **8**, 114-121 (2021).

[155] R. Raussendorf and H. J. Briegel, A One-Way Quantum Computer, Phys. Rev. Lett. **86**, 5188

(2001).

[156] M. J. Bremner, C. M. Dawson, J. L. Dodd, A. Gilchrist, A. W. Harrow, D. Mortimer, M. A. Nielsen, and T. J. Osborne, Practical Scheme for Quantum Computation with Any Two-Qubit Entangling Gate, Phys. Rev. Lett. **89**, 247902 (2002).

[157] J. G. Rarity, and P. R. Tapster, Experimental violation of Bell's inequality based on phase and momentum, Phys. Rev. Lett. **64**, 2495 (1990).

[158] D. F. V. James, P. G. Kwiat, W. J. Munro, and A. G. White, Measurement of qubits, Phys. Rev. A. **64**, 052312 (2001).

[159] R. T. Thew, K. Nemoto, A. G. White, and W. J. Munro, Qudit quantum-state tomography, Phys. Rev. A. **66**, 012303 (2002).

[160] J. L. O'Brien, G. J. Pryde, A. Gilchrist, D. F. V. James, N. K. Langford, T. C. Ralph, and A. G. White, Quantum process tomography of a controlled-NOT gate, Phys. Rev. Lett. **93**, 080502 (2004).

[161] M. A. Nielsen and I. L. Chuang, *Quantum Computation and Information*, (Cambridge University Press 2010).

[162] N. Brunner, D. Cavalcanti, S. Pironio, V. Scarani, and S. Wehner, Bell nonlocality, Rev. Mod. Phys. **86**, 419 (2014).

[163] J. S. Bell, On the Problem of Hidden Variables in Quantum Mechanics, Rev. Mod. Phys. **38**, 447 (1966).

[164] H. M. Wiseman, S. J. Jones, and A. C. Doherty, Steering, Entanglement, Nonlocality, and the Einstein-Podolsky-Rosen Paradox, Phys. Rev. Lett. **98**, 140402 (2007).

[165] P. Skrzypczyk, M. Navascués, and D. Cavalcanti, Quantifying Einstein-Podolsky-Rosen Steering, Phys. Rev. Lett. **112**, 180404 (2014).

[166] D. J. Saunders, S. J. Jones, H. M. Wiseman, and G. J. Pryde, Experimental EPR-steering using Bell-local states, Nat. Phys. **6**, 845-849 (2010).

[167] J. F. Clauser, M. A. Horne, A. Shimony, and R. A. Holt, Proposed Experiment To Test Local Hidden-Variable Theories, Phys. Rev. Lett. **23**, 880 (1969).

[168] D. Collins, N. Gisin, N. Linden, S. Massar, S. Popescu, Bell inequalities for arbitrarily high-dimensional systems, Phys. Rev. Lett. **88**, 040404 (2002).

[169] R. T. Thew, A. Acin, H. Zbinden, N. Gisin, Bell-type test of energy-time entangled qutrits, Phys. Rev. Lett. **93**, 010503 (2004).

[170] J. Wang, D. Bonneau, M. Villa, J. W. Silverstone, R. Santagati, S. Miki, T. Yamashita, M. Fujiwara, M. Sasaki, H. Terai, M. G. Tanner, C. M. Natarajan, R. H. Hadfield, J. L. O'Brien, and M. G. Thompson, Chip-to-chip quantum photonic interconnect by path-polarization interconversion, Optica **3**, 407-413 (2016).

[171] T. Kim, M. Fiorentino, and F. N. C. Wong, Phase-Stable Source of Polarization-Entangled Photons Using a Polarization Sagnac Interferometer, Phys. Rev. A **73**, 012316 (2006).

[172] O. Kuzucu and F. N. C. Wong, Pulsed Sagnac source of narrow-band polarization-entangled photons, Phys. Rev. A **77**, 032314 (2008).

[173] I. Marcikic, H. de Riedmatten, W. Tittel, V. Scarani, H. Zbinden, and N. Gisin, Time-bin entangled qubits for quantum communication created by femtosecond pulses, Phys. Rev. A **66**, 062308 (2002).

[174] C. Bernhard, B. Bessire, T. Feurer, A. Stefanov, Shaping frequency-entangled qudits, Phys. Rev. A. **88**, 032322 (2013).

[175] J. Brendel, N. Gisin, W. Tittel, and H. Zbinden, Pulsed energy-time entangled twin-photon

source for quantum communication, Phys. Rev. Lett. **82**, 2594 (1999).

[176] P. C. Humphreys, B. J. Metcalf, J. B. Spring, M. Moore, X.-M. Jin, M. Barbieri, W. Steven Kolthammer, and I. A. Walmsley, Linear Optical Quantum Computing in a Single Spatial Mode, Phys. Rev. Lett. **111**, 150501 (2013).

[177] R. Ikuta, R. Tani, M. Ishizaki, S. Miki, M. Yabuno, H. Terai, N. Imoto, and T. Yamamoto, Frequency-multiplexed photon pairs over 1000 modes from a quadratic nonlinear optical waveguide resonator with a singly resonant configuration, Phys. Rev. Lett. **123**, 193603 (2019).

[178] X. Cheng, M. C. Sarihan, K.-C. Chang, Y. S. Lee, F. Laudenbach, Z. Yu, and C. W. Wong, Design of Spontaneous Parametric Downconversion in Integrated Hybrid Si_xN_y-PPLN Waveguides for High-Dimension Qubit Entanglement, Opt. Express **27**, 30773-30787 (2019).

[179] X. Cheng, M. C. Sarihan, K.-C. Chang, Y. S. Lee, F. Laudenbach, Z. Yu, and C. W. Wong, Spontaneous parametric down-conversion in integrated hybrid Si_xN_y-PPLN waveguides for high-dimensional qubit entanglement, in Conference on Lasers and Electro-Optics, OSA Technical Digest (Optical Society of America, 2019), paper FTh1D.6.

[180] P. J. Mosley, J. S. Lundeen, B. J. Smith, and I. A. Walmsley, Conditional preparation of single photons using parametric downconversion: a recipe for purity, New J. Phys. **10**, 093011 (2008).

[181] F. Laudenbach, H. Hübel, M. Hentschel, P. Walther, and A. Poppe, Modelling parametric down-conversion yielding spectrally pure photon pairs, Opt. Express **24**, 2712-2727 (2016).

[182] C. Chen, C. Bo, M. Y. Niu, F. Xu, Z. Zhang, J. H. Shapiro, and F. N. C. Wong, Efficient generation and characterization of spectrally factorable biphotons, Opt. Express **25**, 7300-7312 (2017).

[183] F. Graffitti, J. K. Massicotte, A. Fedrizzi, and A. M. Brańczyk, Design considerations for high-purity heralded single-photon sources, Phys. Rev. A **98**, 053811 (2018).

[184] D. Bouwmeester, J. W. Pan, K. Mattle, M. Eibl, H. Weinfurter, and A. Zeilinger, Experimental

quantum teleportation, Nature **390**, 575-579 (1997).

[185] L.-K. Chen, H.-L. Yong, P. Xu, X.-C. Yao, T. Xiang, Z.-D. Li, C. Liu, H. Lu, N.-L. Liu, L. Li, T. Yang, C.-Z. Peng, B. Zhao, Y.-A. Chen, and J.-W. Pan, Experimental nested purification for a linear optical quantum repeater, Nat. Photon. **11**, 695-699 (2017).

[186] R. Kumar and J. Ghosh, Parametric down-conversion in ppLN ridge waveguide: a quantum analysis for efficient twin photons generation at 1550 nm, J. Opt. **20**, 075202 (2018).

[187] F. Laudenbach, R. B. Jin, C. Greganti, M. Hentschel, P. Walther, and H. Hübel, Numerical Investigation of Photon-Pair Generation in Periodically Poled $MTiOX_4$ (M = K, Rb, Cs; X = P, As), Phys. Rev. Appl. **8**, 024035 (2017).

[188] M. Fiorentino, S. M. Spillane, R. G. Beausoleil, T. D. Roberts, P. Battle, and M. W. Munro, Spontaneous parametric down-conversion in periodically poled KTP waveguides and bulk crystals, Opt. Express **15**, 7479-7488 (2007).

[189] T. Zhong, F. N. C. Wong, T. D. Roberts, and P. Battle, High performance photon- pair source based on a fiber-coupled periodically poled $KTiOPO_4$ waveguide, Opt. Express **17**, 12019-12030 (2009).

[190] N. Friis, G. Vitagliano, M. Malik, and M. Huber, Entanglement certification from theory to experiment, Nat. Rev. Phys. **1**, 72-87 (2019).

[191] D. Giovannini, J. Romero, J. Leach, A. Dudley, A. Forbes, and M. J. Padgett, Characterization of high-dimensional entangled systems via mutually unbiased measurements, Phys. Rev. Lett. **110**, 143601 (2013).

[192] A. Martin, T. Guerreiro, A. Tiranov, S. Designolle, F. Fröwis, N. Brunner, M. Huber, and N. Gisin, Quantifying photonic high-dimensional entanglement, Phys. Rev. Lett. **118**, 110501 (2017).

[193] J. Bavaresco, N. H. Valencia, C. Klöckl, M. Pivoluska, P. Erker, N. Friis, M. Malik, and M.

Huber, Measurements in two bases are sufficient for certifying high-dimensional entanglement, Nat. Phys. **14**, 1032-1037 (2018).

[194] J.-P. W. MacLean, J. M. Donohue, and K. J. Resch, Direct characterization of ultrafast energy-time entangled photon pairs, Phys. Rev. Lett. **120**, 053601 (2018).

[195] J. M. Lukens, H. H. Lu, B. Qi, P. Lougovski, A. M. Weiner, and B. P. Williams, All-optical frequency processor for networking applications, J. Lightwave Technol. **38**, 1678-1687 (2020).

[196] A. Weiner, *Ultrafast optics* (Vol. 72), (John Wiley & Sons 2009).

[197] S.-W. Huang, H. Zhou, J. Yang, J. F. McMillan, A. Matsko, M. Yu, D.-L. Kwong, L. Maleki, and C. W. Wong, Mode-Locked Ultrashort Pulse Generation from On-Chip Normal Dispersion Microresonators, Phys. Rev. Lett. **114**, 053901 (2015).

[198] X. Xue, Y. Xuan, Y. Liu, P.-H. Wang, S. Chen, J. Wang, D. E. Leaird, M. Qi, and A. M. Weiner, Mode-locked dark pulse Kerr combs in normal-dispersion microresonators, Nat. Photon. **9**, 594-600 (2015).

[199] J. H. Shapiro, Coincidence dips and revivals from a Type-II optical parametric amplifier, Technical Digest of Topical Conference on Nonlinear Optics, paper FC7-1, Maui, HI, (2002).

[200] P. G. Kwiat, K. Mattle, H. Weinfurter, A. Zeilinger, A. V. Sergienko, and Y. Shih, New high-intensity source of polarization-entangled photon pairs, Phys. Rev. Lett. **75**, 4337 (1995).

[201] V. Giovannetti, L. Maccone, J. H. Shapiro, and F. N. C. Wong, Generating entangled two-photon states with coincident frequencies, Phys. Rev. Lett. **88**, 183602 (2002).

[202] X. Xu, Z. Xie, J. Zheng, J. Liang, T. Zhong, M. Yu, S. Kocaman, G. Q., Lo, D. L. Kwong, D. R. Englund, F. N. C. Wong, and C. W. Wong, Near-infrared Hong-Ou-Mandel interference on a silicon quantum photonic chip, Opt. Express **21**, 5014-5024 (2013).

[203] Y. Chen, S. Ecker, J. Bavaresco, T. Scheidl, L. Chen, F. Steinlechner, M. Huber, and R. Ursin, Verification of high-dimensional entanglement generated in quantum interference, Phys. Rev. A **101**, 032302 (2020).

[204] O. Kuzucu, F. N. C. Wong, S. Kurimura, and S. Tovstonog, Joint temporal density measurements for two-photon state characterization, Phys. Rev. Lett. **101**, 153602 (2008).

[205] S. Sensarn, G. Y. Yin, and S. E. Harris, Observation of nonlocal modulation with entangled photons, Phys. Rev. Lett. **103**, 163601 (2009).

[206] U. Herzog, M. Scholz, and O. Benson, Theory of biphoton generation in a single-resonant optical parametric oscillator far below threshold, Phys. Rev. A **77**, 023826 (2008).

[207] M. Scholz, F. Wolfgramm, U. Herzog, and O. Benson, Narrow-band single photons from a single-resonant optical parametric oscillator far below threshold, Appl. Phys. Lett. **91**, 191104 (2007).

[208] T. Yamazaki, R. Ikuta, T. Kobayashi, S. Miki, F. China, H. Terai, N. Imoto, and, T. Yamamoto, Massive-mode polarization entangled biphoton frequency comb, arXiv:2101.04410 (2020).

[209] S. Wengerowsky, S. Koduru, F. Steinlechner, H. Hubel, and R. Ursin, An entanglement-based wavelength-multiplexed quantum communication network, Nature **564**, 225-228 (2018).

[210] X. M. Hu, Y. Guo, B. H. Liu, Y. F. Huang, C. F. Li, and G. C. Guo, Beating the channel capacity limit for superdense coding with entangled ququarts, Sci. Adv. **4**, eaat9304 (2018).

[211] T. M. Graham, H. J. Bernstein, T.-C. Wei, M. Junge, and P. G. Kwiat, Superdense teleportation using hyperentangled photons, Nat. Commun. **6**, 1-9 (2015).

[212] J. Wang, F. Sciarrino, A. Laing, and M. G. Thompson, Integrated photonic quantum technologies, Nat. Photon. **14**, 273-284 (2020).

[213] S. Wehner, D. Elkouss, and R. Hanson, Quantum internet: a vision for the road ahead, Science **362**, eaam9288 (2018).

[214] N. Sangouard, C. Simon, H. De Riedmatten, and N. Gisin, Quantum repeaters based on atomic ensembles and linear optics, Rev. Mod. Phys. **83**, 33 (2011).

[215] T. Ikuta, and H. Takesue, Four-dimensional entanglement distribution over 100 km, Sci. Rep. **8**, 7 (2018).

[216] A. Lenhard, M. Bock, C. Becher, S. Kucera, J. Brito, P. Eich, P. Müller, and J. Eschner, Telecom-heralded single-photon absorption by a single atom, Phys. Rev. A **92**, 063827 (2015).

[217] O. Slattery, L. Ma, K. Zong, and X. Tang, Background and review of cavity-enhanced spontaneous parametric down-conversion, J. of Research of the Natl Institute of Standards and Techno. **124**, 1 (2019).

[218] E. Pomarico, B. Sanguinetti, N. Gisin, R. Thew, H. Zbinden, G. Schreiber, A. Thomas, and W. Sohler, Waveguide-based OPO source of entangled photon pairs, New J. Phys. **11**, 113042 (2009).

[219] C. S. Chuu, G. Y. Yin, and S. E. Harris, A miniature ultrabright source of temporally long, narrowband biphotons, Appl. Phys. Lett. **101**, 051108 (2012).

[220] J. Fekete, D. Rieländer, M. Cristiani, and H. de Riedmatten, Ultranarrow-band photon-pair source compatible with solid state quantum memories and telecommunication networks, Phys. Rev. Lett. **110**, 220502 (2013).

[221] A. Ahlrichs, and O. Benson, Bright source of indistinguishable photons based on cavity-enhanced parametric down-conversion utilizing the cluster effect, Appl. Phys. Lett. **108**, 021111 (2016).

[222] N. Fiaschi, B. Hensen,, A. Wallucks, R. Benevides, J. Li, T. P. M. Alegre and S. Gröblacher, Optomechanical quantum teleportation, Nat. Photon. **15**, 817-821 (2021).

[223] J. A. Usman, J. Ling, J, Staffa, M, Li, Y, He, and Q. Lin, Ultrabroadband Entangled Photons on a Nanophotonic Chip, Phys. Rev. Lett. **127**, 183601 (2021).

[224] Y. Wang, K. D. Jöns, and Z. Sun, Integrated photon-pair sources with nonlinear optics, Appl. Phys. Rev. **8**, 011314 (2021).

[225] M. Rambach, A. Nikolova, T. J. Weinhold, and A. G. White, Sub-megahertz linewidth single photon source, APL Photon. **1**, 096101 (2016).

[226] C. Liu, Y. Sun, L. Zhao, S. Zhang, M. M. T. Loy, and S. Du, Efficiently loading a single photon into a single-sided fabry-perot cavity, Phys. Rev. Lett. **113**, 133601 (2014).

[227] B. Srivathsan, G. K. Gulati, A. Cere, B. Chng, and C. Kurtsiefer, Reversing the temporal envelope of a heralded single photon using a cavity, Phys. Rev. Lett. **113**, 163601 (2014).

[228] A. Tiranov, S. Designolle, E. Z. Cruzeiro, J. Lavoie, N. Brunner, M. Afzelius, M. Huber, and N. Gisin, Quantification of multidimensional entanglement stored in a crystal, Phys. Rev. A **96**, 040303 (2017).

[229] C. E. Kuklewicz, E. Keskiner, F. N. C. Wong, and J. H. Shapiro, A high-flux entanglement source based on a doubly resonant optical parametric amplifier, J. Opt. Soc. Am. B **4**, S162-S168 (2002).

[230] C. E. Kuklewicz, F. N. C. Wong, and J. H. Shapiro, Time-bin-modulated biphotons from cavity-enhanced down-conversion, Phys. Rev. Lett. **97**, 223601 (2006).

[231] X. H. Bao, Y. Qian, J. Yang, H. Zhang, Z. B. Chen, T. Yang, and J. W. Pan, Generation of narrow-band polarization-entangled photon pairs for atomic quantum memories, Phys. Rev. Lett. **101**, 190501 (2008).

[232] K. H. Luo, H. Herrmann, S. Krapick, B. Brecht, R. Ricken, V. Quiring, H. Suche, W. Sohler,

and C. Silberhorn, Direct generation of genuine single-longitudinal-mode narrowband photon pairs, New J. Phys. **17**, 073039 (2015).

[233] P. J. Tsai, and Y. C. Chen, Ultrabright, narrow-band photon-pair source for atomic quantum memories, Quan. Sci. Technol. **3**, 034005 (2018).

[234] A. Moqanaki, F. Massa, and P. Walther, Novel single-mode narrow-band photon source of high brightness tuned to cesium D2 line, APL Photon. **4**, 090804 (2019).

[235] A. Seri, D. Lago-Rivera, A. Lenhard, G. Corrielli, R. Osellame, M. Mazzera, and H. de Riedmatten, Quantum storage of frequency-multiplexed heralded single photons, Phys. Rev. Lett. **123**, 080502 (2019).

[236] K. Niizeki, D. Yoshida, K. Ito, I. Nakamura, N. Takei, K. Okamura, M. Y. Zheng, X. P. Xie, and T. Horikiri, Two-photon comb with wavelength conversion and 20-km distribution for quantum communication, Commun. Phys. **3**, 1-7 (2020).

[237] J. Liu, J. Liu, P. Yu, and G. Zhang, Sub-megahertz narrow-band photon pairs at 606 nm for solid-state quantum memories, APL Photon. **5**, 066105 (2020).

[238] H. De Riedmatten, I. Marcikic, V. Scarani, W. Tittel, H. Zbinden, and N. Gisin, Tailoring photonic entanglement in high-dimensional Hilbert spaces, Phys. Rev. A **69**, 050304 (2004).

[239] L. Zhang, C. Silberhorn, and I. A. Walmsley, Secure quantum key distribution using continuous variables of single photons, Phys. Rev. Lett. **100**, 110504 (2008).

[240] H. Zhou, V. Chandar, and G. Wornell, Low-density random matrices for secret key extraction, In 2013 IEEE International Symposium on Information Theory (2607-2611), IEEE.

[241] H. Zhou, L. Wang, and G. Wornell, Layered schemes for large-alphabet secret key distribution, In 2013 Information Theory and Applications Workshop (1-10), IEEE.

[242] T. Zhong, and F. N. C. Wong, Nonlocal cancellation of dispersion in Franson interferometry, Phys. Rev. A **88**, 020103 (2013).

[243] D. Lachance-Quirion, S. P. Wolski, Y. Tabuchi, S. Kono, K. Usami, and Y. Nakamura, Entanglement-based single-shot detection of a single magnon with a superconducting qubit, Science **367**, 425-428 (2020).

[244] A. W. Elshaari, W. Pernice, K. Srinivasan, O. Benson, and V. Zwiller, Hybrid integrated quantum photonic circuits, Nat. Photon. **14**, 285-298 (2020).

[245] A. Javadi, D. Ding, M. H. Appel, S. Mahmoodian, M. C. Löbl, I. Söllner, R. Schott, C. Papon, T. Pregnolato, S. Stobbe, L. Midolo, T. Schröder, A. D. Wieck, A. Ludwig, R. J. Warburton, and P. Lodahl, Spin–photon interface and spin-controlled photon switching in a nanobeam waveguide, Nat. Nanotechnol. **13**, 398-403 (2018).

[246] W. Jiang, C. J. Sarabalis, Y. D. Dahmani, R. N. Patel, F. M. Mayor, T. P. McKenna, R. Van Laer, and A. H. Safavi-Naeini, Efficient bidirectional piezo-optomechanical transduction between microwave and optical frequency, Nat. Commun. **11**, 1-7 (2020).

[247] Y. Zhong, H.-S. Chang, A. Bienfait, É. Dumur, M.-H. Chou, C. R. Conner, J. Grebel, R. G. Povey, H. Yan, D. I. Schuster, and A. N. Cleland, Deterministic multi-qubit entanglement in a quantum network, Nature **590**, 571-575 (2021).

[248] M. Fiorentino, T. Kim, and F. N. C. Wong, Single-photon two-qubit SWAP gate for entanglement manipulation, Phys. Rev. A **72**, 012318 (2005).

[249] Y. Zhang, F. S. Roux, T. Konrad, M. Agnew, J. Leach, and A. Forbes, Engineering two-photon high-dimensional states through quantum interference, Sci. Adv. **2**, e1501165 (2016).

[250] K. Wang, J. G. Titchener, S. S. Kruk, L. Xu, H.-P. Chung, M. Parry, I. I. Kravchenko, Y.-H. Chen, A. S. Solntsev, Y. S. Kivshar, D. N. Neshev, A. A. Sukhorukov, Quantum metasurface for multiphoton interference and state reconstruction, Science **361**, 1104-1108 (2018).

[251] M. Fiorentino and F. N. C. Wong, Deterministic controlled-NOT gate for single-photon two-qubit quantum logic, Phys. Rev. Lett. **93**, 070502 (2004).

[252] K. H. Kagalwala, G. Di Giuseppe, A. F. Abouraddy, and B. E. A. Saleh, Single-photon three-qubit quantum logic using spatial light modulators, Nat. Commun. **8**, 1-11 (2017).

[253] M. Zhang, L. Feng, M. Li, Y. Chen, L. Zhang, D. He, G. Guo, G. Guo, X. Ren, and D. Dai, Supercompact photonic quantum logic gate on a silicon chip, Phys. Rev. Lett. **126**, 130501 (2021).

[254] J.-P. Li, X. Gu, J. Qin, D. Wu, X. You, H. Wang, C. Schneider, S. Höfling, Y.-H. Huo, C.-Y. Lu, N.-L. Liu, L. Li, and J.-W. Pan, Heralded nondestructive quantum entangling gate with single-photon sources, Phys. Rev. Lett. **126**, 140501 (2021).

[255] E. Desurvire, *Classical and quantum information theory: an introduction for the telecom scientist*, (Cambridge University Press 2009).

[256] T. Barwicz, M. R. Watts, M. A. Popović, P. T. Rakich, L. Socci, F. X. Kärtner, E. P. Ippen, and H. I. Smith, Polarization-transparent microphotonic devices in the strong confinement limit, Nat. Photon. **1**, 57-60 (2007).

[257] Y. Su, Y. Zhang, C. Qiu, X. Guo, and L. Sun, Silicon photonic platform for passive waveguide devices: materials, fabrication, and applications, Adv. Mater. Technol. **5**, 1901153 (2020).

[258] Y. Kim, Y. S. Teo, D. Ahn, D.-G. Im, Y.-W. Cho, G. Leuchs, L. L. Sánchez-Soto, H. Jeong, and Y.-H. Kim, Universal compressive characterization of quantum dynamics, Phys. Rev. Lett. **124**, 210401 (2020).

[259] X. Gao, M. Erhard, A. Zeilinger, and M. Krenn, Computer-inspired concept for high-dimensional multipartite quantum gates, Phys. Rev. Lett. **125**, 050501 (2020).

[260] F. Flamini, N. Spagnolo, and F. Sciarrino, Photonic quantum information processing: a review,

Rep. Prog. Phys. **82**, 016001 (2019).

[261] B. M. Terhal, and P. Horodecki, Schmidt number for density matrices, Phys. Rev. A **61**, 040301 (2000).

[262] J. H. Eberly, Schmidt analysis of pure-state entanglement, Laser Phys. **16**, 921-926 (2006).

[263] K. Zielnicki, K. Garay-Palmett, D. Cruz-Delgado, H. Cruz-Ramirez, M. F. O'Boyle, B. Fang, V. O. Lorenz, A. B. U'Ren, and P. G. Kwiat, Joint spectral characterization of photon-pair sources, J. Mod. Opt. **65**, 1141-1160 (2018).

[264] K. Goi, A. Oka, H. Kusaka, K. Ogawa, T.-Y. Liow, X. Tu, G.-Q. Lo, and D.-L. Kwong, Low-loss partial rib polarization rotator consisting only of silicon core and silica cladding, Opt. Lett. **40**, 1410-1413 (2015).

[265] T. Horikawa, D. Shimura, H. Okayama, S. Jeong, H. Takahashi, J. Ushida, Y. Sobu, A. Shiina, M. Tokushima, K. Kinoshita, and T. Mogami, A 300-mm silicon photonics platform for large-scale device integration, IEEE J. Sel. Top. Quan. Electron. **24**, 1-15 (2018).

[266] M. R. Watts, H. A. Haus, and E. P. Ippen, Integrated mode-evolution-based polarization splitter, Opt. Lett. **30**, 967-969 (2005).

[267] H. Fukuda, K. Yamada, T. Tsuchizawa, T. Watanabe, H. Shinojima, and S. Itabashi, Polarization rotator based on silicon wire waveguides, Opt. Express **16**, 2628-2635 (2008).

[268] H. Fukuda, K. Yamada, T. Tsuchizawa, T. Watanabe, H. Shinojima, and S. Itabashi, Silicon photonic circuit with polarization diversity, Opt. Express **16**, 4872-4880 (2008).

[269] Y. Yue, L. Zhang, M. Song, R. G. Beausoleil, and A. E. Willner, Higher-order-mode assisted silicon-on-insulator 90 degree polarization rotator, Opt. Express **17**, 20694-20699 (2009).

[270] J. Zhang, T.-Y. Liow, M. Yu, G.-Q. Lo, and D.-L. Kwong, Silicon waveguide based TE mode

converter, Opt. Express **18**, 25264-25270 (2010).

[271] L. Chen, C. R. Doerr, and Y.-K. Chen. Compact polarization rotator on silicon for polarization-diversified circuits, Opt. Lett. **36**, 469-471 (2011).

[272] W. D. Sacher, Y. Huang, L. Ding, T. Barwicz, J. C. Mikkelsen, B. J. F. Taylor, G.-Q. Lo, and J. K. S. Poon, Polarization rotator-splitters and controllers in a Si_3N_4-on-SOI integrated photonics platform, Opt. Express **22**, 11167-11174 (2014).

[273] J. Wang, S. He, and D. Dai, On-chip silicon 8-channel hybrid (de)multiplexer enabling simultaneous mode- and polarization-division-multiplexing, Laser Photon. Rev. **8**, L18-L22 (2014).

[274] J. Zhang, M. Yu, G. Lo and D.-L. Kwong, Silicon waveguide-based mode-evolution polarization rotator, Proc. SPIE 7719, Silicon Photonics and Photonic Integrated Circuits II, 77190C (2010).

[275] S. K. Selvaraja, G. Murdoch, A. Milenin, C. Delvaux, P. Ong, S. Pathak, D. Vermeulen, G. Sterckx, G. Winroth, P. Verheyen, W. Bogaerts, R. Baets, J. Van Campenhout, and P. Absil, Advanced 300-mm waferscale patterning for silicon photonics devices with record low loss and phase errors, in Proc. Opto-Electronics and Communications Conference, Busan, South Korea, PDP2-2 (2012).

[276] T. Horikawa, D. Shimura, and T. Mogami, Low-loss silicon wire waveguides for optical integrated circuits, MRS Commun. **6**, 9-15 (2016).

[277] B. S. Tsirelson, Quantum generalizations of Bell's inequality, Lett. Math. Phys. **4**, 93-100 (1980).